

Estimating Rock Strength of Moderately Fractured EDZ in Hard Rock Tunnels: *Äspö
Hard Rock Laboratory*

by

Yun Lu

A thesis submitted in partial fulfillment of the requirements for the degree of

Doctor of Philosophy

in

Geotechnical Engineering

Civil and Environmental Engineering

University of Alberta

© Yun Lu, 2014

Abstract

Underground openings create various excavation-induced responses. The most noticeable response is the readily observed excavation damaged zone (EDZ) where the mechanical properties of the rock mass have been irreversibly altered, i.e., damaged. Within this damaged zone the stresses and displacements cannot be predicted using elastic theory. This damaged zone contains a region of reduced stresses and increased displacements and forms a rock mass ring that can contribute to the stability of the underground opening. This concept is well known and provided the stability of EDZ support ring is maintained, large underground excavations can be created at a great depth. However, predicting and quantifying the extent and properties of the rock mass mechanical damage that can occur in the EDZ has remained a challenge.

The damage that occurs in the EDZ in typical strong rocks (ISRM Class R3 to R6) can be characterised as stress-induced and/or blast-induced fractures. These fractures can range from the millimetre to the metre scale. It is well known that the addition of cracks to a solid changes its mechanical properties and characteristics. Hence to quantify these changes both geometry and properties of the induced fractures must be known. Once these changes are quantified, the biggest challenge is translating these changes into rock mass mechanical properties.

Recent developments with numerical methods have shown that discrete element modelling offers the most realistic methodology for estimating rock mass properties, provided the characteristics and geometry of the discrete fractures are known with confidence. The methodology, which has been termed the

Grain-based Model (GBM), can incorporate both intact blocks and discrete fractures. The GBM utilizes a voronoi tessellation scheme to simulate the microstructure of rocks by creating randomly composed blocks that are similar to the polygonal grains of intact rocks. The GBM can be calibrated to the conventional laboratory tests (UCS test, direct tension test and triaxial compression test) on intact rocks. It is shown that such calibration is not path dependent, i.e., calibrating to the direct tensile strength is able to predict the compressive strength. Once the GBM calibration with the intact properties was carried out, large-scale discrete fractures were added to the GBM to determine the effect of these fractures on the rock mass mechanical properties.

To validate the GBM approach, several models were developed and the mechanical responses were compared to published results. The models increased in complexity from a single inclined fracture to two regular and uniformly spaced fracture sets. The responses from the GBM models were in good agreement with the results from the physical models. When the fractures are not uniformly spaced there is no simple means to establish the complex geometry of the fractures. At the Äspö Hard Rock Laboratory in Sweden, a unique experiment was carried out to establish the geometry of the excavation-induced and naturally occurring fractures found at the boundary of tunnel excavated by careful drill-and-blast technique. The fractures were measured at the mm scale. A methodology was developed to import the geometry of the fractures into the GBM. This model was then loaded to establish the mechanical properties. The results from the models were compared to the rock mass strength derived using the empirical Hoek-Brown failure criteria. The finding from the research demonstrates that the GBM provides a reasonable approach to establish the rock mass strength at the tunnel scale. The

methodology also provides an approach for establishing the effect of the blast-induced damage on the rock mass strength.

Acknowledgements

I would like to express my sincere appreciation to my wife, Yao HU who has been supporting me all the time, no matter how tough the obstacles we have met in life since we came to Canada.

I would like to thank my supervisor, Dr. Derek Martin, who recruited me as his student to carry out this interesting research. He treats me kindly and also strictly just as a father instructs his son. Acknowledgements are also given to the examination committee who will take their precious time to assess my thesis proposal and give me their invaluable advice, suggestions and critical comments on it.

I am very grateful to my parents and parents-in-law in China for their understanding and financial support. I can feel their love even when I am studying on a far-away continent.

I would also like to thank Dr. Lan hengxing for his consistent assistance to me regarding many instructions on the software codes of UDEC. Appreciation also is given to my colleagues: Ying Zhang, Ming Liu, Yifei Cui, Tanyu Xiong, and Xunhao Li, etc.

Finally, I wish to thank NSERC (Natural Sciences and Engineering Research Council of Canada), Swedish Nuclear Fuel and Waste Management Co. (SKB) for supporting my research work.

Table of Contents

Abstract	ii
Acknowledgements	v
List of Figures.....	ix
List of Tables.....	xvii
1 Introduction.....	1
1.1 Problem Statement.....	2
1.2 Äspö Hard Rock Laboratory	5
1.3 Research Objective and Methodology	7
1.4 Outline of Thesis.....	8
2 Literature Review.....	11
2.1 Previous Studies on Excavation Damage Zone (EDZ)	11
2.1.1 The EDZ studies at the Underground Research Laboratory (URL)	13
2.1.2 Case studies of numerically modelling of the EDZ.....	19
2.2 Numerical Modelling of Rock Failure	22
2.2.1 Continuum approach.....	22
2.2.2 Discrete element method (DEM).....	23
2.2.3 Theory and background of UDEC	24
2.3 Grained-based Model.....	27
2.3.1 Voronoi tessellation technique	28
2.3.2 Micro-structural model	29
2.3.3 Model calibration.....	30
2.4 Empirical Hoek-Brown Failure Criteria and GSI	31
2.5 Summary	36
3 GBM Parameters and Calibration	37
3.1 Calibration Parameters.....	37
3.1.1 Constitutive models for blocks and joints	38
3.1.2 Grain size distribution and minerals	40

3.1.3	Contact stiffness and properties.....	43
3.2	Calibration to uniaxial compressive strength.....	45
3.3	Triaxial Compressive Strength Calibration.....	48
3.4	GBM Failure Envelope for Lac du Bonnet Granite.....	54
3.5	Summary.....	55
4	Factors Affecting Strength and Stiffness of Intact Rock	56
4.1	Factors Influencing Laboratory Strength and Stiffness	56
4.1.1	Sample scale and stiffness	57
4.1.2	Sample scale and strength.....	61
4.1.3	Summary.....	65
4.2	Factors Affecting Grain-based Models	65
4.2.1	Selection of marble for GBM modelling.....	65
4.2.2	Modelling procedure.....	66
4.2.3	Effect of grain size.....	69
4.2.4	Effect of sample shape.....	73
4.2.5	Effect of scale	75
4.3	Effect of Model Grid on GBM.....	78
4.3.1	GBM uniform and randomized grid	79
4.3.2	Tensile stress development	80
4.4	Summary	83
5	Effect of Flaws on Rock Strength	85
5.1	Effect of a Single Inclined Flaw	86
5.2	Strength of Rocks Containing Regularly Distributed Flaws.....	90
5.2.1	Parallel inclined flaws	91
5.2.2	Discontinuous parallel vertical flaws.....	93
5.2.3	Uniform pattern of continuous flaws.....	97
5.3	Strength of Rocks Containing Random Discontinuous Flaws.....	101
5.3.1	Fracture intensity	102
5.3.2	Randomly distributed flaws.....	104
5.3.3	Influence of flaw interaction on rock strength.....	112

5.4	Summary	115
6	Effect of Natural and Blast-induced Fractures on Rock Strength.....	117
6.1	Modelling Tangential Stresses	117
6.2	Mapping Fractures in the EDZ – TASS Tunnel.....	122
6.3	GBM Methodology for Incorporating EDZ Fractures.....	127
6.4	GBM Fracture Properties.....	134
6.5	GBM Strength and Geological Fractures.....	135
6.6	GBM Strength and Blast-induced Fractures	149
6.7	Summary	157
7	Conclusions and Future Research	159
7.1	Modelling of Intact Rock.....	160
7.1.1	Effect of scale and sample shape	160
7.1.2	Effect of confining stress	161
7.2	Effect of Uniform Flaws on Strength.....	161
7.3	Effect of Natural Geological Fractures on Rock Strength	163
7.4	Effect of Blast-induced Fractures on Rock Strength.....	164
7.5	Future Research	165
	Bibliography	167
	Appendix A: Additional Results and Figures	178
A1.	Laboratory tests and modelling on the scale effect.....	178
A2.	Study on the geometric heterogeneity through tensile stress generation	184
	Appendix B: Primary FISH Functions used in Simulations	188
B1.	Setting up global variable	188
B2.	Assigning material properties.....	190
B3.	Read flaw distribution from existing files and make plot.....	191
	Appendix C: RQD for Block Containing Natural Fractures	193
	Appendix D: RQD for Block Containing Blast-induced & Natural fractures	197
	Appendix E: Conference Papers regarding Findings from SRM Approach	199

List of Figures

Figure 1-1:	The map of underground HRL, from [Andersson and Malmtorp, 2009]. The location of the TASS tunnel is labeled in the figure.	6
Figure 2-1:	Summary of the factors relating to the EDZ.	12
Figure 2-2:	Layout of the main working levels at the URL [Martino and Chandler, 2004].	14
Figure 2-3:	In situ stresses at the URL [Martino and Chandler, 2004].	15
Figure 2-4:	Layout of the excavations on the 420 Level at the URL (from [Martin’s thesis, 1993]).	16
Figure 2-5:	Progressive development of the V-Shaped notch failure in the Mine-by test tunnel [Martino and Chandler, 2004].	18
Figure 2-6:	The full development of the notch in the roof and floor in Mine-by test tunnel. (a) excavated using mechanical method; (b) a parallel circular tunnel excavated using drill and blast method [Martino and Chandler, 2004].	18
Figure 2-7:	Force-displacement law applied onto the contacts to find the contact force (modified from [Itasca, 2004]).	25
Figure 2-8:	Illustration of rounded corners in UDEC (modified from [Itasca, 2004]).	26
Figure 2-9:	Definition of domains and illustration of contacts between two adjacent blocks.	27
Figure 2-10:	Illustration of physical mechanisms for compression-induced tensile cracking and an example of bonded assembly of circular particles (modified from Potyondy [2004]).	28
Figure 2-11:	Schematic illustration of Voronoi tessellation (modified from [Shin’s Ph.D thesis, 2010]). (a) The convex hull around randomly generated interior points is formed by half planes. (b) The illustration of polygons formed by edges and vertices is shown under the voronoi tessellation.	29
Figure 2-12:	The illustration of generation of grain-based model and a flow chart presenting the process of numerical modeling. (a) Simulation process of grain-based model in UDEC combined with voronoi tessellation (modified from Lan [2010]), (b) UDEC rock ‘sample’	

	generated to simulate the grain structure.	31
Figure 2-13:	An illustration of rock block with three groups of joints which are set in different angles α and spaced at different distance S_j	34
Figure 2-14:	An illustration of the estimation of rock mass strengths using a combination of the Geological Strength Index (GSI) and the Hoek-Brown Failure criterion.	35
Figure 3-1:	Mean grain size of four representative minerals for LdB granite. (From Kelly et al., [1994])	41
Figure 3-2:	Grain size distributions of LdB granite (Adapted from Lan et al., [2010])	41
Figure 3-3:	Stress-strain response under uniaxial compressive test for Lac du Bonnet granite in which three important rock strength parameters modified from Martin and Chandler [1994].	46
Figure 3-4:	Stress-strain diagram from uniaxial compression tests comparing the laboratory tests to modelling results.	47
Figure 3-5:	Comparison of total and crack volumetric strain observed in laboratory tests and modelling results.	47
Figure 3-6:	Stress-strain curve of GBM and Lac du Bonnet laboratory test (confining stress equal to 20 MPa).	49
Figure 3-7:	A complete stress-strain curve of biaxial tests with confining stress ranging from 10 MPa to 60 MPa.	50
Figure 3-8:	Peak strengths from triaxial/biaxial tests with confining stress ranging from 10 MPa to 60 MPa (Lab data from CANMET).	51
Figure 3-9:	Identifying the onset of strain localization (σ_{cd}) from the GBM stress-strain response.	52
Figure 3-10:	The effect of confining stress on the volumetric strain for the grain based models for Lac du Bonnet granite.	53
Figure 3-11:	Failure envelopes for the Lac du Bonnet (CANMET) granite compared to that for the GBM. (Data from Table 3-6).	54
Figure 4-1:	Effect of diameter of cylindrical samples on the modulus. 28 days and 90 days age of concrete are shown in top and bottom respectively.	58
Figure 4-2:	Influence of specimen size and shape on the stress-strain curves of UCS tests for marble, modified from J. A. Hudson [1971].	59
Figure 4-3:	Effect of sample diameter on Young's modulus for Lac du Bonnet	

	granite, (modified from Martin et al. [2012]).....	60
Figure 4-4:	Effect of size of test cylinder on the compressive strength of concrete (Data from Blanks et al. [1935]).....	61
Figure 4-5:	Effect of sample diameter on the uniaxial compressive strength of Lac du Bonnet granite, modified from Martin et al. [2012].....	62
Figure 4-6:	Illustration of relationship between increasing diameter and UCS, data from Hoek and Brown [1980]. The UCS has been normalized to that of sample in 50-mm diameter. (Modified from Martin et al. [2012]).....	63
Figure 4-7:	Summary of UCS test results of strengths for concrete and rocks, normalized to the minimum representative diameter, together with the approach by Martin et al. [2012]......	64
Figure 4-8:	Mineral grain structure (under polarizing microscope) of the marble from a quarry at Gaoligong Mount. (Yunnan Province, China).....	66
Figure 4-9:	Grain-based model and mineral composition of the marble. (a) The polygonal grains from the voronoi generator. (b) the GBM with assigned grain properties (95% calcite and 5% quartz).	67
Figure 4-10:	(a) Example of the uniaxial compression test on marble; and (b) comparison of GBM stress-strain response with laboratory test data for the marbles.	68
Figure 4-11:	Illustration of scaling the same grain size distribution for various GBM with different mean grain sizes.	70
Figure 4-12:	The variation relationship between rock strength (UCS) and grain size for various types of marbles reported by different researchers.....	71
Figure 4-13:	Numerically obtained values of Young's modulus of marble under unconfined compressive loading, with increasing grain size.....	72
Figure 4-14:	Eight stress-strain curves representative of the models of marbles with eight different mean grain sizes.	72
Figure 4-15:	Effect of sample shape (length to diameter ratios) on the stress-strain response and peak strength for GBM marbles.	74
Figure 4-16:	Relation between normalized strength and ratio of the length to diameter.....	75
Figure 4-17:	The gradual reduction in normalised Young's moduli for the mean 1 mm and 3 mm grain size related to sample diameter.	77

Figure 4-18:	The reduction in normalised uniaxial compressive strength for the mean 1 mm and 3 mm grain size related to sample diameter, compared to the laboratory results and the results given by Equation (4-1) and Equation (4-2).	78
Figure 4-19:	Comparison of the grain size used for uniform square grid and the random grid in the GBM modelling.	79
Figure 4-20:	Stress-strain curves of two grid models showing rock strength and stiffness.	80
Figure 4-21:	Analysis of tensile stress occurred along contacts.	81
Figure 4-22:	Illustration of frequencies of tensile stress occurrence at grain contacts based on all the contacts, for three different sized samples whose diameter is 30 mm, 60 mm and 105 mm separately.	82
Figure 4-23:	The average crack length and cracking density versus sample diameter. The results are obtained from the recorded data through statistical analysis.	83
Figure 5-1:	Photo of rock mass containing intact blocks and fractures blocks.	85
Figure 5-2:	(a) Illustration of rock specimen with a single weak plane inclined at a certain angle of β to the maximum primary stress; (b) Variation of the peak strength of rock with a weak plane inclined at various angles β .	87
Figure 5-3:	Variation of the peak strength with different angles of inclination of the flaw, β .	90
Figure 5-4:	(a) The effect of number of flaws and (b) the effect of spacing between the flaws on the uniaxial compressive strength obtained using the GBM modeling.	95
Figure 5-5:	Variation of rock strengths as a function of distance between flaws and free surface.	97
Figure 5-6:	(a) Examples of the physical model samples used by Brown and Trollope [1970]; (b), (c), (d) and (e) GBMs with various joint geometries.	98
Figure 5-7:	Physical model test results from Brown and Trollope [1970] for gypsum plaster. The results have been normalized to unconfined compressive strength of the intact sample (20.75 MPa).	99
Figure 5-8:	GBM Lac du Bonnet granite peak strength for the model geometry given in Figure 5-6.	100
Figure 5-9:	Example of the randomly distributed flaws in a 76-mm-diameter	

drill core.....	102
Figure 5-10: Illustration of typical sample configurations of flaw distribution, and compared to the flaws in a drill core. The length of each flaw is constant.....	104
Figure 5-11: UCS results of LdB granite on the different-sized samples, compared to the intact UCS and fitted rock strength curves.....	108
Figure 5-12: The relation between fracture intensity and strengths for the GBM UCS values in Table 5-10 normalised to the intact UCS value.....	110
Figure 5-13: The onset of unstable crack growth in the GBM models and the associated fracture patterns.....	111
Figure 5-14: Illustration of flaw distribution in three samples with same specification (specimen size and number of flaws). (a) Closer flaw tips (small circles, $A_{in}=10$ mm); (b) Original flaw distribution (medium circles, $A_{in}=14.2$ mm); and (c) Separating flaw tips (large circles, $A_{in}=16.9$ mm).	113
Figure 5-15: Stress-strain curve of three samples with different flaw interaction patterns. Note that the sudden stress drop reflected from the lateral strain part of the curves is accentuated in the circled area.....	114
Figure 5-16: Illustration of crack propagation initiated from the flaw tip and coalescence process under uniaxial compressive loading.....	115
Figure 6-1: Tangential stress on the boundary of an excavation.....	118
Figure 6-2: Stress distribution around a circular hole in plane strain (for an isotropic, linearly elastic, homogeneous material).....	119
Figure 6-3: Boundary stresses at roof and sidewall around a circular opening, which as a function of the stress ratio, K	119
Figure 6-4: Illustration of model of rock mass around a circular opening at the tunnel roof and its boundary condition.	120
Figure 6-5: Tangential stress distribution in the block, subdivided into eight regions in which the tangential stress decreases from 167 MPa (left side) to 86 MPa (right side).....	121
Figure 6-6: Tangential stress (σ_{yy} -stresses) contours of rock mass block (shown in Figure 6-5) after redistribution caused by the cracking in the GBM.	122
Figure 6-7: Typical fracture patterns of rock blocks excavated from tunnel wall.....	123

Figure 6-8:	Illustration of the process of extracting blocks, sawing into slabs, photographing, digitizing and referencing in 3D. (From [Olsson et al., 2009])	124
Figure 6-9:	Photo of a rock block removal and the completed work.....	125
Figure 6-10:	Photo of the block after red-dye coloring. (a) Without fracture identification. (b) A digitized block showing blast, blast-induced and natural fractures. (From Olsson et al. [2009])	126
Figure 6-11:	Photo of tunnel wall showing the planned location of the blocks relative to the location of the blast-rounds.....	127
Figure 6-12:	Location of the blocks relative to the blast-rounds, and the boreholes used for wire-saws used to produce the geometry of each block.....	128
Figure 6-13:	Wire sawing of the blocks into 100-mm-thick slabs.....	128
Figure 6-14:	Example of the initial stage in detailed mapping process used to identify the fractures.	129
Figure 6-15:	Photos of block fracture pattern and the resulting digital mapping.	130
Figure 6-16:	Illustration of the digital fracture maps from three blocks.....	131
Figure 6-17:	Example of the irregular interlocking geometry of a natural fracture.....	132
Figure 6-18:	Example of the GBM for Block 36-01. The fracture pattern is identical to that obtained from the field mapping.	133
Figure 6-19:	Shear model for: (a) Through-going fracture; (b) Open discontinuous flaw.....	135
Figure 6-20:	Strengths from GBM biaxial tests compared to the Hoek-Brown failure envelope (UCS=211 MPa, $m_i=211/10$, $s=1$). The block fracturing is given in Figure 6-16.....	136
Figure 6-21:	Strengths from GBM biaxial compressive tests.....	137
Figure 6-22:	50% Tangent modulus versus confining stresses.....	139
Figure 6-23:	Illustration of the methodology used to establish the average RQD for each Block.....	141
Figure 6-24:	Relationship between average RQD values for different blocks and the P_{21} values for the same blocks.....	142
Figure 6-25:	Quantification of GSI by Joint Condition and RQD, from [Hoek et al., 2013].	143

Figure 6-26: Comparison of Grain-based model strengths and the GSI values providing a reasonable fit using the Hoek-Brown failure criterion (UCS=211 MPa, $m_i=211/10$. The top black line represents the Hoek-Brown failure envelope for the intact rock.....	145
Figure 6-27: Correlation between the GSI values obtained from the RQD values and the GSI values back-calculated using the Grain-based model.	146
Figure 6-28: Comparison of UCS versus fracture intensity (P_{21}) for the Grain-based models using Blocks 36B, 37B and 39B.	147
Figure 6-29: Relationship for GBM-UCS and RQD.	147
Figure 6-30: Comparison of UCS versus fracture intensity (P_{21}) for various GBMs with discrete flaws and natural fractures.	148
Figure 6-31: Illustration of Grain-based models for B36-06 (left) and B36-08 (right) with both blast-induced fractures and natural open fractures.....	149
Figure 6-32: Effect of blasting on the fracture intensity, P_{21} and RQD, for blocks 36B-06 and 36B-08.....	151
Figure 6-33: Effect of blast-induced fracturing on the GBM uniaxial compressive strengths (UCS) compared to the strength relationship established for the blocks with the natural fractures.	152
Figure 6-34: The blast-induced fracturing in block 36B-08 resulted in a near continuous through-going fracture (dashed red ellipse) inclined to the direction of loading.	152
Figure 6-35: Hoek-Brown failure envelopes for the GBM strength for Blocks 36B-06 and 36B-08 with/without blast-induced fractures and the associated GSI values.....	155
Figure 6-36: Blast-induced reduction in GBM strength with confining stress.	156
Figure 6-37: Hoek-Brown failure envelopes for the GBM strength for Block 36B-06 and 36B-08 with/without blast-induced fractures and the associated GSI values. (Note, the confining stress is plotted as a log-scale).....	156
Figure A. 1: Stress-strain curve for sample E072 of UCS test.	178
Figure A. 2: Laboratory tests results for Marbles. (a) Sample 4-3#. (b) Sample 4-4#. (c) Sample (4-5#). (d). Mohr-Coulomb failure envelop for four sets of data.	181
Figure A. 3: Peak strengths for various rocks with a confinement of 5MPa.....	182

Figure A. 4: Comparison of the rock blocks between a regular voronoi model (top) and a homogeneous model (bottom).	184
Figure A. 5: UCS results for the grain-based model and regular grain models (honeycomb shape voronoi) in three grain sizes.	185
Figure A. 6: Statistical analysis of tensile stress for two different models. (a) the regular voronoi model; (b) homogeneous model.	186

List of Tables

Table 2-1:	In situ stress tensors measured at the 240 and 420 Levels of the URL [Martino and Chandler, 2004].	16
Table 2-2:	Research teams and their numerical tools [J. A. Hudson et. al., 2009].	20
Table 2-3:	The Geological Strength Index (GSI) proposed by Hoek and Brown [1997] to estimate the rock mass strength using the Hoek-Brown Failure Criterion (From Hoek et al. [1997], Marinos et al. [2006] and Cai [2004]).	33
Table 3-1:	Grain-scale input parameters and the measured laboratory properties used in the GBM calibration process.	37
Table 3-2:	Values of elastic constants from laboratory tests for selected rocks (adapted from R. E. Goodman [1980]).	39
Table 3-3:	Ten indices of grain contacts of LdB Granite based upon permutation and combination rules.	42
Table 3-4:	Material properties of minerals in Granite. (After Lan et al., [2010])	43
Table 3-5:	Contact properties for Lac du Bonnet Granite (LdB). Stiffness ratio is assumed to be a constant value. The residual strength is also listed in the table for the Coulomb slip with residual strength model.	44
Table 3-6:	Comparison of Lac du Bonnet granite peak strength from laboratory triaxial test results with the confined GBM results.	51
Table 4-1:	Comparison of laboratory test results and modeling results of marble.	69
Table 4-2:	Deformation properties and peak uniaxial strength, for different GBM marble models with various mean grain sizes, R .	70
Table 4-3:	Sample configurations and a comparison between original laboratory test data from Hudson [1971] and GBM modeling results.	74
Table 4-4:	GBM marble model peak strength and deformation results for samples with different diameters.	76
Table 5-1:	Summary of micro-properties of natural fractures of rock blocks.	88

Table 5-2:	The configuration of sample and UCS test results of rock sample with tilted single flaw.....	89
Table 5-3:	The configuration of sample and UCS test results of rock sample with discontinuous flaws inclined at 45 degree.	92
Table 5-4:	The configurations of samples and UCS test results of samples with a set of vertical flaws.	94
Table 5-5:	The UCS and strength ratios of samples containing up to seven flaws. Unit: d (mm).....	96
Table 5-6:	Peak strengths obtained for the GBM.	100
Table 5-7:	The P_{ij} system of fracture intensity, modified from [Rogers et al., 2009].	103
Table 5-8:	GBM results for UCS tests for different sized samples with two different configurations of flaw length. Peak strengths of rock are normalized to that for standard sized sample (50 mm×100 mm). All the samples have a same value of flaw intensity, $P_{21}=P_{32}=0.02$. Parameter ‘ n ’ represents the number of flaws in the sample.....	106
Table 5-9:	Results of GBM UCS tests for intact samples in the same size configuration as compared to that of GBMs with the flaws.....	107
Table 5-10:	GBM UCS results for samples (50 mm×100 mm) with two different flaw length configurations. Parameter ‘ n ’ represents the number of flaws in the sample.	109
Table 6-1:	Summary of results of shear tests performed on natural fractures. [From Hakami, E. et al., 2008].....	134
Table 6-2:	Uniaxial and biaxial compressive strengths for various blocks of GBM. The strength of a block containing a single vertical discontinuous flaw is provided for comparison.	138
Table 6-3:	Fracture intensity based upon total fracture length, RQD and estimated GSI for each GBM.....	140
Table 6-4:	Comparison of the effect of the blast induced fracturing on the fracture intensity and the GBM uniaxial compressive strength.	150
Table 6-5:	GBM uniaxial compressive strength for two Blocks containing both blast-induced and natural fractures.	153

1 Introduction

Today, many underground excavations are made at a depth between 300m to 1000m. At these depths, the main concern when creating these underground excavations is the control of the stability of underground openings. Thus, the design of these openings requires an estimate of rock mass strength. The rock mass is generally composed of intact blocks which are separated by either continuous or discontinuous fractures. While the intact rock strength can be easily determined using conventional laboratory tests, quantifying the rock mass strength remains a challenging task.

One of the traditional methods for obtaining the rock mass strength is the empirical failure criterion developed by Hoek and Brown [1980]. While that process has worked well for highly fractured rocks, there is growing evidence that the approach used by Hoek and Brown to establish the rock mass strength is not appropriate for hard moderately fractured rock. Over the past ten years there have been significant advances in geo-mechanical modelling of rock masses, which may provide a methodology to replace the empirical Hoek and Brown failure criterion. These advances have resulted from a general realization and acceptance that the failure of a rock mass has two distinct components: (1) fracture of intact rock and (2) movement along existing discrete fractures. Most continuum or dis-continuum modelling procedures do not treat these components as two separate processes but simply combine them using a descriptive constitutive model to simulate the failure process along predefined failure surfaces. The Synthetic Rock Mass (SRM) takes a different approach using discrete element logic to capture the failure of the individual components and their interactions. In this formulation there is no predefined failure surface or

complex constitutive model. One of the main developers of the SRM has been Itasca Consulting Group Inc. While the SRM has assembled a powerful set of commercial tools that are the most advanced available to us today, the methodology has not been validated so far.

The objective of this research is to develop a numerical methodology for establishing the rock mass strength using a SRM approach, i.e., discrete element formulation that incorporates continuous and discontinuous discrete fractures. As the excavation damage zone (EDZ) that forms around an underground excavation is the most critical zone for establishing the opening stability, the methodology is focused on development of the EDZ and characteristics of rock mass in EDZ. Once the methodology is developed, the effect of support on the EDZ will also be evaluated.

1.1 Problem Statement

The Swedish Nuclear fuel and Waste Management Company (SKB) is planning on a nuclear used-fuel repository at the Forsmark Site at a depth of about 470 m in crystalline rock. The excavation of underground openings usually accompanies the formation of an excavation damaged zone (EDZ) and an excavation-disturbed zone (EdZ). Unlike the excavation disturbed zone, stresses and displacements cannot be predicted by elastic theory within the damage zone. i.e., damage of the rock mass has occurred. The EDZ develops during an unloading-loading process and results in a zone of reduced stresses and increased displacements in a rock mass ring that contributes to stability of the underground opening. This concept is well known and, provided the stability of the EDZ support ring is maintained, underground excavations can be created at a great

depth. This study is focused on a methodology that can be used to quantify the rock mass strength associated with the EDZ.

Since the early 1980s several mine-by type experiments have been carried out to measure the development of the EDZ as excavation progressed. These measurements were carried out using borehole cameras, radial extensometers, micro-seismic monitoring, seismic velocity evaluation and strain change monitoring [Emsley et al., 1997; Read et al., 1997; Sugihara et al., 1999; Bächblom and Martin, 1999]. None of these techniques can measure the rock mass strength directly and hence these measurements can only be used in back-analysis to estimate the rock mass strength and properties within the EDZ. When the underground opening is excavated using drill-and-blast techniques, the energy associated with the blasting will induce additional damage, referred to as blast-induced damage. While the EDZ can be created by excavation-induced damage and/or blast induced damage, it is often very difficult to separate the effect of these different processes.

With the development of computing power, many studies have been carried out using numerical approaches to mimic and interpret intact failure processes. Generally speaking, numerical approaches can be divided into two groups: (1) the Continuum approach; and (2) the Discrete Element Method (DEM). Some researchers assumed that an EDZ could be treated as a continuous, homogeneous, isotropic, and linear elastic continuum to determine the distribution of stress in this zone [G. Frantziskonis and C. S. Desai, 1987]. Other researchers [Hashin, 1988 and Cai and Horii, 1992] applied continuum approaches containing fractures in order to determine the region of brittle yield. However, as noted by Hudson and Harrison [1997], rock is a complex natural material that is discontinuous, inhomogeneous, anisotropic and non-elastic.

It is now widely accepted that numerically simulating a rock mass requires a methodology that can discretely simulate the intact rock and the rock fractures. Itasca Consulting, Inc. has provided a number of discrete element codes in both two and three dimensions for this purpose. Besides, Potyondy [2012] reviewed the development of these codes and the different approaches that have been taken in their development. The fundamental difference in the various Itasca discrete element codes is that the intact rock is represented by either a ball-like structure or a polygonal-like structure. Regardless of the method used to represent the intact rock the fractures are handled as discrete elements. In porous rocks such as sandstones, the ball-like structure may be appropriate while in low porosity crystalline rock polygonal blocks would appear more representative of the tightly interlocked mineral grains.

A grain-based model (GBM) based on the Itasca two-dimensional discrete element software UDEC, has been shown by Lan et al. [2010] to provide an adequate representation of crystalline intact rock. In this model, both mineral grains and edges with their individual material properties are deformable and are able to break along grain contacts. The GBM was purposely developed to simulate low porosity crystalline rock and the name has been retained to note that this approach is different from the ‘Bonded Particle Model (BPM, ball-like model)’ described by Potyondy and Cundall [2004]. The BPM approach has been developed and extended to form the basis of the Synthetic Rock Mass (SRM). The SRM used the BPM and the Flat-joint Model to combine the behaviour of intact rock blocks with discrete fractures [Mas Ivars, et al., 2011]. Despite the advances in the SRM and the GBM there is limited data for evaluating the results obtained from the numerical models. In this research a GBM methodology is developed to evaluate the rock mass strength around underground

openings. This methodology is applied to the underground excavations at the Swedish Äspö Hard Rock Laboratory.

1.2 Äspö Hard Rock Laboratory

The Äspö Hard Rock Laboratory (HRL) is a unique research facility for geological disposal at the Swedish Nuclear Fuel and Waste Management Company (SKB) on the island of Äspö. Much of the research is related to the final disposal for used nuclear fuel in a deep geological repository. One of the key research objectives is quantification of the effects of the excavation-damaged zone associated with drill-and-blast tunnels [Christiansson, et al., 2009]. A series of experiments at a depth of approximately 450 meters was carried out to investigate the EDZ.

One of the large scale experiments at the Äspö HRL is the TASS Tunnel (Figure 1-1). The TASS tunnel extends to a depth of 450 m with a cross section area of 20 m², and a length of about 90 meters. The focus for experiment consisted of a portion of the tunnel wall approximately 8 m long, 1.5 m high and 0.7 m deep. The tunnel wall was extracted using a wire-saw cutting technique to minimize the disturbance to the excavation and blast-induced fractures. The fractures were mapped and digitized at the millimetre scale. The detailed methodology used to digitize the fractures observed in the tunnel wall was described by Olsson [2009]. The methodology can be summarized as:

1. The blocks were excavated from the tunnel wall using wire saw technology. The size configuration of each block was about 1 m wide, 1.5 m high and 0.7 m deep.
2. The individual blocks were cut into 100-mm-thick slabs which were surveyed, cleaned and examined to map and identify the fractures.

3. The fractures were classified into natural fractures and blast-induced fractures.
4. All fractures and block geometries were digitally archived.

The results from this detailed mapping were used in the development of the GBM methodology described in Chapter 6.

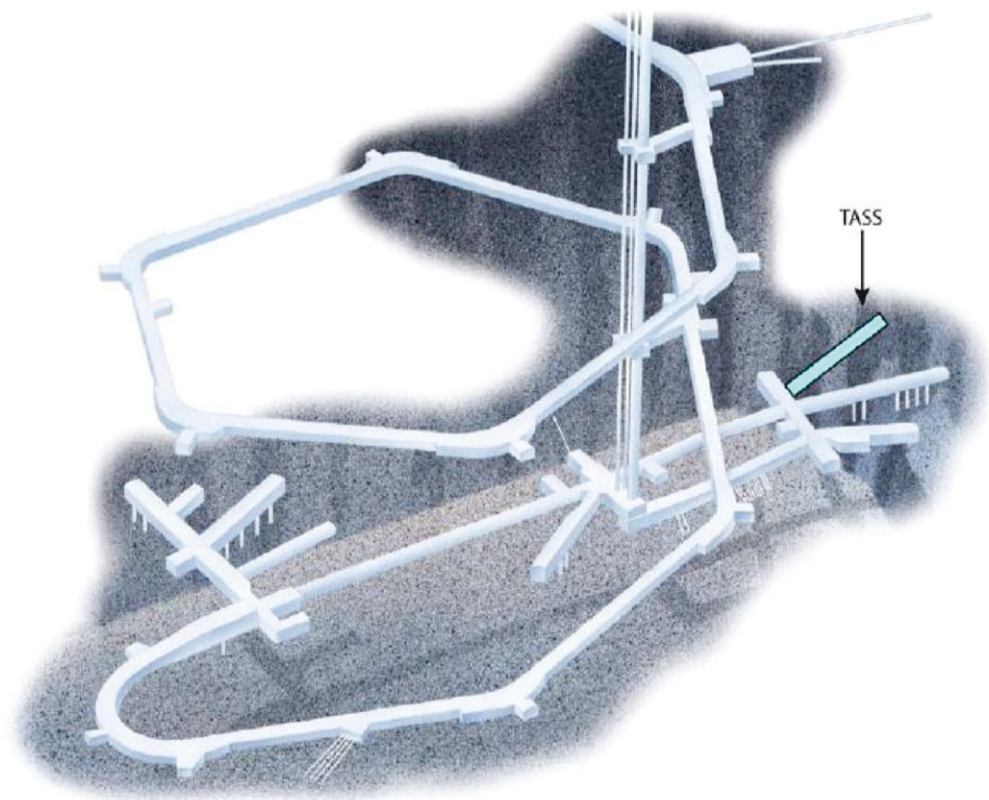


Figure 1-1: The map of underground HRL, from [Andersson and Malmatorp, 2009]. The location of the TASS tunnel is labeled in the figure.

1.3 Research Objective and Methodology

In the nuclear waste industry there is a significant reliance on numerical modelling to forecast the in situ rock mass response. This research will focus on the development of a numerical methodology that can be used to simulate the macroscopic behaviour of moderately fractured hard rocks and to quantify the strength and deformation properties of the Excavation Damaged Zone (EDZ). The main research objectives are summarized as follows:

1. A numerical GBM methodology was established using the discrete element method to analyze the development of an EDZ in a hard-rock tunnel. The methodology considers the combined response of the intact rock and the discrete excavation-induced and blast-induced fractures.
2. To assess the influence of scale effects on the rock strength and deformation characteristics encountered in DEM when modelling large-scale problems.
3. To explore the influence of natural fractures/flaws on the rock strength. The results from the GBM of these ‘fractured’ rocks (regularly or irregularly distributed) are compared to physical model results.
4. To establish a numerical approach with a discrete fracture network (DFN) system. Heterogeneous rock mass always has some uncertainties relating to fracture intensity, size, and orientation, which are the three most important parameters in the DFN system. One of the objectives of this study is to develop a numerical methodology in the way that seeks to describe the rock mass fracture system by building a series of discrete fracture objects based on field observation and measurements of such fracture properties.
5. To simulate the non-uniform stress distribution around a circular

underground opening that is applicable at the scale of the EDZ.

To meet the objectives of the research, it is essential to create a GBM that will be tested under various stress paths. Each situation is based on the different internal conditions of rocks and external conditions of boundary and loading stress. The following part lists three cases relating to three different rock conditions.

1. Intact rock: These rocks are assumed to be perfectly intact and don't contain any fractures or flaws. In this case, various loading paths will be analyzed in order to match laboratory test results.
2. Moderately fractured rock: Normally, these rocks contain some fractures, but the blocks between fractures are intact. In order to determine the effect of the fractures will have on the rock strength, some simple cases are used which include single fracture inclined at various angles. Several sample cases will combine natural fractures characterised using DFN system.
3. Blocky rock: These rocks consist of intact rock blocks, which are entirely separated from each other and perfectly interlocked. The uniaxial and confined results from the physical model studies were used to simulate the blocky rock.

1.4 Outline of Thesis

The thesis will contain seven chapters. The contents of each chapter are summarized as follows:

Chapter 1 provides an introduction of the problem definition with respect to mechanical properties of the EDZ. The research objectives and organization are also outlined in this chapter.

Chapter 2 is divided into four parts. First, it reviews previous EDZ studies, and describes the damage processes and some case studies. Second, it provides a review of the various numerical modelling approaches used to simulate damage of hard rock and discusses their limitation. In the third part the concept of the grain-based model, which has the capability of representing intact rock and rock fractures, is introduced. The final section describes the empirical Hoek-Brown rock strength criterion, together with the application of the geological strength index.

Chapter 3 presents the methodology for calibration of the Grain-based Model using laboratory properties. As the GBM has characteristics of mineral heterogeneity, a reasonable constitutive model for rock block and suitable joint model for grain contacts are selected to ensure that not only mineral composition but relations between two adjacent mineral grains are representative of real rocks. A series of modelling tests are carried out to simulate the damage process under various stress paths including uniaxial compression, direct tension and biaxial compression. The Hoek-Brown parameters obtained from laboratory triaxial compressive tests are also compared to the GBM results.

Chapter 4 examines the scale effects on the rock strengths and stiffness in terms of grain size, specimen size and sample shape. Laboratory results from the literature are reviewed. The modelling results from GBM are compared to the measured laboratory scale effects on rock strength and deformation properties. The effect of the numerical methodology is also examined, particularly the size of the numerical grid.

Chapter 5 has four sections. The first section reviews the strength resulting from a single weak plane at various inclinations. The GBM modeling results are

compared to the theory and the laboratory test results from Roy [1993] and Teja [2008]. The second section applies the GBM to a rock containing regularly discontinuous fractures. Three fracture patterns investigate the influence of regular fracture patterns on rock strength. The third section investigates the effect of rocks with randomly distributed discontinuous fractures on rock strength. All fractures have the same length and material properties. The geometry characteristics of the fractures are captured using fracture intensity. The fracture intensity is calculated in a statistical way such that the results of randomly distributed flaws can be used in comparison to the modelling results of rocks with natural and blast-induced fractures in Chapter 6. Finally, a discussion of the influence of flaw pattern is presented in the fourth section.

Chapter 6 examines the EDZ mapped in the TASS tunnel. The effect of non-uniform tangential stresses on the EDZ is evaluated. The spacing, orientation and fracture intensity that define the geometry of discrete fracture system is described. A case study is given in the third part with respect to the TASS tunnel excavated in the Scandinavian Shield at a depth of 450 m. The GBM methodology is used to simulate with the EDZ blocks mapped in the TASS Tunnel to establish the triaxial compressive strength. The effect of the blast-induced fractures on rock strength is also evaluated. The GBM results are compared to Hoek-Brown strength predicted using the Geological Strength Index.

Chapter 7 presents a summary of the results in this research in terms of grain-based model, scale problems, effect of confinement and fracture intensity, which indicates the contribution of the GBM modelling. Conclusions of this thesis are given and some comments on the future research are also presented in this chapter.

2 Literature Review

The excavation-damaged zone (EDZ) is often considered the Achilles heel of the deep geological repository. It is speculated that the EDZ could be so extensive that the sealing capacity of the repository rock mass will be compromised. In this chapter, previous studies on the EDZ will first be reviewed and results from AECL's Underground Research Lab (URL) were used to illustrate the attempts made to characterise the EDZ in highly stressed massive rock. After that, a review of two different modelling approaches is presented and compared in terms of assumptions, merits and limitations. Thereafter, a dis-continuum method is introduced and discussed in detail to illustrate the concepts captured by the Grained-based Model. In the end, rock strength criteria and application of the Geological Strength Index is reviewed.

2.1 Previous Studies on Excavation Damage Zone (EDZ)

The creation and evolution of the EDZ is a major issue for the safety of nuclear waste repositories. According to Tsang et al., [2005], the EDZ is a specific zone in which thermal-hydro-mechanical and geochemical modification induces significant changes in flow and transport properties. The stress re-distribution is inevitable due to the removal of rock during the construction process. The experience from AECL's Underground Research Laboratory has shown that in highly stressed massive granite damage is induced in the rocks surrounding the tunnels through a combination of the effects of the excavation method and stress re-distribution. These changes can increase the permeability in the tunnel by two to three orders of magnitude due to the formation of new fractures [Bäckblom and Martin, 1999].

As established in studies by Bäckblom and Martin [1999]; Rutqvist and Stephansson [2003]; and Tsang et al. [2005], the EDZ includes a damaged zone of excavation-induced rock failure and fracturing stemming from the excavation method, the properties of the rock itself, as well as the altered stress distribution and confining pressure (see Figure 2-1). Firstly, it is accepted that all underground openings will create an EDZ. The characteristics and extent of the EDZ is a function of the factors outlined in Figure 2-1.

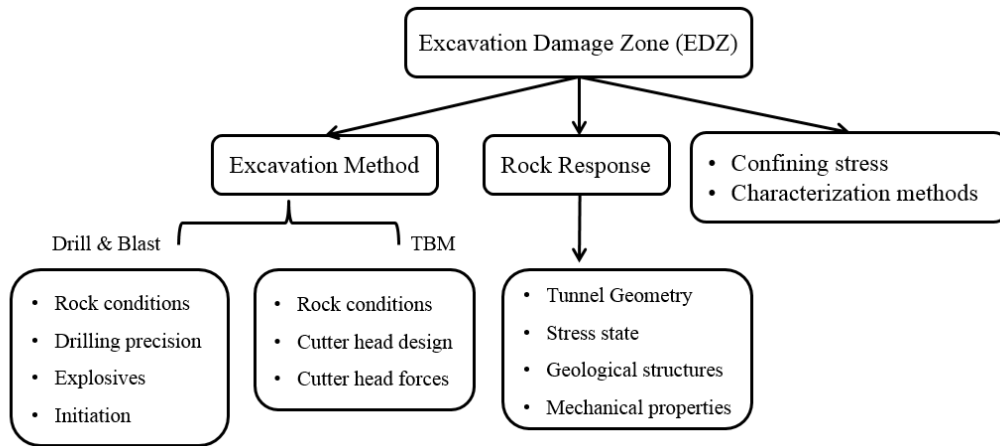


Figure 2-1: Summary of the factors relating to the EDZ.

In many cases, the underground openings are excavated using drill-and-blast methods. A combination of drilling and blasting will cause the gas expansion process to crack the rock inside the tunnel, the effect of which could be minimized, but could not be eliminated. For a mechanical excavation (without blasting) in a moderate stress condition, the damage zone can be limited to a few centimeters, where only a limited change in permeability and porosity may take place [Bäckblom and Martin, 1999]. Secondly, the excavated opening will result in stress redistribution. If the induced stresses exceed the rock strength, the excavation-induced fracturing will reduce the stiffness and strength of the rock

mass. Often the zone of overstressing is localized to the boundary of the tunnel resulting in a V-shaped notch that involves spalling and slabbing.

2.1.1 The EDZ studies at the Underground Research Laboratory (URL)

Atomic Energy of Canada Limited constructed and operated the Underground Research Laboratory (URL) in south-eastern Manitoba. The facility was operated until 2010 to carry out underground research in the Lac du Bonnet Granite batholith located near the western edge of the Canadian Shield. Several of the experiments at the URL were carried out to investigate the responses of the highly stressed massive rock mass to excavation and thermal loads. The results from these experiments are briefly reviewed.

The Lac du Bonnet (LdB) granite batholith is a relatively simple structure with pink and grey massive granite-granodiorite. The main body of the granite batholith is medium-grained granite while intrusive mafic rich granite dykes are fine-grained and some pegmatite dykes are coarse-grained. The variation in grain size is thought to be a good index for representing the micro-heterogeneity [Blair and Cook, 1998a, b; Zavattieri et al., 2001]. LdB granite is usually composed of approximately 40% of K-feldspar, 20% of plagioclase, 30% of quartz and 10% of mafic minerals, mainly biotite. Although similar in mineral composition as LdB granite, the granodiorite exhibits a different behavior as grain size distribution is more uniform [Martin et al., 1997].

The schematic view of the working level at the URL is shown Figure 2-2, [Martino and Chandler, 2004]. The URL has several main levels including 240 and 420 levels and two drilling stations (130 and 300 levels) accessed by a 443 m deep shaft. The upper part of the shaft has a depth of 255 m from surface and is rectangular (2.8 m×4.9 m). The lower part is circular and is 5 m in diameter.

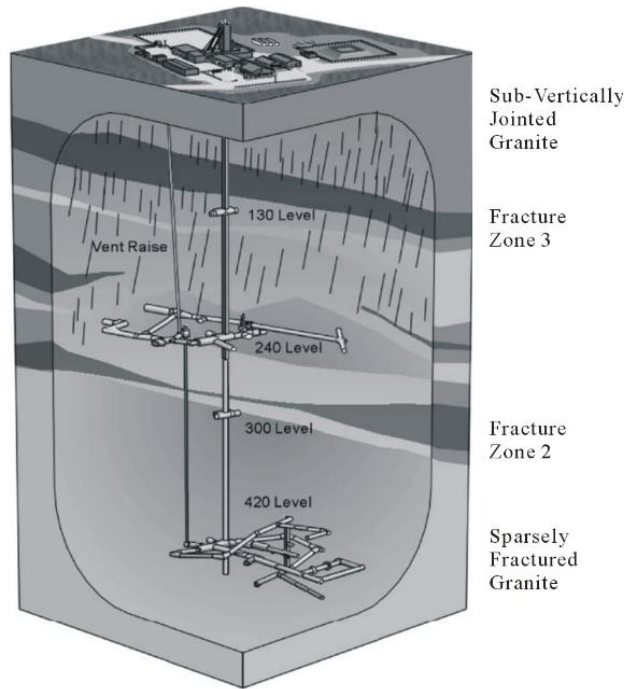


Figure 2-2: Layout of the main working levels at the URL [Martino and Chandler, 2004].

The shaft and the majority of the tunnels were created using full-face drill and blast techniques [Everitt et al., 1989] and detailed information about stress distribution and excavation layout are shown in Figure 2-3 and Figure 2-4. When comparing the measured laboratory strength to calculated stresses around tunnels, it is necessary to establish the intact state of stress prior to tunnel excavation. Hence, the in situ stresses are studied at the URL. The in situ stress at the URL has been extensively determined with over 1,000 over-coring tests, about 80 hydraulic fracturing tests, as well as back calculation of convergence measurements and instrument response calculations [Martino et al., 1997]. As can be seen from Figure 2-2, the granite within the first few hundred meters below the surface contains sub-vertical joint sets and some major low-dipping thrust faults called Fracture Zone or FZ.

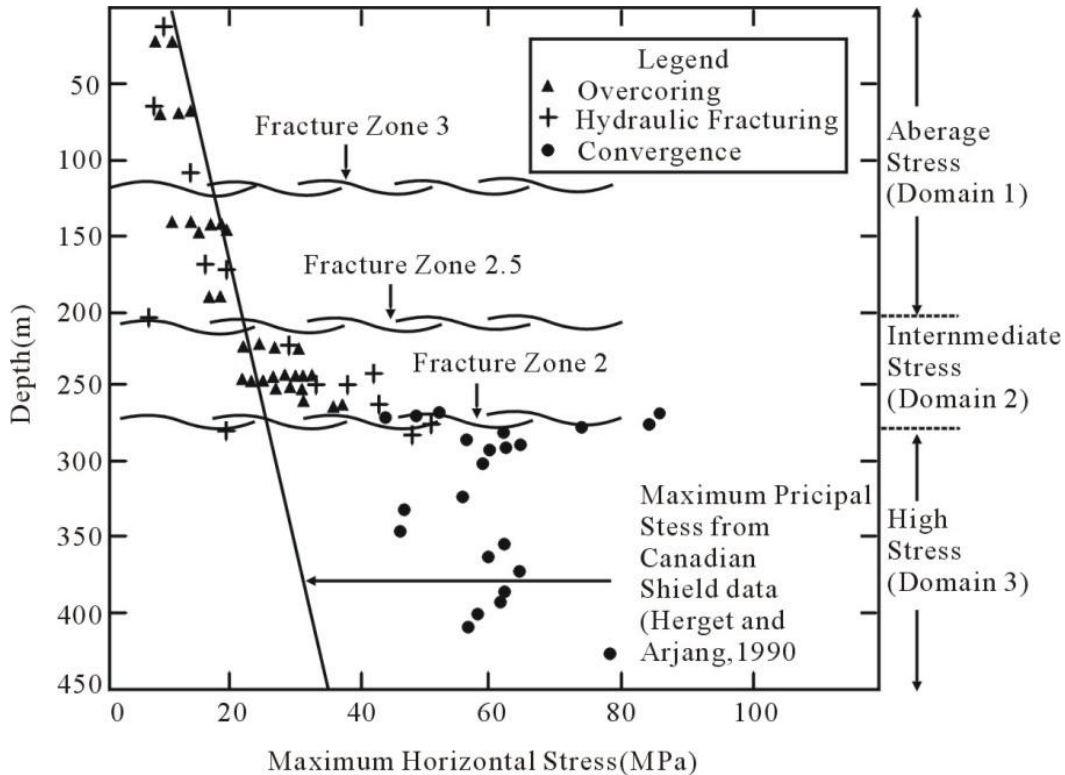


Figure 2-3: In situ stresses at the URL [Martino and Chandler, 2004].

There are three in situ stress domains at the URL [Martino and Chandler, 2004 (Figure 2-3). Horizontal stresses above FZ 2.5 are located in Domain 1 and the values are close to the maximum principal stresses measured elsewhere in the Canadian Shield. Domain 2 sits between FZ 2.5 and 2 where the rock has largely been oxidized to a pink color by secondary alteration processes. The stresses in this domain begin to increase and in Domain 3 below FZ2, the stresses are high compared to maximum principal stresses measured at other sites in the Canadian Shield at similar depths. At 1000 m depth, the horizontal in situ stress magnitudes converged to the average stress magnitude of the Canadian Shield [Herget and Arjang, 1990; and Martino et al., 1997].

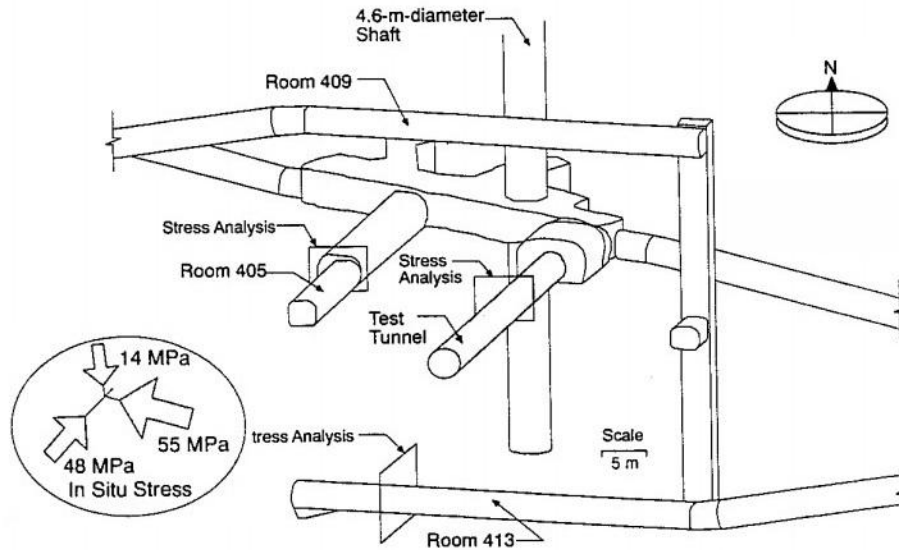


Figure 2-4: Layout of the excavations on the 420 Level at the URL (from [Martin's thesis, 1993]).

The orientation of the stress tensor changes among domains. The maximum principal stress is oriented sub-horizontally approximately along azimuth 40° in Domain 1. In Domain 2, the orientation begins to change and in Domain 3, at the 420 Level, the maximum principal stress is along azimuth 135° . The magnitudes and orientations of principal stresses at the 240 and 420 Levels are provided in Table 2-1, which gives an in situ stress distribution in three mutually perpendicular directions.

Table 2-1: In situ stress tensors measured at the 240 and 420 Levels of the URL [Martino and Chandler, 2004].

Level	σ_1 (MPa)	Trend/Plunge ($^\circ$)	σ_2 (MPa)	Trend/Plunge ($^\circ$)	σ_3 (MPa)	Trend/Plunge ($^\circ$)
240	26	228/8	16	135/28	12	335/65
420	60	145/11	45	54/8	11	290/77

In addition to the excavations using drilling and blasting methods, a special 3.5m-diameter test tunnel was also excavated to investigate the response of the rock mass. The major excavations on the 420 Level were called ‘Rooms’ and had been aligned with the general direction of the principal stresses, such that Room 405 and the test tunnel are approximately parallel to σ_2 , and Room 409 and 413 are approximately parallel to σ_1 (Figure 2-4). The difference in the magnitude between σ_1 and σ_2 is only 7 MPa, yet the difference in excavation response is dramatic.

As stated by Martin [1993], based on a comparison the maximum tangential stresses on the boundaries of Rooms 405 (120 MPa) and 413 (110 MPa) to the uniaxial compressive strength (UCS) of Lac du Bonnet granite (220 MPa), the tunnels were assumed to be stable. However, in reality this was not the case. In this compressive stress region of tunnel, rock slabbing and spalling failure were observed in the region of maximum compressive stress concentration. If we take the tangential stress of 110 MPa for Room 413 as the limiting stress for failure, we would conclude that the strength around the underground openings at the 420 Level of the URL is about 0.5UCS.

A V-shaped notch failure was observed at the roof and floor of the Mine-by experiment tunnel (M-B tunnel), which conformed to the 14° plunge of σ_1 . The maximum depth of the notch in the roof of the Mine-by tunnel was 1.3 times the radius of the tunnel measured from the tunnel center. Figure 2-5 illustrates a progressive development at one cross-section of the tunnel, which includes: (1) initiation, where micro-cracking occurred, (2) crushing in a narrow process zone on the tunnel periphery, (3) formation and spalling of slabs on the flanks of the process zone, and (4) the transient stabilization of the process zone when notch geometry provides sufficient confining pressure.

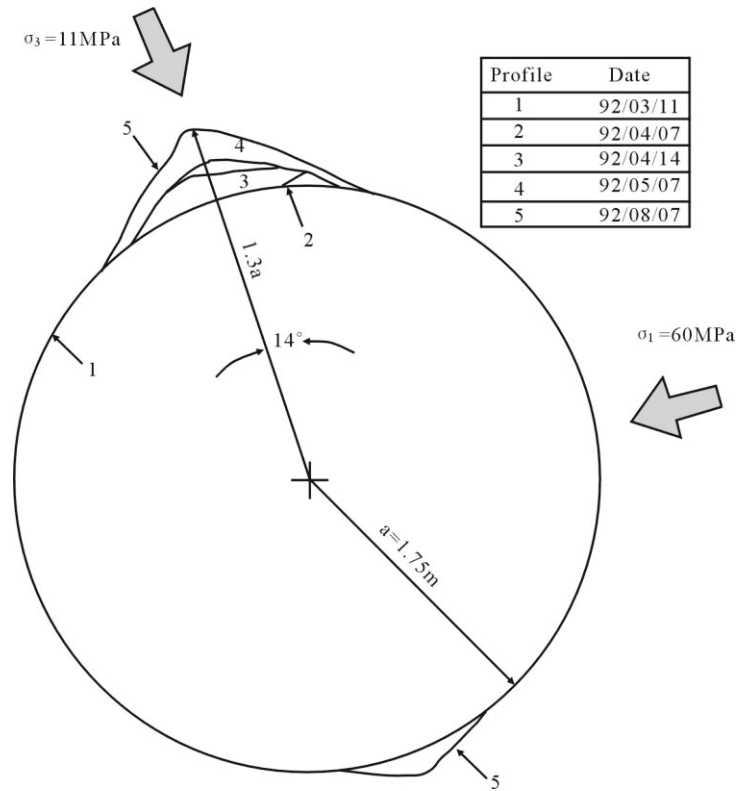
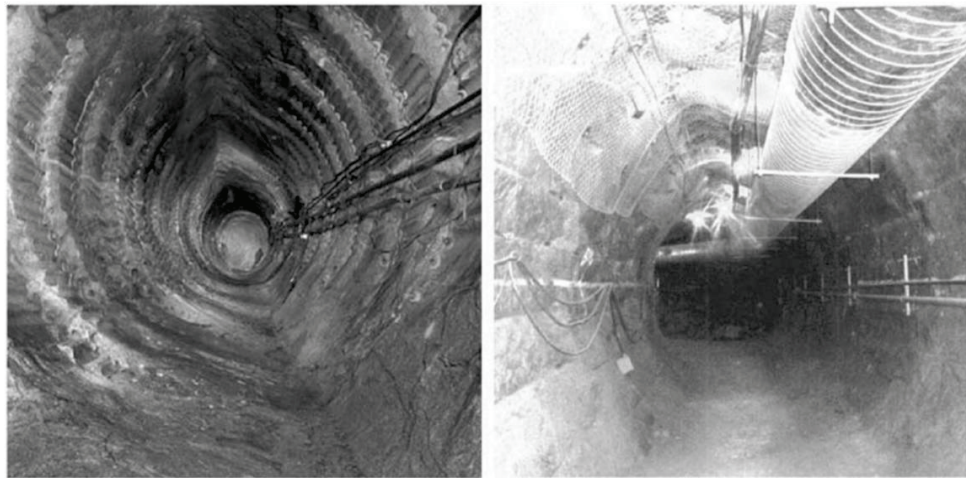


Figure 2-5: Progressive development of the V-Shaped notch failure in the Mine-by test tunnel [Martino and Chandler, 2004].



(a)

(b)

Figure 2-6: The full development of the notch in the roof and floor in Mine-by test tunnel. (a) excavated using mechanical method; (b) a parallel circular tunnel excavated using drill and blast method [Martino and Chandler, 2004].

The two different excavation methods were used to construct the tunnels: (1) line drilling and mechanical excavation for the Mine-by Tunnel and 2) drill and blast for the Room 405. Despite the different excavation methods similar yielding patterns were observed in both tunnels (Figure 2-6b). This suggests that under high compressive stress conditions, the EDZ in the high compressive stress region is a result of stress magnitudes than of excavation method.

2.1.2 Case studies of numerically modelling of the EDZ

For any rock engineer, it is imperative to be able to predict the consequences of different design options. These predictions often necessitate the use of various numerical modelling techniques. If the EDZ is to be evaluated a numerical model needs to be established to describe the development and behaviour of the EDZ, in both the short- and long-term.

In this section, a numerical modelling approach for evaluating the EDZ around the underground excavations will be described. The approach is based on Task B of the “Development of Coupled Models and their Validation against Experiments”, DECOVALEX-THM research project carried out from 2004 to 2007. The DECOVALEX Project is an international research collaboration for advancing the numerical modeling of coupled thermo-hydro-mechanical (THM) and thermo-hydro-chemical (THC) processes in geological systems. The project has been conducted by research teams supported by a large number of radioactive-waste-management organizations and regulatory authorities, including those of Canada, China, Finland, France, Japan, Germany, Spain, Sweden, UK, South Korea, Czech Republic, and the USA.

Task B describes the occurrence, nature, and evolution of the EDZ in the context of a radioactive waste repository in crystalline rock. Different models

were used to simulate the complete stress-strain curves for Ävrö granite from the Swedish Äspö Hard Rock Laboratory in Sweden. A series of laboratory tests were conducted on the Ävrö granite, which is determined as a very brittle rock, in order to obtain the complete stress-strain curves and to address the time-dependent influences on the mechanical strength of an intact crystalline intact rock.

There were four research teams who were working on the simulation by numerical modeling techniques. Each technique is introduced briefly in the following section. Table 2-2 provides a summary of the research team and their numerical approaches.

Table 2-2: Research teams and their numerical tools [J. A. Hudson et. al., 2009].

Research Team	Numerical approaches
CAS: Chinese Academy of Science	Elasto-plastic cellular automaton (EPCA)
FRACOM: FRACOM Ltd., Finland	FRACOD boundary element (BEM) code with discrete fracture propagation
JAEA: Japan Atomic Energy Agency	Damage expansion model using finite element analysis
SKI: Swedish Nuclear Power Inspectorate	PFC distinct element particle flow code

The EPCA is a 2-D cellular based model, which can describe the heterogeneity of the rock matrix and detailed mechanical properties for each element, such as Poisson’s ratio, Young’s modulus, and cohesive strength. In this method, three important conditions are considered: stress loading, constant strain rate, and the linear combination of stress and strain. During the loading process, the cell state is updated according to the cellular automata rule for

updating. The rock is assumed to obey the modified Mohr-Coulomb criterion, the yielding of a cell will follow a plastic strain locus based on the elasto-brittle-plastic constitutive theory. The stress and deformation distribution will be adjusted automatically after each rupture to reach equilibrium.

FRACOD was applied to show the propagation of the surfaces of existing discontinuity (micro or macro). It can distinguish an entire process of fracture initiation and propagation. Two failure modes (tensile failure and shear failure) are considered in the FRACOD. The fractures initiate from some pre-existing flaws in the intact homogeneous elastic rocks. Cracks can coalesce, and this coalescence is governed by two main parameters — fracture toughness and crack length used in the FRACOD model. The result of the simulation of the Ävrö granite shows that the tensile fracture propagation is restrained by the application of a small confinement. The post-peak behavior of the rock is strongly affected by the loading configuration, and material properties, etc.

The PFC code is widely used in the field of micro-behavior of rocks and is represented as an assemblage of many small rigid circular particles. Park et al. [2004] applied the bonded particle model in PFC2D. A more detailed introduction of the PFC code to simulate the hard rock damage will be given in the next section.

As discussed above there are several numerical approaches that can be used to simulate the formation of an EDZ. Unfortunately very few of these codes can simulate the fracturing of intact rock and the interaction with existing and blast-induced fractures.

2.2 Numerical Modelling of Rock Failure

Modelling of intact rock failure propagation has received considerable attention over the last twenty years. There are two general modelling approaches that can be used to represent the physical process of rock failure: (1) continuum modelling, (2) discrete element modelling. Both are briefly reviewed in this chapter.

2.2.1 Continuum approach

According to Frantziskonis and Desai [1987], it is assumed that a rock can be represented as a continuous, homogeneous, isotropic, linearly elastic (CHILE) continuum. Furthermore, the yield model for rocks can be expressed as a function of the principal stresses:

$$f(\sigma_1, \sigma_2, \sigma_3) = 0 \quad (2-1)$$

The rock yield and ultimate strengths are typically assumed to be independent of the intermediate principal stress (σ_2). Hence, a 2-D expression is obtained from Equation (2-1),

$$f(\sigma_1, \sigma_3) = 0 \quad (2-2)$$

or

$$(\sigma_1 - \sigma_3) = f(\sigma_1 + \sigma_3) \quad (2-3)$$

As noted by Diederichs [1999], damage initiation and propagation is more sensitive to σ_3 than it is to the full hydrostatic component, $\sigma_1 + \sigma_3$. A number of yield loci and failure criteria used for rocks have been summarized by Hudson and Harrison [1997], Hoek and Brown [1980], and others.

2.2.2 Discrete element method (DEM)

A discontinuous medium is basically distinguished from a continuous medium by the existence of internal contacts or interfaces between the discrete bodies, which make up the material. Thus, the mechanical behaviour of the discontinuities and the solid must be considered. Cundall [2001] reviewed the advantages of the dis-continuum modelling approach.

Cundall and Strack [1979] introduced the concept of the DEM for modeling of granular materials. The original work was extended to the Particle Flow Codes (PFC) currently available from Itasca Consulting Group, Inc. These codes use two-dimensional disk elements and three dimensional spherical elements. The development of these codes is described by Potyondy and Cundall [2004] and Potyondy [2012].

One of the early DEM models developed by Itasca Consulting Group, Inc. was the Universal Discrete Element Code (UDEC). The code was later extended to three dimensions and named 3DEC. The fundamental difference between the UDEC/3DEC and the PFC modeling approaches is that UDEC/3DEC utilizes polygons to represent the intact rock while PFC uses disks/spheres. Both approaches represent the discrete fractures using simple planes or lines with appropriate contact logic.

While both approaches appear similar there are subtle differences that have led to confusion in the research community. Diederichs [2007] and Cho et al. [2007] showed that the PFC was limited by its results being calibration path dependent. In other words if PFC was calibrated to the tensile strength it under predicted the compressive strength. Also the failure envelope remained linear and could never achieve the high friction angles observed in laboratory tests.

These issues do not arise with the polygonal structure used in UDEC. A solution to overcome these shortcomings of PFC was provided by Cho et al. [2007]. More recently Scholtès and Donzé [2013] showed that the open-source DEM project (YADE) that utilizes disks and spheres, also resolved these early issues.

Lan et al. [2010] and Shin [2010] successfully used UDEC to simulate the laboratory and in-situ rock damage of Lac du Bonnet granite. The important finding from these studies showed that grain-interlocking was a key for capturing the nonlinear failure envelope of rock and that this interlocking was linked to the block size distribution. As demonstrated by Lan et al. [2010], once the geometry of the rock structure was captured, the properties of the intact rock were also found to be realistic.

2.2.3 Theory and background of UDEC

Based on the paper by Hart, Cundall and Lemos [1988], the importance of the distinct element formulation that relates to rock mass stability is outlined as follows:

1. Both stability and instability are modeled. When a net force exists on the block, it accelerates and moves to a new position. If the forces balance, then either the system remains at rest, or it moves with constant velocity.
2. Forces arise between two blocks when the blocks intersect. Normally, the overlap is small in relation to block dimensions.
3. The calculation marches from one state to another in small increments of time. The "final solution" may be equilibrium or it may be a state of continuing motion.

The UDEC models numerically represent the rock by an assembly of discrete blocks. As the blocks are deemed to be intact and impermeable, the attention

will be diverted from the whole model to the contacts between blocks. Thus, the calculation performed in the UDEC respects Newton's second law which is used to find the contact forces based on the known displacements (Figure 2-7).

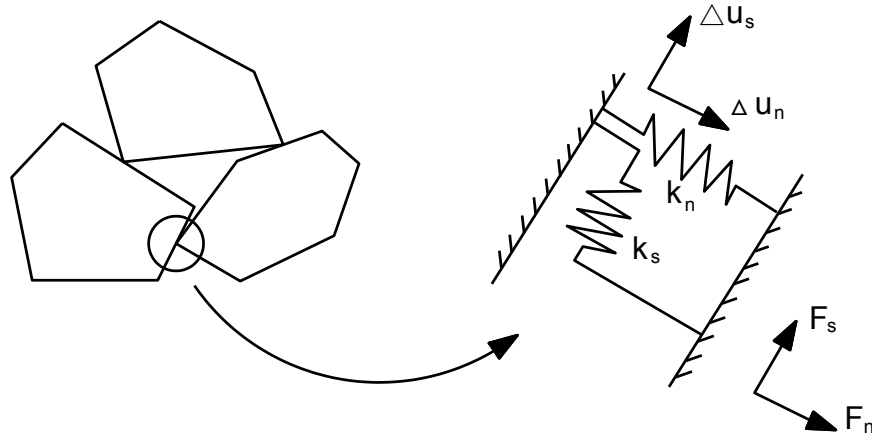


Figure 2-7: Force-displacement law applied onto the contacts to find the contact force (modified from [Itasca, 2004]).

The equations of contact forces and displacements can be written in the form

$$F_n := F_n - k_n \Delta u_n \quad (2-4)$$

and

$$F_s := F_s - k_s \Delta u_s \quad (2-5)$$

in which the k_n and k_s are the joint/contact normal stiffness and shear stiffness controlling the model behaviour. Hence, the selection of values of k_n and k_s will have an obvious influence on the block motion.

When blocks can rotate, an issue of block penetration follows. The penetration can cause problems of stress concentration at block corners, which presents numerical challenges (Figure 2-8). Thus, the concept of corner rounding is introduced by specifying a value of arc for each corner such that two

adjacent blocks can slide/rotate smoothly along the adjoining edge. As stated in the UDEC manual, the rounding length is required to be kept to about 1% of the representative block edge length in the model (which is approximately 1-1.5mm for LdB granite) in order to obtain reasonable accuracy (Figure 2-8).

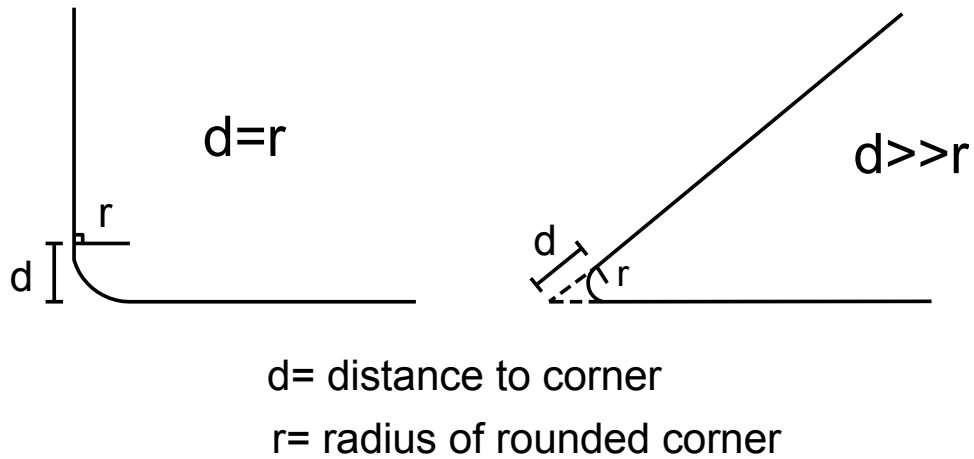


Figure 2-8: Illustration of rounded corners in UDEC (modified from [Itasca, 2004]).

There is another important computational parameter in UDEC for creation of the block assembly and mechanical analysis, called ‘Domains’, which are defined as D1 and D2 in Figure 2-9. Domains are denoted as the regions of space between two adjacent blocks. The contacts that constitute a certain domain can be recognized through commands using the internal language FISH. The contacts can be assigned discrete properties.

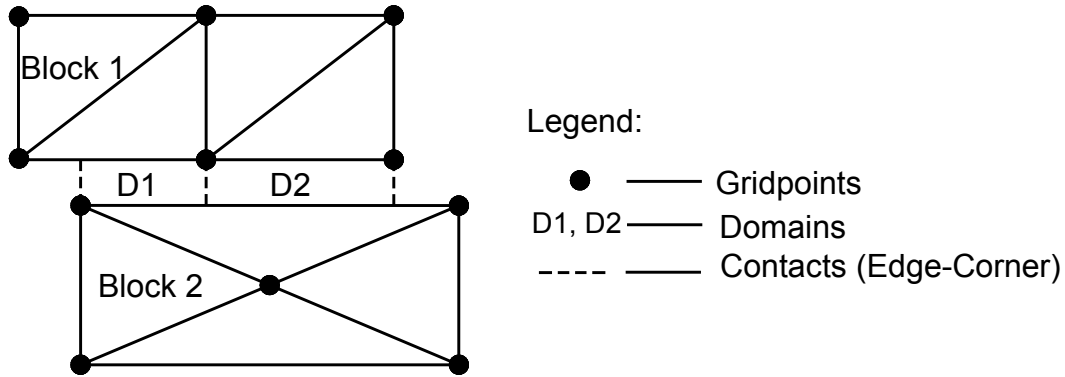


Figure 2-9: Definition of domains and illustration of contacts between two adjacent blocks.

In addition to the Domain parameters discrete contacts must be assigned a joint model. There are four built-in joint models in UDEC program. The Coulomb-slip model is the preferred one for simulating the contacts in intact rock [Lan et al., 2010]. For the Coulomb slip model, the required properties are: (1) normal stiffness, (2) shear stiffness, (3) friction angle, (4) cohesion, (5) dilation angle and (6) tensile strength.

2.3 Grained-based Model

It is now recognized that in low porosity crystalline rocks subjected to all round compression, tensile cracking is the primary mode of damage [Kemeny, 1991; Wong, 2006, Lan et al. 2010]. These tensile cracks occur because of the geometry and material heterogeneity (See Figure 2-10). The Grained based Model (GBM), described by Lan et al. [2010] clearly captures the development of this tensile damage. One of the key factors in the GBM is obtaining a reasonable representation of the polygonal block structure. In the GBM this structure is generated using a voronoi tessellation technique.

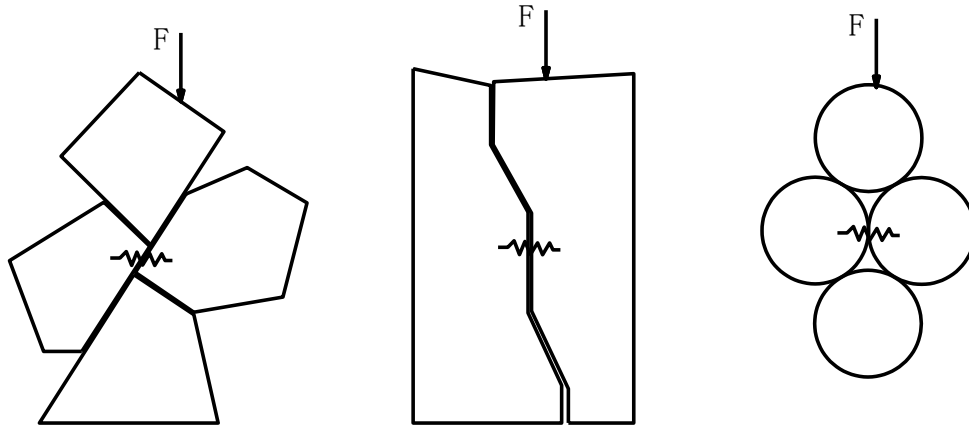


Figure 2-10: Illustration of physical mechanisms for compression-induced tensile cracking and an example of bonded assembly of circular particles (modified from Potyondy [2004]).

2.3.1 Voronoi tessellation technique

Rocks are heterogeneous at the micro and macro scale. In crystalline rocks the voronoi tessellation scheme has often been applied to simulate microstructures [Zhang et al., 2004; Li et al., 2006]. The voronoi-tessellation algorithm was initially described by Finney [1979] and can be summarized as:

- 1) the voronoi polyhedral associated with a given ‘center’ i , in an assembly of N ‘centers’ is defined as the volume of space containing all points closer to i than to any other center j (Figure 2-11a);
- 2) the bounding surfaces are the contacts perpendicular to inter-center vectors ij at their midpoints; and
- 3) the intersections of these planes form the polyhedron edges and vertices, as can be seen in Figure 2-11b.

An ideal polygonal grain-generation procedure should have the ability to produce a polygonal structure with statistical geometry block-size distribution similar to those of real rocks. The ability to generate a non-uniform size

distribution is deemed imperative. However, the voronoi generator in UDEC produces only a near-uniform size distribution. Lan et al. [2010] modified the general purpose voronoi generator proposed by Zöllner, [2006] to generate more irregular grain shapes with grain size distributions representative of crystalline rock for the Grained Based Model. Recently Gao and Stead [2014] suggested and used a triangular voronoi scheme to represent intact rock. Their work did not attempt to represent the grain size distribution.

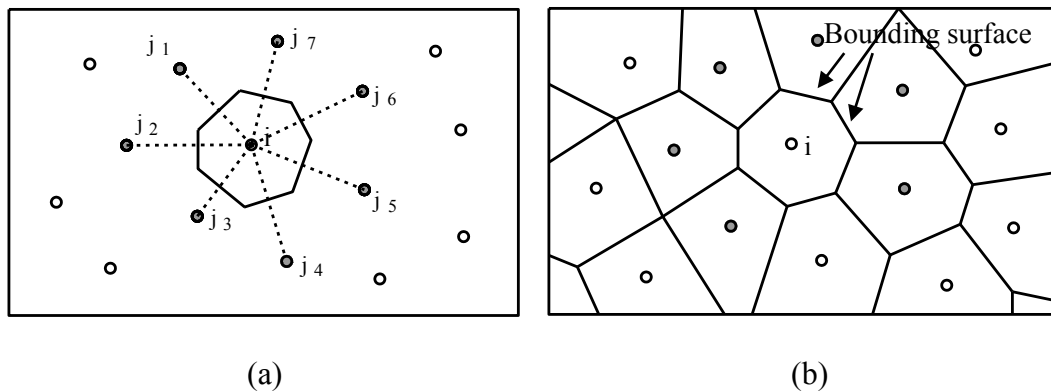


Figure 2-11: Schematic illustration of Voronoi tessellation (modified from [Shin’s Ph.D thesis, 2010]). (a) The convex hull around randomly generated interior points is formed by half planes. (b) The illustration of polygons formed by edges and vertices is shown under the voronoi tessellation.

2.3.2 Micro-structural model

The basis for the Grain-based model is the random polygonal blocks representing the rock structure. This geometric heterogeneity is created using the special purpose voronoi generator. This is done outside the UDEC program and hence must be imported once the voronoi polygons are generated. The information of polygon edges and nodes are stored in an ASCII file which is imported into UDEC using UDEC’s internal macro-language Fish. For example,

Lac du Bonnet granite is composed of four mineral grain types accounting for 90% or more of the mineral composition. The information for the grain structures, i.e., grain size, grain type, grain contact, is tracked and the properties are assigned. The detailed modelling process is shown in the flow chart in Figure 2-12.

2.3.3 Model calibration

Numerical models require calibration before their results can be used in a predictive capacity. The UDEC Grain-based model must be calibrated to measured laboratory responses using micro-scale input properties. This is a tedious process that is, in essence, trial and error. However the range of micro properties is restricted to the properties of the individual grains. For example when quartz grains are used, the Young's modulus for quartz is assigned to the quartz grains. The greatest uncertainty is related to the contact stiffness for quartz grains in contact or when quartz grains are in contact with other minerals, e.g., calcite or mica. In these situations, the contact stiffness is a small strain stiffness but unfortunately there are no guidelines or measurements for these properties. The trial and error calibration process is associated with these parameters but guided by the macro-scale stiffness of the laboratory sample, which must be obtained. Once the calibration process is complete these micro-scale properties are used for all the macro-scale modelling.

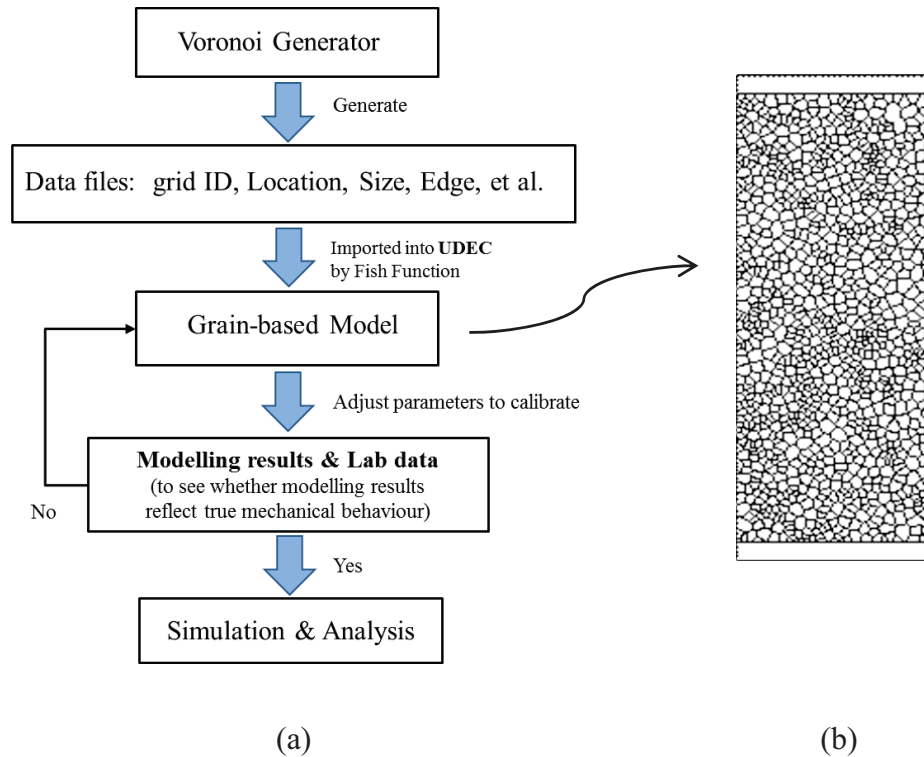


Figure 2-12: The illustration of generation of grain-based model and a flow chart presenting the process of numerical modeling. (a) Simulation process of grain-based model in UDEC combined with voronoi tessellation (modified from Lan [2010]), (b) UDEC rock ‘sample’ generated to simulate the grain structure.

2.4 Empirical Hoek-Brown Failure Criteria and GSI

The application of the discrete element modelling approach that captures both the intact rock and the discrete fractures requires many input parameters including the geometry of the fractures. An alternative to this numerical modelling approach is the Empirical Hoek-Brown failure criterion and the Geological Strength Index (GSI). This empirical criterion was first introduced by Hoek and Brown [1980] and the Geological Strength Index was formally introduced by Marinos and Hoek [2000]. Today the Hoek-Brown failure criterion is given as [Hoek et al., 2002]:

$$\sigma_1 - \sigma_3 = \sigma_{ci} \left(m_b \frac{\sigma_3}{\sigma_{ci}} + s \right)^a \quad (2-6)$$

$$m_b = m_i \exp \left(\frac{GSI-100}{28-14D} \right) \quad (2-7)$$


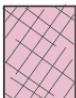


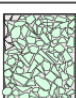

$$s = \exp \left(\frac{GSI-100}{9-3D} \right) \quad (2-8)$$

$$a = \frac{1}{2} + \frac{1}{6} \left[\exp \left(\frac{-GSI}{15} \right) - \exp \left(\frac{-20}{153} \right) \right] \quad (2-9)$$

where, m_i , is the parameter for intact rock and depends on rock type; σ_{ci} is the uniaxial compressive strength of the intact rock; GSI is the Geological Strength Index which varies from 0 to 100; and D is the Damage Factor which varies from 0 (no damage) to 1 (maximum damage). When GSI is equal to 100, the failure envelope is highly nonlinear and provides the strength of intact rock. While the tensile strength is not used directly in developing the failure criteria, it is embedded in m_i , which is the ratio of compressive strength to tensile strength.

The Geological Strength Index was introduced to provide a methodology for degrading the intact rock strength as both the fracture intensity increased and the fracture shear strength decreased. Table 2-3 illustrates the changes in the GSI as the quality of the rock mass decreases. Selecting a GSI value is subjective and depends on the users' experience. In the original formulation it was suggested that the selection of the GSI value be made with the help of an engineering geologist.

Table 2-3: The Geological Strength Index (GSI) proposed by Hoek and Brown [1997] to estimate the rock mass strength using the Hoek-Brown Failure Criterion (From Hoek et al. [1997], Marinos et al. [2006] and Cai [2004]).

GEOLOGICAL STRENGTH INDEX FOR JOINTED ROCKS (Hoek and Marinos, 2000) From the lithology, structure and surface conditions of the discontinuities, estimate the average value of GSI. Do not try to be too precise. Quoting a range from 33 to 37 is more realistic than stating that GSI = 35. Note that the table does not apply to structurally controlled failures. Where weak planar structural planes are present in an unfavourable orientation with respect to the excavation face, these will dominate the rock mass behaviour. The shear strength of surfaces in rocks that are prone to deterioration as a result of changes in moisture content will be reduced if water is present. When working with rocks in the fair to very poor categories, a shift to the right may be made for wet conditions. Water pressure is dealt with by effective stress analysis.		SURFACE CONDITIONS					
		VERY GOOD Very rough, fresh unweathered surfaces	GOOD Rough, slightly weathered, iron stained surfaces	FAIR Smooth, moderately weathered and altered surfaces	POOR Slickensided, highly weathered surfaces with compact coatings or fillings or angular fragments	VERY POOR Slickensided, highly weathered surfaces with soft clay coatings or fillings	
STRUCTURE  INTACT OR MASSIVE intact rock specimens or massive in situ rock with few widely spaced discontinuities		DECREASING SURFACE QUALITY →					
 BLOCKY - well interlocked undisturbed rock mass consisting of cubical blocks formed by three intersecting discontinuity sets		90	80		N/A	N/A	10x10 ⁶
 VERY BLOCKY - interlocked, partially disturbed mass with multi-faceted angular blocks formed by 4 or more joint sets			70	60			1 x 10 ⁶
 BLOCKY/DISTURBED/SEAMY folded with angular blocks formed by many intersecting discontinuity sets. Persistence of bedding planes or schistosity				50	40		100 x 10 ³
 DISINTEGRATED poorly interlocked, heavily broken rock mass with mixture of angular and rounded rock pieces					30	20	1 x 10 ³
 LAMINATED/SHEARED Lack of blockiness due to close spacing of weak schistosity or shear planes		N/A	N/A			10	100
						10	10
							1.0
							0.1

One of the criticisms of the GSI concept is a lack of guidance in choosing the GSI value. Cai et al. [2004] attempted to fill this gap by linking block size to the visual descriptions, which is illustrated on the right y-axis of Table 2-3. The volume size can be calculated through

$$V = \frac{s_1 s_2 s_3}{\sin \alpha_1 \sin \alpha_2 \sin \alpha_3} \quad (2-10)$$

where s_i and α_i are the joint spacing and relative angle between joints (Figure 2-13). The challenge with simply using a block volume to determine GSI is that it ignores the effect of the project scale. For example a GSI value of 30, for a power house cavern would lead to very different strength issues if the cavern was replaced with a small diameter tunnel. Hence block volume, while certainly an important factor, lacks the influence of project scale.

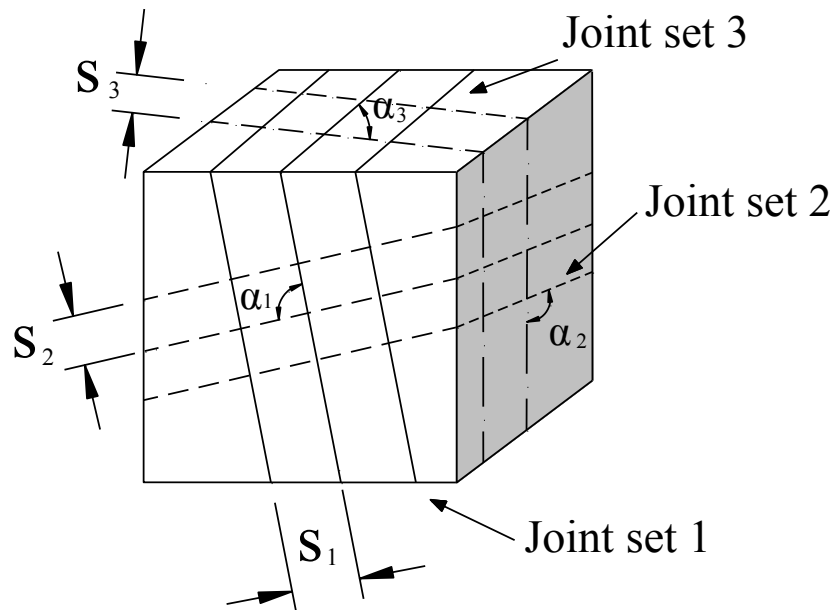


Figure 2-13: An illustration of rock block with three groups of joints which are set in different angles α and spaced at different distance S_i .

Also included in the Hoek-Brown failure criterion is the disturbance factor “*D*”. This was originally introduced to account for the poor blasting quality that is sometimes found in practice. It varies from 0 (undisturbed) to 1 (disturbed) and is a function of the amount of stress relief, weathering, and the blast-induced damage observed. In underground openings *D*, was originally intended to account for the reduction in rock strength due to blast induced damage and fracturing.

An example of the changes in rock strength for the granite with a uniaxial compressive strength of 210 MPa as GSI degrades from 100 to 25 is illustrated in Figure 2-14. Figure 2-14 shows that both the compressive strength and tensile strength degrade with a decreasing GSI and that the greatest changes occur when GSI decreases from 100 to 75.

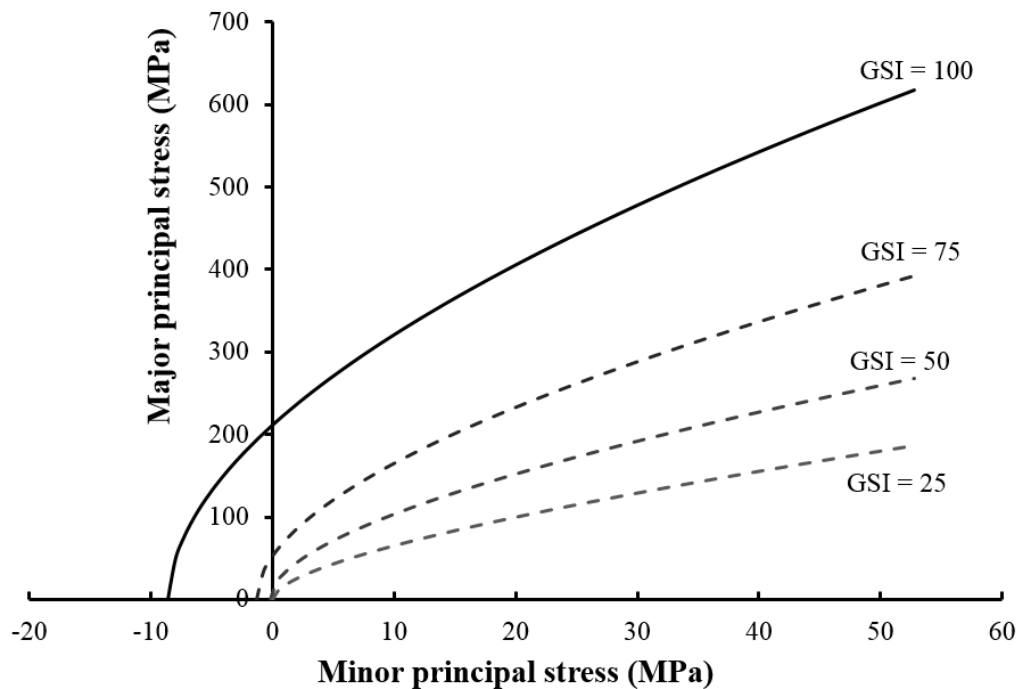


Figure 2-14: An illustration of the estimation of rock mass strengths using a combination of the Geological Strength Index (GSI) and the Hoek-Brown Failure criterion.

In the rock masses that are intended to host the geological repositories for nuclear waste, the amount of fracturing should be limited and the quality of the rock mass is expected to be high. In other words, the GSI values should be greater than 75. The Hoek-Brown failure criterion is an empirical approach and hence relies on calibration to real case histories. The majority of rock engineering projects take place in rock masses that range in GSI values between 25 and 75. Hence there is limited experience with applying this methodology to high quality rock masses. As demonstrated by Andersson et al. [2009] the Hoek-Brown failure criterion was not adequate in predicting the strength of the Äspö Diorite around 1.8-m diameter shafts.

2.5 Summary

Underground excavations are inevitably accompanied by the formation of an excavation-damaged zone. This damage zone is recognized as a significant potentially serious limitation in the ability of a underground geological repository to safely contain nuclear waste. Hence quantifying the properties of this EDZ is necessary. Establishing the properties of this damage zone requires a modelling approach that can simulate the intact rock, the natural fractures, the excavation-induced fractures and the blast-induced fractures. The Grain-based model provides a methodology that can explore the effect of these fractures on the mechanical properties of the EDZ. Despite the shortcoming of the Hoek-Brown failure criterion, it does provide a methodology for checking the results from the Grain-based model.

3 GBM Parameters and Calibration

3.1 Calibration Parameters

The objective of the calibration is to establish a representative range of input grain-scale parameters that will give the macro-scale parameters measured in the laboratory samples. Table 3-1 lists the grain-scale input parameters and the commonly measured laboratory properties. These input parameters are reviewed in the following sections. The success of this calibration at the present time is subjective. Wang and Tonon [2010] suggested a calibration methodology for the sample stiffness that was based on a statistical methodology, but this approach is not practical when the other laboratory properties given in Table 3-1 are considered.

Table 3-1: Grain-scale input parameters and the measured laboratory properties used in the GBM calibration process.

Grain-Scale Input Parameters				Measured Laboratory Properties	
Geometry	Grain size distribution			Stiffness	Young's modulus
Mineralogy	Intact block properties	Bulk modulus, K (GPa)			Poisson's ratio
		Shear modulus, G (GPa)			
		Unit weight, γ (N/m ³)			
	Contact properties for Voronoi joints	Normal stiffness, k_n (GPa/m)		Strength	Uniaxial compression
		Shear stiffness, k_s (GPa/m)			
		k_s/k_n			
		Initial joint strength	Cohesion, c (MPa)		Triaxial compression
			Friction angle, ϕ (°)		
			Tensile strength (MPa)		
		Residual joint strength	Cohesion, c (MPa)		Stress parameters
Friction angle, ϕ (°)					
Tensile strength (MPa)			Crack coalescence		

3.1.1 Constitutive models for blocks and joints

In addition to the grain-scale parameters in Table 3-1, a basic constitutive model is also required for both the blocks and joints before the modelling proceeds. There are several built-in constitutive models provided in UDEC to capture the dominant mechanisms of most physical problems, which generally include null model, elastic model and plastic model. In crystalline rock, the behaviour of the individual grains up to the point of rupture is essentially elastic. When fracturing occurs, it has been shown that most of the fracturing will take place at the grain contacts [Lim and Martin, 2012]. Hence, all material models for deformable blocks are assumed to behave isotropically in the elastic range. Furthermore, this model is capable of exhibiting linear stress-strain behaviour with reversible deformations upon unloading, which gives results compatible to laboratory behaviour. In terms of the elastic models, the basic properties are:

- (1) Mass density, d ;
- (2) Bulk modulus, K ; and
- (3) Shear modulus, G .

Where, the bulk and shear modulus are related to Young's modulus, E and Poisson's ratio, ν . These parameters are correlated to each other via

$$K = \frac{E}{3(1-2\nu)} \quad (3-1)$$

$$G = \frac{E}{2(1+\nu)} \quad (3-2)$$

An initial value for K and G is estimated based on the rock type. Some typical values of the elastic constants for some rocks are summarized in Table 3-2.

Table 3-2: Values of elastic constants from laboratory tests for selected rocks (adapted from R. E. Goodman [1980]).

Rock type	Laboratory tests		Calculated	
	E (GPa)	ν	K (GPa)	G (GPa)
Berea sandstone	19.3	0.38	26.8	7.0
Hackensack siltstone	26.3	0.22	15.6	10.8
Bedford limestone	28.5	0.29	22.6	11.1
Taconic marble	47.9	0.40	79.8	17.1
Cherokee marble	55.8	0.25	37.2	22.3
Pikes Peak granite	70.5	0.18	36.7	29.9
Nevada Test Site granite	73.8	0.22	43.9	30.2

The joint constitutive models are selected to be representative of the physical response of rock joints. The Coulomb slip model represents the contact between two blocks and exhibits the behaviour of joints, faults, and bedding planes in rock. It provides a linear representation of joint stiffness and yield limit and is based upon elastic stiffness, frictional, cohesive, and tensile strength properties. The concept of the residual model is fairly similar to the Coulomb slip model except that the residual model has an internal flag set for each joint segment. It can simulate displacement weakening of joints due to a loss of cohesion, where the brittle failure process dominates at low confining stresses.

For the Coulomb slip model, the required properties are:

- (1) Normal stiffness, k_n and shear stiffness k_s ;
- (2) Friction angle, ϕ and cohesion, c ;
- (3) Tensile strength, σ_t .

For the residual-strength version, another two additional parameters, the residual values for cohesive and frictional strengths, are also required, c_r and ϕ_r .

3.1.2 Grain size distribution and minerals

It is well known that grain size distribution and the size of mineral grains can influence rock strength (Fredrich et al. [1990]; Berbenni et al. [2007]). Thus, both mineralogy and grain size distribution need to be considered in the GBM. In an attempt to generate a model with similar grain distribution to the real rocks, a sorting coefficient (S_o) developed by Trask [1932] was used to reflect the micro-geometric heterogeneity. The sorting coefficient (S_o) is defined as:

$$S_o = \sqrt{\frac{Q_1}{Q_2}} \quad (3-3)$$

where Q_1 is the diameter that has 75% of the cumulative size-frequency (by weight) distribution smaller than itself and 25% larger than itself, and Q_2 is that diameter having 25% of the distribution smaller and 75% larger than itself. As the sorting coefficient approaches 1, the grain size distribution becomes more uniform. As introduced before, there are four main minerals in Lac du Bonnet granite. The size of each grain is shown in Figure 3-1 and the range in grain size distribution for Lac du Bonnet granite based on these mineral grains is shown in Figure 3-2.

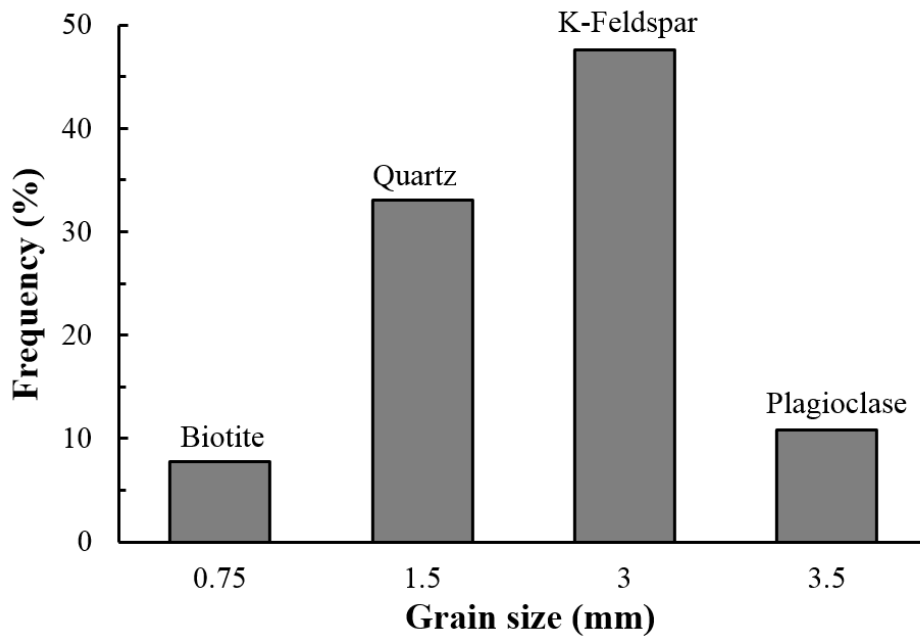


Figure 3-1: Mean grain size of four representative minerals for LdB granite. (From Kelly et al., [1994])

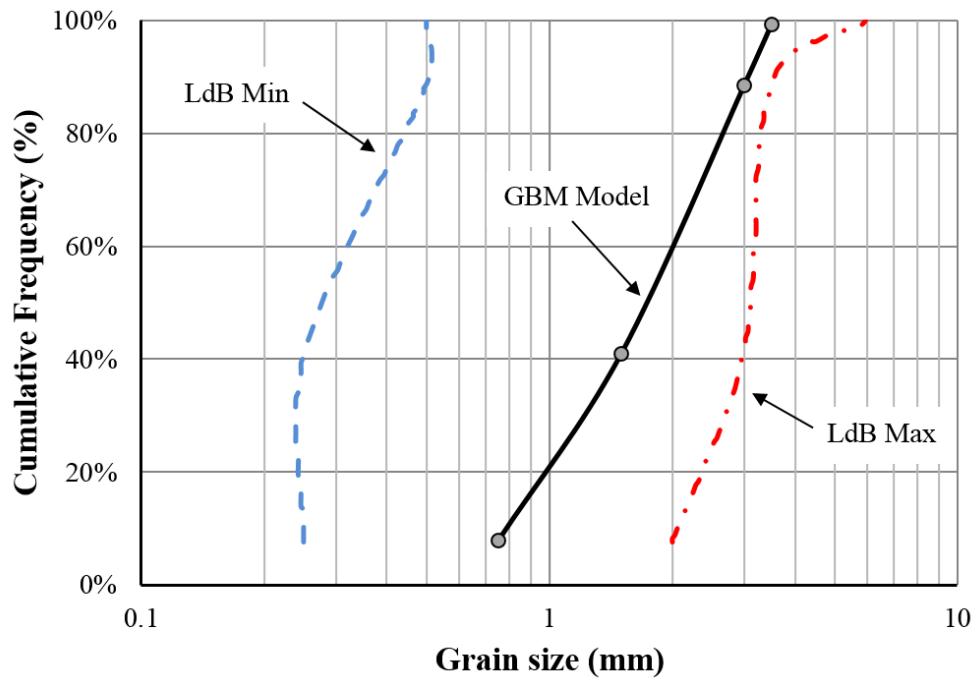


Figure 3-2: Grain size distributions of LdB granite (Adapted from Lan et al., [2010]).

A number of grain size models were created using the voronoi tessellation methodology to achieve an S_0 equal to 1.25. A typical grain size distribution used in the GBM model is chosen for Lac du Bonnet granite which is shown in Figure 3-2. Once the grain size distribution is established, the joint/contact properties are then assigned. Because there are four main constitutive mineral types, using permutation and combination rules, there are ten possible contacts between four grains. For example, the contact between Plagioclase and Feldspar is denoted as index number 2 (Table 3-3). The properties of the four minerals in Table 3-3 are given in Table 3-4.

Table 3-3: Ten indices of grain contacts of LdB Granite based upon permutation and combination rules.

Mineral Type	Plagioclase	Feldspar	Quartz	Biotite
Plagioclase	1	2	3	4
Feldspar		5	6	7
Quartz			8	9
Biotite				10

*The number refers to the index, which is used to assign the particular properties to the contacts.

Table 3-4: Material properties of minerals in Granite. (After Lan et al., [2010])

Grain type (%)	Unit weight (N/m ³)	Elastic Modulus (GPa)	Bulk/Shear Modulus <i>K, G</i> (GPa)	Poisson's ratio
K-feldspar (47.6%)	2580	69.7	53.7, 27.2	0.31
Plagioclase (10.8%)	2680	80.4	50.8, 29.3	0.30
Quartz (33.1%)	2620	95.6	37, 44	0.08
Biotite (7.8%)	3090	88.1	41.1, 12.4	0.25

3.1.3 Contact stiffness and properties

One of the more challenging questions in grain-based modelling is the relationship between normal stiffness (k_n) and shear stiffness (k_s). While these properties are well established for large scale joints tested in laboratory direct shear tests, little information is available to guide the selection of the grain-scale contact stiffness. Generally, values of normal and shear stiffness of rock joints range from approximately 10 ~ 100 MPa/m for the joints with soft clay in-fillings, to over 100 GPa/m for the tight joints in granite and basalt [Zangerl et al., 2010]. According to Sherif and Kossa [1991], the ratio of normal stiffness to shear stiffness is a constant as a function of the Poisson's ratio.

$$\frac{k_n}{k_s} = \frac{2(2-\gamma)}{\pi(1-\gamma)} \quad (3-4)$$

where k_n is normal stiffness, k_s is shear stiffness, γ is Poisson's ratio. As Poisson's ratio is equal to 0.28 for the granite, the ratio of normal stiffness to shear stiffness is taken as 1.5 for initial calibration. The contact properties after calibration are listed in Table 3-5.

Table 3-5: Contact properties for Lac du Bonnet Granite (LdB). Stiffness ratio is assumed to be a constant value. The residual strength is also listed in the table for the Coulomb slip with residual strength model.

Contact Index	Normal stiffness, k_n (N/m)	Stiffness ratio, k_n / k_s	initial joint strength			residual joint strength		
			Cohesion, c (MPa)	Friction angle, φ (°)	Tensile strength, σ_t (MPa)	Cohesion, c_r (MPa)	Friction angle, φ_r (°)	Tensile strength, σ_t (MPa)
1	9.28E+13							
2	8.56E+13							
3	1.24E+14							
4	1.49E+14							
5	9.20E+13							
6	1.29E+14	1.5	37	34	14	0	30	0
7	1.51E+14							
8	2.55E+14							
9	3.13E+14							
10	4.70E+14							

3.2 Calibration to uniaxial compressive strength

The most common laboratory test is the uniaxial compressive strength (UCS) test. The test utilizes a cylindrical sample of length-to-diameter ratio of 2.0 to 2.5 with a nominal diameter of 50 mm. A diameter of 50 mm provides more than 10 grains, assuming a maximum grain size of 5 mm, which is considered adequate to avoid geometry bias. Following the ISRM Suggested methods [ISRM, 1983], this test provides the peak strength and Young's modulus and Poisson's ratio. Regardless of the grain-scale input parameters, the macro-scale response must match the properties obtained from the laboratory test.

The stress-strain response for UCS tests on Lac du Bonnet granite was characterised by Martin and Chandler [1994] and is illustrated in Figure 3-3. They pointed out five important regions in the stress-strain curves for the Lac du Bonnet granite under unconfined compressive stresses. The first region represents the closure of existing micro-cracks in the sample, which may or may not be present, depending on the initial crack density and crack geometry. Once the existing cracks are closed, a linear, homogeneous, elastic material behaviour is observed in Region II. The elastic properties of a rock sample can be determined from this portion of the stress-strain curve. New crack growth initiates at a stress level of about 40%-60% of the peak strength [Brace et al., 1966] and propagates gradually through the sample until it reaches a stress level between 70% and 90% of the short-term peak strength during Region III. These axial cracks in Region III are almost parallel to the direction of the maximum applied load and the growth of these cracks is considered stable, i.e., additional loading is required to create crack growth. The strength of sample will continue

to increase until the peak strength (σ_f) is reached. In Region IV crack growth is considered unstable as defined by Bienawaski [1967].

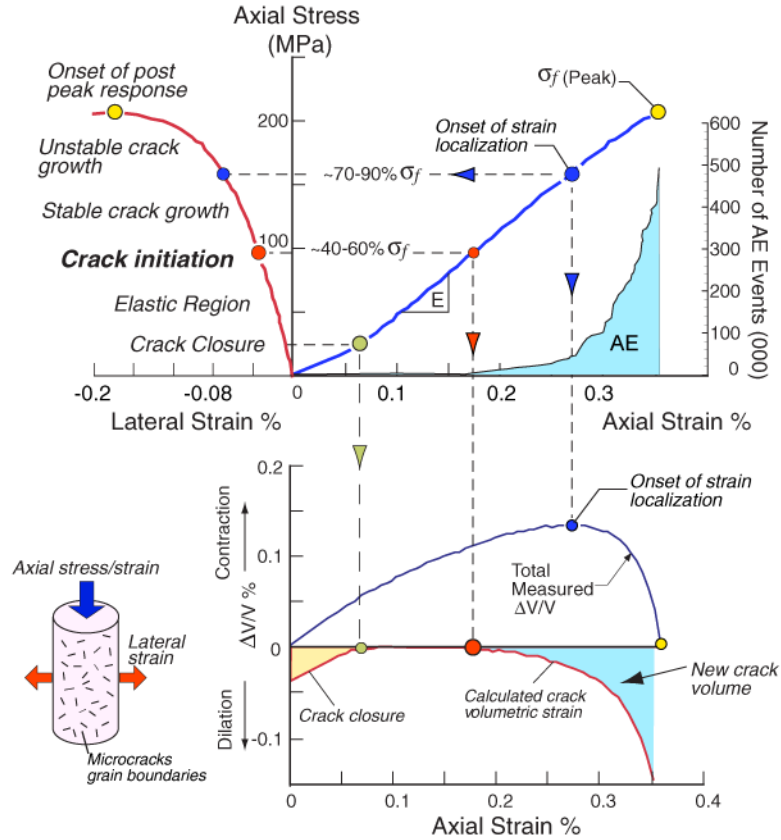


Figure 3-3: Stress-strain response under uniaxial compressive test for Lac du Bonnet granite in which three important rock strength parameters modified from Martin and Chandler [1994].

Figure 3-4 provides an example of the stress strain response from the GBM compared to the laboratory stress-strain response from a uniaxial compressive strength tests for Lac du Bonnet granite. It is clear from Figure 3-4 that GBM is capable of capturing the peak uniaxial strength. As shown in Figure 3-3 the measured volumetric strain and the calculated crack volumetric strain are also relevant parameters that can be used to assess the GBM results.

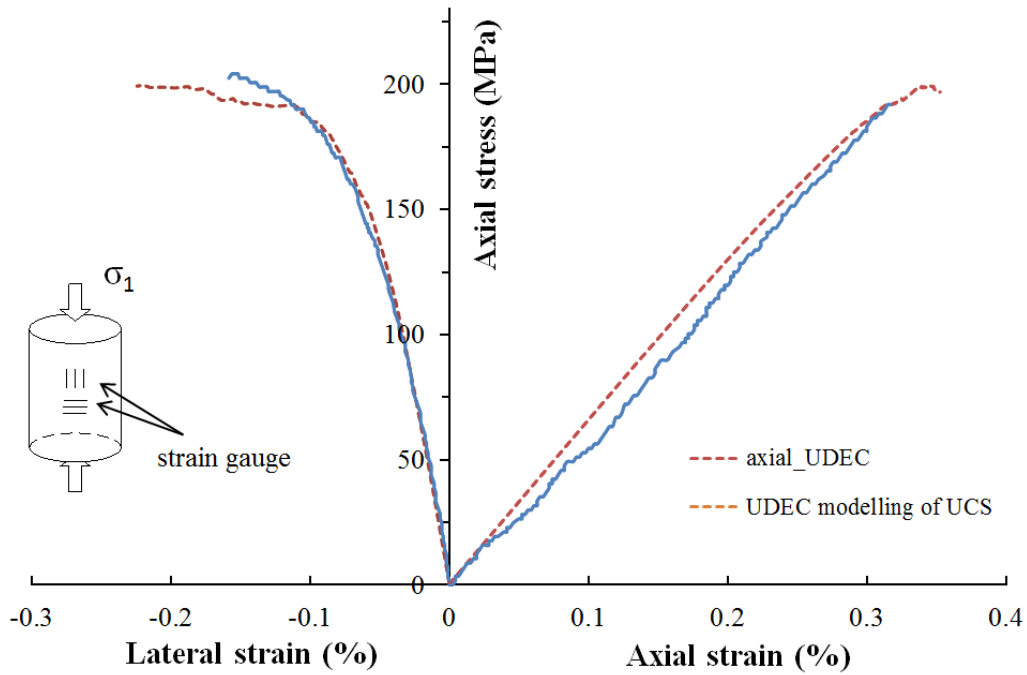


Figure 3-4: Stress-strain diagram from uniaxial compression tests comparing the laboratory tests to modelling results.

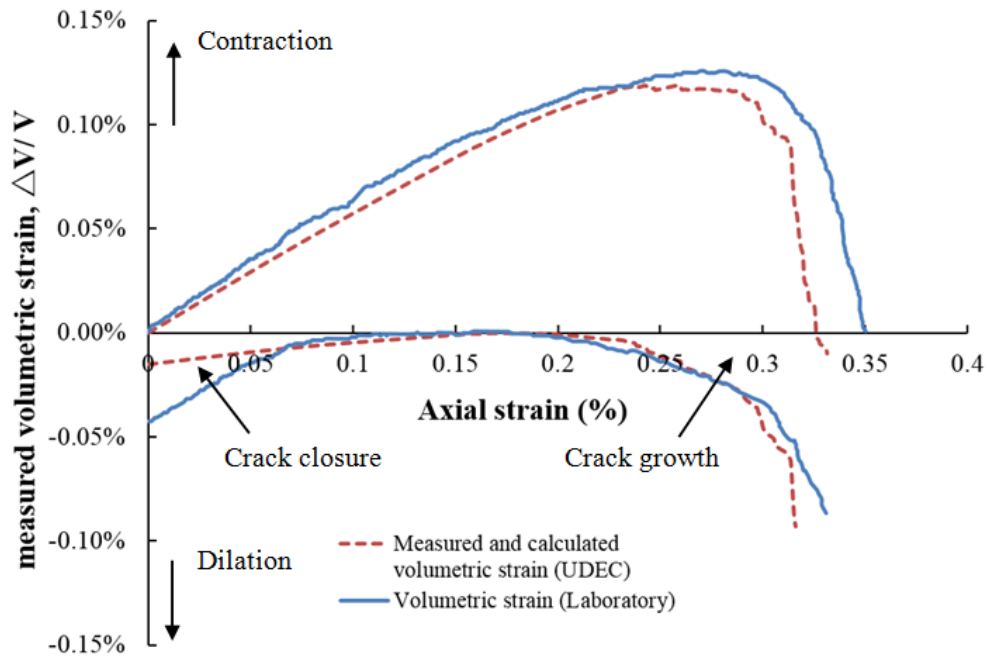


Figure 3-5: Comparison of total and crack volumetric strain observed in laboratory tests and modelling results.

Figure 3-5 shows the total measured volumetric strain curve together with the calculated crack volumetric strain curve, which clearly reflects the process of crack initiation and propagation. The results in Figure 3-4 and Figure 3-5 demonstrate that the GBM is a practical tool for simulating the progressive development of cracks in compressive loading and for capturing the peak strength and stiffness. In the next section the effect of a confining stress on the GBM is examined.

3.3 Triaxial Compressive Strength Calibration

Most rocks are significantly strengthened if the rock is confined laterally when compressed axially. This is true for highly fissured rock and for intact rock. Hence, the triaxial compression tests are widely used to characterize the strength of rock. A series of GBM modelling were carried out with confining stresses ranging from 10 MPa to 60 MPa. The objective of this study was to determine the effect of confining pressure, loading speed and voronoi joint stiffness on the GBM.

The basic steps for confined GBM tests are as follows:

1. Fix the bottom of sample;
2. Apply the confining stresses in both horizontal and vertical direction, with an initial principal stress ratio $K (\sigma_3/\sigma_1) = 1$;
3. Continuously apply an infinitely small velocity in the vertical direction at the top of sample; (The load is applied by ‘velocity’ in order to minimize the effect of concentrated load causing early failure near the top of sample).
4. The values of stress and strain during compression are recorded and stored in the ‘save’ file;

The command 'history' is used to record the stress-strain development to make a complete stress-strain curve plot. An example of the GBM result for a confining stress of 20 MPa is presented in Figure 3-6 and compared with the laboratory results for Lac du Bonnet granite. Inspection of Figure 3-6 indicates that the peak strength, Young's Modulus and Poisson's ratio from modelling results are in good agreement with the laboratory tests results. It should be noted that the grain-scale properties for the GBM model are the same as those used in the uniaxial compressive strength GBM.

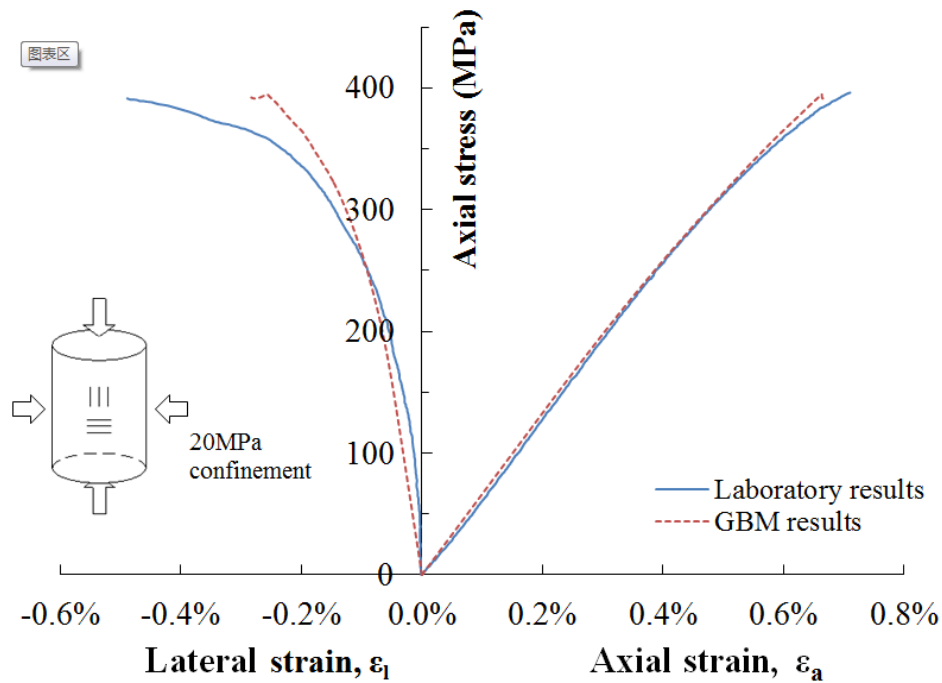


Figure 3-6: Stress-strain curve of GBM and Lac du Bonnet laboratory test (confining stress equal to 20 MPa).

Figure 3-7 shows the stress-strain response for all the GBMs with confining stresses ranging from 10 to 60 MPa. Inspection of Figure 3-7 illustrates the linear form of the axial-stress versus axial-strain plots. This phenomenon was also noted by Jackson [1992] for the LdB granite. The axial-stress versus

lateral-strain indicates that after the stress magnitudes reach approximately 0.4 of the peak strength the lateral strain is no longer linear. This is also in agreement with laboratory results indicating the onset of crack initiation, regardless of the level of confinement.

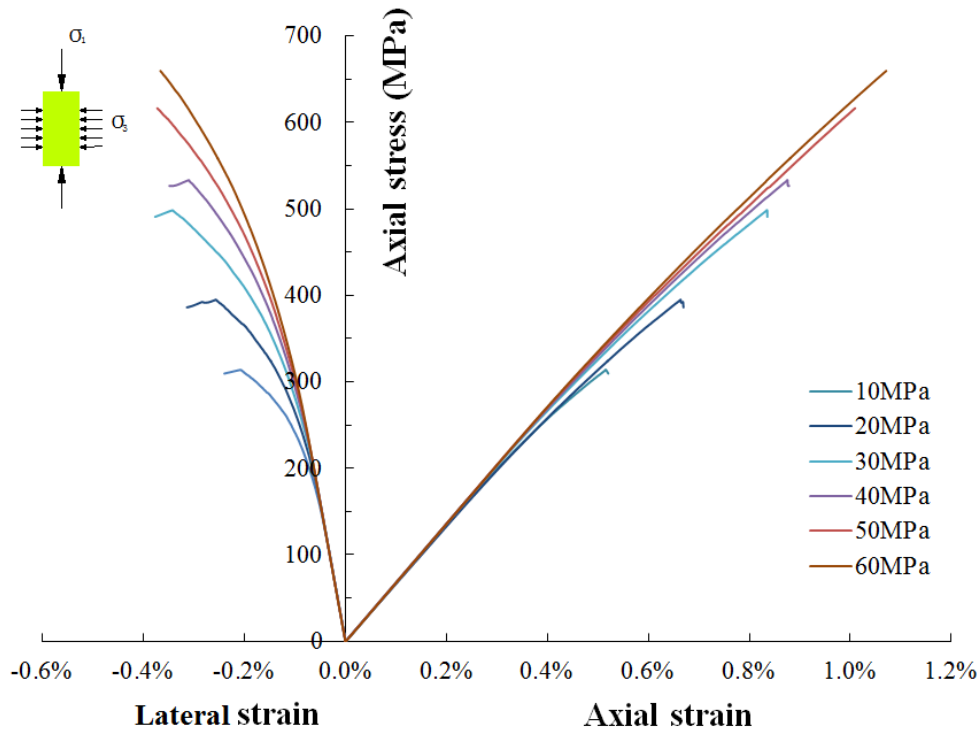


Figure 3-7: A complete stress-strain curve of biaxial tests with confining stress ranging from 10 MPa to 60 MPa.

The effect of confining stress on the rock failure peak strength is clearly shown from the six sets of data, in Figure 3-7 from the lowest value of 221MPa (UCS) to 645 MPa for the case of 60 MPa confinement. All these values are in good agreement with the measured laboratory tests results (Figure 3-8). The results in Figure 3-8 are tabulated in Table 3-6 to illustrate the difference between the GBM and the laboratory results. At confining stresses greater than 30 MPa, the modelling strength shows a higher value than that observed in laboratory tests but the difference is still less than 6%.

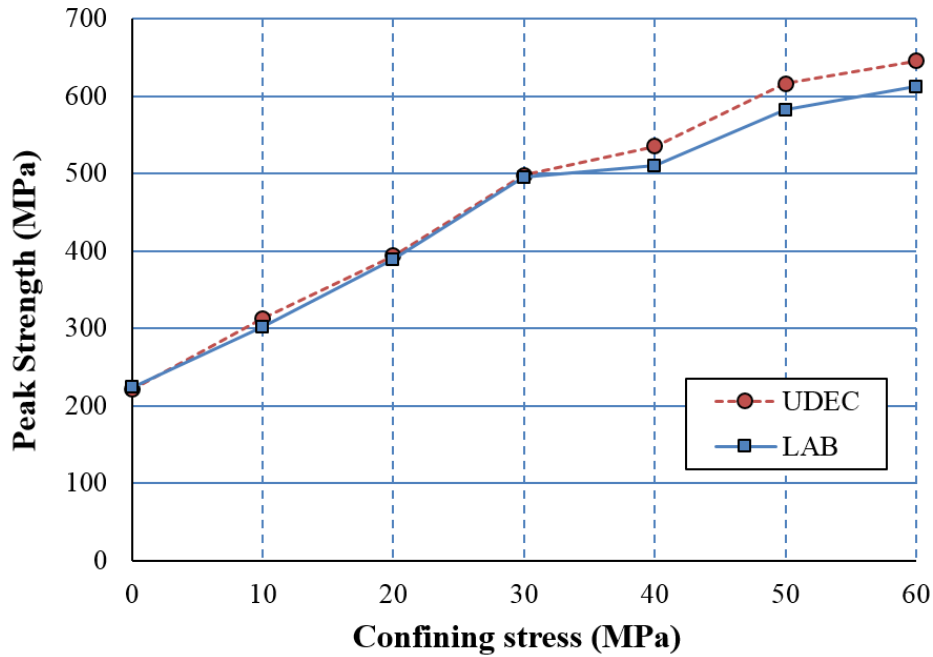


Figure 3-8: Peak strengths from triaxial/biaxial tests with confining stress ranging from 10 MPa to 60 MPa (Lab data from CANMET).

Table 3-6: Comparison of Lac du Bonnet granite peak strength from laboratory triaxial test results with the confined GBM results.

Confining stress σ_3 (MPa)	Peak strength (MPa)		Difference (%)
	GBM, σ_f	Laboratory, σ_f	
0	215	221	2.71%
10	313	302	-3.64%
20	394	389	-1.29%
30	498	495	-0.61%
40	535	510	-4.90%
50	616	582	-5.84%
60	645	612	-5.39%

As suggested by Martin and Chandler [1994] the volumetric strain can be used to define the onset of strain localization. Figure 3-9 shows the onset of strain localization using the stress-strain response from the confined GBM results. The results indicate that strain localization occurs at approximately 0.79 of the peak strength. Again these results are in good agreement with laboratory results, which falls within the range of 0.76 to 0.86 for the onset of strain localization identified by Abdelaziz et al. [2005].

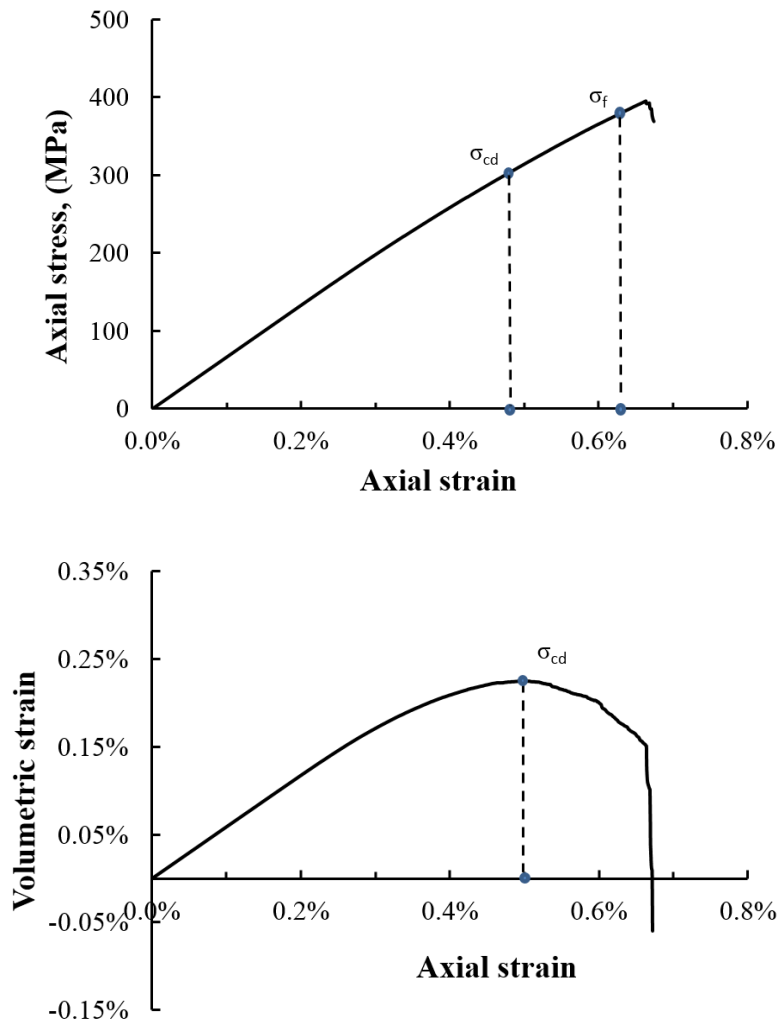


Figure 3-9: Identifying the onset of strain localization (σ_{cd}) from the GBM stress-strain response.

The effect of confining stress on the volumetric strain response is illustrated in Figure 3-10. As the confining stress increases the change in the volumetric strain from compression to dilation becomes more gradual. This reflects the gradual change from a brittle post peak response to a less brittle response. These GBMs were not carried out in sufficient number to investigate the effect of confinement on the post peak response and hence these findings are not conclusive. However the trends from the GBM modelling are similar to the findings from laboratory post-peak tests for Lac du Bonnet granite [Jackson, 1990].

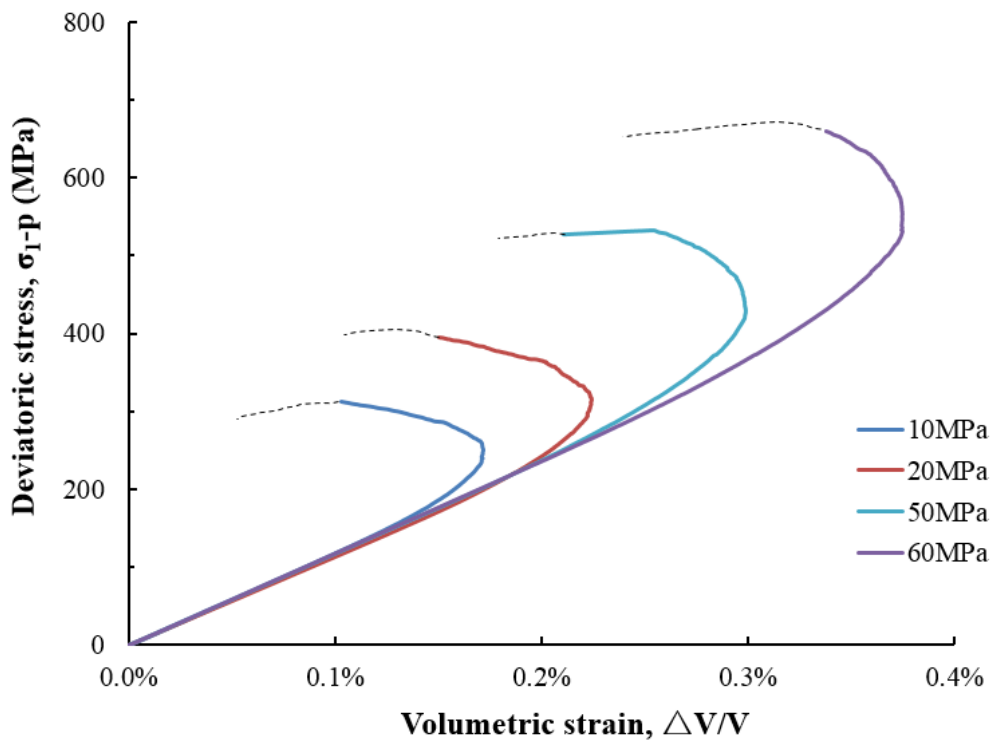


Figure 3-10: The effect of confining stress on the volumetric strain for the grain based models for Lac du Bonnet granite.

3.4 GBM Failure Envelope for Lac du Bonnet Granite

The failure envelopes for the laboratory and GBM results for Lac du Bonnet granite data given in Table 3-6 are plotted in Figure 3-11. The failure envelopes were generated using the statistical technique in the software ‘RocLab’. The nonlinear Hoek-Brown failure envelope for the laboratory and GBM data are very similar. This is not surprising given the agreement between the data given in Table 3-6. Note that the uniaxial strength (UCS) in the Hoek-Brown parameters is not the measured value but the value required for the statistical fit. Hence because of the less than 6% difference between the laboratory data and GBM data for confining stresses greater than 30 MPa, the UCS values in Figure 3-11 are different. In an underground environment, the strength near the opening is under very low confining stresses and this must be considered when selecting strengths given by the Hoek-Brown failure envelope. The linear Mohr-Coulomb failure envelope is also given for comparison purposes in Figure 3-11.

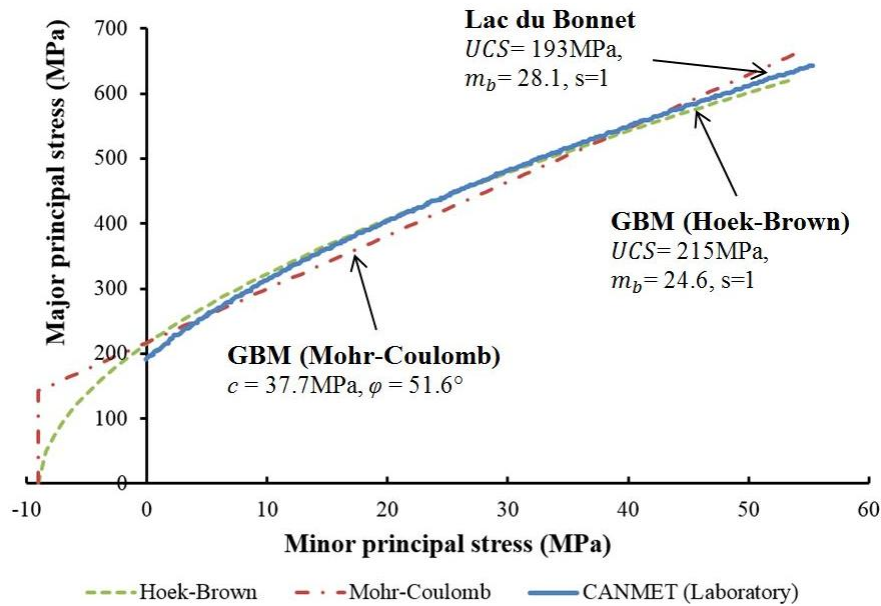


Figure 3-11: Failure envelopes for the Lac du Bonnet (CANMET) granite compared to that for the GBM. (Data from Table 3-6).

3.5 Summary

The grain-size distribution and percentages of the major minerals form the primary basis for the Grain-based modelling (GBM) methodology for crystalline rock. This is a major departure from most modelling approaches. The geometry of the grain-size distribution is difficult to capture in discrete element modelling because of the wide ranges in grain size. The approach used for the GBM in this research is based on a generalized polygon voronoi generator. This polygonal voronoi network is created outside the numerical discrete element software. The polygonal grain geometry is then imported into the numerical software UDEC using the internal FISH language.

The GBM requires calibration, which is carried out using the uniaxial compression tests. The grain-scale parameters are taken from physical properties for the individual mineral grains and assigned to the individual polygons. The results from the GBM are interpreted using the stress-strain response and the methodology given by Martin and Chandler [1993]. Once the uniaxial compression calibration is completed, the grain-scale input parameters are unchanged. The additional GBM testing for intact rock is also interpreted using the stress-strain response.

The results from the GBM are in good agreement with the laboratory test results for Lac du Bonnet granite at all confining stresses tested (0 to 60 MPa). The same calibration methodology demonstrated here was also applied to the Äspö diorite and will be used in Chapter 6.

4 Factors Affecting Strength and Stiffness of Intact Rock

It is well known that the laboratory strength and stiffness properties are influenced by factors such as grain size, sample size, sample shape and loading rate. In this chapter, the GBM will be used to assess whether the numerical methodology can capture the effect of those factors. For these analyses, a parametric control method was used where only the parameter being evaluated is varied.

4.1 Factors Influencing Laboratory Strength and Stiffness

Intact rock laboratory tests are conducted using the ISRM Suggested methods or other applicable ‘Standards’. This avoids issues associated with reporting results that were not carried out using accepted methods. For example, it is well known changing the geometry of the specimen will change the rock strength and stiffness, e.g., Bandis [1990], Cunha [1993], Hoek and Brown [1997], and Yoshinaka et al. [2008].

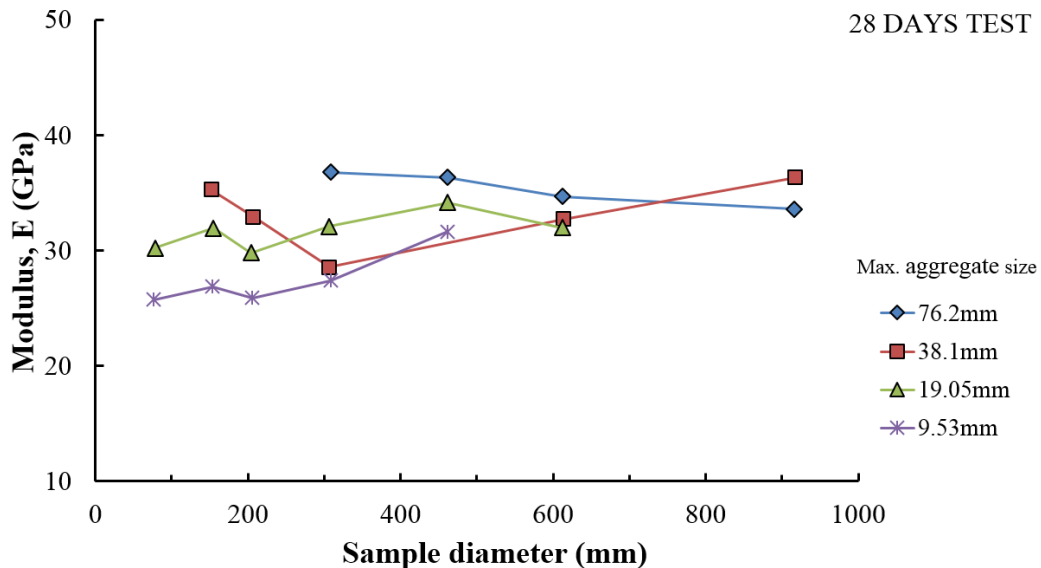
In addition to specimen geometry, the grain size may also affect the intact properties. The first report regarding the variation of rock strengths with grain sizes was suggested by [Robertson, 1955]. The effect of grain size on the strength of rocks was also investigated by Skinner [1959] who pointed out that the uniaxial compressive strengths (UCS) of anhydrite decreased as the grain size increased. Similar phenomenon was observed by Wong [1996] who confirmed that the peak strength decreased with the inverse square root of mean grain size for fine-grain ($\leq 200 \mu\text{m}$) Yuen Long marbles. However, Wong also noted the

grain size in coarse-grain marbles played no significant role in affecting peak strength. Some other researchers have conducted studies of scale effects related to mineralogy such as Olsson [1974] for dolomite and recently Prikryl [2001] for granite, indicating that the typical grain size was deemed to be a main micro-structural factor controlling strength variation.

4.1.1 Sample scale and stiffness

Only a few studies have systematically discussed the effect of sample scale effect on deformation properties, e.g. Young's modulus and Poisson's ratio.

Blanks et al. [1935] carried out tests on concrete cylinders with sizes ranging from 50.8 mm × 101.6 mm to 914 mm × 1828 mm. Figure 4-1 gives results from the concrete compression tests at 28 and 90 days. Figure 4-1 shows that there is no apparent variation of modulus with diameter of the test cylinders diameter.



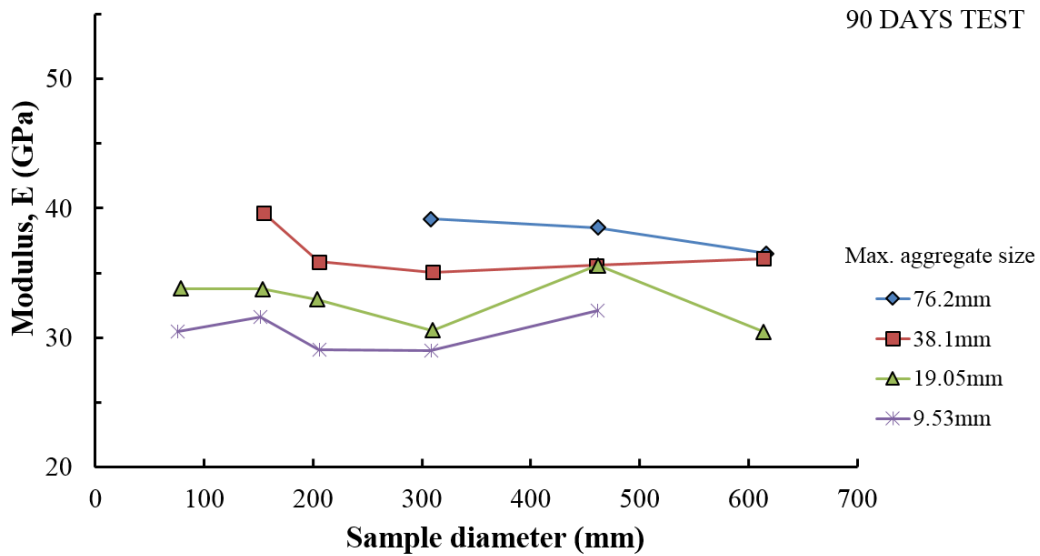
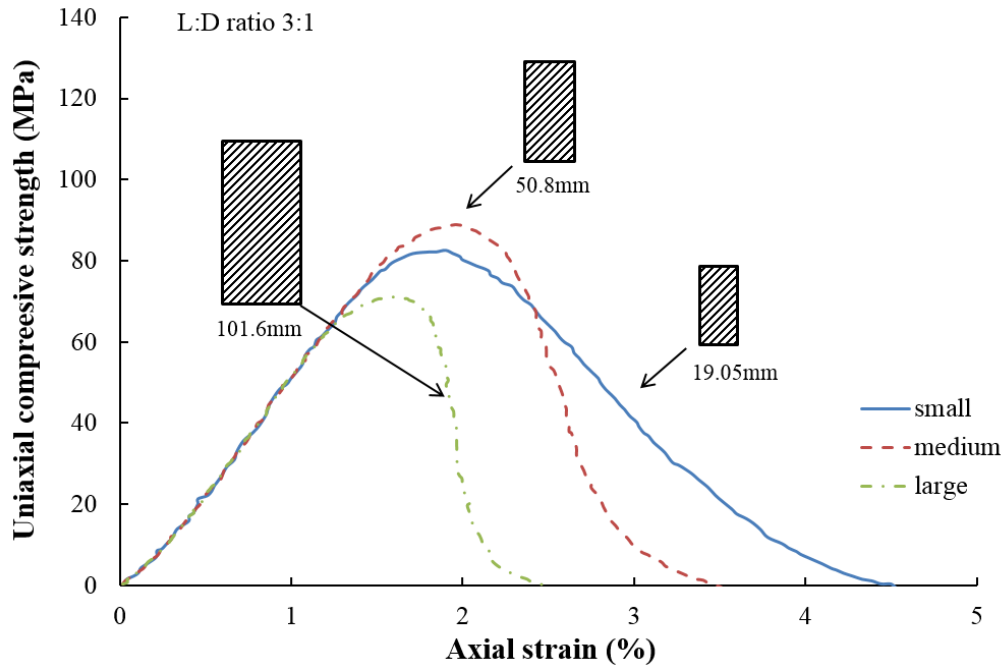
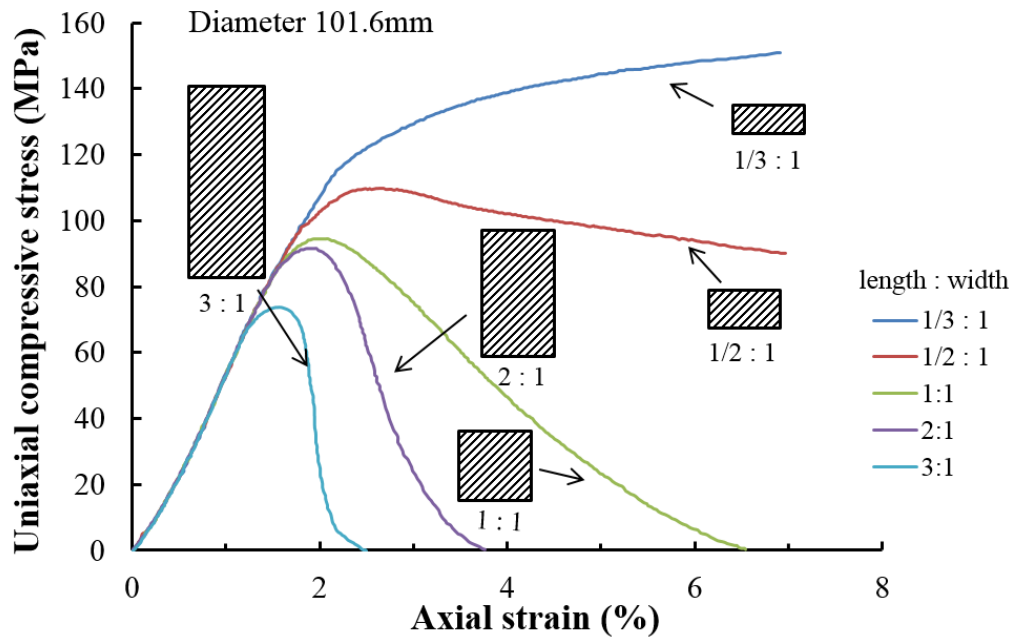


Figure 4-1: Effect of diameter of cylindrical samples on the modulus. 28 days and 90 days age of concrete are shown in top and bottom respectively.

Hudson et al. [1971] determined the influence of specimen geometry on the complete stress-strain curve of intact rock specimens of Georgia Cherokee marble. The influences of scales in terms of specimen size and shape were studied by comparing the curves obtained from specimens with the same shape but different diameters ranging from 12.7 mm to 101.6 mm with different length to diameter ratios. Figure 4-2a gives the stress-strain results for different diameters and Figure 4-2b provides the stress-strain results for various sample shapes. Even if the tested samples have totally different geometrical configurations, the elastic moduli reflected from the slope of stress-strain curve are essentially unchanged. Thus, the modulus seems to be unaffected by the sample scale and geometry.



(a)



(b)

Figure 4-2: Influence of specimen size and shape on the stress-strain curves of UCS tests for marble, modified from J. A. Hudson [1971].

Jackson and Lau [1990] conducted a study on the effect of scale for Lac du Bonnet granite sampled from a depth of 240m in the Underground Research Laboratory (URL) in Canada. The diameters of their samples ranged from 33 mm to 294 mm with a fixed height to diameter ratio 2. The Young's modulus results obtained from uniaxial compression tests, at 50% of ultimate compressive strengths, are summarized in Figure 4-3. The results show that the Young's modulus was relatively consistent with a mean value of around 60 GPa when the sample diameter was equal to or greater than 100 mm. For those samples with diameters less than 100 mm, the Young's Modulus increases as the sample diameter decreases. The maximum grain size of Lac du Bonnet granite is approximately 5 mm, and therefore samples less than 50 mm diameter may not be statistically representative.

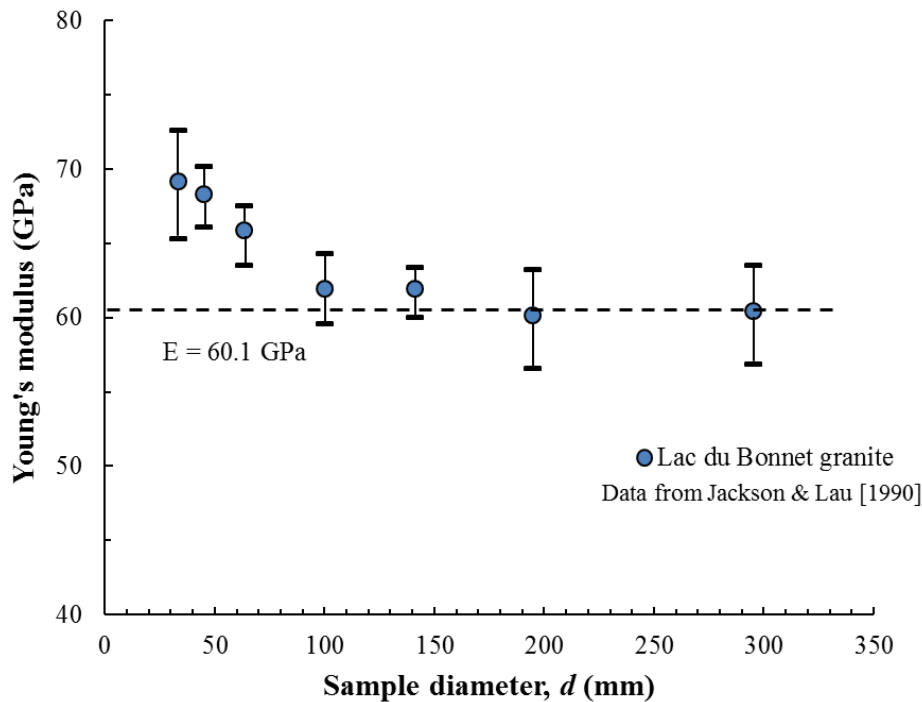


Figure 4-3: Effect of sample diameter on Young's modulus for Lac du Bonnet granite, (modified from Martin et al. [2012]).

4.1.2 Sample scale and strength

The most comprehensive study on the effect of scale on strength was carried out by Blanks et al. [1935] on concrete cylinders. The concrete cylinders ranged in diameter from 50.8 mm up to 914 mm and the uniaxial compressive strength results are summarized in Figure 4-4. The compressive strength results are normalized to the 50.8 mm diameter results. Note that strength reduction is most noticeable for samples less than 400 mm diameter and that the maximum scale effect is approximately 0.8 of the peak strength at 50.8 mm diameter. In these concrete studies there is also the issue of aggregate size.

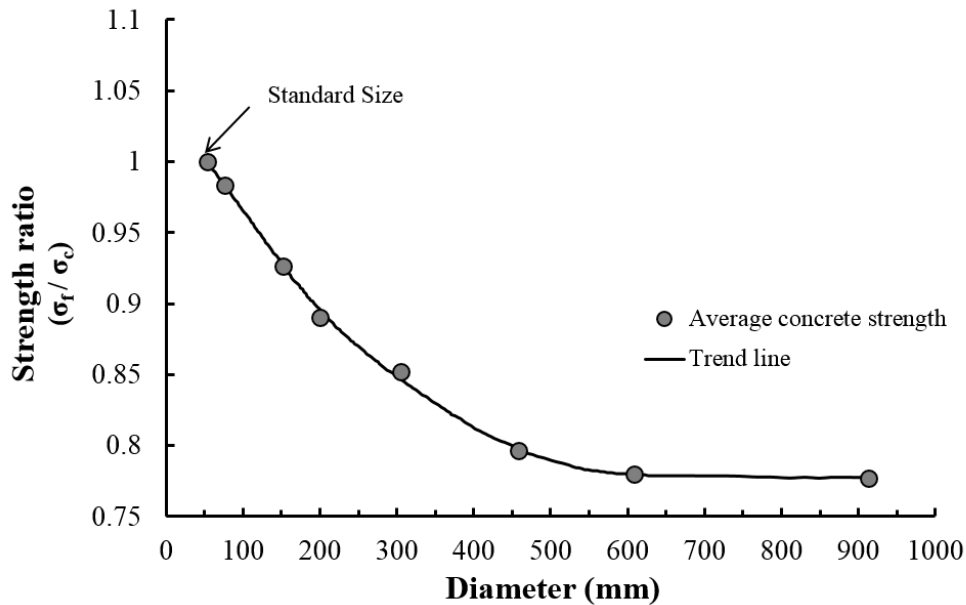


Figure 4-4: Effect of size of test cylinder on the compressive strength of concrete (Data from Blanks et al. [1935]).

Jackson and Lau [1990] also reported their findings for uniaxial strengths of Lac du Bonnet granite for various diameters (Figure 4-5). Figure 4-5 illustrates a reduction in uniaxial strength for diameters less than 150 mm. Beyond 150 mm there is essentially no reduction in strength as the diameter increases.

Similar findings for intact rock have been reported by (Yokobori [1974]; Jaeger and Cook [1979]; Hoek and Brown [1980]; Yoshinaka et al. [2008]).

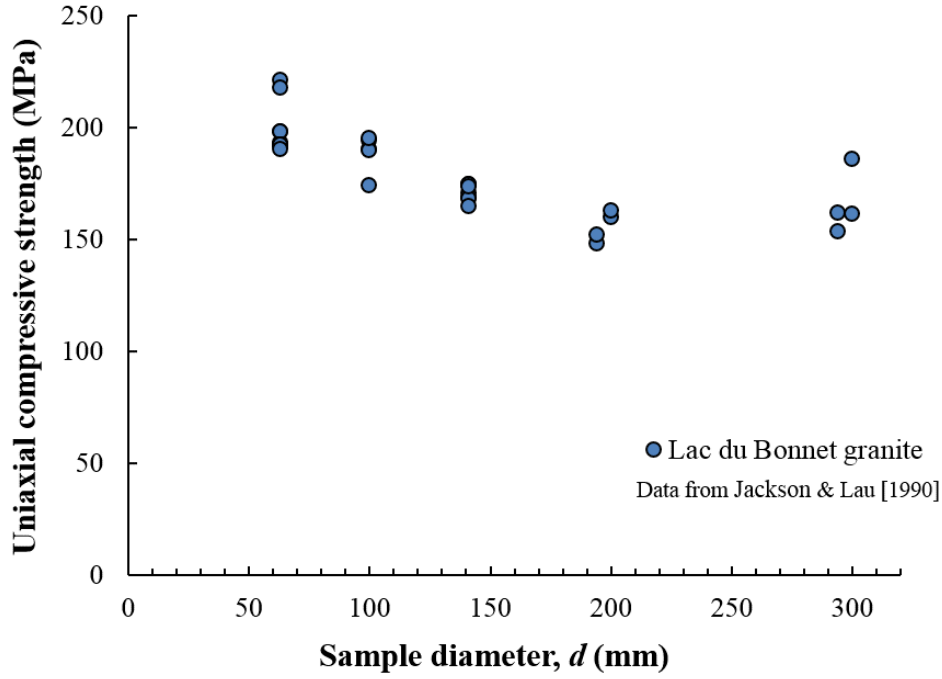


Figure 4-5: Effect of sample diameter on the uniaxial compressive strength of Lac du Bonnet granite, modified from Martin et al. [2012].

Hoek and Brown [1980] compiled the laboratory test results of various rock types, and expressed the scale dependency on the compressive strength of intact rock as:

$$\sigma_c = \sigma_{c50} \left(\frac{50}{d}\right)^{0.18} \quad (4-1)$$

where σ_{c50} is the uniaxial compressive strength of a standard testing sample with a 50-mm diameter and d is the arbitrary diameter of the testing core. σ_c is the uniaxial compressive strength of a specimen with a diameter, d . The ratio of length to diameter ratio ($L: D$) is approximately 2. Equation (4-1) is also used to establish the representative UCS strengths for the synthetic rock mass (SRM),

which gives a comparison between the results from numerical modeling and values from the equation.

Figure 4-6 shows the results compiled by Hoek and Brown [1980] and their fitted curve defined by Equation (4-1). The data in Figure 4-6 is limited to a maximum diameter of 200 mm and various rock types. Equation (4-1) in Figure 4-6 shows that the uniaxial strength continues to decrease as the diameter of the sample increases. Extending the curve to diameters greater than 200 mm, suggests the strength will continue to decrease. However inspection of Figure 4-6 indicates that there is no data supporting this notion, and the data indicates that the strength reduction from 50 mm diameter does not decrease to values less than approximately 0.8 UCS (50 mm). This is similar to the results reported by Blanks et al. [1935] and Jackson and Lau [1990].

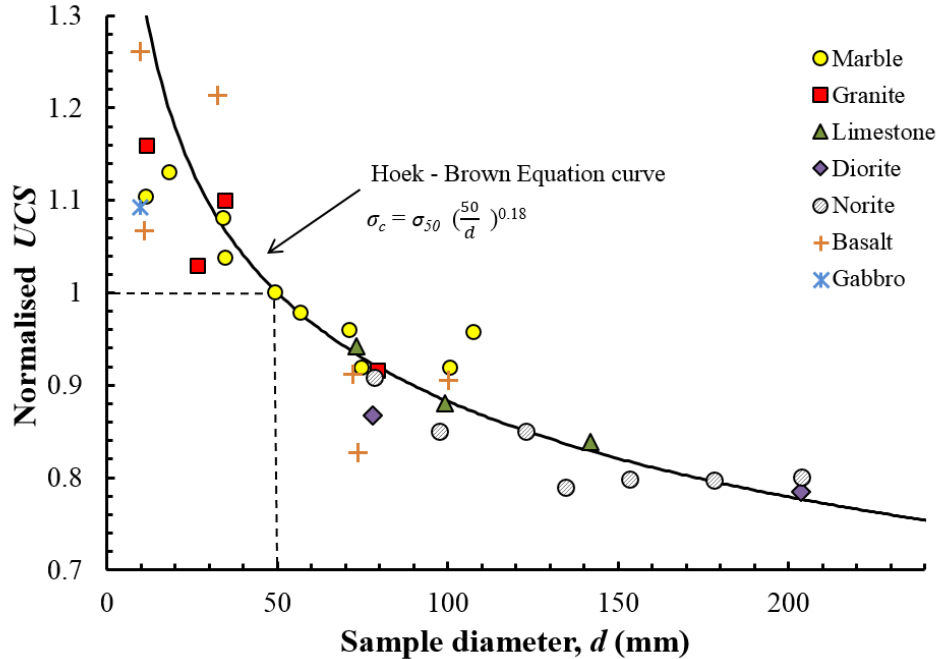


Figure 4-6: Illustration of relationship between increasing diameter and UCS, data from Hoek and Brown [1980]. The UCS has been normalized to that of sample in 50-mm diameter. (Modified from Martin et al. [2012])

More recently, Martin et al. [2012] summarized the test results from Blanks and McNamara [1935] for concrete, and Jackson and Lau [1990] for LdB granite, along with data from Hoek and Brown [1980] for hard rocks (Figure 4-7). They proposed a function for the data in the form of:

$$\sigma_c = A + \left(\frac{B}{\text{Exp}(D/C)} \right) \quad (4-2)$$

where $A = 0.81$, $B = 0.4$, $C = 1.21$ and D is the normalized diameter. This function does not go below a uniaxial strength of 0.8 UCS (50 mm) regardless of the sample diameter.

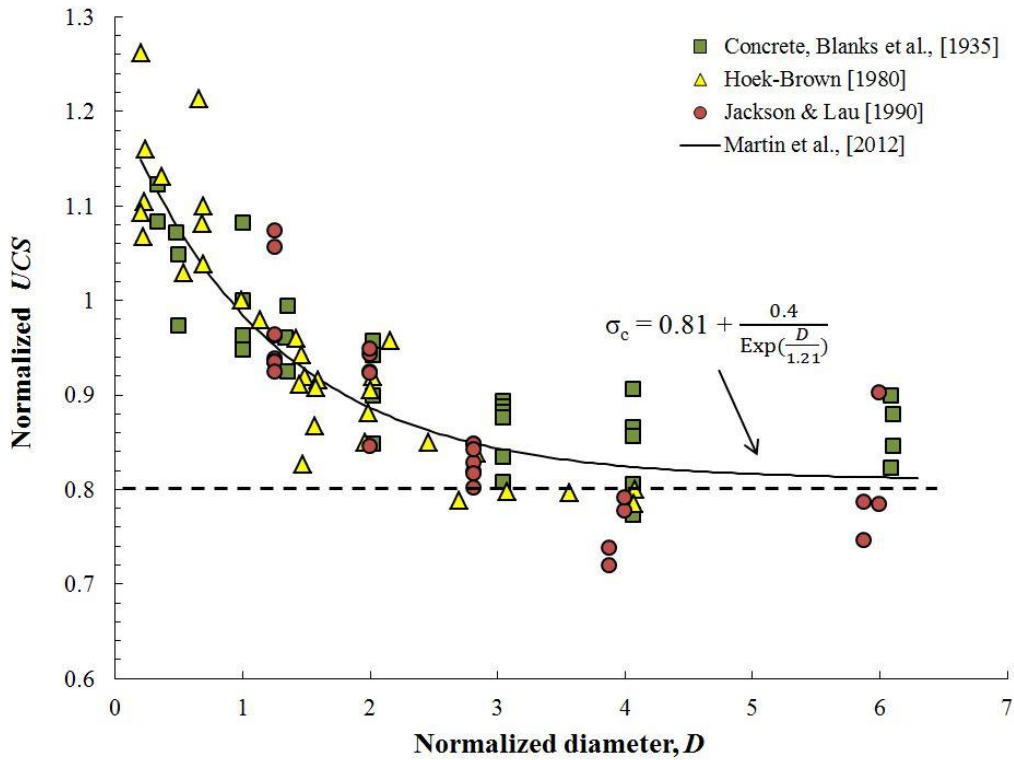


Figure 4-7: Summary of UCS test results of strengths for concrete and rocks, normalized to the minimum representative diameter, together with the approach by Martin et al. [2012].

4.1.3 Summary

In traditional numerical modeling, the strength and stiffness must be scaled to the physical problem size. For example, when modelling a large diameter tunnel, the strength and stiffness values should be appropriate for that tunnel model. The laboratory data compiled in this section demonstrates that there is no evidence for reducing the model values for the uniaxial strength and Young's modulus to less than approximately 0.8 of the laboratory scale (50 mm) values.

4.2 Factors Affecting Grain-based Models

The results in the previous section demonstrated the effect of scale, geometry and grain size on laboratory tests. In this section the effect of grain size, scale and geometry on the Grain-based model is examined.

4.2.1 Selection of marble for GBM modelling

To demonstrate the versatility of the GBM methodology, the factors that could affect GBM results are examined using a fine-grained marble from a quarry at Gaoligong Mount in Yunnan Province, in southwest China. The marble was sampled from an open pit at a depth of about 50 m. Laboratory tests and thin-section examination demonstrated that marble was homogeneous and intact. The marble is composed of 95% Calcite and 5% Quartz and the mean values of the grain sizes are about 1 mm and 0.75 mm, respectively. (Figure 4-8)

Comparison of the marble and LdB granite, reveals the following. First, both rocks can be classified as Strong Rocks (ISRM R3 to R6), since their uniaxial compressive strengths are greater than 25 MPa. Second, both rocks have low porosity, i.e., less than 1% to 2%. From this aspect, any porosity-induced factors that affect rock strength and deformation are eliminated.

Third, both are composed of several fine-grained and fine-medium grained minerals. Also, the main components of both rocks (i.e. feldspar in LdB granite and calcite in the marble) are polycrystalline, which is suitable for simulation by using the polygonal structure in the GBM.

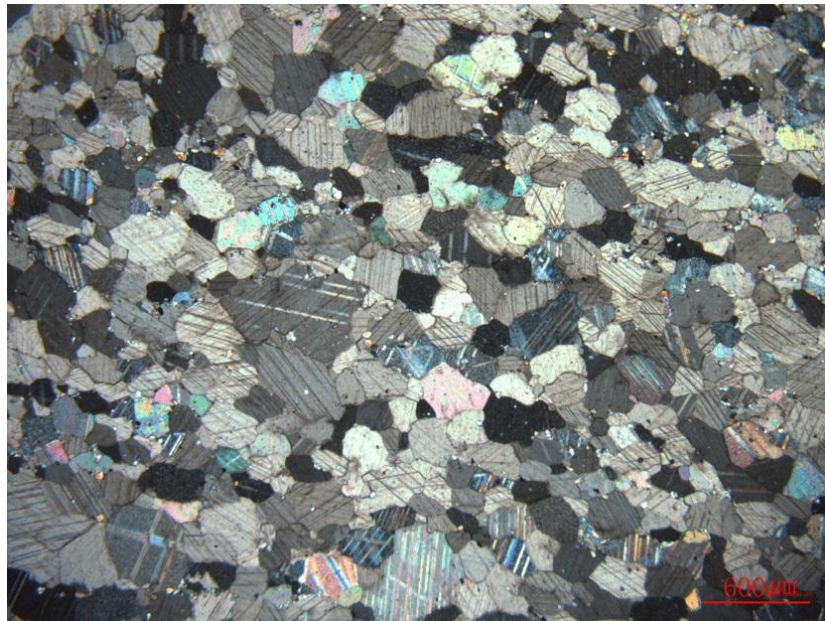


Figure 4-8: Mineral grain structure (under polarizing microscope) of the marble from a quarry at Gaoligong Mount. (Yunnan Province, China)

4.2.2 Modelling procedure

The GBM was created using the same methodology given in Chapter 3. Figure 4-9 illustrates the geometric model of the marble that divides the space into two minerals using voronoi tessellation. The grains in light colour represent calcite accounting for 95% of total mineral composition and the dark colour grains are representative of quartz with a mineral composition of 5%. It should be noted that the size difference between calcite and quartz is small (1 mm for calcite and 0.75 mm for quartz), which causes minor geometric and material heterogeneity.

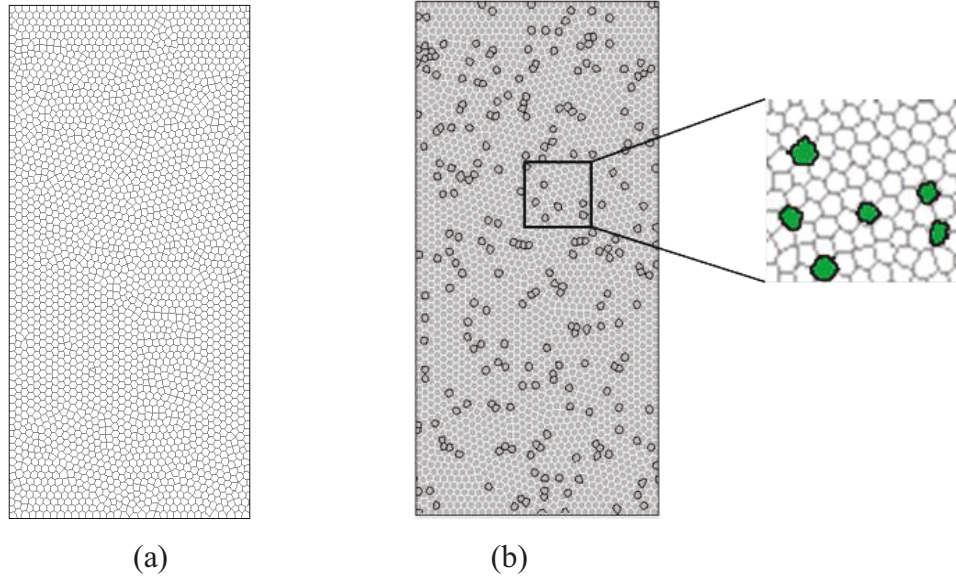
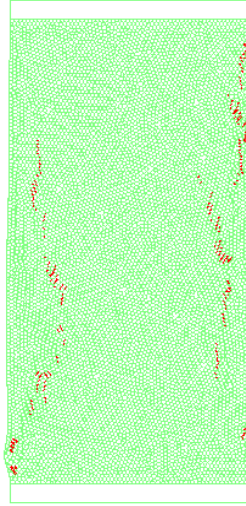


Figure 4-9: Grain-based model and mineral composition of the marble. (a) The polygonal grains from the voronoi generator. (b) the GBM with assigned grain properties (95% calcite and 5% quartz).

The ratio of the normal stiffness (K_n) to shear stiffness (K_s) was taken as 1.8 for initial calibration, based on the Poisson's ratio of 0.34. The initial calibration of the GBM to the peak uniaxial strength and Young's Modulus is compared to the stress-strain response in Figure 4-10 and the laboratory values in Table 4-1. As illustrated in Figure 4-10 there is good agreement between the GBM modelling results and the laboratory stress-strain response. The discrepancy between the properties obtained with the GBM and the measured laboratory properties varies from -6.2% to 4.2% (Table 4-1). The GBM marble strengths and the measured UCS differ by only 0.7%.

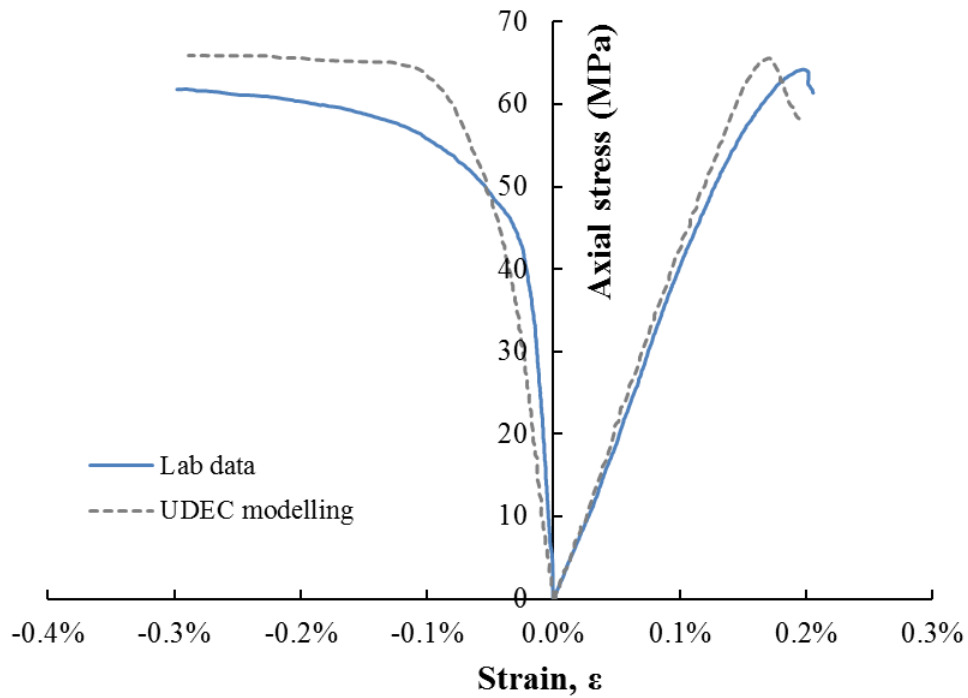


Marble at UCS failure



GBM failure

(a) Marble sample failure and GBM model failure in uniaxial compression.



(b) Comparison of stress-strain curves.

Figure 4-10: (a) Example of the uniaxial compression test on marble; and (b) comparison of GBM stress-strain response with laboratory test data for the marbles.

Table 4-1: Comparison of laboratory test results and modeling results of marble.

Properties	Marble	GBM	Error
P-Wave (m/s)	5780	N/A	
UCS, σ_c (MPa)	64.8	65.3	+0.7%
Tensile strength, σ_t (MPa)	3.71	N/A	
Young's modulus, E (GPa)	38.1	39.7	+4.2%
Poisson's ratio, μ	0.34	0.327	-3.8%
Cohesion, c (MPa)	38.1		
Friction angle, ϕ (degree)	34.2		
Crack damage stress, σ_{cd} (MPa)	51.8 (80% of σ_c)	48.6	-6.2%

4.2.3 Effect of grain size

As suggested by ISRM, the diameter of the laboratory specimen should be greater than 10 times the largest grain of rock. [Brown, 1981] When the grain size is increased, the laboratory sample size should be increased if this criterion is not fulfilled. In the GBM the grain size distribution is imported to capture the geometric heterogeneity. When the grain size in the GBM is increased the grain size distribution is maintained and the polygons grains are simply scaled, as illustrated in Figure 4-11. In this study, the GBM of the marble were generated with a composition of different mean grain sizes (from R to $5R$) using the same micro-properties. R represents the mean grain size for original sample. Figure 4-11 illustrates a process that the mean grain sizes have been amplified up to 5 times the original size R , but still with the same grain size distribution. From this aspect, any influence caused by the grain size is directly linked to the particle size and the effect of randomly distributed pattern was eliminated.

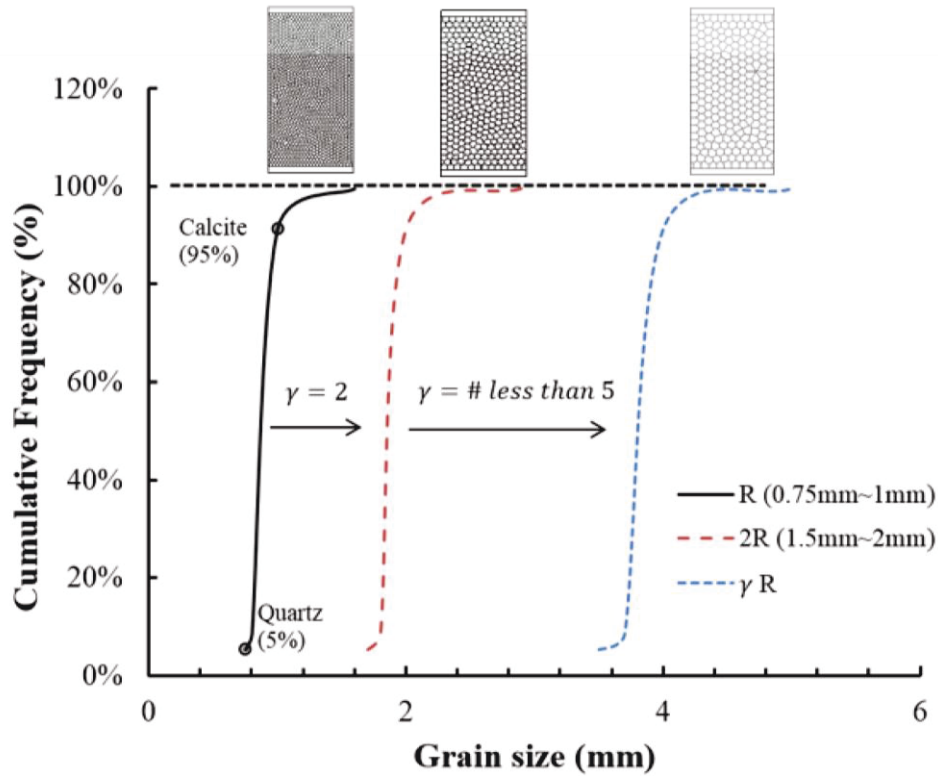


Figure 4-11: Illustration of scaling the same grain size distribution for various GBM with different mean grain sizes.

Table 4-2: Deformation properties and peak uniaxial strength, for different GBM marble models with various mean grain sizes, R .

mean grain size (mm)	UCS (MPa)	Young's modulus E (GPa)	Poisson's ratio
1.0R (0.75~1 mm)	60	39.7	0.327
1.2R (0.9~1.2 mm)	102	48	0.321
1.5R (1.125~1.5 mm)	118	52.7	0.323
2.0R (1.5~2 mm)	88	57.5	0.324
2.5R (1.875~2.5 mm)	99	62.2	0.318
3.0R (2.25~3 mm)	116	65.6	0.331
4.0R (3~4 mm)	102	70.1	0.325
5.0R (3.75~5 mm)	98	73.0	0.332

A series of GBMs were carried out to assess the effect of grain size. The uniaxial strength and deformation properties are given in Table 4-2 and summarised in Figure 4-12 and Figure 4-13, along with the associated stress-strain curves in Figure 4-14.

As seen in Table 4-2, Poisson’s ratio, appears to be independent of particle size. Potyondy and Cundall [2004] using the discrete element technique based on disks also concluded Poisson’s ratio to be independent of particle size.

Figure 4-12 shows the effect of grain size on the GBM uniaxial strength. The GBM results in Figure 4-12 exhibit no clear increasing or decreasing trend along with increase in the mean grain size. This is similar to the laboratory data by Su [2004] and William et al. [1974].

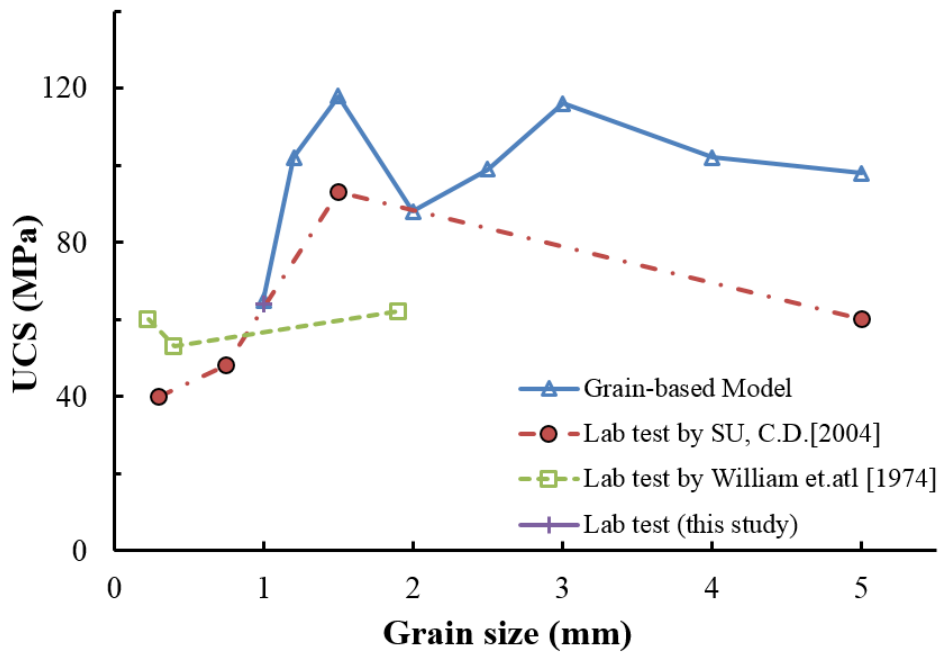


Figure 4-12: The variation relationship between rock strength (UCS) and grain size for various types of marbles reported by different researchers.

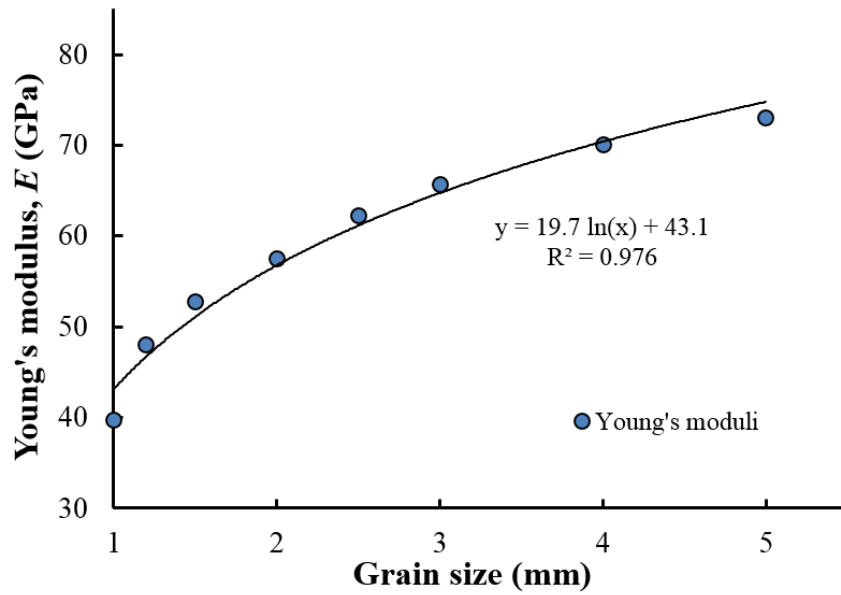


Figure 4-13: Numerically obtained values of Young's modulus of marble under unconfined compressive loading, with increasing grain size.

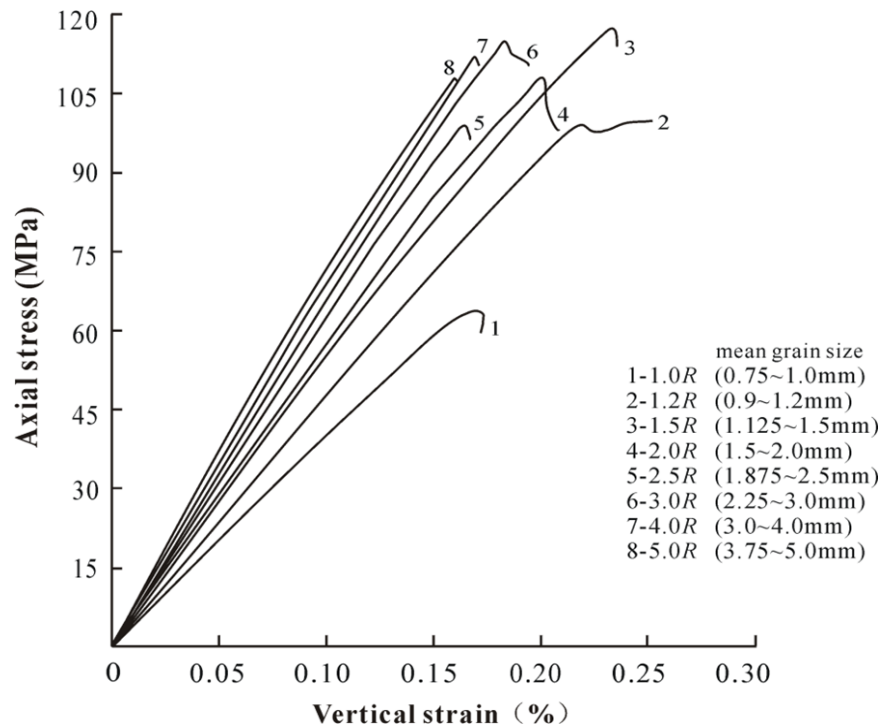


Figure 4-14: Eight stress-strain curves representative of the models of marbles with eight different mean grain sizes.

Unlike the uniaxial compressive strength, Young's modulus was found to be strongly influenced by mean grain size (Figure 4-13). This increase is also readily observed in the stress-strain results in Figure 4-14. This increase is simply related to the reduction in the number of grains being tested without any adjustment for the contact stiffness. Carried to the extreme, if only one grain was tested the modulus would simply be the modulus of the single grain. Hence these results are simply an artefact of the modelling input but do illustrate that the contact stiffness plays a major role in controlling the macro-scale Young's modulus.

4.2.4 Effect of sample shape

A series of GBMs were tested to investigate the effect of sample shape on the laboratory results reported by Hudson [1971]. Figure 4-15 shows the stress-strain response and the peak uniaxial strength for the GBM models as the ratio of the height to diameter is varied from 1 to 3. As shown in Figure 4-16 there is a significant change in the behaviour and normalised strength as the ratio of height to diameter increases from 1 to 2. The GBM modelling results are compared to the laboratory results in Table 4-3.

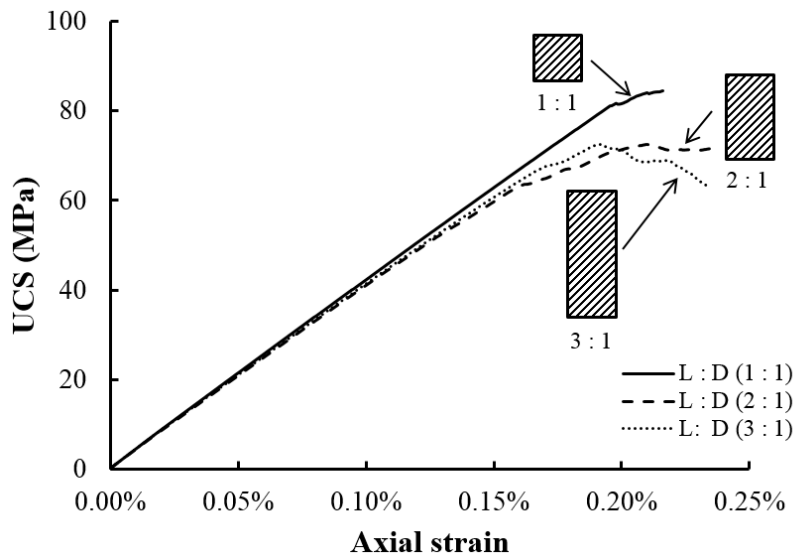


Figure 4-15: Effect of sample shape (length to diameter ratios) on the stress-strain response and peak strength for GBM marbles.

Table 4-3: Sample configurations and a comparison between original laboratory test data from Hudson [1971] and GBM modeling results.

L:D ratio	Lab data		GBM Modelling	
	UCS (MPa)	normalized ratio $\sigma / \sigma_{(2-1)}$	UCS (MPa)	normalized ratio $\sigma / \sigma_{(2-1)}$
1:1	103.0	1.14	82.0	1.26
2:1	90.2	1.00	65.3	1.00
3:1	88.5	0.98	64.2	0.98

The GBMs were not calibrated to the laboratory marble samples used by Hudson [1971] and hence the absolute values cannot be compared directly. In order to compare the results in Table 4-3 they are normalised to the results for the Length: Diameter = 2. It is clear from the results in Table 4-3 that the greatest changes occur when $L: D > 1$. The GBM modelling results agree well with the conclusion that the sample shape (length to diameter ratio) has a distinct influence

on the compressive strength especially for the specimen with $L:D < 2$. The findings from both the GBM models and the laboratory data support the ISRM Suggested Method [1981], which specifies the ratio of height (length) to diameter is preferably 2.5-3.0.

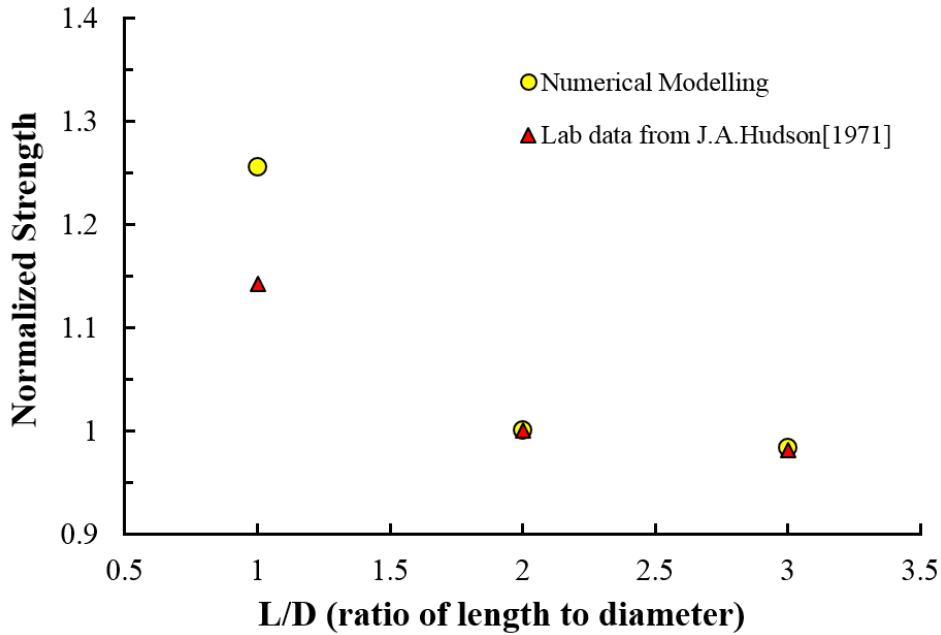


Figure 4-16: Relation between normalized strength and ratio of the length to diameter.

4.2.5 Effect of scale

Another series of GBM marble models were carried out to investigate the effect of scale on the compressive strength. Two modelled groups were examined: Group 1 was based on the 1 mm mean grain size while Group 2 had a mean grain size of 3 mm. The model diameter in Group 1 ranged from 20 to 80 mm while the diameters in Group 2 ranged from 30 to 100 mm. The $L:D = 2$ for all models. Table 4-4 gives the strength and deformation results for all the GBM of marbles.

Table 4-4: GBM marble model peak strength and deformation results for samples with different diameters.

Group 1(1R) : Calcite-1mm, Quartz-0.75mm			
Size (mm×mm)	Young's Modulus (GPa)	GBM UCS (MPa)	GBM UCS Difference
20×40	41.1	73.1	-5.0%
25×50	40.7	71.8	-2.8%
30×60	40.1	68.7	-3.9%
50×100	39.7	65.3	0.0%
60×120	39.2	62.8	-0.6%
80×160	39.2	60.9	+1.5%
Group 2(3R): Calcite-3mm, Quartz-2.25mm			
30×60	67.4	123.8	-2.7%
40×80	67.2	118.3	-2.1%
50×100	66.9	116	0.0%
60×120	66.2	111.6	-0.6%
80×160	65.5	108.7	+2.0%
100×200	64.1	102.7	+0.3%

From Table 4-4, the Young's modulus for Group 1 (1 mm grain size) decreases slightly from 41 GPa to 39 GPa (4.6%) while Group 2 (3 mm grain size) decreases from 67 GPa to 64 GPa (4.9%) as the sample size increases. The results in Table 4-4 are summarized in Figure 4-17 and demonstrate that the gradual reduction in Young's moduli for the mean 1 mm and 3 mm grain size related to sample diameter is similar.

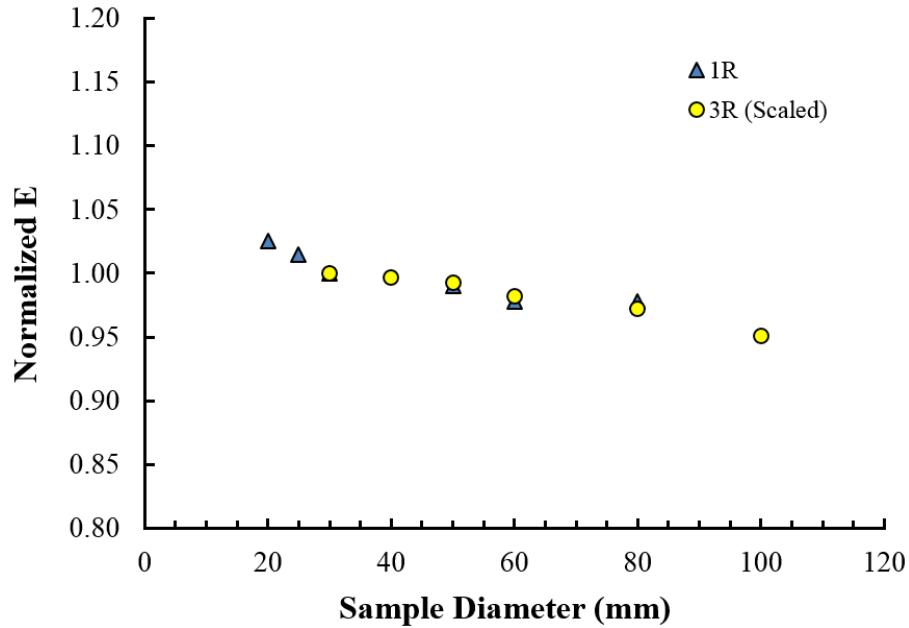


Figure 4-17: The gradual reduction in normalised Young’s moduli for the mean 1 mm and 3 mm grain size related to sample diameter.

The uniaxial compressive strengths in Table 4-4 are summarised in Figure 4-18. In Figure 4-18 the strength is normalised to the strength at 50 mm diameter and the diameters are normalised to 50 mm. In Figure 4-18 the GBM model results are compared to both laboratory results and the predicted strength using the equation by Hoek and Brown [1980] and the equation by Martin et al [2012]. In all GBM cases there is a noticeable influence on the effect of increasing model sample diameter. It is not clear from these results if at large diameters, i.e., $> 5D$ if the GBM strength would plateau in the same way as observed in the laboratory results (see Figure 4-7). This aspect is explored in the following section.

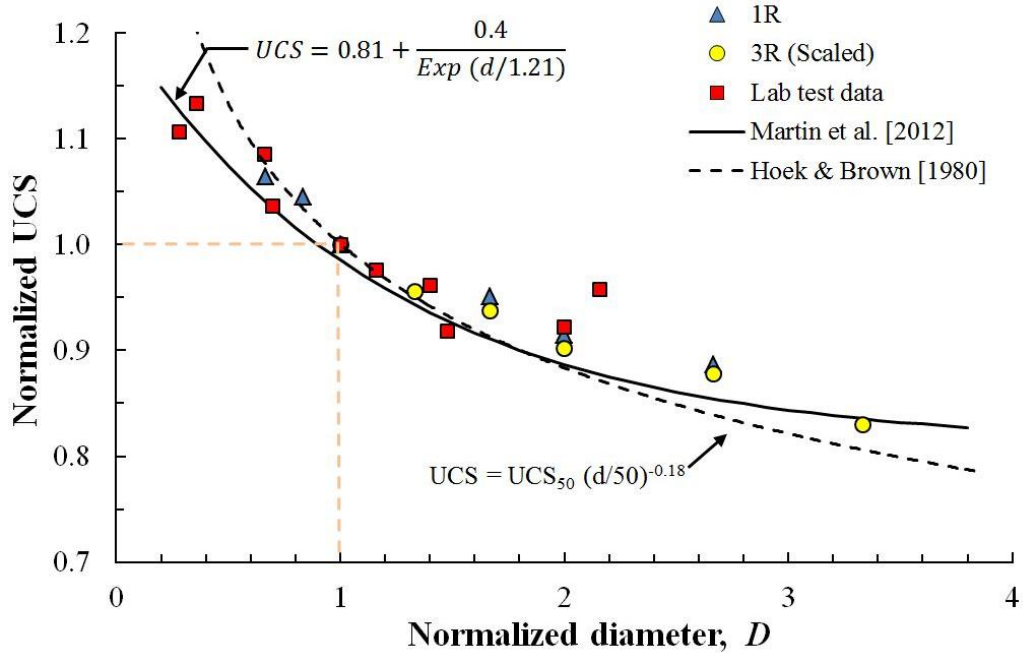


Figure 4-18: The reduction in normalised uniaxial compressive strength for the mean 1 mm and 3 mm grain size related to sample diameter, compared to the laboratory results and the results given by Equation (4-1) and Equation (4-2).

4.3 Effect of Model Grid on GBM

In the previous section, both the Young's modulus and the uniaxial compressive strength obtained from the GBMs showed a reduction in magnitude as the diameter of the models increased. While the laboratory data showed that the reduction in magnitudes tended to plateau when samples reached a critical diameter (about 100 mm for rock) this observation was not evident in the GBM modelling. It is well known that mesh regularity can affect GBM modelling results [Lan et al., 2010]. In this section the effect of a uniform and random grid on the GBM scale effects results are examined.

4.3.1 GBM uniform and randomized grid

Despite the polygonal structure of rock, in this example a uniform square grid is used to represent the rock structure. The GBM is created in the same manner as described previously, the only change being the introduction of the square grid. The grain contacts are assumed to be linear and parallel and/or perpendicular to other contacts. For comparison, the other GBM modelling utilises the standard GBM random polygonal model.

In order to minimize the influence of heterogeneity due to mineral compositions, both models have only one mineral grain (calcite). In terms of the uniform square grid model, all the grains are assumed to be square. In comparison, the random grid model is composed two different sized grains, 5% with 0.75mm diameter grains and 95% with 1mm size grains. The grain size distributions for both models are illustrated in Figure 4-19.

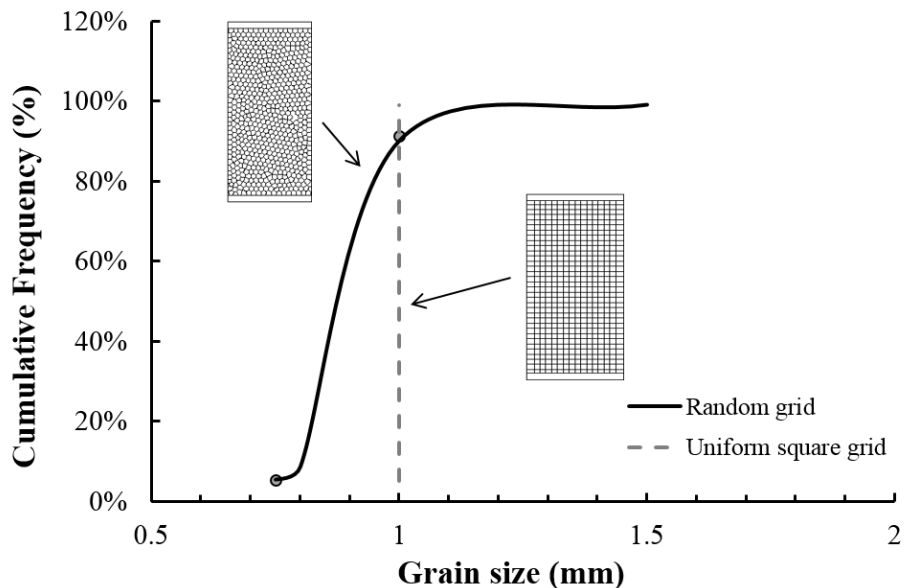


Figure 4-19: Comparison of the grain size used for uniform square grid and the random grid in the GBM modelling.

The stress-strain response for the uniform square grid and the random grid in the GBM modelling is given in Figure 4-20. Inspection of Figure 4-20 reveals that the grid generation has little effect on the Young's modulus. However, the peak strength in Figure 4-20 is influenced by the grid selection with the square uniform grid increasing the peak strength.

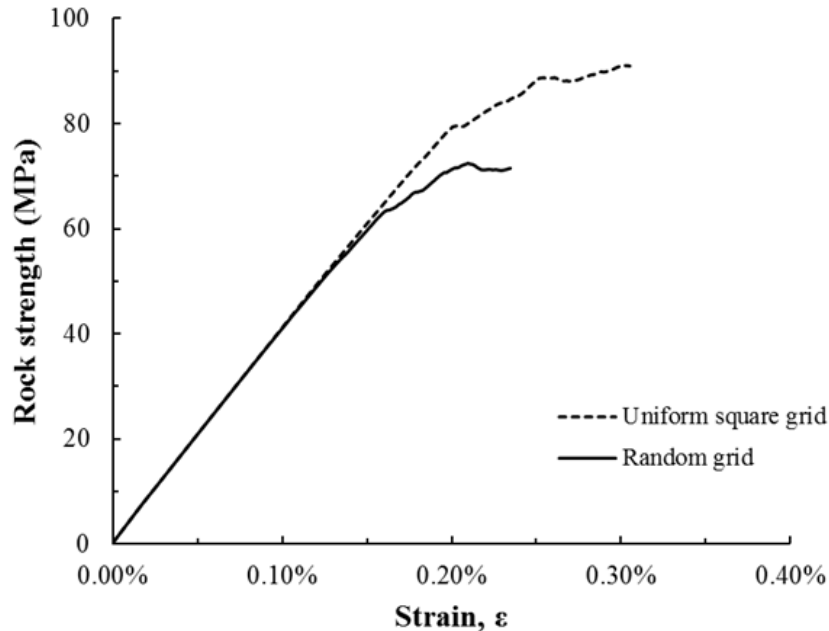


Figure 4-20: Stress-strain curves of two grid models showing rock strength and stiffness.

4.3.2 Tensile stress development

As noted by Lan et al. [2010] and more recently by Bewick et al. [2012] the randomized polygonal grid produces geometric heterogeneity that increases the tensile stress distribution. Because the GBM uniaxial compressive strength is controlled indirectly by the tensile strength, any changes to the model that increases the distribution and magnitude of tensile stress can influence the peak strength. When investigating the effect of sample size using numerical models it is important to maintain the same grain size distribution so that the influence of

geometric heterogeneity is minimised as much as possible. With the GBM Model it is not possible to control and reproduce identical grain size distributions. Hence each model will produce a sample distribution and therefore the result from each model is a statistical sampling of the strength.

Three GBM samples with diameters of 30 mm, 60 mm and 105 mm were used to investigate the effect of heterogeneity on contact breakage between grains and the tensile stress generation. The tensile stress development was investigated for the grain contacts in the middle part of the GBM where the effect of the end-cap boundary conditions is minimised (Figure 4-21). The magnitude of the tensile stress at each contact together and the total number of tensile cracks were recorded for the middle third of the GBM.

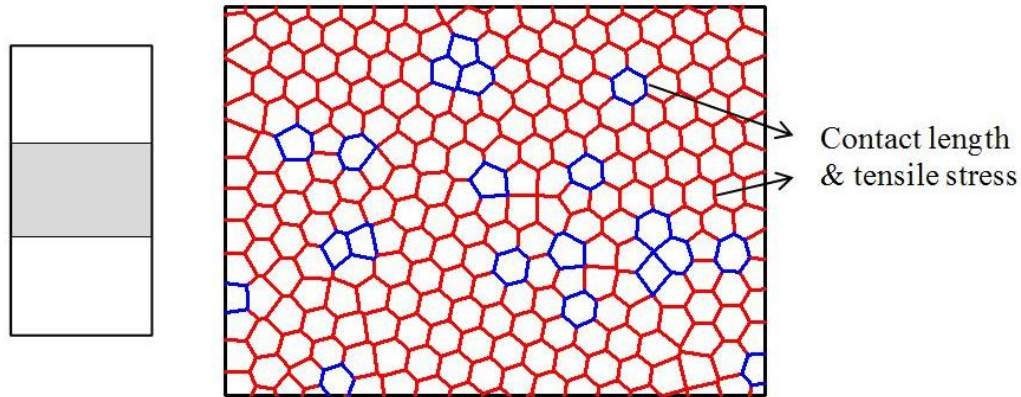


Figure 4-21: Analysis of tensile stress occurred along contacts.

The tensile stress in the middle third of the GBM sample was determined for three sample diameters: 30mm, 60mm and 105mm. The distribution of the tensile stresses at the grain contacts in the middle third of the sample when the compressive axial strain is at 0.1% is summarised in (Figure 4-22). The laboratory tensile strength for the marble is 3.5 MPa and the tensile stress distribution is divided into seven equal tiers ranging from 0 to 3.5 MPa. The

smallest sample (30-mm diameter) has the lowest tensile stress level in terms of frequency, while the 105-mm-diameter sample has the largest tensile stress distribution.

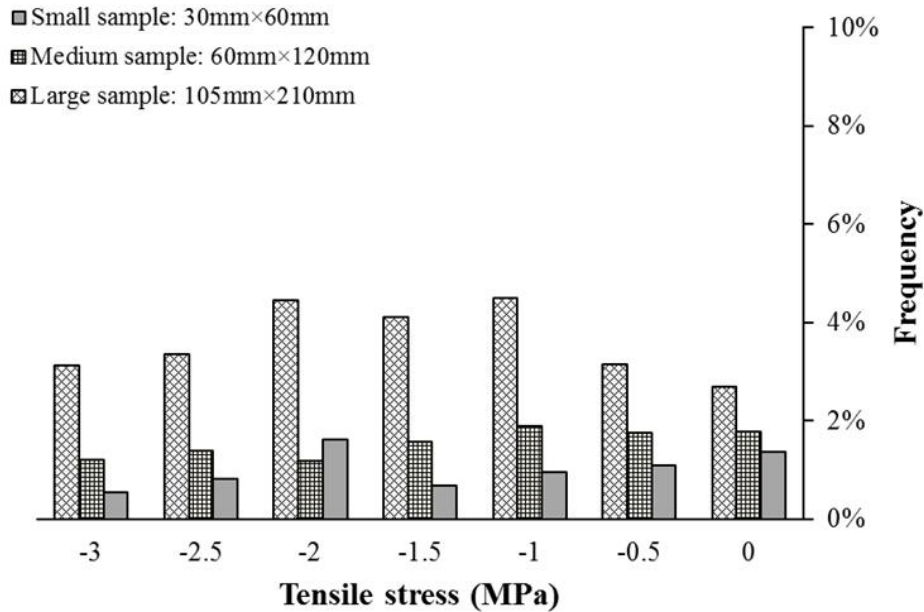


Figure 4-22: Illustration of frequencies of tensile stress occurrence at grain contacts based on all the contacts, for three different sized samples whose diameter is 30 mm, 60 mm and 105 mm separately.

It has been long recognized that the development of the tensile stresses is associated with the process of crack initiation. The number of cracks in the middle third of the sample was examined to assess the impact of sample size on the crack density (Figure 4-23). The results in Figure 4-23 suggest that the crack density increases linearly with sample size, also supporting the notion that the tensile stresses are greater in the larger sample. It is clear from these analyses that the development of tensile stresses is a major factor in controlling uniaxial strength in these GBMs, and that the tensile strength magnitude is significantly influenced by geometric heterogeneity.

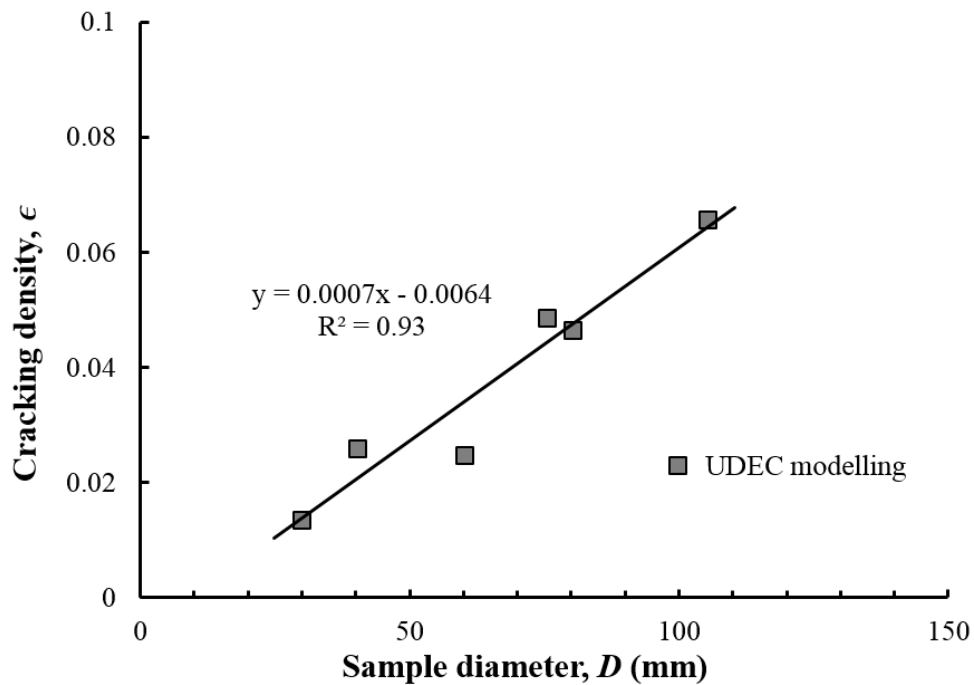


Figure 4-23: The average crack length and cracking density versus sample diameter. The results are obtained from the recorded data through statistical analysis.

4.4 Summary

This chapter briefly examines the application of the Grained-based models (GBMs) to simulate the effects of grain size and geometry on laboratory strength. The GBM model was calibrated to fine grained marble. A series of GBMs were carried out and the results provide the following conclusions:

- When grain size increases, the Young's modulus of similar size samples also increase. This is an artefact of the GBM model. Poisson's ratio is almost the same for the model of all grain sizes.
- There is little or no scale effect on uniaxial GBM strengths with respect to the mean grain size. This is also supported by laboratory results.

- The GBM samples with $L: D < 2$, shows a significant increase in peak strength. This finding supports the ISRM [1981] suggested method where $L: D > 2$ is recommended to minimise the effect of sample geometry.
- The GBM model results suggest that the Young's modulus is not sensitive to sample diameter. This is also supported by laboratory data.
- The GBM model results supports the notion that the uniaxial strength show a noticeable scale effect at least for samples up to 100 mm diameter. These findings are also supported by laboratory results
- In the GBM modelling the generation of tensile stresses is linked to the observed scale-strength effects. These tensile stress magnitudes increase as the sample size grows. The geometric heterogeneity created by the polygonal grains in the GBM is responsible for the tensile stress generation. These findings support the notion that geometric heterogeneity plays a significant role in controlling brittle rock strength.

5 Effect of Flaws on Rock Strength

Rock mass strength is made up of strength of intact blocks and strength of weak planes referred to as flaws or fractures. As noted by many researchers, the existence of discontinuities such as flaws or fractures in a rock mass significantly impacts its behaviour. Figure 5-1 highlights the visual impact of multiple fractures on a rock slope. It is clear from Figure 5-1 that these fractures are responsible for local failures and that these failures are occurring on the discrete fractures. The strength of the intact blocks and the shear strength of the single discrete flaw can be measured in the laboratory using well-established testing procedures. However, estimating the combined strength of intact blocks and multiple fractures at different orientations remains a significant challenge. The Grain-based model (GBM) has been developed for modelling intact rock. In this chapter, the GBM will be used to investigate the effect of uniformly distributed flaws on the compressive strength.



Figure 5-1: Photo of rock mass containing intact blocks and fractures blocks.

5.1 Effect of a Single Inclined Flaw

Goodman [1989] defined the rock mass strength for an engineered structure as the maximum stress level that is tolerable, with respect to the consequence of local or gross failure. In a rock mass fractures govern the rock strength, deformability and permeability of the rock mass. Before examining the effect of fractures on rock strength, in this section the relationship between the rock strength and the occurrence of a single flaw will be discussed. In this Chapter flaw and/or fracture is used to denote a discontinuity in the rock that has strength properties significantly weaker than the intact material.

Rock masses cut by a single set of natural discontinuities, such as bedding or uniformly spaced fractures, will display strength anisotropy. Jaeger [1960] and Donath [1961] examined the shear strength anisotropy of a single discrete flaw inclined at various angles β to the direction of the applied load (Figure 5-2). Their findings showed the strength of intact rock is reduced when a weak plane occurs at an angle that allows slip to occur before the peak intact strength is reached (Figure 5-2).

According to the Brady and Brown [1993], the principal stress difference required to produce slip $(\sigma_1 - \sigma_3)_s$ tends to infinity as $\beta \rightarrow 90^\circ$ and as $\beta \rightarrow \emptyset$ where \emptyset is the friction angle of the inclined plane. Hence slip will occur only when

$$(\sigma_1 - \sigma_3)_s = \frac{2(c + \sigma_3 \tan \emptyset)}{(1 - \tan \emptyset \cot \beta) \sin 2\beta} \quad (5-1)$$

where c = cohesion, \emptyset = friction angle and σ_3 = confining stress. When the inequality for Equation (5-1) is not satisfied, slip on the discontinuity cannot occur and the only alternative is fracture of the intact rock. The minimum

strength of the material containing the weak plane is illustrated in Figure 5-2 and occurs when $\beta = (45^\circ + \phi/2)$.

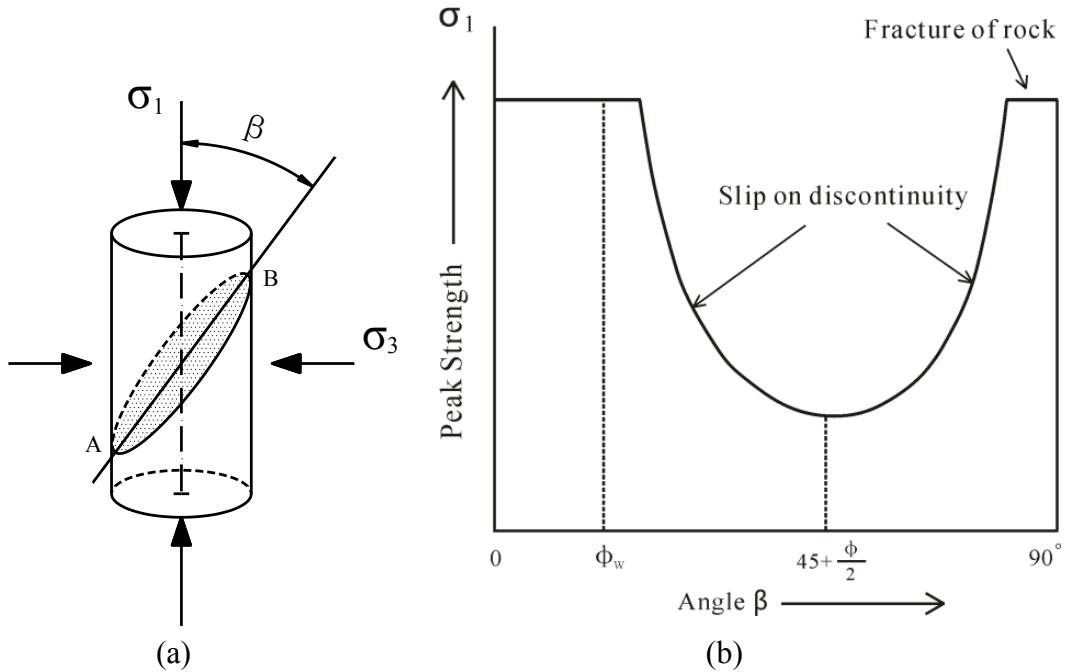


Figure 5-2: (a) Illustration of rock specimen with a single weak plane inclined at a certain angle of β to the maximum primary stress; (b) Variation of the peak strength of rock with a weak plane inclined at various angles β .

A number of Grain-based models were developed to assess the influence of a single inclined weak plane on the uniaxial compressive strength. A flaw in the Grain-based models was created using Coulomb slip residual model, which incorporates five separate parameters (normal stiffness k_n , shear stiffness k_s , joint cohesion c , joint friction ϕ and joint tension t) together with three related residual values (cohesion c_r , friction ϕ_r and tension t_r). The mechanical properties of an open flaw used in the GBM modelling are listed in Table 5-1.

Table 5-1: Summary of micro-properties of natural fractures of rock blocks.

Normal stiffness, k_n (MPa/mm)	1280
Shear stiffness, k_s (MPa/mm)	860
Peak friction angle, φ ($^\circ$)	30
Peak cohesion, c (MPa)	0
Residual friction angle φ_r ($^\circ$)	30
Residual cohesion, c_r (MPa)	0

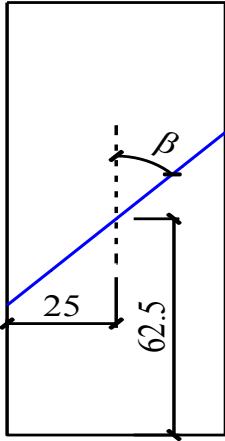
The GBMs were used to simulate the laboratory experiments carried out by Roy [1993] and Teja [2008]. The GBM samples were 50 mm wide and 125 mm high and detailed sample configurations are given in Table 5-2. All samples were subjected to a vertical compressive loading, which designates the direction of the maximum principal stress (σ_1). The properties used for the GBM modelling are those for Lac du Bonnet granite. Roy [1993] and Teja [2008] used plaster of Paris for their experimental work. In order to compare the GBM results to the experimental results, both results are normalised to the uniaxial compressive strength of the intact material.

Based on the single plane of weakness theory introduced by Jaeger [1960], the relationship between the ratio of weak plane strength and intact strength (S_i) and the inclination angle β can be described as a continuous function given by:

$$S_i = A - B[\cos 2(\beta - \beta_{min})]^n \quad (5-2)$$

where A , B and n are constants; β_{min} is the value of β corresponding to minima in S_i .

Table 5-2: The configuration of sample and UCS test results of rock sample with tilted single flaw.

Test Description	Specification	UCS (MPa)
one through-going flaw dipping at various angles: (a. 0°; b.10°; c. 20°; d. 30°; e.45°; f. 60°; g.70°; h. 75°). The flaw is centered in the middle of the sample.		a=187 b=152 c=84 d=29 e=69 f=164 g=179 h=186

The results from the GBM modelling are compared with the laboratory tests results in Figure 5-3. Equation (5-2) is also shown in Figure 5-3 and provides a reasonable fit to both the laboratory and GBM modelling data. Hoek and Brown [1980] showed that the anisotropic strength of the inclined flaws reaches the maximum at $\beta = 0^\circ$ and 90° , and the minimum when $\beta = 20^\circ$ to 30° . While minimum rock strength is in reasonable agreement theoretical strength, the intact strength is generally less than the theoretical value of 1 at $\beta = 0^\circ$ and 90° . In other words the presence of the vertically oriented flaw does reduce the strength in both the GBM and laboratory models.

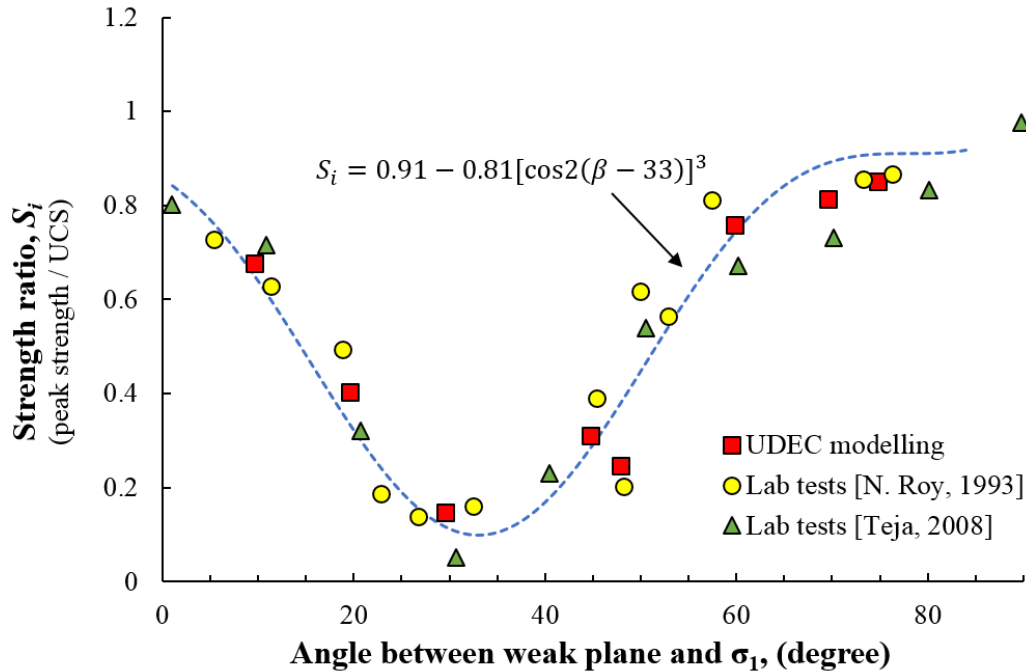


Figure 5-3: Variation of the peak strength with different angles of inclination of the flaw, β .

5.2 Strength of Rocks Containing Regularly Distributed Flaws

The previous section established that the GBM modelling approach was suitable for investigating the effect of a single flaw on rock strength. The most challenging situation encountered in rock engineering is establishing the rock mass strength when the flaws are discontinuous. Discontinuous flaws are analysed in this section. Two cases are assumed for this study: (1) a set of parallel flaws inclined at 45° in the center domain of the sample, and (2) discontinuous regularly distributed flaws inclined in vertical direction and spaced uniformly.

In the grain-based model when the grain-boundary contacts representing intact rock reach their peak strength, a residual strength model is used to capture the brittle nature of grain boundary fracture. Once the tensile or shear strength

reaches the internal flag set for each grain contact strength, residual strength value is assigned to the ruptured contact, which creates associated stress redistribution. While this creates long run times, the process is considered representative of compressive loading of intact rocks [Lan et al., 2010].

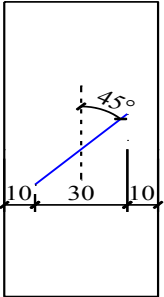
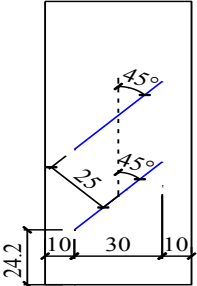
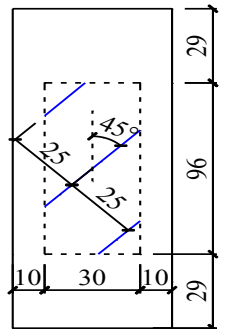
5.2.1 Parallel inclined flaws

To investigate the influence of pre-existing flaws on the strength of samples, a single discontinuous flaw inclined at 45° was placed in the center of the GBM. Then two and three flaws were added to the model with the same inclination angle such that the influence of direction of flaw was excluded. The discontinuous flaws are limited within a region of 30 mm wide and 96 mm height, which means that the flaws are 10 mm away from the free boundary. The failure must occur through intact rock. Table 5-3 gives the geometry used for each of the Lac du Bonnet granite GBM.

The results for the uniaxial compressive strength are also summarised in Table 5-3. From Table 5-3 we can see that the UCS decreases from 105 MPa to 100 MPa as the number of flaws increases from one to three. With the single inclined discontinuous flaw the UCS stress is reduced by approximately 50%, from 200 MPa to 100 MPa.

It is interesting that the ratios of total flaw length to sample area containing the flaws are very similar for all three GBM modelling results. Detailed discussion regarding this specific ratio will be given in the following section.

Table 5-3: The configuration of sample and UCS test results of rock sample with discontinuous flaws inclined at 45 degree.

Test Description	Specification	UCS (MPa)
one inclined flaw		105
two perfect parallel inclined flaws (spacing of 25mm)		102
three perfect parallel inclined flaws (spacing of 25mm)		100

5.2.2 Discontinuous parallel vertical flaws

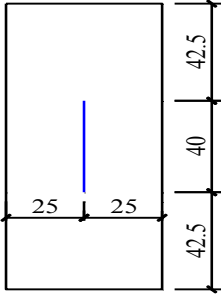
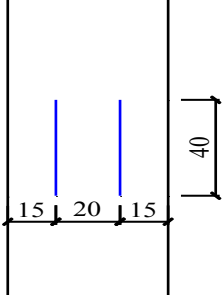
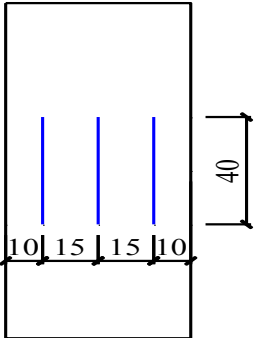
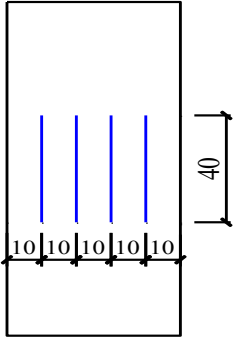
As discussed previously, inclined flaws create an obvious anisotropic influence on the rock strength. In this section, all the flaws are vertical such that the number of flaws and flaw spacing remain the primary factors to be evaluated. The samples were created with the number of vertical flaws ranging one 1 to 7 in the center part of it. The length of each flaw was limited to 40 mm and located approximately in the middle 1/3 of the sample. The flaw spacing in the model was adjusted between 10 mm to 20 mm. Table 5-4 shows a general configuration of the model with discontinuous vertical flaws and the uniaxial strength obtained for each GBM.

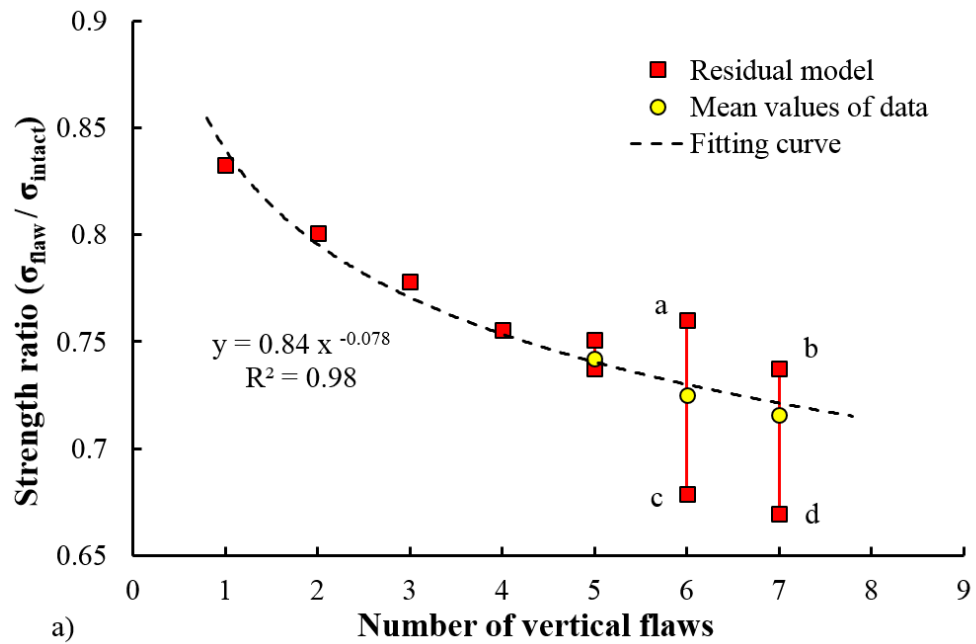
The uniaxial strengths from the GBM for the various spacing between the flaws (d) are summarised in Table 5-4. The GBM strengths are normalized to the intact strength and shown in Figure 5-4a as a function of the number of flaws. Figure 5-4a clearly shows the reduction in uniaxial strength from 0.83 to 0.75 as the number of flaws increases from one to four, respectively. When there are more than four flaws in the model, the strength reduction becomes more scattered with the highest variability occurring when the number of flaws reaches 6 or 7. When there are 6 or 7 flaws but the spacing between the flaws is reduced, the rock strength increases (see point a, b in Figure 5-4a). When the spacing between the 6 or 7 flaws is increased, the strength drops significantly (Point c, d). It is clear from Figure 5-4a the number of the flaws is not the only factor influencing the GBM strengths.

As is mentioned above, the spacing between the flaws also affects the rock strength. Figure 5-4b shows the results for the uniaxial strength for the samples in Table 5-5 as a function of spacing between the flaws. There is a clear

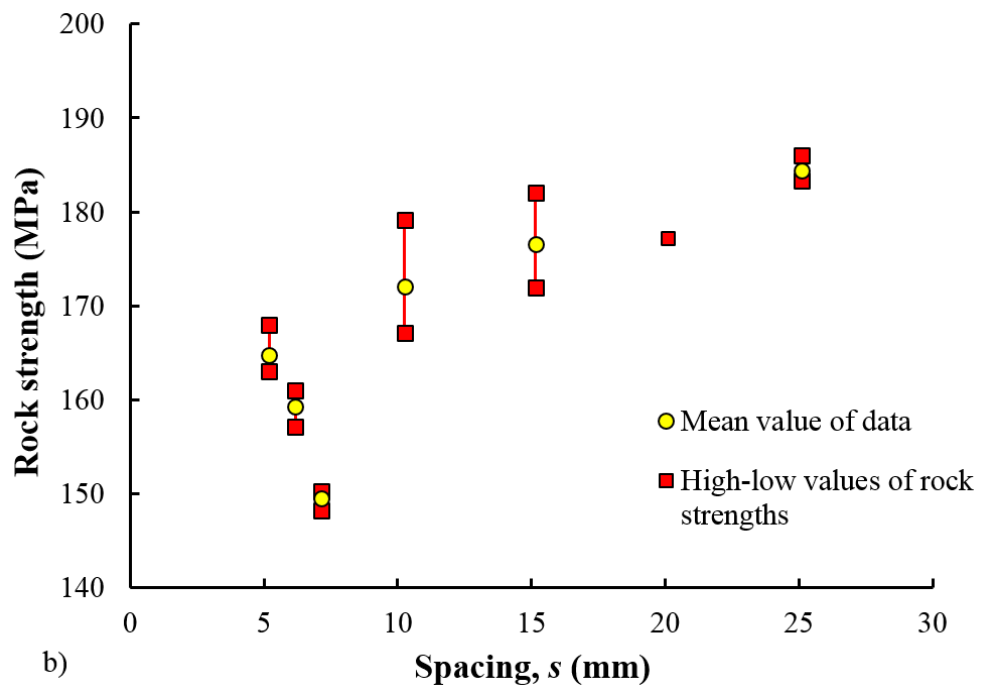
increase in strength with flaw spacing when the spacing exceeds 10 mm. However, when the spacing is less than 10 mm, the uniaxial strength does not appear to be a function of the spacing between the flaws.

Table 5-4: The configurations of samples and UCS test results of samples with a set of vertical flaws.

Configuration & UCS (MPa)	
 <p>One flaw UCS=184 MPa</p>	 <p>Two flaws UCS=177 MPa</p>
 <p>Three flaws UCS=172 MPa</p>	 <p>Four and more flaws UCS=174MPa (4 flaws), 171 MPa (5 flaws), 168 MPa (6 flaws), 166 MPa (7 flaws)</p>



a)



b)

Figure 5-4: (a) The effect of number of flaws and (b) the effect of spacing between the flaws on the uniaxial compressive strength obtained using the GBM modeling.

Table 5-5: The UCS and strength ratios of samples containing up to seven flaws.
Unit: d (mm).

No. of flaws	GBM model					
	Strength σ (MPa)			Strength ratio		
1	184			0.83		
2	177			0.80		
3	172			0.78		
4	167			0.76		
5	(d=7)	(d=7.5)		(d=7)	(d=7.5)	
	166	163		0.75	0.74	
6	(d=5)	(d=6)	(d=7)	(d=5)	(d=6)	(d=7)
	168	161	150	0.76	0.73	0.68
7	(d=5)	(d=6)	(d=7)	d=5	d=6	(d=7)
	163	158	148	0.74	0.71	0.67

It is well known that strain localization in compression loading of laboratory sample initiates on the boundary of the sample. In order to uncover the complex relationship between number of flaws and spacing of flaws, a third factor is introduced which measures the distance from a margin flaw to the free surface of the sample. Figure 5-5 shows the uniaxial strength as a function of the distance of the nearest flaw from the sample boundary. In general, the uniaxial strength increases as the distance from the flaw to a free surface increases. This trend appears more pronounced in the samples with more than three flaws. By increasing the distance from the free boundary from 5 mm to 10 mm the uniaxial strength increases approximately 150 MPa to about 165-170 MPa. It is clear from Figure 5-5 that both the number of flaws and the distance the flaw is from the free boundary impacts on the uniaxial compressive strength.

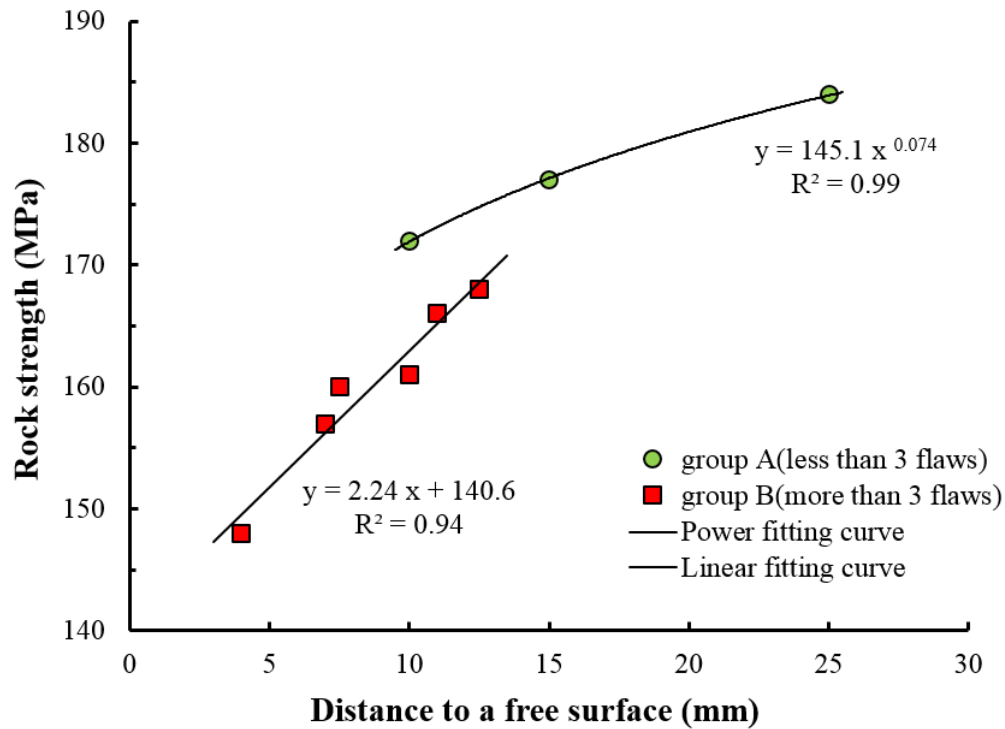


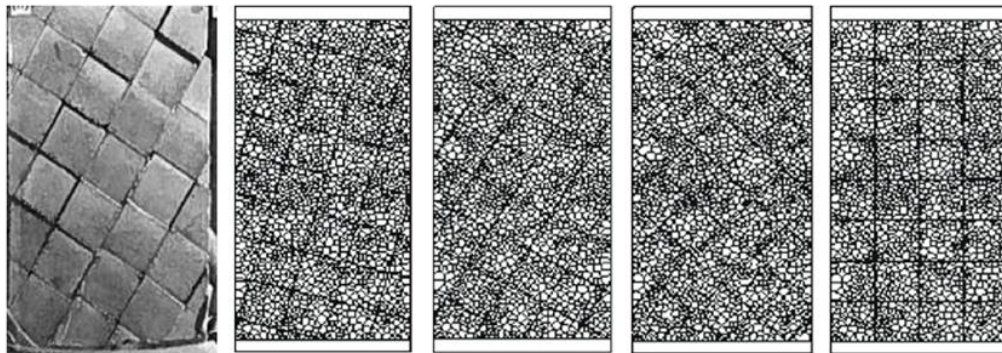
Figure 5-5: Variation of rock strengths as a function of distance between flaws and free surface.

5.2.3 Uniform pattern of continuous flaws

Many researchers have used physical model tests to analyze the stability of structures built on jointed rocks. [e.g., Venter and Strasse, 1958; Goldstein et al., 1966; Grishin et al., 1967; and Fumagalli, 1968] Given the limitation at that time the physical models often utilised regular patterns of flaws which in a model consisting of an assemblage of small blocks.

Brown and Trollope [1970] and Einstein et al. [1969] conducted a number of physical model tests to establish the effect of uniform flaws on rock strength. Their tests were carried out using a plaster model with continuous planes. Figure 5-6 shows the nominal 100 mm x 100 mm x 200 mm physical models used by Brown and Trollope [1970]. The uniaxial compressive strength of the solid

material was 20.75 MPa with a porosity of 30% and the confinement used for the tests ranged from 0 to 6.9 MPa. While the porosity of the plaster is far greater than that observed in most rocks, plaster reproduces many of the brittle characteristics of rock provided the confining stress is relatively low. The results from the model studies carried out by Brown and Trollope [1970] are shown in Figure 5-7. The results in Figure 5-7 have been normalized to the unconfined compressive strength of the intact sample (20.75 MPa). The results in Figure 5-7 clearly demonstrate the effect of confinement and the inclination of the through-going fractures on the model strength. It is also clear from Figure 5-7 that at the high confining stress stresses, the brittle nature of the plaster was replaced with more ductile/plastic behaviour.



(a) Model test (b) 15-75° (c) 30-60° (d) 45-45° (e) 0-90°

Figure 5-6: (a) Examples of the physical model samples used by Brown and Trollope [1970]; (b), (c), (d) and (e) GBMs with various joint geometries.

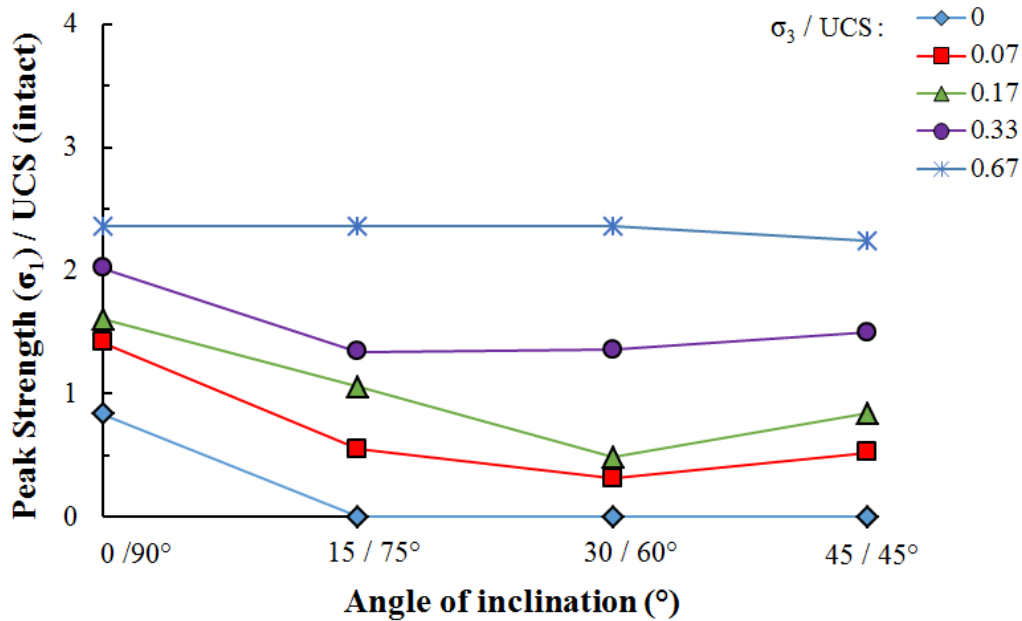


Figure 5-7: Physical model test results from Brown and Trollope [1970] for gypsum plaster. The results have been normalized to unconfined compressive strength of the intact sample (20.75 MPa).

The physical models used by Brown and Trollope [1970] were created and analyzed using the GBM modelling. Instead of using the plaster samples, four samples of Lac du Bonnet (LdB) granite were created. The LdB block had a width of 50 mm with a height of 100 mm and each of the small blocks measured 12.5 mm × 12.5 mm. The strength of the through-going fractures was set to 30 degrees with zero cohesion. The confining stress used in the simulations was 0, 15, 35, 55 and 70 MPa. The results for Lac du Bonnet granite are summarised in Table 5-6 and shown in Figure 5-8. Like the results from Brown and Trollope [1970], the GBM results also illustrate that when the fracture is inclined to the direction of loading the orientation of the fractures controls the strength. The blocky nature of the material had no effect on the ultimate strength when fractures were inclined parallel and perpendicular (0/90°) to the direction of loading. In fact the blocks at this orientation had essentially the same strength as the uniaxial

compressive strength of the intact material suggesting no scale effects for this inclination. These results also highlight the difficulty of determining the strength based only on block size.

Table 5-6: Peak strengths obtained for the GBM.

Confining stress (MPa)	Peak solid strength (MPa)	Peak strength (MPa) angle of joint inclination, i/β , degree			
		0°-90°	15°-75°	30°-60°	45°-45°
0	221	238	0	0	0
15	368	409	126	118	138
35	510	516	179	151	186
55	664	684	218	192	247
70	722	746	292	265	288

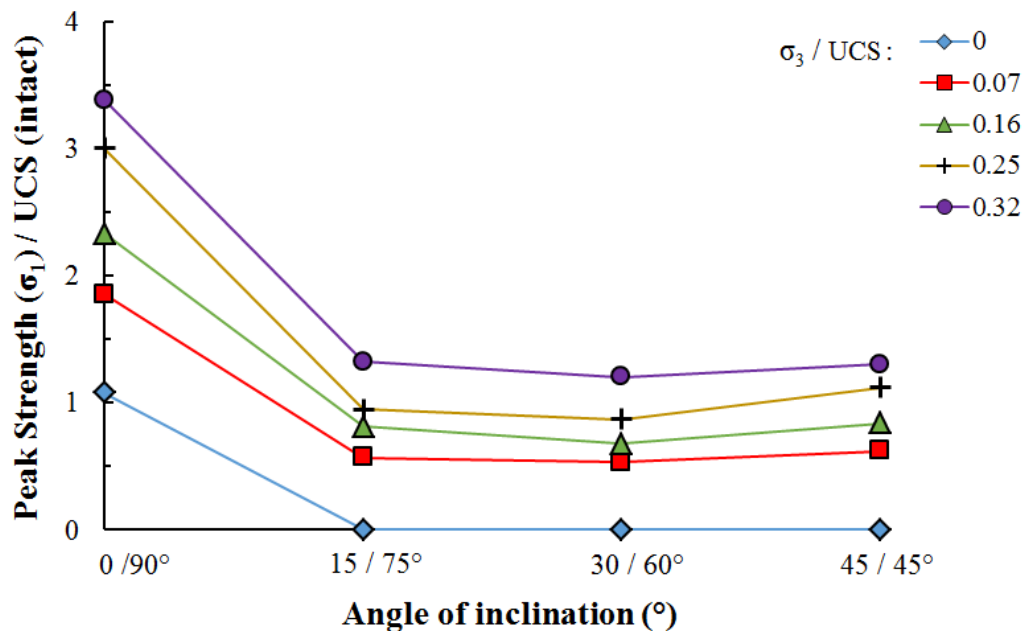


Figure 5-8: GBM Lac du Bonnet granite peak strength for the model geometry given in Figure 5-6.

Under the lower confining stresses, the peak strength distribution for the GBM model is similar to the laboratory results from Brown and Trollope [1970] for all the four sets of models. However, at higher confining stress ratios (σ_3/UCS) of 0.32 the LdB GBMs remain very brittle. This is not surprising as the triaxial laboratory results for Lac du Bonnet granite also show a brittle response at similar confining stress ratios [Martin, 1997]. The more ductile behaviour in the plaster of Paris used by Brown and Trollope [1970] may be the results of the small sample size, 12.5 mm cubes, and the high porosity of the material.

These GBM results again highlight the effect of inclined through-going flaws on the model strength. More importantly, the GBM results also demonstrate the robustness of the approach when simulating not only intact material but material containing through-going and discontinuous flaws.

5.3 Strength of Rocks Containing Random Discontinuous Flaws

In many rock masses flaws are randomly distributed such as illustrated in Figure 5-9. For such rocks determining the uniaxial compressive strength is very difficult. The ISRM Suggest Methods [Brown, 1981] recommend the diameter of the sample be 10 times greater than the largest grain size or flaw size. Following these suggested methods implies a minimum diameter for testing equal to 10 times the flaw-size of 76 mm (assuming the flaw-size is no greater than the core diameter). Such tests are not practical to conduct and hence the Grain-based model offers an alternative to establish the rock strength when the rock contains large flaws. A challenge with this approach is developing a metric that can be used to capture the distribution of the random flaws.



Figure 5-9: Example of the randomly distributed flaws in a 76-mm-diameter drill core.

5.3.1 Fracture intensity

Dershowitz and Einstein [1988] suggested the following four parameters are required to describe the fracturing found in rock masses: (1) orientation of the fractures, (2) fracture size, (3) fracture intensity, and (4) spatial variation of the fractures. These four fundamental parameters describe the complexity and variability of the fractures. There are some secondary properties of interest such as fracture termination, aperture distribution, and transmissivity, which can be determined by conventional tools if necessary. Today these parameters are quantified using the Discrete Fracture Network (DFN) [Rogers et al., 2009]

Among the listed parameters described by Dershowitz and Einstein [1988], fracture intensity is used to describe the heterogeneous statistical nature of fracture systems. Measurement of fracture intensity involves the dimension of the measurement area and the size of the fractures. It could be defined either from 1-Dimensional data or from 2-Dimensional (surface mapping), or even from a

3-Dimensional data, which considers the area of fractures in a volume. Rogers et al. [2009] have provided an overview of a fracture intensity used in discrete fracture network (DFN) characterisation (Table 5-7). The fracture intensity is expressed using a P_{ij} system (P_{10} , P_{21} and P_{32}), describing the fractures in 1, 2 or 3 dimensions [Rogers et al., 2006, and 2009]. The simplest fracture intensity measurement, P_{10} , describes the numbers of fractures per unit length of scan line [$\#/L^{-1}$]. P_{21} is defined as the sum of the length of fractures per unit area (m/m^2) and directly incorporates fracture size and hence is not scale-dependent. P_{32} is defined as the sum of the area of fractures per unit volume (m^2/m^3). The P_{21} and P_{32} provide more information than fracture spacing alone. Like P_{21} , the fracture intensity P_{32} is considered to be a preferred measurement of DFN models and is an intrinsic rock mass property. While it cannot be easily measured, it can be inferred from the 1-D and 2-D data.

Table 5-7: The P_{ij} system of fracture intensity, modified from [Rogers et al., 2009].

		Dimension of Measurement			
		0	1	2	3
Dimension of Sample	1	P_{10} No. of fractures per unit length of borehole	P_{11} <i>length of fractures per unit length</i>		
	2	P_{20} No. of fractures per unit area	P_{21} length of fractures per unit area	P_{22} <i>area of fractures per area</i>	
	3	P_{30} No. of fractures per unit volume		P_{32} area of fractures per unit volume	P_{33} <i>volume of fractures per volume</i>
Parameter		Density		Intensity	Porosity

5.3.2 Randomly distributed flaws

A number of GBMs were used to assess the effect of randomly distributed discontinuous flaws on uniaxial strength. All flaws have the same properties and length with only their orientation randomly distributed. Figure 5-10 shows the typical distribution of flaws in a sample. In all of these samples the fracture intensity, as defined by P_{21} , are the same. Because of the two-dimensional nature of the GBM, P_{21} is numerically equal to P_{32} .

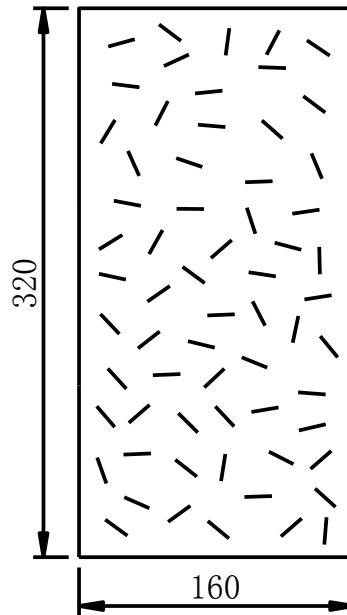


Figure 5-10: Illustration of typical sample configurations of flaw distribution, and compared to the flaws in a drill core. The length of each flaw is constant.

In the sample in Figure 5-10, a single flaw length (c_i) was set equal to 14 mm, which is approximately 3~5 times the mean grain size. The number of flaws in each sample can be determined by fixing P_{21} equal to a constant. For example using $P_{21}=0.02 \text{ m/m}^2$, a $50 \text{ mm} \times 100 \text{ mm}$ sample, the total length $\Sigma c = P_{21} \times 50 \times 100 = 100$. Hence, the number of flaws: $n = (\Sigma c) / c_i = 100/14 \cong 7$. With an increase in sample size, the number of flaws will also increase

accordingly in order to meet the requirement for constant fracture intensity. Alternatively, if the number of flaws are increased but the sample volume remains constant the fracture intensity increases. Two groups of models were carried out with a flaw length of 14 mm and 16 mm respectively. The GBM-UCS results for samples containing flaws are listed in Table 5-8 and the GBM-UCS results for the intact samples are given in Table 5-9.

From the results in Table 5-8, it is clear the GBM modelling with the 16 mm long flaws is weaker when compared to GBM modelling with the 14 mm long flaws. This reduction in peak strength occurs despite both groups of samples having the same value of fracture intensity, P_{21} , equal to 0.02.

Last point, it should be noted that the two dimensional situation was the main concern that would be encountered in the following sections. Hence, the fracture intensity P_{32} (mm^2/mm^3) could be converted to the corresponding value, P_{21} (mm/mm^2), representative of 2-D cases. The values for P_{21} and P_{32} would be numerically equal as 3-D configuration has been simplified to 2-D. However, the units will be still different. In order to avoid being confused, the units will be temporarily neglected especially when conversion between P_{32} and P_{21} is made. The units will be emphasized only when it encounters a scale related problem and units of either mm^2/mm^3 or m^2/m^3 have to be chosen.

Table 5-8: GBM results for UCS tests for different sized samples with two different configurations of flaw length. Peak strengths of rock are normalized to that for standard sized sample (50 mm×100 mm). All the samples have a same value of flaw intensity, $P_{21}=P_{32}=0.02$. Parameter ‘ n ’ represents the number of flaws in the sample.

Sample No.	Size (mm x mm)	$l = 14\text{mm}$				$l = 16\text{mm}$			
		n	GBM-UCS (MPa)	Normalized UCS	E (GPa)	n	GBM-UCS (MPa)	Normalized UCS	E (GPa)
1	50-100	7	206	1	77.8	6	196	1	76.9
2	60-120	10	198	0.961	77.2				
3	80-160	18	193	0.937	78.1				
4	100-200	29	182	0.883	77.8	25	176	0.90	77.8
5	130-260	48	175	0.85	77.7				
6	160-320	73	171	0.83	78.4	64	165	0.84	77.3
7	200-400	114	168	0.816	77.3	100	158	0.79	76.8
8	220-440	138	166	0.806	77.3				

Note: P_{21} is numerically equal to P_{32} . Detailed explanation regarding conversion between P_{21} and P_{32} is given on Page 105.

Table 5-9: Results of GBM UCS tests for intact samples in the same size configuration as compared to that of GBMs with the flaws.

Sample No.	Size (mm x mm)	UCS (MPa)	Normalized UCS	Hoek-Brown Equation	Young's Modulus, E (GPa)	Normalized E	Poisson's ratio
1	50-100	213	1.000	213.0	79.2	1	0.238
2	60-120	209	0.981	206.1	79.3	1.001	0.248
3	80-160	201	0.944	195.7	79.1	0.999	0.249
4	100-200	190	0.892	188.0	79.8	1.008	0.242
5	130-260	183	0.859	179.3	79.8	1.008	0.237
6	160-320	179	0.840	172.8	79.9	1.009	0.232
7	200-400	171	0.803	166.0	79.7	1.006	0.235
8	220-440	166	0.779	163.1	79.8	1.008	0.236

The UCS results for GBMs with randomly distributed flaws and increasing sample diameters are given in Figure 5-11. Figure 5-11 also gives the results for the intact GBM modelling and the scale effects equations given by Hoek-Brown [1980] and Martin et al [2011]. As discussed in Chapter 4, the GBM of intact rocks automatically illustrate scale effects when a polygonal grid structure is employed. However, when the flaws are introduced, as the flaw length is increased the strength is reduced for the same sample size.

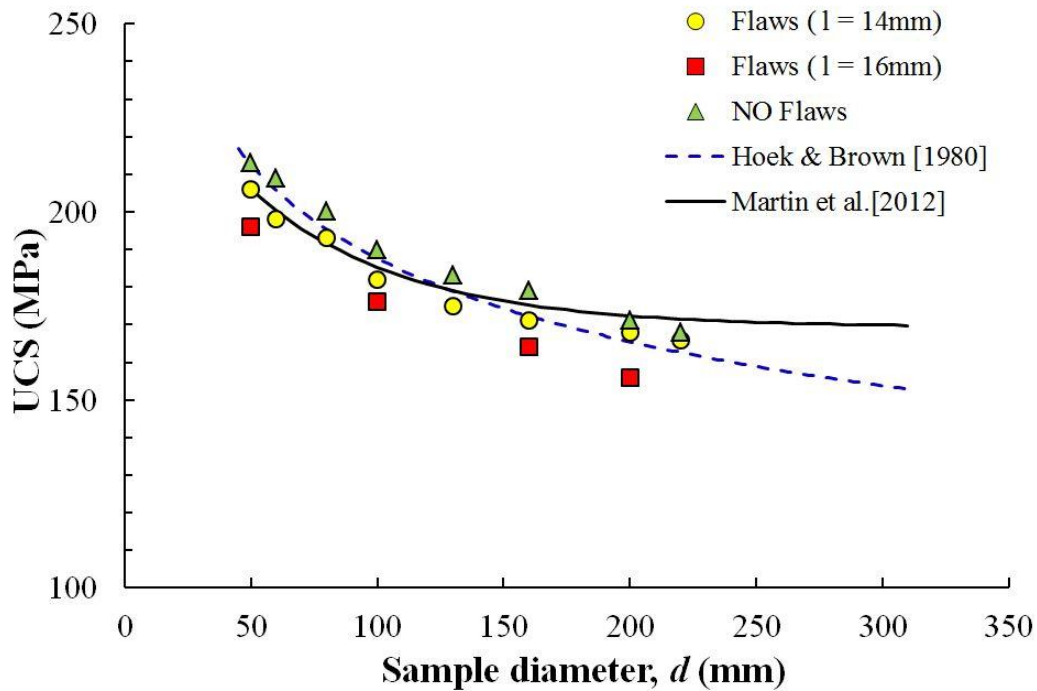


Figure 5-11: UCS results of LdB granite on the different-sized samples, compared to the intact UCS and fitted rock strength curves.

From the results in Figure 5-11 there is a reduction in GBM UCS values as the sample size increases, despite the constant fracture intensity. In order to investigate the influence of fracture intensity distribution on the UCS values the distribution of the flaws in the GBM modelling was varied in order to generate

varying P_{21} values. The GBM samples with varying fracture intensities are listed in Table 5-10. The first group of models were carried out with a flaw length of 14 mm. As shown in Table 5-10, as the fracture intensity increases from 0.02 to 0.10, i.e., number of flaws increases from 7 to 36. For a flaw length of 16 mm, the number of flaws increases from 6 to 32 as the fracture intensity increases from 0.02 to 0.10. The GBM UCS values for each fracture intensity and flaw length is also summarised in Table 5-10.

Table 5-10: GBM UCS results for samples (50 mm×100 mm) with two different flaw length configurations. Parameter ‘ n ’ represents the number of flaws in the sample.

P_{21}	$l = 14\text{mm}$			$l = 16\text{mm}$		
	n	UCS (MPa)	Young's modulus E (GPa)	n	UCS (MPa)	Young's modulus E (GPa)
0.02	7	206	77.8	6	196	79.2
0.03	11	202	74.5	10	189	76.8
0.04	14	194	74.8	13	183	74.7
0.05	18	188	74.2	16	177	73.6
0.06	21	178	73.5	20	138	72.0
0.08	28	169	71.8	25	94.8	72.3
0.10	36	114	71.4	32	71.4	71.8

The strength results for the GBM models in Table 5-10 are normalized to the intact strength (221 MPa) with no flaws and are summarized in Figure 5-12. As expected the strength decreases as the fracture intensity increases. However, as shown in Figure 5-12 the strength reduction is not linear but appears to decrease significantly when the fracture intensity reaches a threshold value. This threshold value appears not to be a unique value but a function of the length of the flaw. For reference, also plotted in Figure 5-12 is the minimum strength of the single through-going inclined flaw discussed in previous section. The inclined

through going flaw represents a lower bound for the UCS. It is clear from Figure 5-12 that the relationship between fracture intensity and strength is not unique and depends on the length of the flaw relative to the sample size. Nonetheless, such approaches may be useful for bounding rock mass strength.

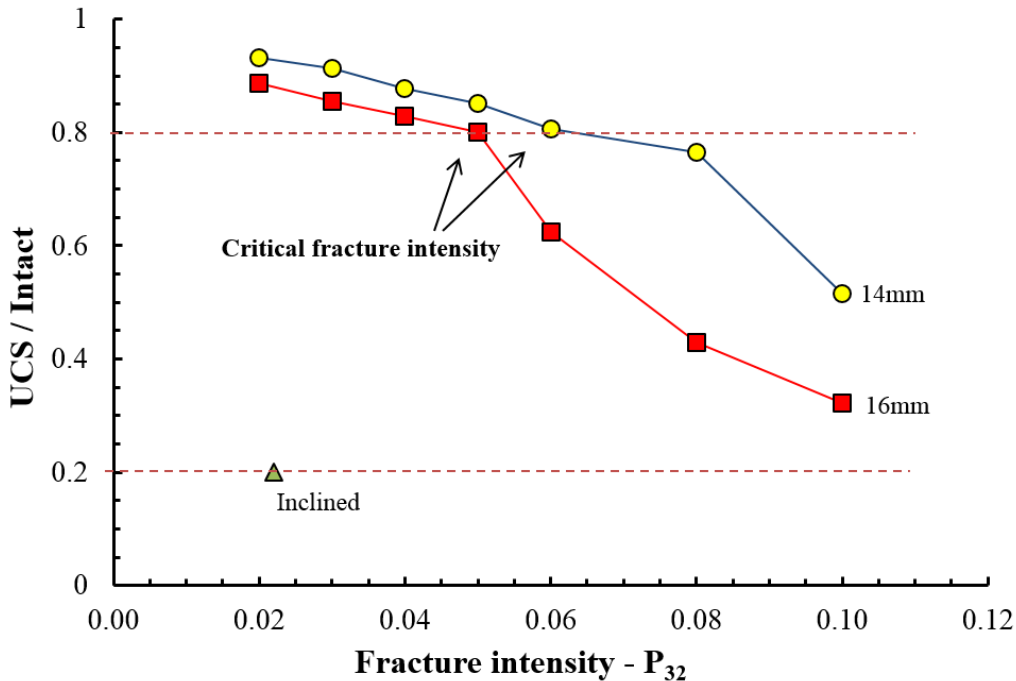
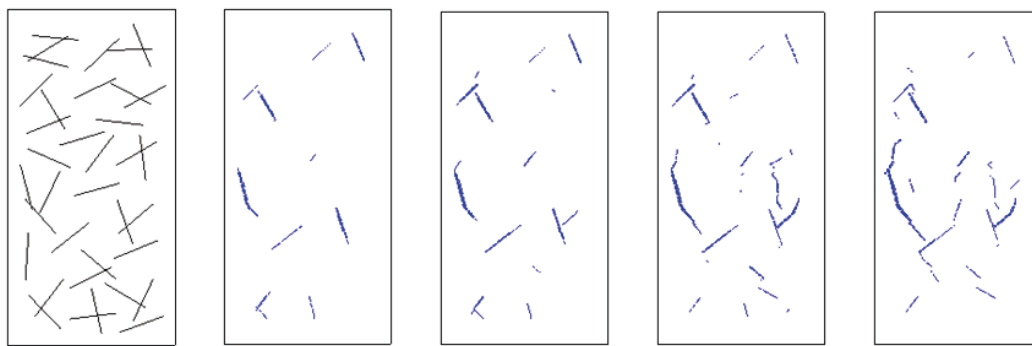
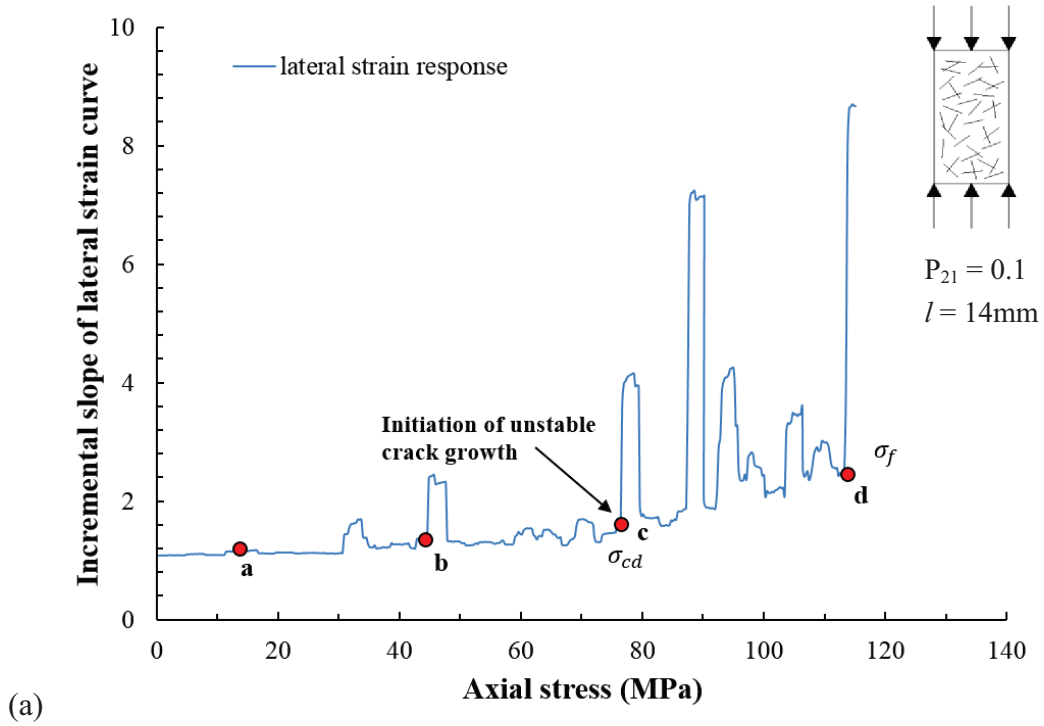


Figure 5-12: The relation between fracture intensity and strengths for the GBM UCS values in Table 5-10 normalised to the intact UCS value.

As noted in Chapter 2, yielding in UCS tests initiates with the onset of strain localization (unstable crack growth) which occurs at approximately 0.8 of the peak strength. The results from the GBM modelling were examined to evaluate the influence of fracture intensity associated with the unstable crack growth. The lateral strain response from UCS tests was used to determine onset of unstable crack growth. The lateral strain response is illustrated in Figure 5-13 with the initiation of unstable crack growth noted. The corresponding fracture

patterns in the sample are given in Figure 5-13. From the Figure 5-13 flow interaction appears to be a dominant characteristic of rocks containing flaws.



(b) Model a. 12% of peak b. 40% of peak c. 70% of peak d. failure

Figure 5-13: The onset of unstable crack growth in the GBM models and the associated fracture patterns.

5.3.3 Influence of flaw interaction on rock strength

As discussed in the previous sections, the strength of the GBMs can be related to the number of discrete flaws together with the distance to the free boundary, and the critical fracture intensity denoted as total trace length of flaws per unit area. However, it appears a single factor is not sufficient to establish reliable correlations to compressive strength. Studies by Hoek and Bieniawski [1965], Wong and Chau [2001], Wong et al. [2008] and Miller and Einstein [2008] reached similar conclusions. In this section, GBM unconfined models are used to examine the effect of flaw interaction on rock strength. The configurations of specimens are kept the same as discussed in the previous section (50 mm×100 mm) with constant fracture intensities, P_{21} .

Before various flaw distributions are assigned to different specimens, a specific flaw pattern is selected as a base model, from which other flaw distributions can be adjusted by flaw inclination, position or distance between flaw tips. A parameter (A_{in}) is introduced, which is defined by the circular area separating adjacent flaw tips. The GBM samples are illustrated in Figure 5-14.

From Figure 5-14 we can see that the general distribution patterns for the three specimens are almost same, except that distances between each flaw tips are increased or decreased (three different-sized circles in Figure 5-14). In addition, the average distance to sample boundary for all the flaws is essentially unchanged. Hence the change in GBM strengths will be attributed to the flaw interaction.

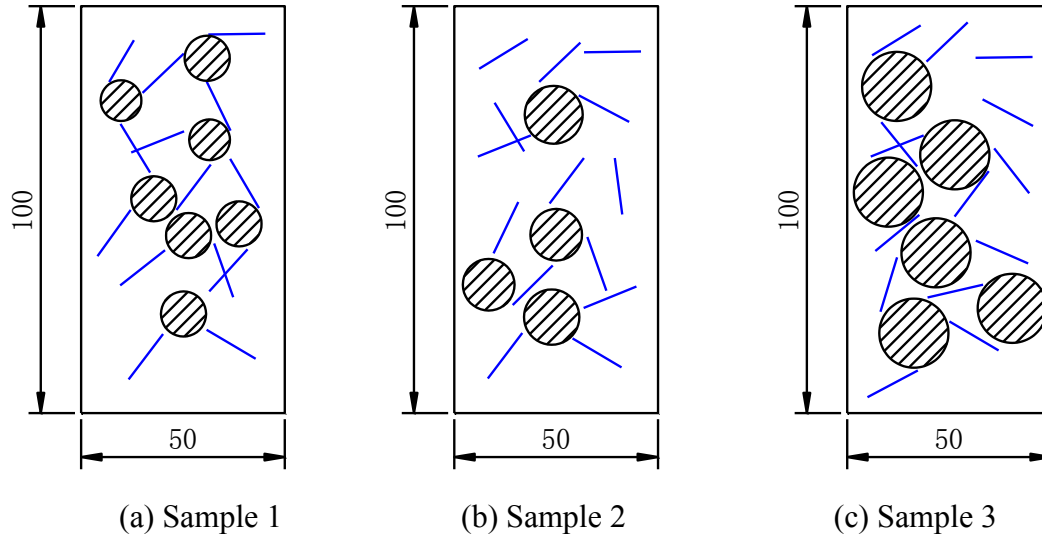


Figure 5-14: Illustration of flaw distribution in three samples with same specification (specimen size and number of flaws). (a) Closer flaw tips (small circles, $A_{in}=10$ mm); (b) Original flaw distribution (medium circles, $A_{in}=14.2$ mm); and (c) Separating flaw tips (large circles, $A_{in}=16.9$ mm).

The GBM samples were loaded in uniaxial compression and the stress-strain relationship recorded for each sample. The stress strain responses are compiled in Figure 5-15. From the stress-strain responses the following results are noteworthy:

1. Sample-1 with the smallest interaction area has the lowest strength.
2. Sample-3 has the largest interaction area and the highest strength.

The difference in the interaction area for the Sample-2 and -3 is $A=1.58$ cm² and 2.24 cm² respectively. We can find the stress- strain curves for Sample-2 and -3 are almost identical and there is only a subtle change in the rock strength for these two samples.

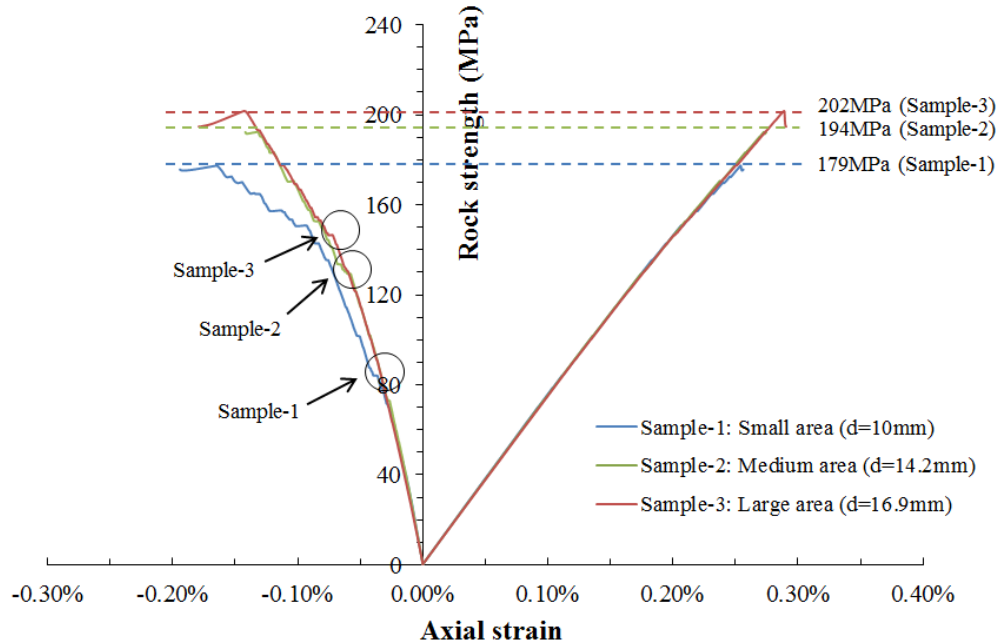


Figure 5-15: Stress-strain curve of three samples with different flaw interaction patterns. Note that the sudden stress drop reflected from the lateral strain part of the curves is accentuated in the circled area.

Inspection of Figure 5-15 reveals that there are critical points on the stress-strain response, which is indicative of an abrupt change in the gradient of stress-lateral strain during the process of compression. This phenomenon was also noted by Wong [2007] who suggested that the stress drops occur when the flaw interaction results in a stepping pattern. The circles are noted on the lateral strain curve in Figure 5-15, identifying the stress associated with the flaw interaction.

Crack initiation and propagation in the GBM modelling is complex and largely dependent on the discrete flaw distribution pattern. Even if under the same external loading conditions and same internal flaw specification such as number of flaws, flaw inclination and fracture intensity, there is still a possibility that the flaw pattern will influence the rock strengths. Tensile cracks are

commonly initiated after the initiation of small cracks which are the first to appear at the flaw tips during the cracking process. Thereafter, both tensile cracks and shear cracks act together to develop a flaw-through fashion in the sample. Figure 5-16 shows the growth of the flaws in the GBM model as loading is increased. It is fairly clear from Figure 5-16 that interacting flaws are likely to influence the GBM strength, particularly if the interacting flaw is the flaw closest to the free boundary.

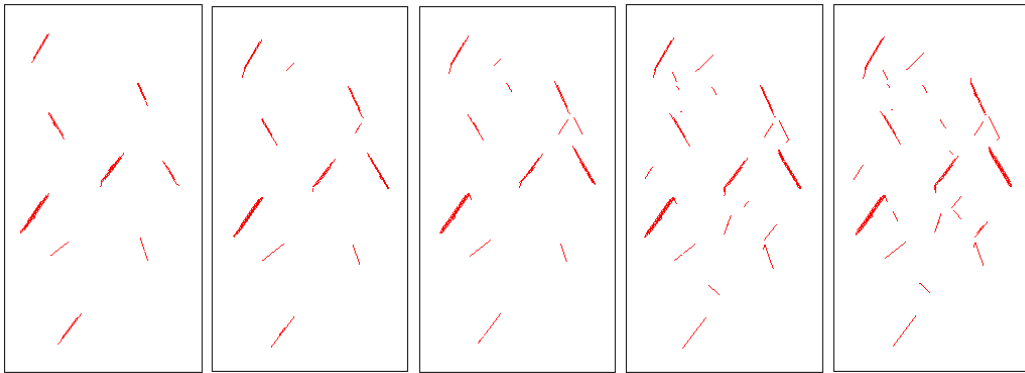


Figure 5-16: Illustration of crack propagation initiated from the flaw tip and coalescence process under uniaxial compressive loading.

5.4 Summary

The Grain-based models were successfully developed for capturing the mechanical behaviour of intact rock containing flaws. The GBM models were calibrated using laboratory results for an inclined through-going discontinuity. Then, the model was used to investigate the effect of a single flaw, regularly distributed flaws and randomly distributed flaws on the uniaxial compressive strength.

Noteworthy results from the GBM simulations are:

1. The uniaxial strength is directly related to the flaw inclination when there is only one through-going flaw. The peak strength approaches that of the intact rock when flaw is approximately vertical or horizontal. The strength reaches its minimum value when the flaw inclination ranges between 20-30°.
2. For uniform discontinuous flaws, both the inclination angle and number of flaws determine the uniaxial strength. In terms of uniform flaws inclined at 45°, the strength is not significantly influenced by the number of flaws. However, the number of flaws and flaw spacing influences the strength of samples containing vertical flaws. Moreover, the strength decreases significantly as distance of the flaw to the free boundary decreases.
3. For uniform flaw patterns (blocky rock), the simulation results agrees well with the laboratory tests with the same flaw configuration. Among the four flaw patterns, the model with 0/90° flaws has the highest peak strengths.
4. For randomly distributed discontinuous flaws, the uniaxial strength decreases as the fracture intensity, expressed as P21 increases. There appears to be a threshold fracture intensity where the strength rapidly decreases but this threshold value is non-unique.
5. Flaw interaction can significantly reduce the uniaxial strength.

6 Effect of Natural and Blast-induced Fractures on Rock Strength

When a tunnel is excavated by drill-and-blast technology the perimeter of the newly formed tunnel will contain (1) naturally occurring fractures and (2) blast-induced fractures. The naturally occurring fractures will likely contain mineral coatings associated with the geological history of the fractures while the blast-induced fracture will be ‘fresh’ and lack mineral coatings. These fresh fractures make up the flaws contained in the excavation damaged zone. In addition to these geological and blast-induced fractures, if the boundary stress magnitudes exceed the rock strength, stress-induced fractures may also be observed.

At the Äspö Hard Rock Laboratory in Sweden, at the 450 m Level, geological and blast-induced fractures are commonly observed around the perimeter of the underground excavations, while stress-induced fractures are seldom observed in practice. As demonstrated in the previous chapters when flaws/fractures are introduced in an intact rock matrix the compressive strength is reduced. In this chapter a Grain-based modelling methodology is developed for assessing the strength of the rock mass within the excavation-damaged zone. In particular the effect of the blast-induced fractures is also quantified.

6.1 Modelling Tangential Stresses

The rock in the EDZ will be loaded in compression by the tangential stresses generated at the boundary of the excavation. These tangential stresses are schematically illustrated in Figure 6-1.

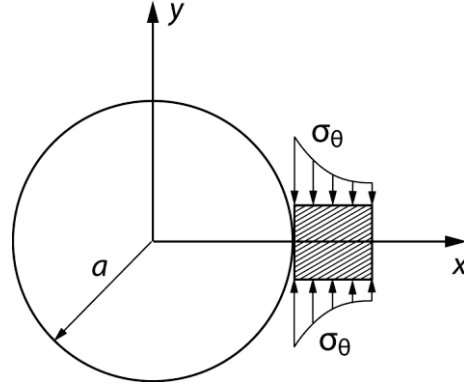


Figure 6-1: Tangential stress on the boundary of an excavation

For a circular excavation the stresses around the excavation are given by the well-known Kirsch equations assuming homogeneous, isotropic, continuous, and linearly elastic material. A point located at a polar coordinate system (r, θ) near an opening with a radius ‘ a ’ has stresses σ_r , σ_θ , and $\tau_{r\theta}$ (Figure 6-2). The Kirsch equations for the conditions in Figure 6-2 are given by:

$$\sigma_r = \frac{p_h + p_z}{2} \left(1 - \frac{a^2}{r^2}\right) + \frac{p_h - p_z}{2} \left(1 - \frac{4a^2}{r^2} + \frac{3a^4}{r^4}\right) \cos 2\theta \quad (6-1)$$

$$\sigma_\theta = \frac{p_h + p_z}{2} \left(1 + \frac{a^2}{r^2}\right) - \frac{p_h - p_z}{2} \left(1 + \frac{3a^4}{r^4}\right) \cos 2\theta \quad (6-2)$$

$$\tau_{r\theta} = -\frac{p_h - p_z}{2} \left(1 + \frac{2a^2}{r^2} - \frac{3a^4}{r^4}\right) \sin 2\theta \quad (6-3)$$

$$\sigma_r = 0 \quad (6-4)$$

$$\sigma_\theta = p_z \{(1 + k) + 2(1 - k) \cos 2\theta\} \quad (6-5)$$

$$\tau_{r\theta} = 0 \quad (6-6)$$

where p_h and p_z are maximum and minimum far-field in-situ stress in the plane of the opening. Parameter ‘ r ’ represents the distance of the stress point to the centroid of circle and σ_r , σ_θ and $\tau_{r\theta}$ the stresses on the boundary. The stress ratio k is denoted as the ratio of horizontal stress to vertical stress.

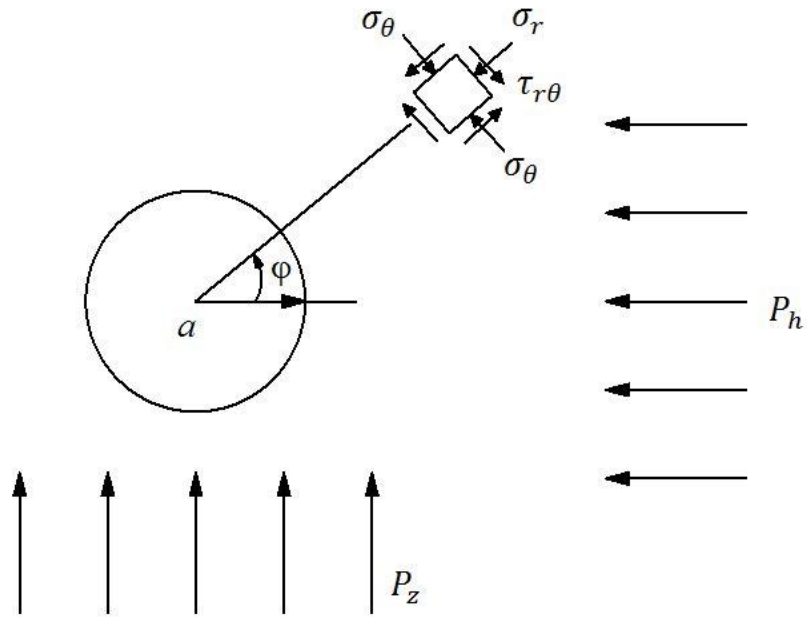


Figure 6-2: Stress distribution around a circular hole in plane strain (for an isotropic, linearly elastic, homogeneous material).

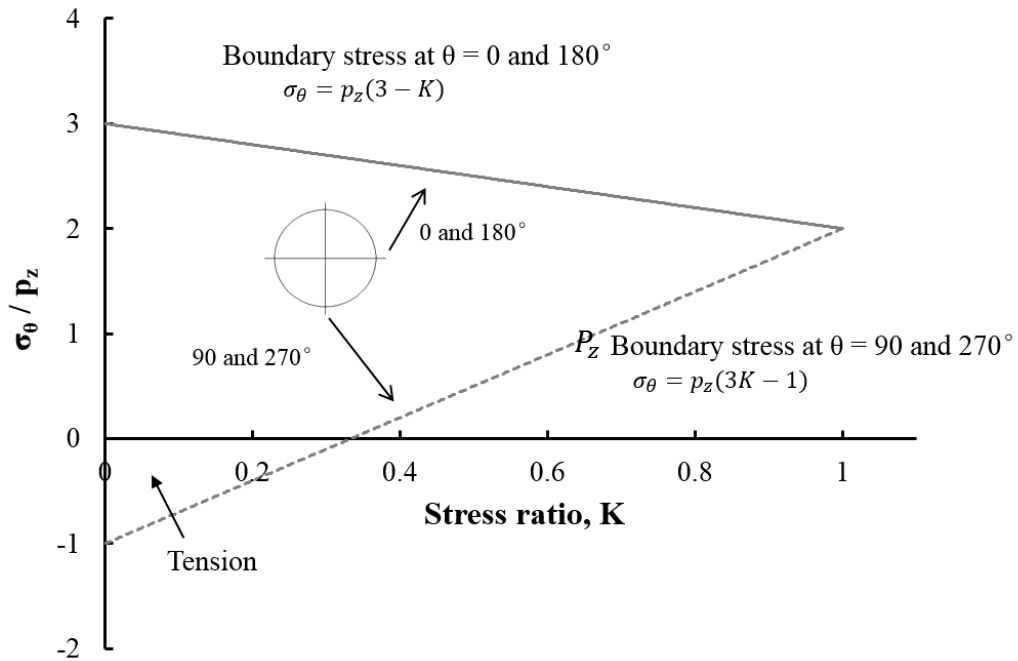


Figure 6-3: Boundary stresses at roof and sidewall around a circular opening, which as a function of the stress ratio, K .

In many cases it is not practical or necessary to conduct a GBM modelling of the complete excavation. To examine the effect of the maximum tangential stress on the tunnel boundary, a 1 m×1 m block was analyzed using the GBM. The model block is subjected to non-uniform loading from the tangential stresses and these are illustrated in Figure 6-4. To simulate this non-uniform stress distribution the block in Figure 6-4 must be loaded non-uniformly at the top and bottom and fixed at the right side. The tunnel boundary side of the block is traction free.

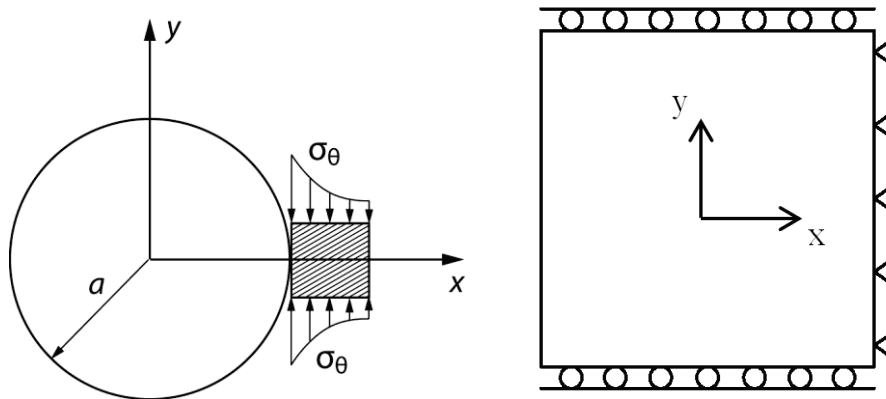


Figure 6-4: Illustration of model of rock mass around a circular opening at the tunnel roof and its boundary condition.

The tangential stresses for the block can be calculated using the Kirsch equations. Using the far-field stresses for the Mine-by Test Tunnel $\sigma_1 = 60$ MPa and $\sigma_3 = 11$ MPa, the maximum tangential stress at the tunnel boundary is 169MPa. [Martin, 1997] The tangential stress at the other side of block in Figure 6-4 is 86 MPa.

The GBM model for Lac du Bonnet granite was used to create the block in Figure 6-4. To represent the tangential stresses on the top and bottom of the block, the tangential elastic stresses are subdivided into eight regions in which the

tangential stress decreases from 169 MPa to 86 MPa (Figure 6-5). Once the GBM elastic model is constructed with the elastic tangential stress distribution, an infinitely small vertical velocity triggers the switch from an elastic state to an elastic-plastic state. The initial stresses in the block will re-distribute and there is a stress relief close to the free boundary at the left side of block.

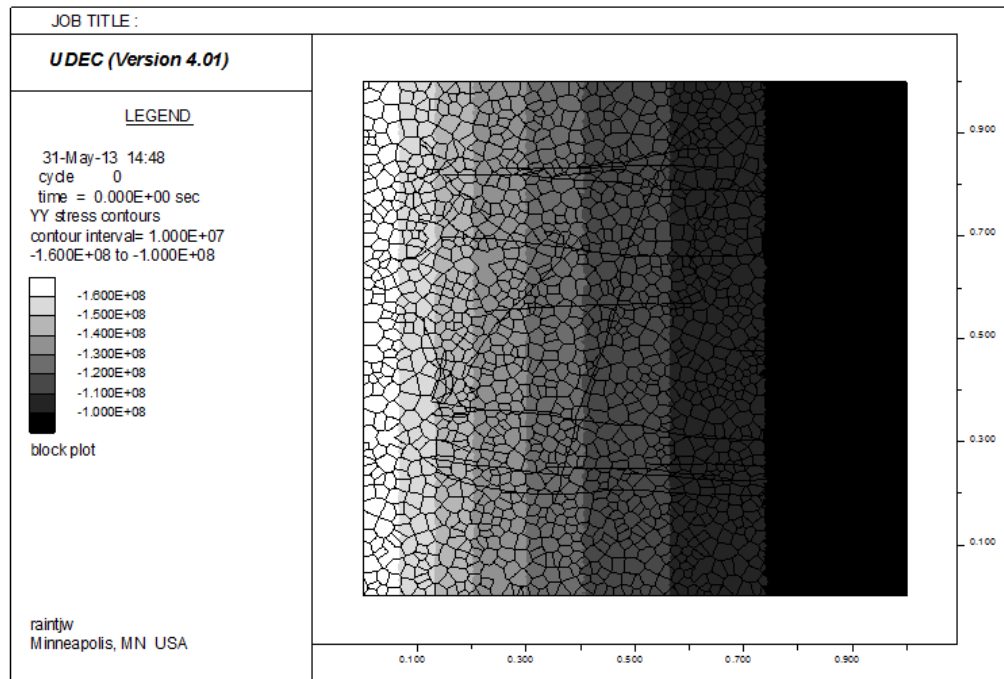


Figure 6-5: Tangential stress distribution in the block, subdivided into eight regions in which the tangential stress decreases from 167 MPa (left side) to 86 MPa (right side).

When the elastic stress state is switched to an elastic-plastic stress state the tangential stresses redistribute. The redistribution is caused by the free boundary at the tunnel wall and the cracking that occurs in the GBM due to the crack initiation stress being exceeded. The resulting redistributed tangential stress (yy stress) contours are plotted in Figure 6-6. The results in Figure 6-6 shows a significant stress-relief zone along the free boundary on the left side and

significant stress heterogeneity with the maximum yy-stress reaching values of 350 MPa at isolated locations.

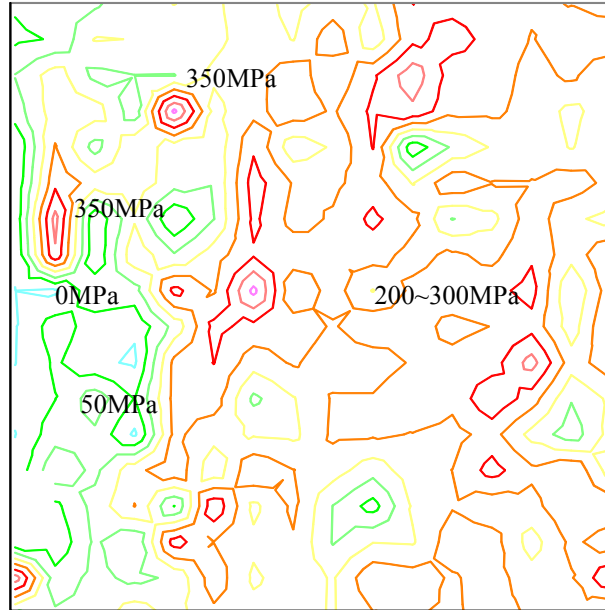


Figure 6-6: Tangential stress (yy-stresses) contours of rock mass block (shown in Figure 6-5) after redistribution caused by the cracking in the GBM.

6.2 Mapping Fractures in the EDZ – TASS Tunnel

The current planning of a geological repository for spent nuclear fuel in Sweden utilises drill-and-blast technology for the tunnel excavations. Despite the improvements in careful drill-and-blast technology it is not possible to excavate the tunnels, using drill-and-blast technology, without fracturing the rocks. Such fracturing may form an excavation-damaged zone. The Swedish Nuclear Fuel and Waste Management Company (SKB) examined in detail a selected area of the TASS tunnel to identify the fracturing that formed in the tunnel wall during the drilling-and-blasting operations [Mats Olsson, 2009].

The TASS tunnel is located at the 450-m depth Level at the Äspö Hard Rock Laboratory (HRL), Sweden. The rock mass is Äspö diorite, typical of the

granitic rock masses found in the Scandinavian Shield. It contains several joint sets that vary in both trace length and fracture frequency. To study the effect of the EDZ, a methodology was developed for mapping the drill-induced fractures and the natural geological fractures (Figure 6-7).

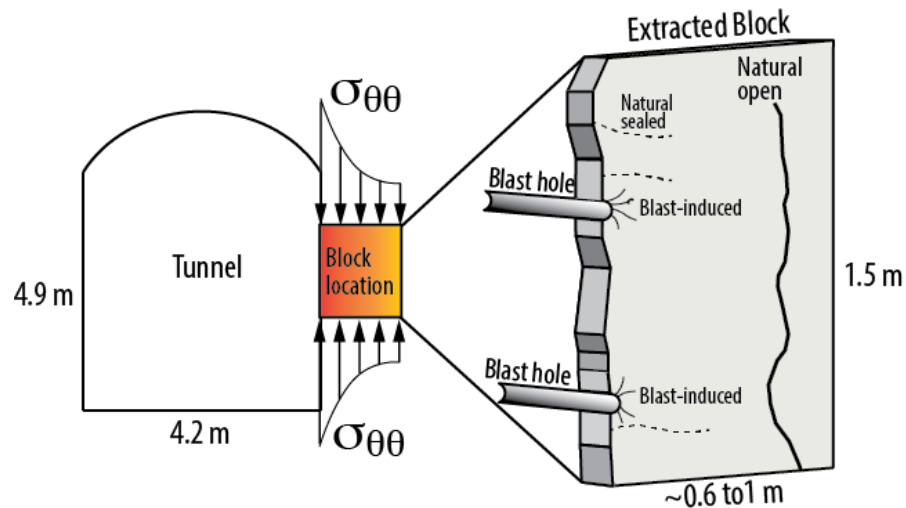


Figure 6-7: Typical fracture patterns of rock blocks excavated from tunnel wall.

The methodology required excavating the fractures from the tunnel wall and conducting detailed mapping, which is illustrated in Figure 6-8 and Figure 6-9 and consisted of several steps:

1. Eight blocks, 1.5 m high, 1.0 m wide and 0.6 – 1.0 m deep were cut out from a wall of the TASS Tunnel. Diamond wires are used to cut and isolate the eight blocks to avoid disturbance.
2. Each block was cut into slices, perpendicular to the tunnel axis. A total of 78 slices was recovered from the 8 blocks.
3. Photos with/without penetrating dye were used to provide a detailed characterization to distinguish between natural and induced fractures.
4. The trace of fractures was digitally recorded to produce a fracture map.

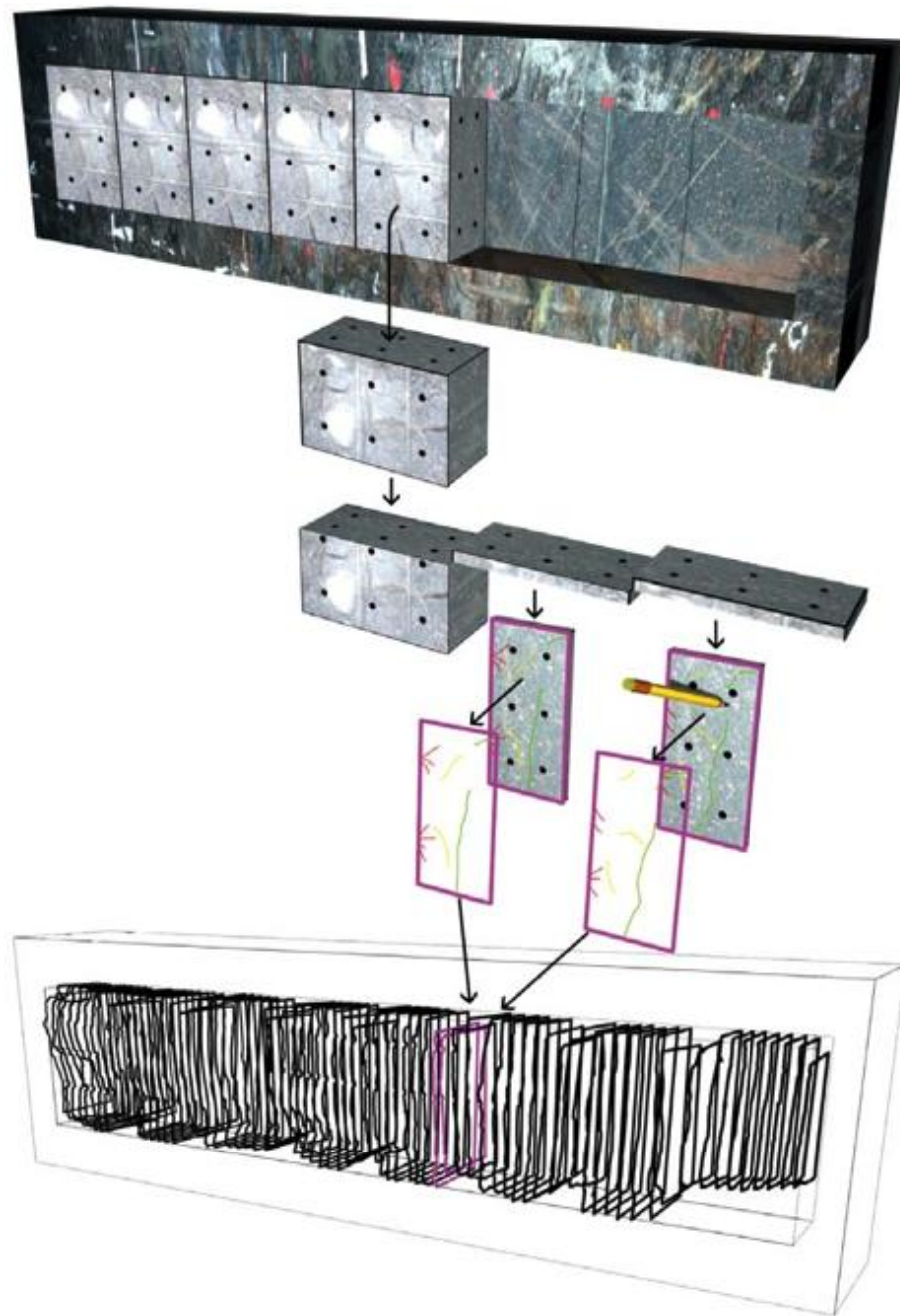


Figure 6-8: Illustration of the process of extracting blocks, sawing into slabs, photographing, digitizing and referencing in 3D. (From [Olsson et al., 2009])



Figure 6-9: Photo of a rock block removal and the completed work.

Once the eight 1.5 m high, 1.0 m wide and 0.6 – 1.0 m deep blocks were excavated from tunnel wall, they were sawn into approximately 100 mm thick slabs. Once the slabs were created they were dyed (red) to help identify the fractures. Figure 6-10 gives an example of a block before and after fracture identification. All the fracture traces on the block surface were digitized and each fracture trace was given its own identification. The fractures were identified as (1) blast fractures (red colour), (2) blast-induced fractures (yellow) and (3) natural fractures (green). Olsson et al. [2009] noted that blast fractures are formed by the blasting process and originate from the blasthole perimeter or very close to it. While blast-induced fractures are also caused by the blasting but they do not originate at the perimeter blasthole. After validation of data, and completion of the fractures mapping, the digitized files were stored in the MicroStation ‘dgn’ format.

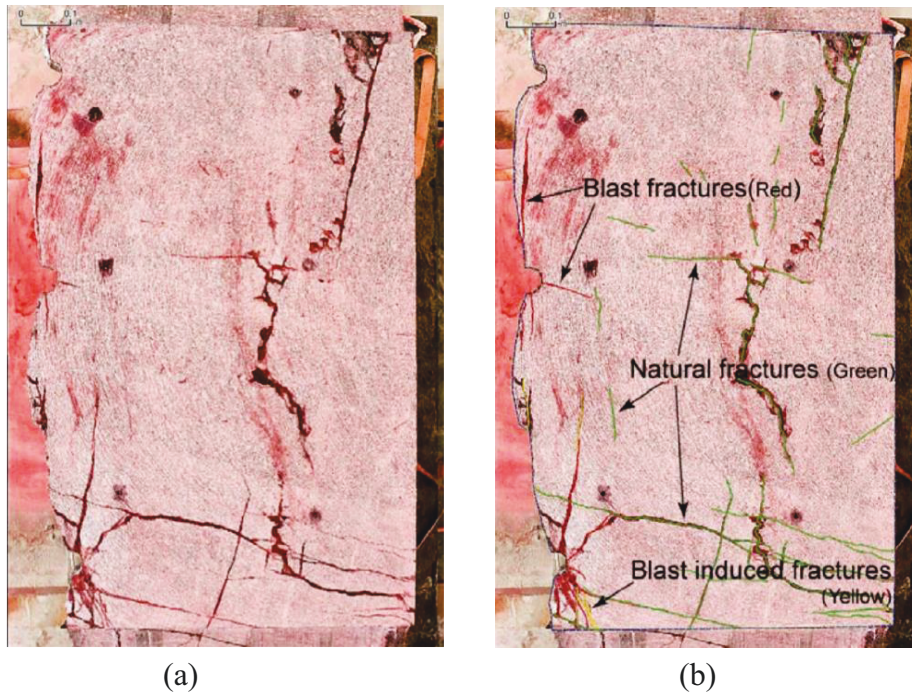


Figure 6-10: Photo of the block after red-dye coloring. (a) Without fracture identification. (b) A digitized block showing blast, blast-induced and natural fractures. (From Olsson et al. [2009])

6.3 GBM Methodology for Incorporating EDZ Fractures

All the digital data describing the fracture geometry and associated attributes is stored in a 'DXF'. Each file is named using a local block naming convention. The digital file name follows the block name, e.g., 36B-1, 37B-2, or 39B-3. The numbers following the 'hyphen' represent the slabs cut from the block with 1 indicating the top of the block (side closest to the TASS tunnel entrance).

The block names used for the GBM modelling are shown in Figure 6-11. The blocks were taken from the end of blast-round 9, blast-round 10 and the first part of blast-round 11. The length of testing area was 8m with each block being 1 m wide, producing 8 blocks. Figure 6-12 presents a plan view of test area and the boreholes used for the wire-sawing and the location of the blocks.

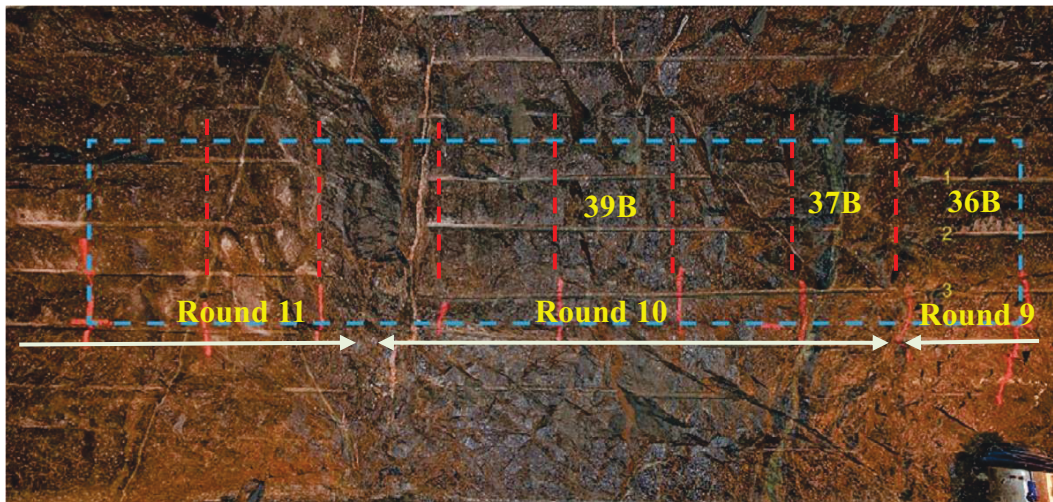


Figure 6-11: Photo of tunnel wall showing the planned location of the blocks relative to the location of the blast-rounds.

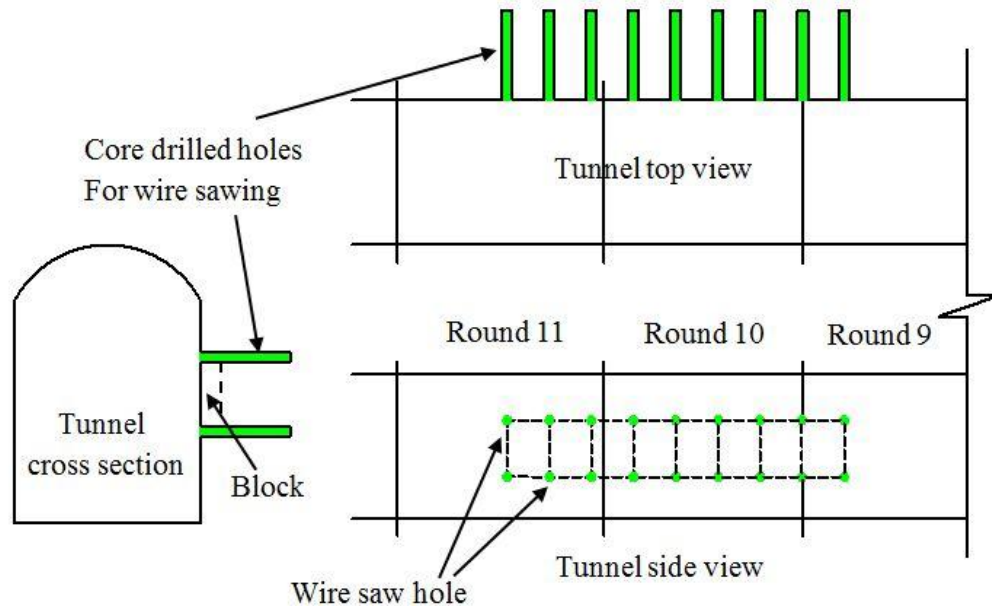


Figure 6-12: Location of the blocks relative to the blast-rounds, and the boreholes used for wire-saws used to produce the geometry of each block.

Once the blocks were extracted they were delivered to the ‘slabbing’ area where the blocks were cut into 100 mm thick slabs using the wire sawing technology (Figure 6-13). Once the slabs were extracted, experienced geologists carried out identification and detailed mapping of the fractures (Figure 6-14).



Figure 6-13: Wire sawing of the blocks into 100-mm-thick slabs.



Figure 6-14: Example of the initial stage in detailed mapping process used to identify the fractures.

Figure 6-15 compares the fractures observed and the mapped fractures for Block 36B and 39B. The fracture mapping had a repeatability of ± 1.5 mm. The red colouring was used to help identify the fractures. The fracture models for Blocks 36, 37 and 39 are shown in Figure 6-16 and illustrate the various degrees of fracturing observed.

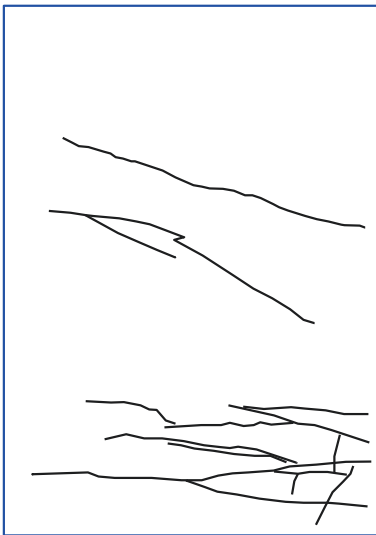


36B-2



39B-3

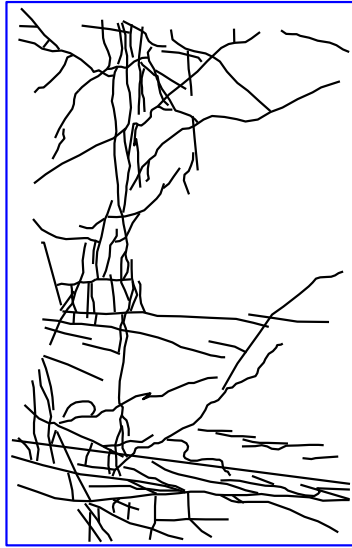
Figure 6-15: Photos of block fracture pattern and the resulting digital mapping.



(a) 36B-1



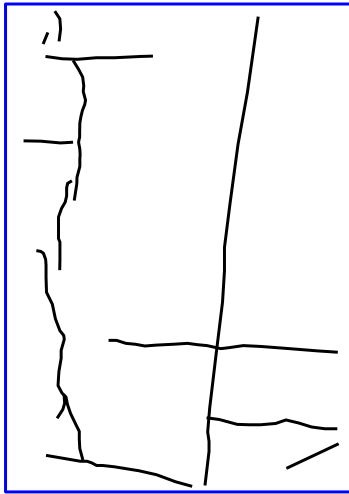
(b) 36B-2



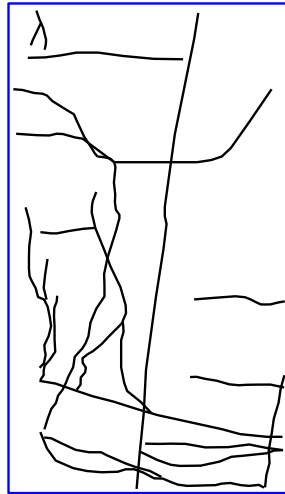
(c) 37B-1



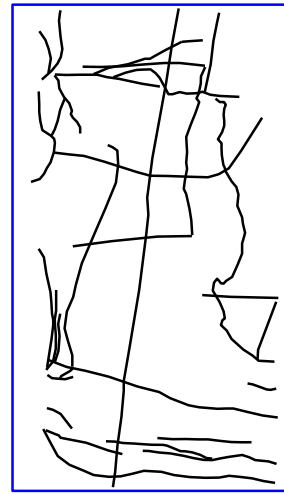
(d) 37B-2



(e) 39B-1



(f) 39B-2



(g) 39B-3

Figure 6-16: Illustration of the digital fracture maps from three blocks.



Figure 6-17: Example of the irregular interlocking geometry of a natural fracture.

Figure 6-17 illustrates the detailed geometry of a natural fracture in one of the blocks. It is clear from Figure 6-17 that representing the natural fractures as a smooth plane is not appropriate. However it is also obvious that it is not possible to capture the exact geometry of the fracture. The fracture mapping was carried out with a resolution of ± 1.5 mm using digital photography and three-dimensional surveying [Olsson et al., 2009]. Once the fracture mapping was completed a GBM was developed using this detailed geometry.

The overall objective of the GBM modelling was to compare the mechanical properties of the EDZ with and without the blast induced fractures. In the previous work in Chapter 4, it was demonstrated that the proximity of the fractures to the free surface had a significant impact on the rock strength. Hence to avoid this issue all models were created with approximately 10 mm of intact between the fractures and the free surface. This should minimise any bias

related to the fracture and the free boundary surface. Another issue relates to the size of the GBM. Because the purpose of the research was to compare results, model dimensions were chosen which balanced computer run times and the number of models evaluated. In the previous chapter, the effect of the grain-scale mesh was established and it was decided that the mesh-size used for all the previous analyses would be maintained and the scale of fractures reduced to fit the grain-scale.

Figure 6-18 illustrates the GBM for block 36B-1. The fractures are placed in the centre third of the model using the exact geometry obtained from the field mapping. As the fractures are assigned specific identification tags properties are assigned based on these tags.

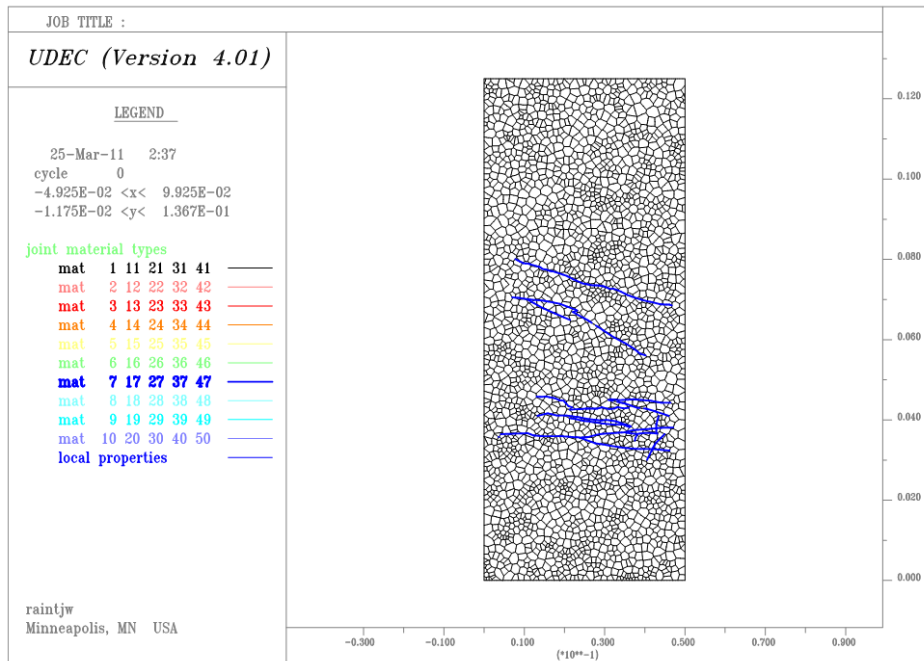


Figure 6-18: Example of the GBM for Block 36-01. The fracture pattern is identical to that obtained from the field mapping.

6.4 GBM Fracture Properties

The GBM modelling used the Coulomb residual model to simulate open natural and blast-induced fractures. This model is suitable for cohesionless fractures. SKB carried laboratory testing of open natural fractures taken from core on the crystalline rocks in the Laxemar-Simpevarp area, which includes the Äspö Hard Rock Laboratory [Hakami, E. et al., 2008]. The strength and deformation of 71 open fractures were established using direct shear tests results. Table 6-1 provides the results from the laboratory tests.

Table 6-1: Summary of results of shear tests performed on natural fractures. [From Hakami, E. et al., 2008]

Parameter	Minimum	Mean	Median	Maximum	Standard deviation
Normal stiffness k_n (MPa/mm)	240	860	791	2059	408
Shear stiffness k_s (MPa/mm)	11	23	21	44	9
Peak friction angle ϕ (°)	33.7	36.6	36.8	40	1.7
Peak cohesion c (MPa)	0.4	0.9	0.8	2.5	0.6
Residual friction angle ϕ_r (°)	31.5	35	35	39.2	1.8
Residual cohesion c_r (MPa)	0.0	0.5	0.4	0.9	0.2

The values given in Table 6-1 are very similar to the values used for the open flaws given in Table 5-1. A notable exception is the shear stiffness of 860 MPa/mm for the open flaws while the natural fractures laboratory results suggest a shear stiffness of 23 MPa/mm. An illustration showing a likely reason for the contrast in shear stiffness is given in Figure 6-19. Nonetheless the shear

stiffness given by the laboratory results appears extremely low and may be related to the methodology used to carry out the tests, which involved repeated shearing of the same specimen. In essence the shearing methodology produces relatively smooth fractures with the repeated shearing, which may account for the low shear stiffness. Also, Figure 6-17 suggests that the shear stiffness of the natural fractures should be relatively high.

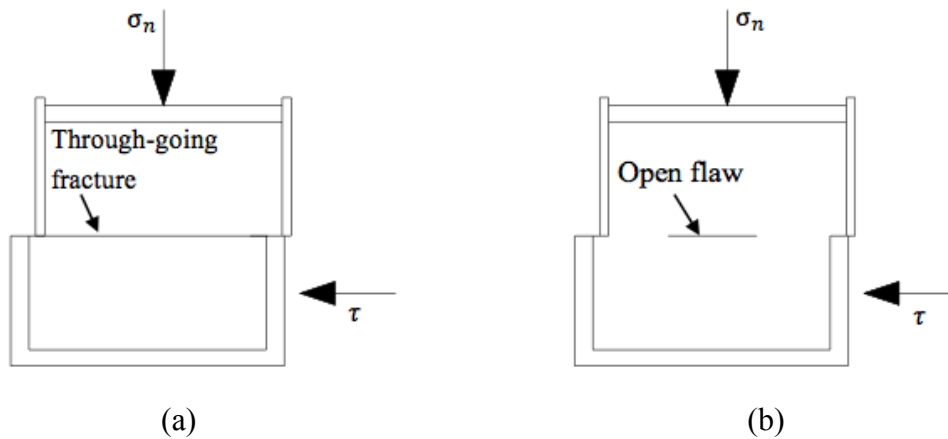


Figure 6-19: Shear model for: (a) Through-going fracture; (b) Open discontinuous flaw.

6.5 GBM Strength and Geological Fractures

Once the GBMs were created, a series of laboratory uniaxial and biaxial compression tests were simulated using only the natural geological fractures, i.e., all the blast-induced fractures were not included in the fracture models. The GBM modelling were carried out with confining stresses ranging from 1 kPa up to 10 MPa and the results are plotted in Figure 6-20. Also shown in Figure 6-20 is the Hoek-Brown failure envelope for the intact rock ($s = 1$). The fracturing for each block is illustrated in Figure 6-16. The biaxial results for GBMs show the expected strength gain with confining stress and that this increase in strength is similar for many of the Blocks regardless of the unconfined strength. This is not

surprising as the slope of the confined failure envelope from 1 MPa to 10 MPa is a measure of the frictional strength component. In essence these results indicate that the friction angle for the rock blocks is similar, regardless of the amount of fracturing. However the uniaxial compressive strength in Figure 6-20 varies from 70 to 160 MPa, suggesting that the cohesive strength component is a function of the amount of fracturing in the blocks.

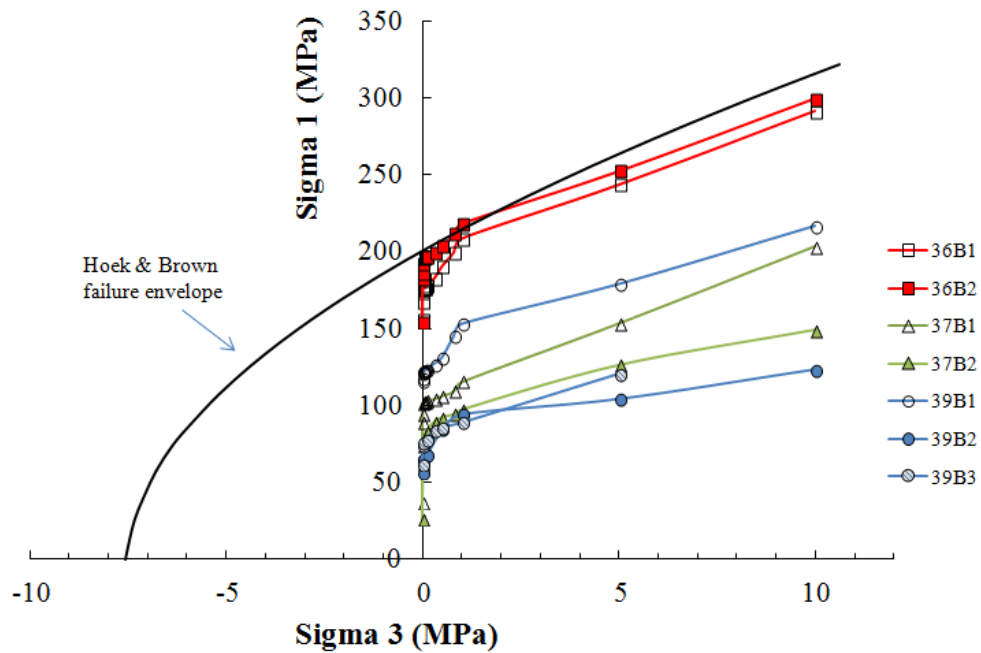


Figure 6-20: Strengths from GBM biaxial tests compared to the Hoek-Brown failure envelope (UCS=211 MPa, $m_i=211/10$, $s=1$). The block fracturing is given in Figure 6-16.

The result in Figure 6-20 shows a noticeable strength gain, when the confining stress increases from 0 to 1 MPa. The data in Figure 6-20 are re-plotted in Figure 6-21 with the confining stress plotted on log scale. It is clear from Figure 6-21 that there is little strength gain as the confining stress increases from 1 kPa to 100 kPa. However there is a significant increase in strength as the confining stress increases from 100 kPa to 2 MPa. When the confining pressure

reaches 1 MPa, there is an increase in strength of about 20%. The results for all the blocks are listed in Table 6-2. For reference, the effect of confinement on the strength of a GBM model containing a single vertical discontinuous fracture is also provided in Table 6-2. In terms of the relatively large confinement up to 10MPa, all the samples have shown a significant increase in the strength especially for those of small crack intensity. It should be noted that the effect of confinement on the strengths of Block 39B-2 and Block 39B-3 is less obvious due to presence of several large macro cracks in the vertical direction that penetrate almost the whole sample. It should be noted that handling the large blocks and cutting slabs, despite the efforts to minimize damage to the samples, did cause some of the large fractures to ‘open up’. It is likely that the blocks with these larger fractures were damaged the most and hence the strengths from those blocks should be treated with caution.

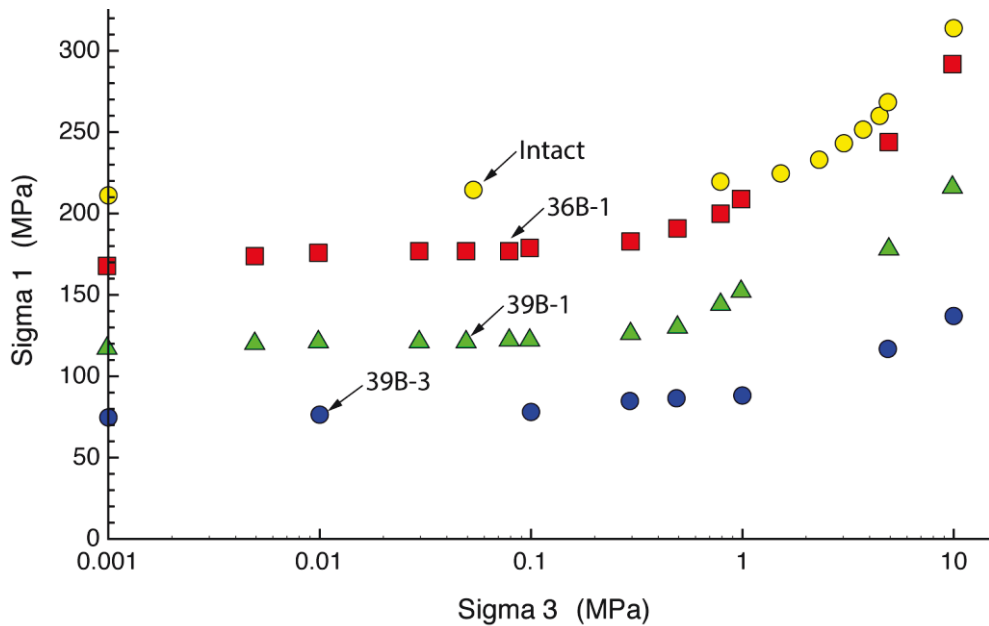


Figure 6-21: Strengths from GBM biaxial compressive tests.

Table 6-2: Uniaxial and biaxial compressive strengths for various blocks of GBM. The strength of a block containing a single vertical discontinuous flaw is provided for comparison.

σ_3 (kPa)	Rock strengths for various blocks (MPa)							one joint
	36B1	36B2	37B1	37B2	39B1	39B2	39B3	
0	155	154	36.5	26	116	56	62	177
1	167	182	89	62	118	65	69	182
5	173	186	94	67	121			184
10	175	192	101	74	122	65	76	185
30	176	195	102	75	122			186
50	176	196	102	76	122			186
80	176	196	102	81	123			188
100	178	196	103	83	123	67	78	189
300	182	199	104	89	127		84	191
500	190	203	106	92	131	84	86	194
800	199	211	109	94	145			206
1000	208	219	114	96	152	93	88	212
5000	243	257	148	121	174	99	116	
10000	291	309	193	139	207	113	133	

The tangent Young's modulus for intact rock is typically taken at 50% of the peak load. The tangent Young's modulus for the GBM biaxial models was also determined at 50% of the peak load. The moduli of the GBMs are shown in Figure 6-22 and as expected the modulus does increase as the confining stress increases. The amount of modulus increase is a function of the number of fractures and the orientation of the fractures. For example the B36 blocks had sub-horizontal fractures and these are not that sensitive to the confining stress. Overall, the modulus increases as a function of confining stress is relatively modest.

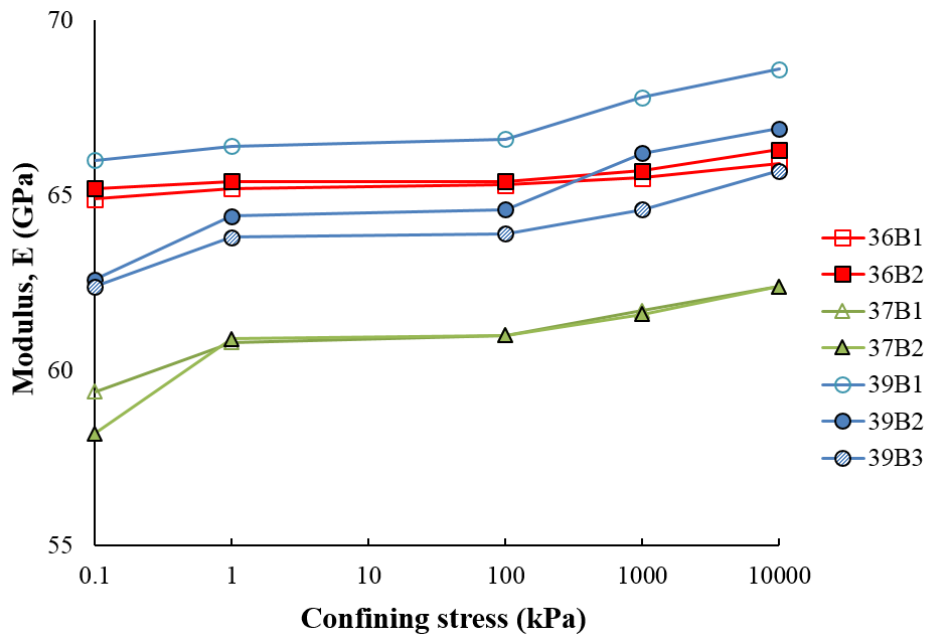


Figure 6-22: 50% Tangent modulus versus confining stresses.

In Section 5.3, the concept of fracture intensity was reviewed with the P_{21} values representing the ratio of total flaw length to the area of specimen. The P_{21} values for each of the blocks were calculated by summing the total lengths of the digitized fractures (Σl) and dividing by the side lengths a , and b obtained from the field mapping. Generally, in 2D problem P_{32} is interchanged with P_{21} denoted as

the trace length of fractures per unit area, hence $P_{32} = P_{21} = \frac{\Sigma l}{a \times b}$. See explanation on Page 105. Table 6-3 provides the total digitized fracture length in each block and the calculated value of P_{21} .

Table 6-3: Fracture intensity based upon total fracture length, RQD and estimated GSI for each GBM.

Block No.	36B1	36B2	37B1	37B2	39B1	39B2	39B3	Intact
Fracture length (mm)	295.7	283	1118	1176	248.5	544.8	684.4	0
P_{21}	0.0473	0.0453	0.1789	0.1882	0.0398	0.0872	0.1095	0
RQD (%)	89	93	64	67	97	84	81	100
GSI_{RQD}	85-90	90-95	60~65	65-70	95-100	80-85	80-85	100
GSI_{GBM}	95-100	95-100	85-90	75-85	87-93	70-85	70-85	100

An alternative to the P_{21} fracture intensity is P_{10} or the more familiar term Rock Quality Designation (RQD). To determine the RQD value for each block eight scan lines, 3 horizontal, 3 vertical and 2 diagonal, were used. The fractures encountered along the scan lines are illustrated in Figure 6-23 with the associated RQD value. The RQD values for Block 39B-3 ranged from 60% to 90% with a mean RQD value of 81%. The detailed RQD values for each block is given in Appendix C and Table 6-3 provides the average RQD value ranging from 64% to 97%.

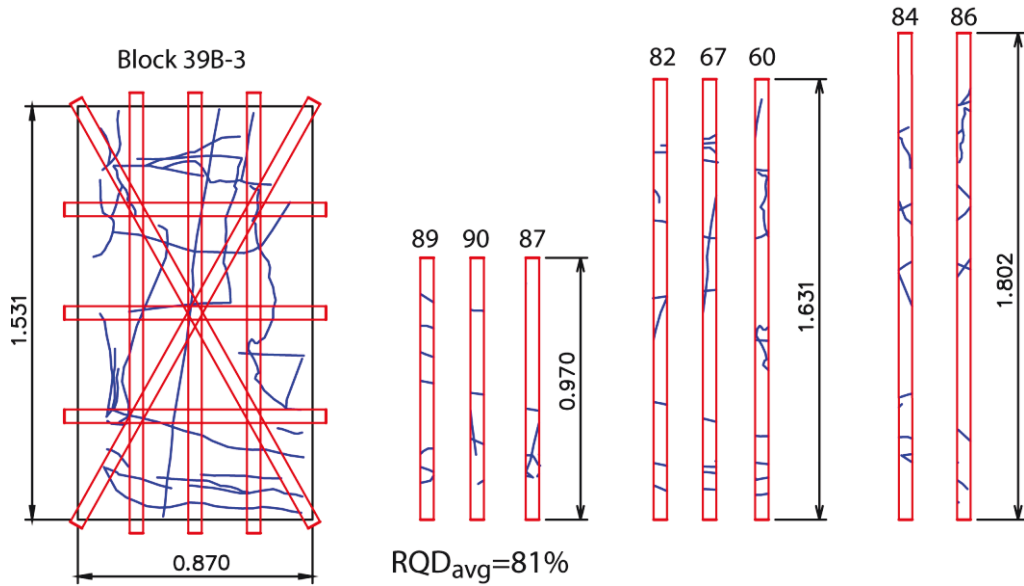


Figure 6-23: Illustration of the methodology used to establish the average RQD for each Block.

A number of authors have examined relationships between the various forms of fracture intensity [e.g., Palmstrom, 2005]. Because of the extensive use of RQD in rock mass classifications systems, the fracture intensity is commonly related to RQD. Figure 6-24 shows the relationship between RQD and P_{21} obtained from this study, and given by:

$$P_{21} = 0.5 - 0.005 \text{ RQD} \quad (6-7)$$

As shown by Palmstrom [2005] the relationship between RQD and volumetric joint count is linear. The P_{21} form of fracture intensity is simply the volumetric joint count normalised to an area and hence the linear relationship is maintained. Several researchers have also attempted to relate volumetric joints count, block size and rock strength. [e.g., Kim et al., 2005] However, while relationships have been proposed, these have not been supported by observations.

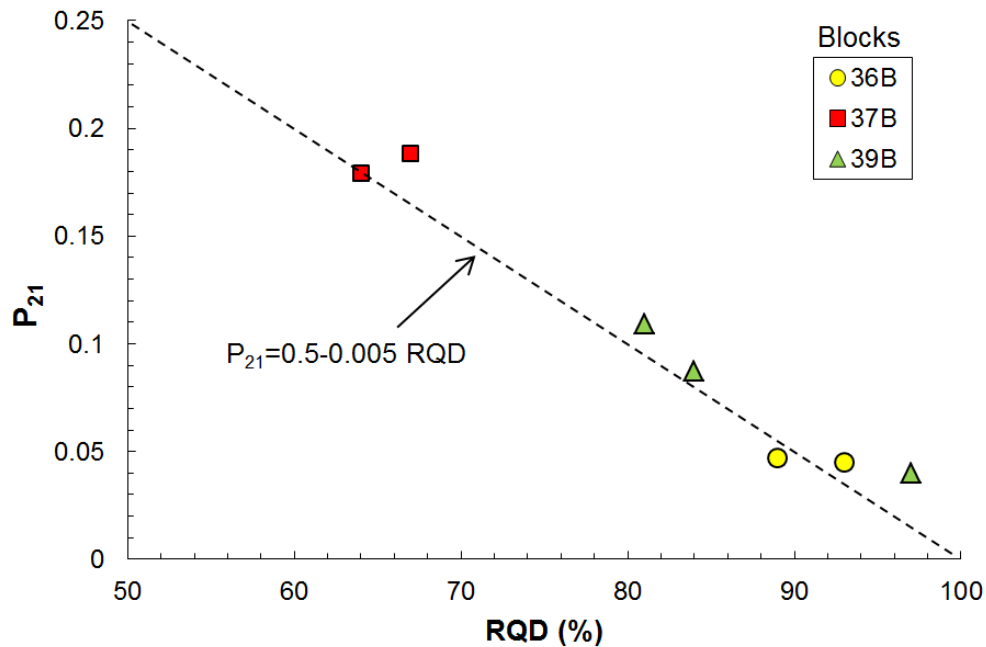


Figure 6-24: Relationship between average RQD values for different blocks and the P_{21} values for the same blocks.

Marinos and Hoek [2000] tried to obtain rock mass properties for input into numerical models introduced the Geological Strength Index (GSI). However, unless GSI is calibrated with in situ measurements, there is essentially no way of knowing if the predicted rock mass strength is valid. At present there is no direct means to correlate the P_{21} fracture intensity values to GSI values. Recently Hoek et al. [2013] showed that two simple linear scales, Rock Quality Designation (RQD) and Bieniawski's Joint Condition ($JCond_{89}$) could be used to capture the blockiness and quality of the rock mass when combined with discontinuity surface conditions (Figure 6-25). Because all the joints encountered in the blocks have essentially identical characteristics, i.e., fresh with no weathering, the Joint Condition can be set to 40 to 45 in Figure 6-25. Hence the GSI values for the Blocks are simply a function of the RQD in Table 6-3.

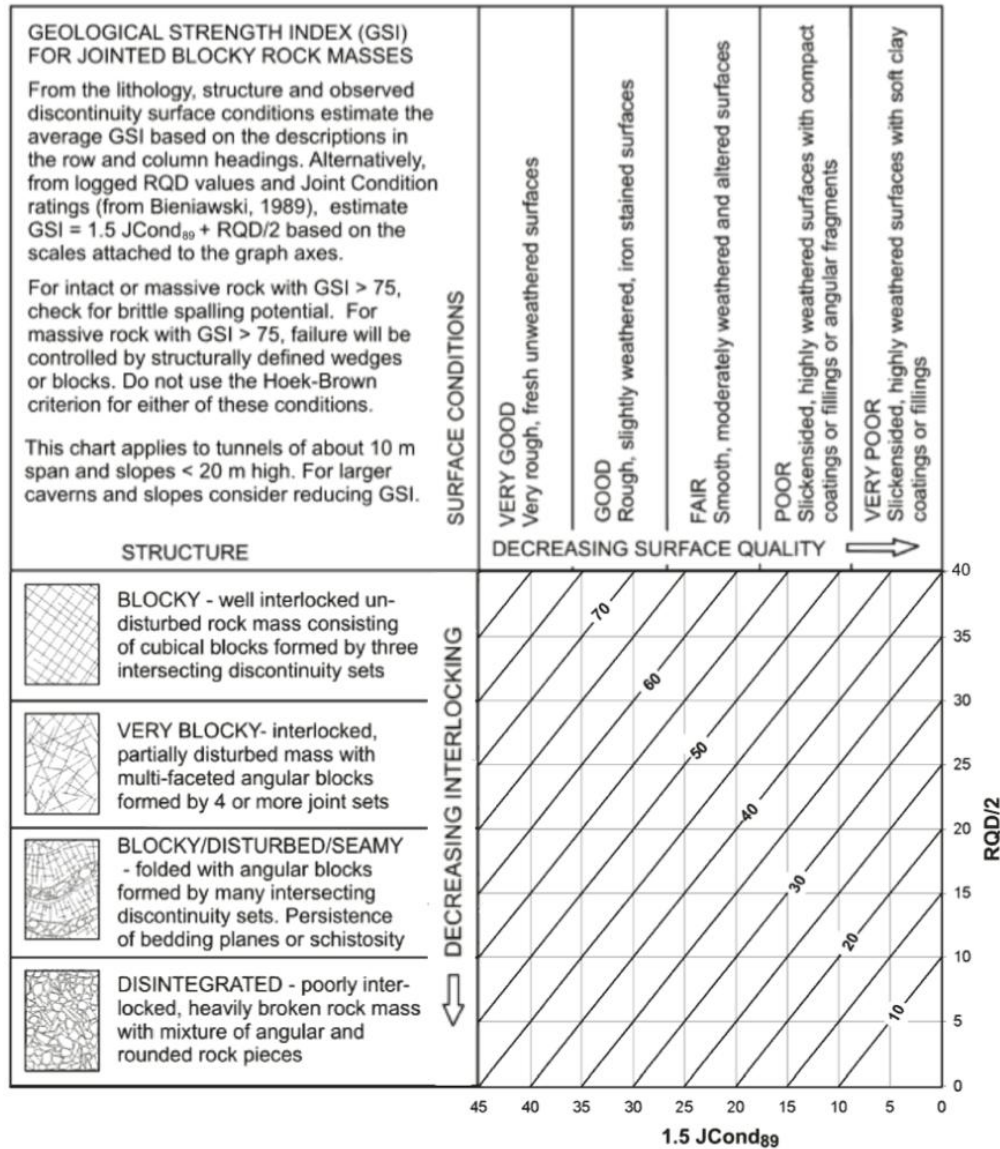
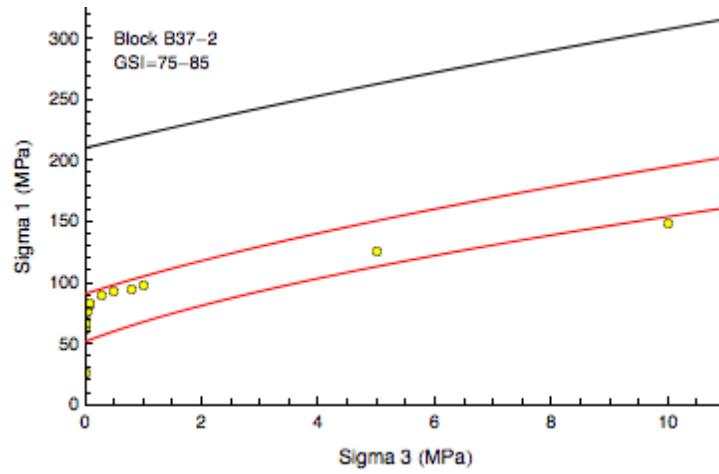
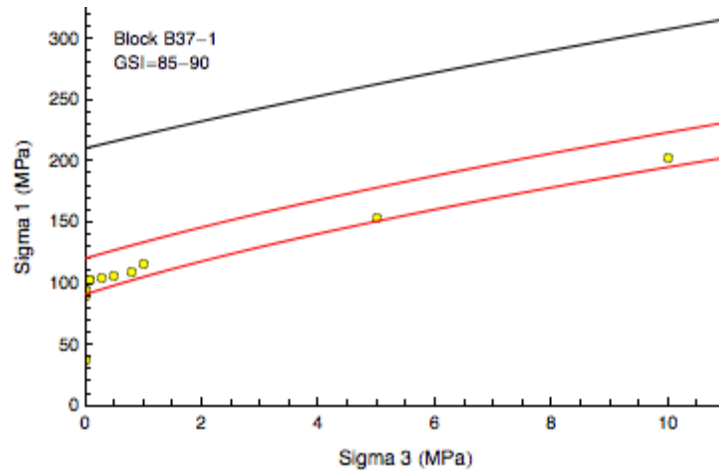
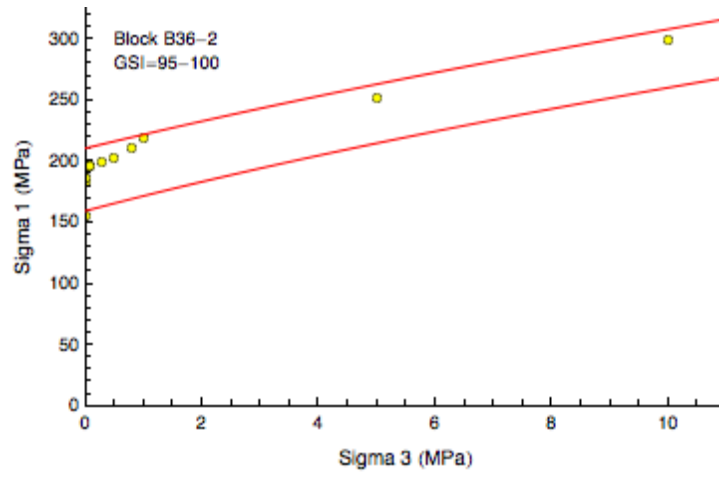


Figure 6-25: Quantification of GSI by Joint Condition and RQD, from [Hoek et al., 2013].

The GBM strength results for the individual blocks were used to establish a range in GSI values that gave a reasonable fit using the Hoek-Brown failure criterion. Figure 6-26 shows the GBM results and the Hoek-Brown failure envelopes for the range in GSI values. The Hoek-Brown intact properties are $UCS=211$ MPa, $m_i=211/10$ and $s=1$.



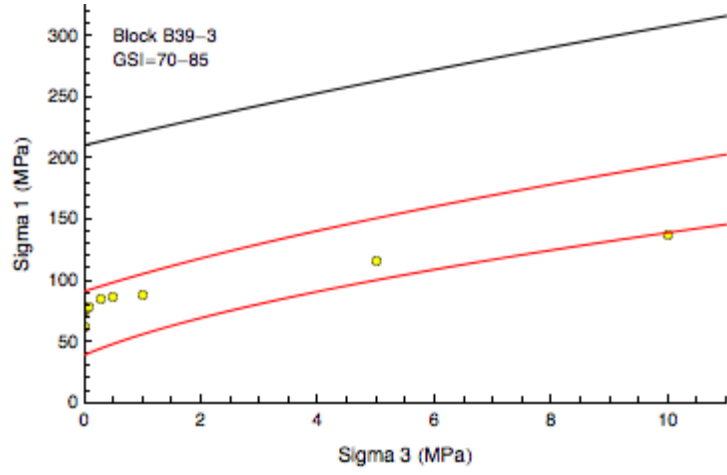
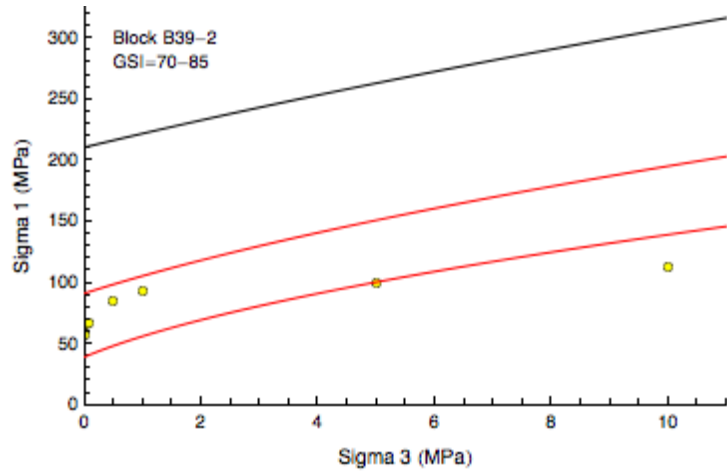
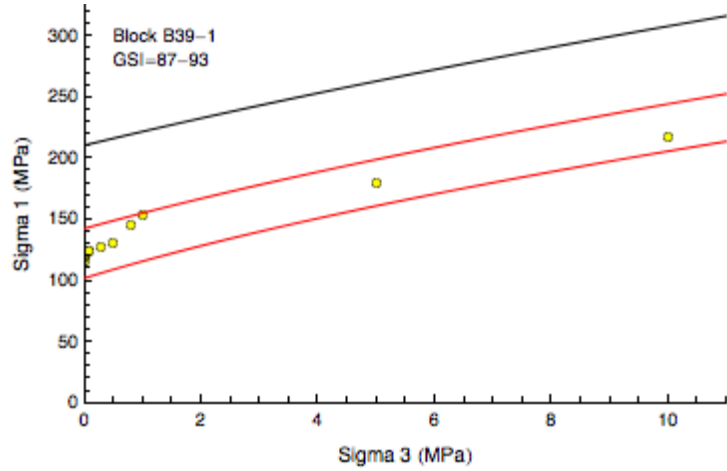


Figure 6-26: Comparison of Grain-based model strengths and the GSI values providing a reasonable fit using the Hoek-Brown failure criterion ($UCS=211$ MPa, $m_i=211/10$). The top black line represents the Hoek-Brown failure envelope for the intact rock.

Comparison of the GSI values derived from the RQD values and the GSI values determined using Grained-based Model is summarized in Table 6-3. These data are plotted in Figure 6-27, which illustrate the weak correlation between the two approaches. While additional data is needed over a broader range of RQD values the current results warrant further investigations and suggest the approach has merit.

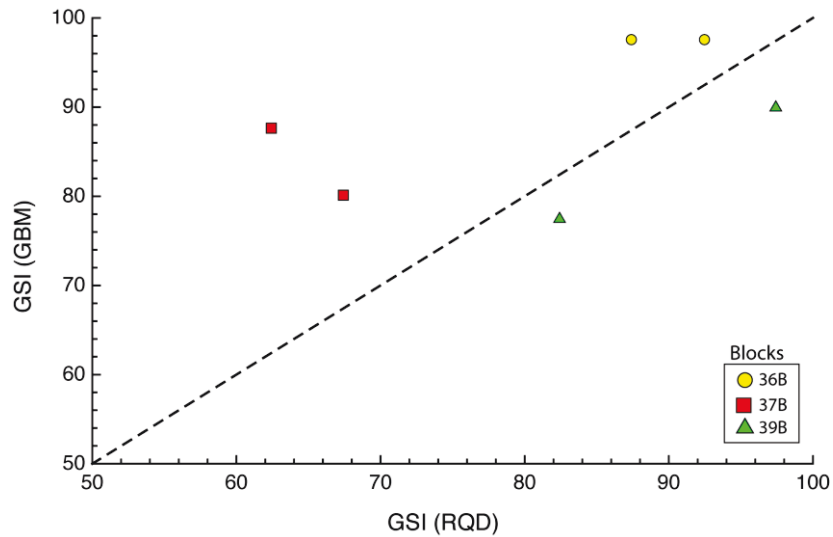


Figure 6-27: Correlation between the GSI values obtained from the RQD values and the GSI values back-calculated using the Grain-based model.

The uniaxial strength obtained from the Grain-based models as a function of the fracture intensity for Blocks 36B, 37B and 39B is given in Figure 6-28. As illustrated in Figure 6-28 there is a strong correlation between P_{21} and the uniaxial compressive strength from the Grain-based model. This correlation can be expressed as:

$$UCS \text{ (MPa)} = 20 + 190 e^{-14 P_{21}} \quad (6-8)$$

In Equation (6-8), 20 (in MPa) is the lowest UCS value possible and $190+20$ (in MPa) is the UCS of intact rock. Using the linear relationship between P_{21} and

RQD given by Equation (6-7), Equation (6-8) can be written as:

$$\text{UCS (MPa)} = 20 + 0.17 e^{0.07 \text{ RQD}} \quad (6-9)$$

The relationship given by Equation (6-9) is illustrated in Figure 6-29. As expected the UCS increases exponentially as the RQD values increase from 50 to 100%.

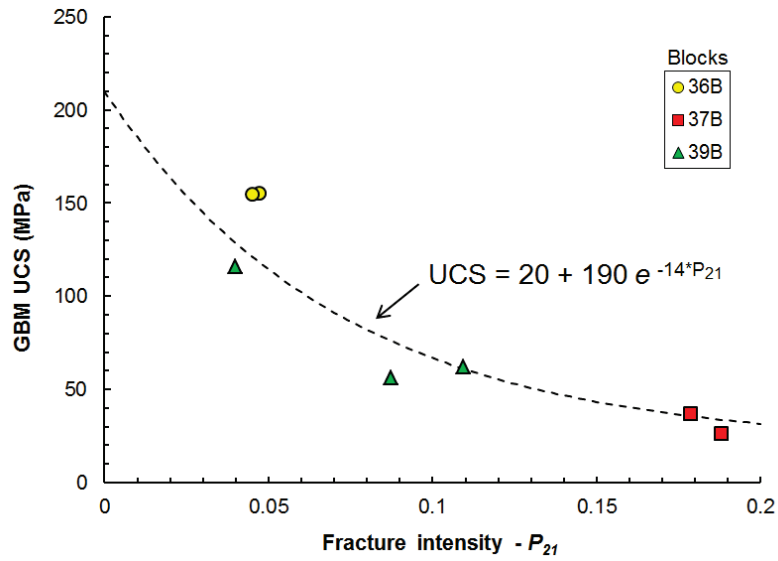


Figure 6-28: Comparison of UCS versus fracture intensity (P_{21}) for the Grain-based models using Blocks 36B, 37B and 39B.

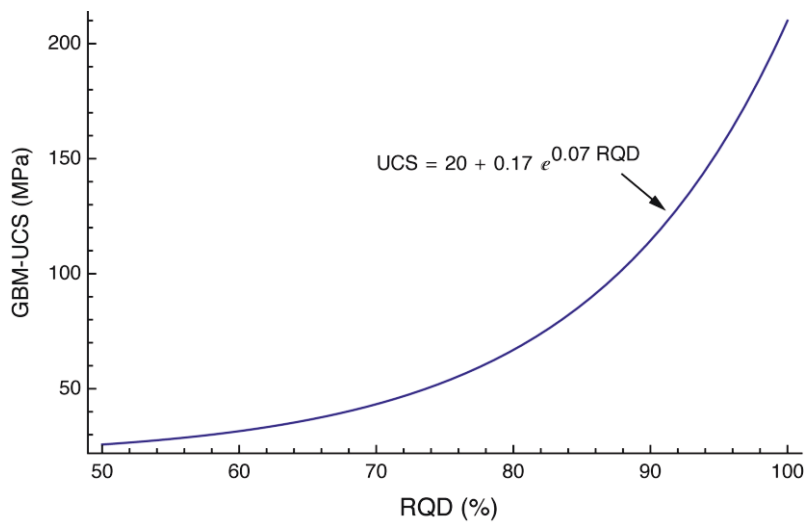


Figure 6-29: Relationship for GBM-UCS and RQD.

The uniaxial strength relationship in Figure 6-28 clearly illustrates the impact of the natural fractures on the rock strength. In Chapter 5, the effect of discontinuous flaws on the rock strength was also examined and summarized in Figure 5-12. Figure 6-30 shows the combined results from Figure 5-12 and Figure 6-28. It appears from Figure 6-30 that as the fracture intensity, expressed as P_{21} , increases there is a general decrease in the rock strength. Regardless of the initial P_{21} value, the lower bound strength can be expressed as:

$$\text{UCS /Intact} = 0.1 + 0.9 e^{-14 P_{21}} \quad (6-10)$$

Provided there is no through-going fracture inclined at the optimum angle to the direction of loading. An approximate strength for the lower bound values in Figure 6-30 for all P_{21} values appears to be the strength of the through-going inclined discontinuity discussed in Chapter 5. Hence estimating the strength of the rock must first start with assessing if a through-going plane of weakness exists. If this condition doesn't exist, then the findings in Figure 6-30 may be applicable.

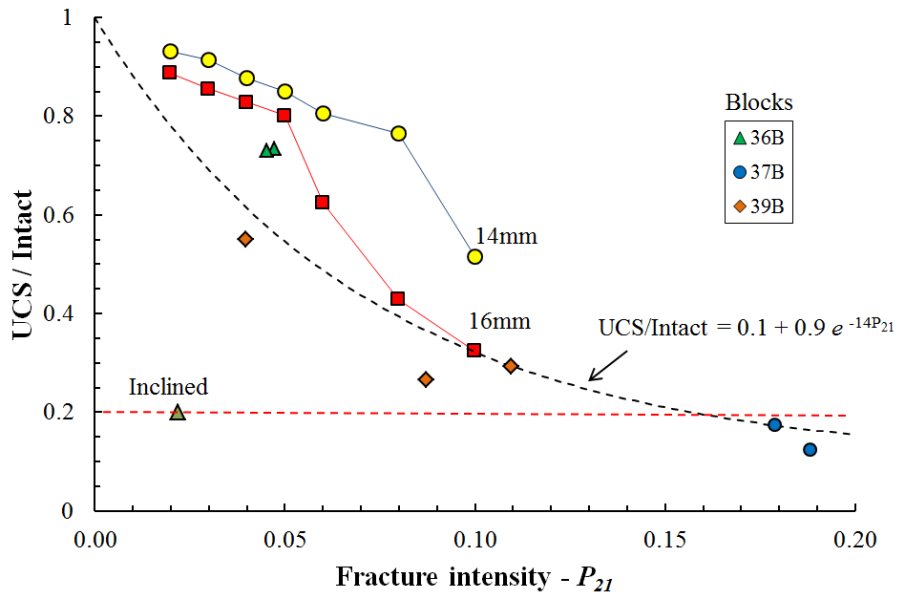


Figure 6-30: Comparison of UCS versus fracture intensity (P_{21}) for various GBMs with discrete flaws and natural fractures.

6.6 GBM Strength and Blast-induced Fractures

The previous sections discussed the influence of natural open fractures on the rock strengths. In this section, the effect of the blast-induced fractures on the block strength is assessed. Before conducting the GBM modelling, all the blast-induced fractures present in the Blocks were removed to first assess the strength of the Blocks with only the natural fractures.

Grained-based models were constructed for Blocks 36B-6 and 36B-8 (Figure 6-31). The dark lines in Figure 6-31 close to the left boundary represent the blast-induced fractures while the light grey lines identify the natural fractures. These two blocks were selected as they represented a significant range in the amount of blast-induced fracturing observed in the blocks examined. As with all the GBM modelling the fracturing did not penetrate the model boundary.

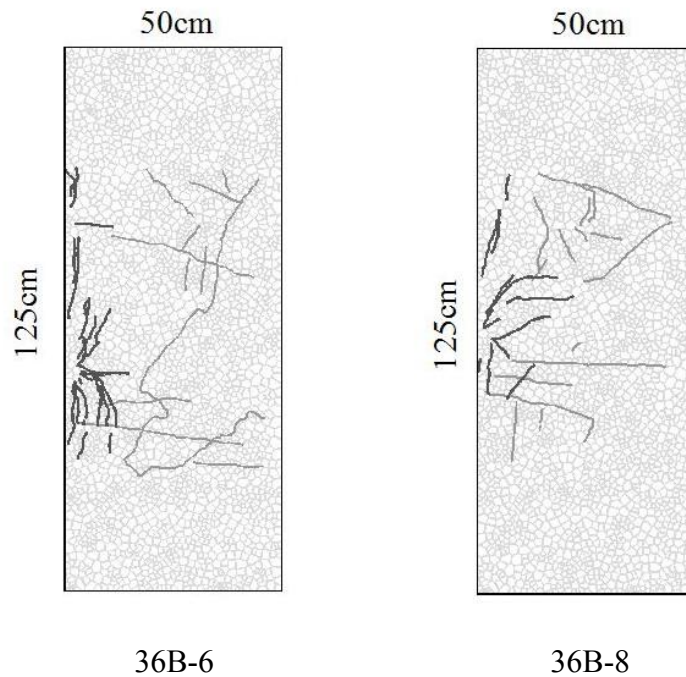


Figure 6-31: Illustration of Grain-based models for B36-06 (left) and B36-08 (right) with both blast-induced fractures and natural open fractures.

The effect of the blast induced fracturing on the fracture intensity for blocks B36-06 and B36-08 was assessed using the P_{21} values and RQD. The detailed RQD values for the blocks are given in Appendix D and the average values are summarized in Table 6-4. The blast-induced fractures decrease the average RQD from 87 to 76 in 36B-06 and from 91 to 83 in 36B-08. Also shown in Table 6-4 is the increase in the P_{21} values caused by the blasting. Note that for block 36B-06 the P_{21} value increased by 90% while the RQD value only decreased 12%. However in block 36B-08 the P_{21} value increased by 60%, while the RQD value decreased by 9%. These changes are plotted in Figure 6-32 and compared to the relationship between RQD and P_{21} establish for the natural fractures. The relationship appears to remain valid.

Table 6-4: Comparison of the effect of the blast induced fracturing on the fracture intensity and the GBM uniaxial compressive strength.

Block No.	36B-06			36B-08		
Fracture length (mm)	Natural	Combined		Natural	Combined	
	361	Natural 361	Blast-induced 325	272	Natural 272	Blast-induced 164
P_{21}	0.0578	0.1098		0.0435	0.0698	
RQD (%)	87	76		91	83	
UCS	94	46		138	39	

The uniaxial compressive strengths for the blocks 36B-06 and 36B-08 were established using the GBM. The strengths were first established for the natural fractures and then the GBM modelling were re-run with the blast-induced fractures added. The blast-induced fractures decreased the uniaxial compressive strength in block 36B-06 from 94 MPa to 46 MPa, and in block 36B-08 from 138

MPa to 39 MPa, a decrease in strength of 51% and 72%, respectively. The decrease in strength is plotted Figure 6-33 and compared to the previously established relationship between P_{21} and the uniaxial compressive strengths for the natural fractures. The reduction in the uniaxial compressive strength in block 36B-06 caused by the blast induced fracturing follows the trend established previously. However the decrease in strength in block 36B-08 appears to be slightly anomalous. Inspection of block 36B-08 shows that the blast-induced fractures created a near continuous through-going fracture that is inclined to the direction of loading (Figure 6-34). This again highlights that even a discontinuous through-going fracture can drastically reduce the rock strength. It also shows why careful blasting techniques are important in reducing the amount of damage in the excavation-damaged zone.

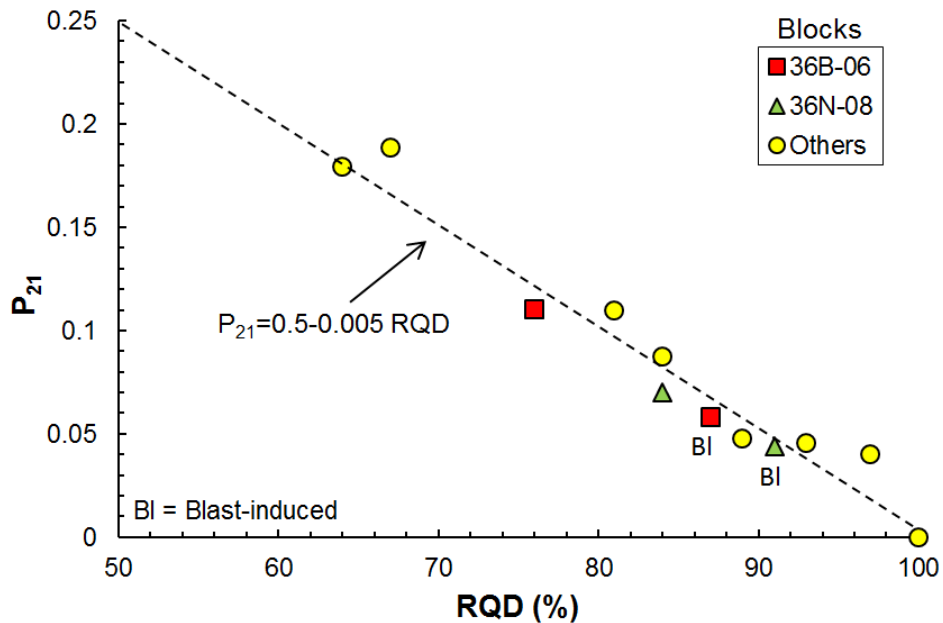


Figure 6-32: Effect of blasting on the fracture intensity, P_{21} and RQD, for blocks 36B-06 and 36B-08.

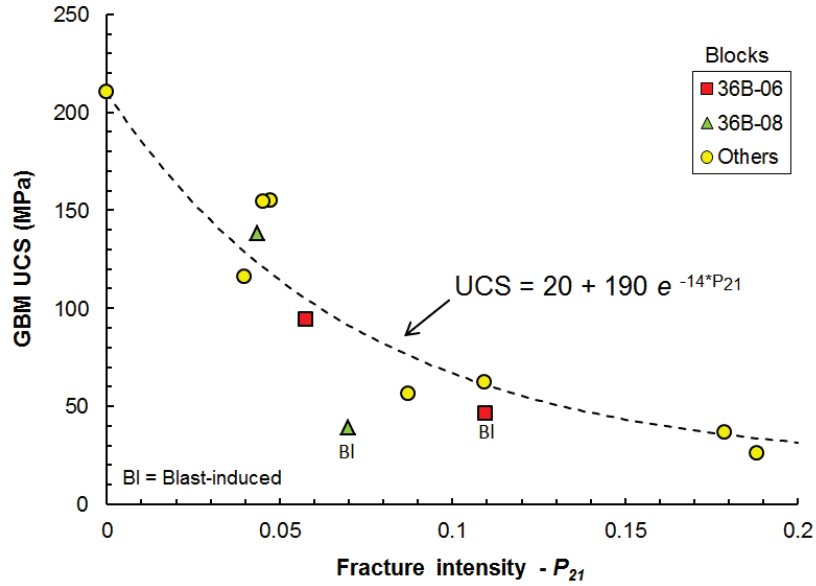


Figure 6-33: Effect of blast-induced fracturing on the GBM uniaxial compressive strengths (UCS) compared to the strength relationship established for the blocks with the natural fractures.

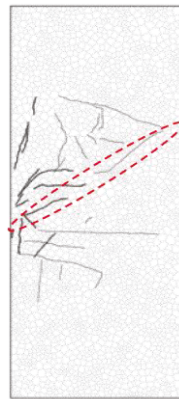


Figure 6-34: The blast-induced fracturing in block 36B-08 resulted in a near continuous through-going fracture (dashed red ellipse) inclined to the direction of loading.

In addition to the uniaxial compressive strengths for the Blocks, the GBMs were also run at various confining stresses to establish the effect of confining stress on the blast induced fractures. The results from these GBM modelling are summarised in Table 6-5.

Table 6-5: GBM uniaxial compressive strength for two Blocks containing both blast-induced and natural fractures.

Confining strength (kPa)	Rock strength (MPa)					
	36B-06			36B-08		
	Blast fractures excluded	Blast fractures included	Reduction (%)	Blast fractures excluded	Blast fractures included	Reduction (%)
0	94	46	51.1	138	39	71.7
1	102	73	28.4	140	82	41.4
10	124	82	33.9	144	85	41.0
100	142	86	39.4	148	86	41.9
500	157	89	43.3	152	99	34.9
1000	173	92	46.8	153	106	30.7
5000	196	104	46.9	178	118	33.7
10000	236	128	45.8	215	133	38.1

The strength results in Table 6-5 for Blocks 36B-06 and 36B-08 are plotted in Figure 6-35. The Hoek-Brown failure envelopes and the range in GSI values needed to fit the GBM strength data are also shown. In Block 36B-06, the GSI values for the natural fractures, 85-95, reduced to 70 – 83 for the natural + blast-induced fractures. In Block 36B-08, the GSI values for the natural fractures, 90-93, reduced to 70 – 85 for the natural + blast-induced fractures. It is clear from Figure 6-35 that the strength of the blast-induced fractured rock is less than that of the intact rock, and the strength of the naturally fractured rock.

The differences in the strength of the GBM models with the natural fractures compared to the GBM models with both the natural and blast-induced fractures are given in Table 6-5 and shown in Figure 6-36. The results show that the reduction in strength caused by the blast induced fractures ranges from approximately 30 to 70%. It appears from Figure 6-36 that the strength reduction caused by the blasting is essentially independent of the confining stresses over the range 0 to 10 MPa. It is not clear why this is observed.

Despite the relatively high GSI values, a wide spread in the GSI values are needed if the complete range of the strength data is to be captured (see Figure 6-35). The results in Figure 6-35 were re-plotted in Figure 6-37 using Log-Linear plot. In this form it is apparent that the Hoek-Brown either fits the lowing confining stress from 0 to 1 MPa or fits 5 to 10 MPa. It is challenging to find a single GSI value that satisfied both the very low (0 to 1 MPa) and medium (5 to 10 MPa) confining stresses.

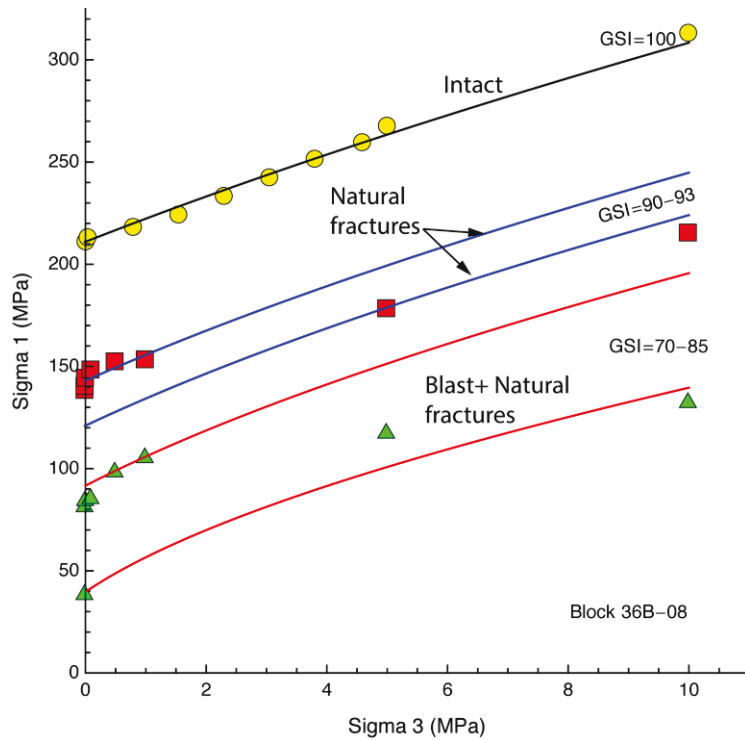
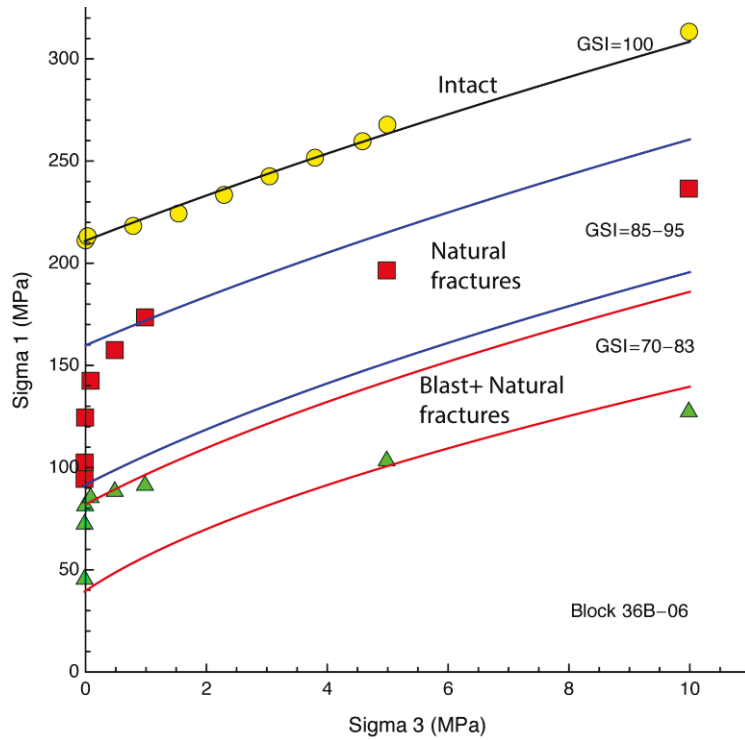


Figure 6-35: Hoek-Brown failure envelopes for the GBM strength for Blocks 36B-06 and 36B-08 with/without blast-induced fractures and the associated GSI values.

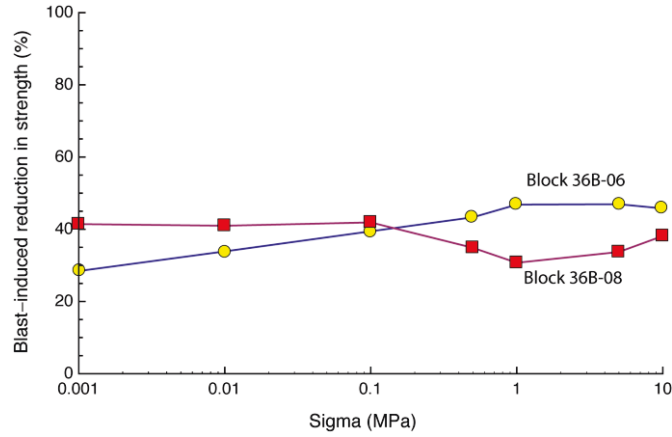


Figure 6-36: Blast-induced reduction in GBM strength with confining stress.

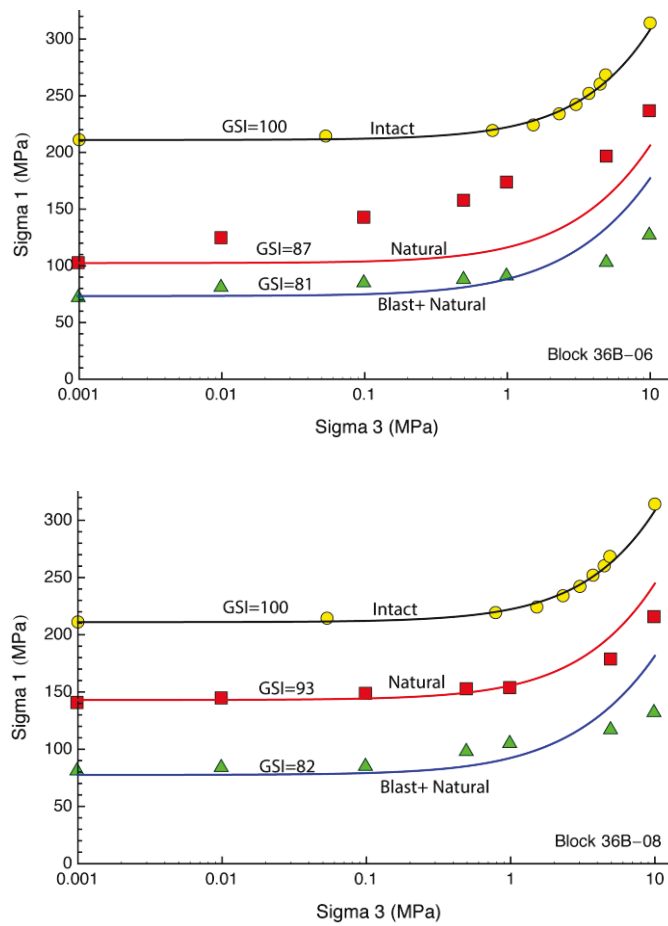


Figure 6-37: Hoek-Brown failure envelopes for the GBM strength for Block 36B-06 and 36B-08 with/without blast-induced fractures and the associated GSI values. (Note, the confining stress is plotted as a log-scale)

6.7 Summary

In this chapter the strength of the rock on the boundary of the TASS tunnel was examined using the Grain-based model. Eight blocks were extracted from the sidewall of the tunnel and the natural geological and blast-induced fractures were mapped to mm accuracy. A methodology was developed to quantify the fracture intensity (P_{21}) and the RQD for these blocks. A methodology was also developed for building the Grain-based models using the detailed mapped fracture geometry.

A number of Grain-based models were carried out to establish the strength for the blocks with only the natural fractures. The RQD values for these blocks ranged from approximately 60 to 100%. The uniaxial and confined strengths of the Grain-based models were determined. The results from the GBM with only the natural fractures suggest:

1. There is a linear relationship between P_{21} and RQD.
2. The relationship between GSI established using the RQD and GSI back estimated from the GBM strength results is poorly correlated.
3. The strength of the GBMs increases significantly when the confining stress is greater than 200 kPa.
4. There is a strong correlation between P_{21} and the uniaxial compressive strength. Hence other relationship with strength can be established, e.g., RQD.
5. Provided a through-going fracture that is optimally inclined to the direction of loading is not encountered, the lower bound uniaxial rock strength can be expressed as $UCS / Intact = 0.1 + 0.9 e^{-14 P_{32}}$

The results from the GBM modelling with both the natural fractures and the blast-induced fractures suggest:

1. The addition of the blast-induced fractures reduces the strength of the GBM models by 30 to 70%.
2. The relationships between P_{21} and RQD, established for the natural fractures, appear to be valid for the blast-induced fractures.
3. The reduction in the uniaxial compressive strength from the GBM models with the blast-induced fractures follows the previously established relationship between P_{21} and UCS.
4. Should the blast-induced fracturing combined with the natural fractures result in through-going inclined fracture, the strength will be governed by this condition and not the P_{21} value. This also highlights the need for careful blasting to minimize the damage in the EDZ.
5. The strength of the blast induced GBM modelling appears to be less sensitive to confinement compared to the GBM modelling with only the natural fractures.
6. The Hoek-Brown failure envelope can be fitted to the data ranging from 0 to 1 MPa or from 5 to 10 MPa. Fitting the Hoek-Brown failure envelope to the data from 0 to 10 MPa confining stress requires GSI values ranging from 73 to 85 for Block 36B-06 and 70 to 85 for Block 36B-08.

7 Conclusions and Future Research

The construction of drill-and-blast underground openings results in an excavation damaged zone (EDZ), regardless of the blasting technique. When careful blasting techniques are used these blast-induced fractures can be relatively small, compared to the size of the excavation. In addition these blast-induced fractures may be discontinuous and not interact with the existing natural fractures. The goal of this research was to develop a methodology that provided a systematic approach for estimating the rock strength and deformability containing both natural geological fractures and blast-induced fractures.

The Grain-based model (GBM) developed at the University of Alberta was used as the basis for the research. The GBM is based on the discrete element formulation and implemented in the commercially available numerical software UDEC from Itasca Consulting Group, Inc. The GBM uses a voronoi tessellation scheme that can capture the grain-size or block-size distribution of the intact rock. It was shown that by capturing the grain-size distribution, the distribution of the tensile stresses and their magnitudes are significantly increased. This improves the ability of the GBM to generate tensile-induced fractures even when loaded in compression. Like all micro-scale based modelling, the GBM requires calibration with the macro-scale laboratory test results. This can be a tedious exercise, but once calibrated the GBM captures all the characteristics of the stress strain response observed in the laboratory, tensile, uniaxial and triaxial compressive tests. The GBM was calibrated to the intact properties of Lac du Bonnet granite, Äspö Diorite and a fine grained marble. While both Lac du Bonnet granite and Äspö Diorite have similar laboratory properties their grain-size distribution is significantly different.

Fractures in rock are statistically represented by fracture intensity defined as P_{10} (Σ No. of fracture /m), P_{21} (Σ fracture length/m²) and P_{32} (Σ fracture area/m³). In addition to fracture intensity, Rock Quality Designation (RQD) is widely used in rock engineering. Both fracture intensity and RQD were used to relate the effect of flaws and fractures on the GBM strength.

7.1 Modelling of Intact Rock

To demonstrate the versatility of the GBM methodology, the factors that could affect GBM modelling results is examined using a fine-grained marble from a quarry at Gaoligong Mount in Yunnan Province, in southwest China. The marble was sampled from an open pit at a depth of about 50 m. Laboratory tests and thin-section examination demonstrated that marble was homogeneous and intact. The marble is composed of 95% Calcite and 5% Quartz and that the mean values of the grain sizes are about 1 mm and 0.75 mm, respectively.

A series of GBM marble models were analysed and the results provide the following conclusions.

7.1.1 Effect of scale and sample shape

- There is little or no scale effect on uniaxial GBM strengths with respect to the mean grain size. This is also supported by laboratory results
- The GBM samples with $L: D < 2$, shows a significant increase in peak strength. This finding supports the ISRM [1981] suggested method where a $L: D > 2$ is recommended to minimise the effect of sample geometry.
- The GBM model results suggest that the Young's modulus is not sensitive to sample diameter. This is also supported by laboratory data.

- The GBM modelling results support the notion that the uniaxial strength shows a noticeable scale effect at least for samples up to 100 mm diameter. These findings are also supported by laboratory results.
- In the GBM modelling the generation of tensile stresses is linked to the observed scale-strength effects. These tensile stress magnitude increases as the sample size grows. The geometric heterogeneity created by the polygonal grains in the GBM is responsible for the tensile stress generation. These findings support the notion that geometric heterogeneity plays a significant role in controlling brittle rock strength.

7.1.2 Effect of confining stress

The GBM model is calibrated to the uniaxial compressive strength and tensile strength. Once this calibration is completed the GBM samples are confined using confining stresses from 1 to 60 MPa. The failure envelope from the GBM results is found to be in excellent agreement with the laboratory failure envelope over these confining stresses.

The GBM modelling not only captured the peak strength but also demonstrated the effect of confining stress on the volumetric strain response. This behaviour also demonstrated that the two-dimensional GBM adequately describe the three-dimensional response of the laboratory cylindrical samples.

7.2 Effect of Uniform Flaws on Strength

The Grain-based models were used to simulate an inclined through-going discontinuity. Then, the models were used to investigate the effect of a single flaw, regularly distributed flaws and randomly distributed flaws on the uniaxial compressive strength.

Noteworthy results from the GBM simulations are:

1. The uniaxial strength is directly related to the flaw inclination when there is only one through-going flaw. The peak strength approaches that of the intact rock when the flaw is approximately vertical or horizontal. The strength reaches its minimum value when the flaw inclination ranges between 20-30°.
2. For uniform discontinuous flaws, both the inclination angle and number of flaws determine the uniaxial compressive strength. In terms of uniform flaws inclined at 45°, the strength is not significantly influenced by the number of flaws. However, the number of flaws and flaw spacing influences the strength of samples containing vertical flaws. Moreover, the strength decreases significantly as distance of the flaw to the free boundary decreases.
3. For uniform flaw patterns (blocky rock), the simulation results agrees well with the laboratory tests with the same flaw configuration. Among the four flaw patterns, the model with 0/90° flaws has the highest peak strengths.
4. For randomly distributed discontinuous flaws, the uniaxial strength decreases as the fracture intensity, expressed as P_{21} increases. There appears to be a threshold fracture intensity where the strength rapidly decreases but this threshold value is non-unique.
5. Flaw interaction can significantly reduce the uniaxial strength.

7.3 Effect of Natural Geological Fractures on Rock Strength

Eight blocks were extracted from the sidewall of the TASS tunnel at the Äspö Hard Rock Laboratory in Southern Sweden. Once the eight 1.5 m high, 1.0 m wide and 0.6 – 1.0 m deep blocks were excavated from tunnel wall, they were sawn into approximately 100mm thick slabs. All the fracture traces on the block surface were digitized and each fracture trace was given its own identification. The fractures were identified as (1) blast-induced fractures and (2) natural fractures. A methodology was also developed for building the Grain-based models using the detailed mapped fracture geometry. A methodology was also developed to quantify the fracture intensity (P_{21}) and the RQD for these blocks.

A number of Grained-based models were carried out to establish the strength for the blocks with only the natural fractures. The RQD values for these blocks ranged from approximately 60 to 100%. The uniaxial and confined strengths of the Grained-based models were determined. The results from the GBM with only the natural fractures suggest:

1. There is a linear relationship between P_{21} and RQD.
2. The relationship between GSI established using the RQD and GSI back estimated from the GBM strength results is poorly correlated.
3. The strength of the GBM models increases significantly when the confining stress is greater than 200 kPa.
4. There is a strong correlation between P_{21} and the uniaxial compressive strength. Hence other relationship with strength can be established, e.g., RQD.

5. Provided a through going fracture that is optimally inclined to the direction of loading is not encountered, the lower bound uniaxial rock strength can be expressed as $UCS /Intact = 0.1 + 0.9 e^{-14 P_{32}}$

7.4 Effect of Blast-induced Fractures on Rock Strength

Grained-based models were carried out to establish the strength for two blocks with both natural and blast-induced fracture. The RQD values for these blocks ranged from approximately 60 to 100%. The uniaxial and confined strengths of the Grained-based models were determined. The results from the GBM with only the natural fractures suggest:

1. The blast induced fracturing reduced the fracture intensity significantly. The average RQD decreased between 12% and 9%, while the P_{21} values increased between 90% and 60%. The relationship between RQD and P_{21} establish for the natural fractures appears to remain valid.
2. The addition of the blast-induced fractures reduces the strength of the GBM models by 30 to 70%. The reduction in the uniaxial compressive strength from the GBMs with the blast-induced fractures follows the previously established relationship between P_{21} and UCS.
3. Should the blast-induced fracturing combined with the natural fractures result in through-going inclined fracture, the strength will be governed by this condition and not the P_{21} value. This also highlights the need for careful blasting to minimize the damage in the EDZ.
4. The strength of the blast induced GBMs appears to be less sensitive to confinement compared to the GBMs with only the natural fractures.

5. The Hoek-Brown failure envelope can be fitted to the data ranging from 0 to 1 MPa or from 5 to 10 MPa. Fitting the Hoek-Brown failure envelope to the data from 0 to 10 MPa confining stress requires GSI values ranging from 73 to 85 for Block 36B-06 and 70 to 85 for Block 36B-08.

7.5 Future Research

The notion of the synthetic rock mass (SRM) to estimate the strength of rock containing fractures is a goal that is definitely worth pursuing. It relies on two assumptions:

1. We can properly model the behaviour of intact rock.
2. We can correctly represent geological fractures in the numerical model and model their constitutive behaviour.

While much has been published on the SRM subject, there are essentially no validated case histories to demonstrate the benefit and correctness of such an approach.

As with all numerical modelling based research there is a need for an improvement in the numerical representation of intact rock behaviour. There are two shortcomings in the current Grained-based model:

1. The mineral grains cannot fracture. Hence all fracturing must go around the grain. While the solid grains can yield plastically, this is clearly not a proper representation of the brittle behaviour of rock.
2. The use of two-dimensional models to represent three-dimensional fractures. This likely plays a significant conservative role in determining the strength of three-dimensional fractures inclined at various orientations.

If the appropriate three-dimensional numerical model could be found, the analysis carried out for this research should be repeated.

There is a lack of quality field data such as that provided by SKB in the TASS Tunnel. It is clear from this research that representing fractures as planes is not realistic. Fracture mapping that captures the detailed geometry of the fractures is needed to truly advance the estimation of rock mass strength.

Bibliography

Andersson, C., and Malmtorp, J. (2009). "Berguttag i TASS tunnel". Delresultat t o m September 2008. *Svensk kärnbränslehantering AB, Report R-08-122*, Stockholm, Sweden, 133.

Andersson, J., Martin, C. D., & Stille, H. (2009). The Äspö Pillar Stability Experiment: Part II--Rock mass response to coupled excavation-induced and thermal-induced stresses. *International Journal of Rock Mechanics & Mining Sciences*, 46(5), 879–895.

Abdelaziz, T., Martin, C.D., Chalaturnyk, R. (2005). "The onset of dilation in soils and rocks". In the *58th Canadian Geotechnical Conference & 6th Joint CGS & IAHCNC Groundwater Specialty Conference*, Saskatoon September 18-21, Vol. 1, 319–325.

Bandis, S.C. (1990). "Scale effects in the strength and deformability of rocks and rock joints". Cunha, A.P. (Ed.), *Scale Effects in Rock Masses*, Balkema, 59–76.

Barton, N., Lien, R., and Lunde, J. (1974). "Engineering classification of rock masses for the design of tunnel support". *Rock Mechanics Felsmechanik Mécanique Des Roches*, 6(4), 189-236.

Barton, N. (2002). "Some new Q-value correlations to assist in site characterisation and tunnel design". *Int. J. Rock Mech. Min. Sci.*, 39(2), 185-216.

Backblom, G., and Martin, C. D. (1999). "Recent experiments in hard rocks to study the excavation response: Implications for the performance of a nuclear waste geological repository". *Tunnel Underground Space Technol.*, 14(3), 377-394.

Berbenni, S., Favier, V., and Berveiller, M. (2007). "Impact of the grain size distribution on the yield stress of heterogeneous materials". *Int. J. Plast.*, 23(1), 114-142.

Bieniawski, Z. T. (1967). "Mechanism of brittle fracture of rock. Part I-theory of the fracture process". *Int. J. Rock Mech. Min. Sci. & Geomech. Abstr* 4(4), 395-404, IN11-IN12, 405-406.

Bieniawski, Z. T. (1968). "The effect of specimen size on compressive strength of coal". *Int. J. Rock Mech. Min. Sci. & Geomech. Abstr* 5(4), 325-326, IN5-IN10, 327-335.

Bieniawski, Z. T. (1973). "ENGINEERING CLASSIFICATION OF JOINTED ROCK MASSES". *Civ. Eng. S. Afr*, 15(12), 335-343.

Bieniawski, Z. T. (1979). "The geomechanics classification in rock engineering applications". In *Proc., 4th International Society of Rock Mechanics Congress*, Montreaux. Vol.2. Balkema, A.A., Rotterdam, 41-48.

Blair, S. C., and Cook, N. G. W. (1998). "Analysis of compressive fracture in rock using statistical techniques: Part I, A non-linear rule-based model". *Int. J. Rock Mech. Min. Sci. & Geomech. Abstr.*, 35(7), 837-848.

Blair, S. C., and Cook, N. G. W. (1998). "Analysis of compressive fracture in rock using statistical techniques: Part II, Effect of microscale heterogeneity on macroscopic deformation". *Int. J. Rock Mech. Min. Sci. & Geomech. Abstr.*, 35(7), 849-861.

Blanks, R. F. and McNamara, C. C. (1935). "Mass concrete tests in large cylinders". *American Concrete Institute -- Journal*, 7(2), 234-262.

Brace, W. F., Paulding, J., B.W., and Scholz, C. (1966). "Dilatancy in fracture of crystalline rocks". *Journal of Geophysical Research*, 71(16), 3939-3953.

Brown, E.T., and Trollope, D.H. (1970). "Strength of a model of jointed rock". *J. of the Soil Mech. Found. Div.*, 96(2), 685-704.

Brown, E.T., editor. (1981). "Rock Characterization, Testing and Monitoring". *ISRM Suggested Methods*. Pergamon Press, Oxford.

Cai, M., and Horii, H. (1992). "A constitutive model of highly jointed rock masses." *Mech.Mater.*, 13(3), 217-46.

Cai, M., Kaiser, P. K., Uno, H., Tasaka, Y., and Minami, M. (2004). "Estimation of rock mass deformation modulus and strength of jointed hard rock masses using the GSI system". *Int. J. Rock Mech. Min. Sci.*, 41(1), 3-19.

Cho, N. (2008). "Discrete Element Modelling of rock: pre-peak fracturing and dilation". PhD thesis, University of Alberta, Edmonton, Canada.

Cho, N., Martin, C. D., and Segou, D. C. (2007). "A clumped particle model for

rock". *Int. J. Rock Mech. Min. Sci.*, 44(7), 997-1010.

Christiansson, R., Ericsson, L. O., & Gustafson, G. (2009). "Hydraulic Characterisation And Conceptual Modelling Of The Excavation Disturbed Zone (EDZ)". In the *Proceedings ISRM-Sponsored International Symposium on Rock Mechanics: Rock Characterisation, Modelling and Engineering Design Methods, SINOROCK 2009*. (pp. 1–5)

Cook, N. G. W. (1970). "Experiment proving that dilatancy is a pervasive volumetric property of brittle rock loaded to failure". *Rock Mech. Rock Engng* 2(4), 181-188.

Cundall, P. A. (2001). A discontinuous future for numerical modelling in geomechanics. *Geotechnical Engineering*, 149(1):41–47.

Cundall, P. A., and Strack, O. D. L. (1979). "Discrete Numerical Model For Granular Assemblies". *Geotechnique*, 29(1), 47-65.

Cundall, P. A., and Hart, R. D. (1992). "Numerical modelling of discontinua". *Eng.Comput.*, 9(2), 101-113.

Cundall, P.A. (2008). "A new approach to the DEM, with applications to brittle, jointed rock". *Lecture, ALERT School, Aussois*.

Cunha, P.A. (Ed.), (1993). "Scale Effects in Rock Masses". *Proc. of the 2nd Int. Workshop*. Balkema, A.A., Portugal.

Dershowitz, W. S., and Einstein, H. H. (1988). " Characterizing rock joint geometry with joint system models ". *Rock Mech. Rock Eng.*, 21(1), 21-51.

Diederichs, M.S. (1999). "Instability of hard rock masses: The role of tensile damage and relaxation". PhD thesis, University of Waterloo, Ontario, Canada.

Donath, F. A. (1961). "Experimental study of shear failure in anisotropic rocks". *Geological Society of America -- Bulletin*, 72(6), 985-990.

Eberhardt, E., Stimpson, B., and Stead, D. (1999). "Effects of grain size on the initiation and propagation thresholds of stress-induced brittle fractures". *Rock Mech. Rock Eng.*, 32(2), 81-99.

- Einstein, H.H., Nelson, R.A., Bruhn, R.W., and Hirschfeld, R.C. (1969). Model studies of jointed-rock behaviour. In *Proc. 11th U.S. Symposium on Rock Mechanics*, Berkeley, pp. 83-103.
- Emsley, S., Olsson, O., Stenberg, L., Alheid, H-J., and Fall, S. (1997). "ZEDEX—a study of damage and disturbance from tunnel excavation by blasting and tunnel boring". *Technical Report 97-30*, Swedish Nuclear Fuel and Waste Management Co (SKB), Stockholm.
- Everitt, R.A., Chemis, P., God, D., and Grogan, A. (1989). "Mapping the excavation damage zone around the circular access shaft at atomic energy of Canada Limited's underground research laboratory". In *Proc. Workshop on Excavation Response in Deep Radioactive Waste Repositories – Implications for Engineering Design and Safety Performance*, 271-282, Winnipeg, Manitoba.
- Finney, J. L. (1979). "A procedure for the construction of Voronoi polyhedra". *Journal of Computational Physics*, 32(1), 137-43.
- Fossum, A. F. (1985). "Effective Elastic Properties For A Randomly Jointed Rock Mass". *Int. J. Rock Mech. Min. Sci. & Geomech. Abstr.*, 22(6), 467-470.
- Frantziskonis, G., and Desai, C. S. (1987). "Analysis of a strain softening constitutive model". *Int. J. Solids Structures*, 23(6), 751-767.
- Fredrich, J. T., Evans, B., and Teng-fong Wong. (1990). "Effect of grain size on brittle and semibrittle strength: implications for micromechanical modelling of failure in compression". *Journal of Geophysical Research*, 95 10907-20.
- Fumagalli, E. (1968). "Model Simulation of Rock Mechanics Problems in Rock Mechanics in Engineering Practice". K.G.Stagg and O.C.Zienkiewicz, (Eds.), John Wiley and Sons, London.
- Gao, F. Q., & Stead, D. (2014). The application of a modified Voronoi logic to brittle fracture modelling at the laboratory and field scale. *International Journal of Rock Mechanics & Mining Sciences*, 68, 1–14. doi:10.1016/j.ijrmms.2014.02.003
- Goldstein, M., Goosev, B., Pvrogovsky, N., Tulinov, R., and Turovskaya, A. (1966). "Investigation of Mechanical Properties of Cracked Rock". *Proceedings, 1st International Congress on Rock Mechanics*, Lisbon. Vol.1, 521-524.

- Griffith, A. A. (1921). "The phenomena of rupture and flow in solids". *Series A, containing papers of a mathematical or physical character*, 221, 163-198. Philos. Trans. Roy. Soc. London.
- Griffith, A.A. (1924). "The Theory of Rupture". In *Proc. 1st International Congress for Applied Mechanics*, 55-63.
- Grishin, M.M., Orekhov, V.G., Pystogov, V.I., and Shimel'mits., G.I. (1967). "The Effect of Characteristics of Geological Structure of the Rock Foundations of the Dams on their Strength and Stability". *Transactions, 9th Congress on Large Dams*, Istanbul. Vol.1, 873-889.
- Hakami, E., Fredriksson, A., Lanaro, F., and Wrafter, J. (2008). "Rock mechanics Laxemar- Site descriptive modelling, SDM-Site Laxemar". *Report: R-08-57*. Swedish Nuclear Fuel and Waste Management Co (SKB), Stockholm.
- Hart, R., Cundall, P. A., and Lemos, J. (1988). "Formulation of a three-dimensional distinct element method - PART II. Mechanical calculations for motion and interaction of a system composed of many polyhedral blocks". *Int. J. Rock Mech. Min. Sci. & Geomech. Abstr.*, 25(3), 117-125.
- Hashin, Z. (1988). "The differential scheme and its application to cracked materials". *J. Mech. Phys. Solids*, 36(6), 719-34.
- Herget, G., and Arjang, B. (1990). "Update on ground stresses in the Canadian Shield". In *Proceedings Specialty Conference on Stresses in Underground Structures*, Ottawa. Energy, Mines and Resources Canada. 33-47.
- Hoek, E. and Brown, E. T. (1980). Empirical strength criteria for rock masses. 106(GT9):1013–1035. Hoek, E. (1994). "Strength of rock and rock masses". *News J. ISRM* 2(2):4-16.
- Hoek, E., and Brown, E. T. (1997). "Practical estimates of rock mass strength". *Int. J. Rock Mech. Min. Sci.*, 34(8), 1165-1186.
- Hoek, E. Kaiser, P.K., and Bawden, W.F. (2005). "Support of underground excavations in hard rock". Balkema, A.A. Fourth print.
- Hoek, E., T. G. Carter, and M. S. Diederichs. 2013. Quantification of the Geological Strength Index chart. In CD-ROM Proceedings 47th US Rock Mechanics/Geomechanics Symposium, San Francisco.

Itasca Consulting Group. (2004). PFC2D(Particle Flow Code in 2 Dimensions) version 3.1.

Hudson, J.A., Brown, E.T., and Fairhurst, C. (1971). "Shape of the complete stress-strain curve for rock". *Proc. 13th U.S. Symp. Rock Mech.*, 773-795, New York. American Society of Civil Engineers.

Hudson, J.A., Harrison, J.P. (1997). "Engineering Rock Mechanics: An Introduction to the Principles". Elsevier, Oxford.

Hudson, J.A., Bäckström, A., Rutqvist, J., Jing, L., Backers, T., Chijimatsu, M., Christiansson, R., Feng, X.-T., Kobayashi, A., Koyama, T., Lee, H.-S., Neretnieks, I., Pan, P.-Z., Rinne, M., and Shen, B.-T. (2009). "Characterising and modelling the excavation damaged zone in crystalline rock in the context of radioactive waste disposal". *Environmental Geology*. 57:1275-1297.

Jackson, R., and Lau, J. S. O. (1990). "The effect of specimen size on the laboratory mechanical properties of Lac du Bonnet grey granite". In *Proc. 1st International Workshop on Scale Effects in Rock Masses*, Pinto da Cunha (ed.), Balkema, 165-174.

Jackson, R. (1992). Laboratory Characterization of the Underground Research Laboratory's 420m Level: Borehole 409-031-MS9. *Mining Research Laboratories 92-007 (TR)*.

Jaeger, J. C. (1960). "Shear failure of anisotropic rocks". *Geol. Mag.*, 97(1), 65-72.

Jing, L., and Stephansson, O. (2007). "Fundamental of Discrete Element Methods for Rock Engineering". Elsevier, 85 Edition.

Kim, B., Cai, M., Kaiser, P., & Yang, H. (2007). Estimation of block sizes for rock masses with non-persistent joints. *Rock Mechanics and Rock Engineering*, 40(2), 169–192.

Kelly, D. D., Peck, D. C. and James, R. S. (1994). Petrography of granitic samples from the 420 m level of the Underground Research Laboratory, Pinawa, Manitoba, report, Laurentian Univ., Sudbury, Ont., Canada.

Kemeny, J. M. (1991). "A Model for non-linear rock deformation under compression due to sub-critical crack growth". *Int. J. Rock Mech. Min. Sci. & Geomech. Abstr.*, 28(6), 459-467.

- Kovari, K., Tisa, A., Einstein, H. H., and Franklin, J. A. (1983). "Suggested methods for determining the strength of rock materials in triaxial compression: revised version". *Int. J. Rock Mech. Min. Sci. & Geomech. Abstr.*, 20(6), 283-90.
- Lan, H., Martin, C. D., and Hu, B. (2010). "Effect of heterogeneity of brittle rock on micromechanical extensile behavior during compression loading". *Journal of Geophysical Research - Part B - Solid Earth*, 115 B01202 (14 pp.).
- Lau, J. S. O., and Chandler, N. A. (2004). "Innovative laboratory testing". *Int. J. Rock Mech. Min. Sci.*, 41(8), 1427-1445.
- Li, H., Li, K., Subhash, G., Kecskes, L. J., and Dowding, R. J. (2006). "Micromechanical modeling of tungsten-based bulk metallic glass matrix composites". *Materials Science and Engineering A*, 429(1-2), 115-123.
- Lim, S. S., Martin, C. D., & Åkesson, U. (2012). In-situ stress and microcracking in granite cores with depth. *Engineering Geology*, 147, 1–13.
- Marinos, P., and Hoek, E. (2000). "GSI: A geological friendly tool for rock mass strength estimation". In *Proc. GeoEng2000, An International Conference on Geotechnical & Geological Engineering*, Melbourne, 1: 1422–1440, Lancaster. Technomic Publishing Co., Inc.
- Marinos, P., Hoek, E., and Marinos, V. (2006). "Variability of the engineering properties of rock masses quantified by the geological strength index: The case of ophiolites with special emphasis on tunnelling". *Bull. Eng. Geol. Env.*, 65(2), 129-142.
- Martin, C.D. (1993). "The Strength of Massive Lac du Bonnet Granite Around Underground Openings". Ph.d thesis. University of Manitoba.
- Martin, C. D., and Chandler, N. A. (1993). "Stress heterogeneity and geological structures". *Int. J. Rock Mech. Min. Sci. & Geomech. Abstr.*, 30(7), 993-999.
- Martin, C. D., and Chandler, N. A. (1994). "Progressive fracture of Lac du Bonnet granite". *Int. J. Rock Mech. Min. Sci.*, 31(6), 643-659.
- Martin, C. D. (1997). "Seventeenth Canadian Geotechnical Colloquium: the effect of cohesion loss and stress path on brittle rock strength". *Canadian Geotechnical Journal*, 34(5), 698-725.

Martin, C. D., Lu, Y., and Lan, H. (2011). "Scale effects in a synthetic rock mass". *12th International Congress on Rock Mechanics of the International Society for Rock Mechanics*, ISRM 2011, October 18, 2011 - October 21, Taylor and Francis Inc., Beijing, China, 473-478.

Marinos, P. and Hoek, E. (2000). GSI: A geological friendly tool for rock mass strength estimation. In Proc. GeoEng2000, An International Conference on Geotechnical & Geological Engineering Melbourne, volume 1: Invited Papers, pages 1422–1440, Lancaster. Technomic Publishing Co., Inc.

Martino, J.B., and Thompson, P.M. (1997). "Status of the development of the deep doorstopper gauge system for in situ stress measurement borehole at the Underground Research Laboratory". *Ontario Hydro, Nuclear Waste Management Division Report: 06819-REP-01200-10031-R00*.

Martino, J.B., Thompson, P.M., Chandler, N.A., and Reader, R.S. (1997). "The in situ stress program at the Underground Research Laboratory". *Ontario Hydro Nuclear Waste Management Division Report: 06819-REP-01200-0053-R00*.

Martino, J. B., and Chandler, N. A. (2004). "Excavation-induced damage studies at the Underground Research Laboratory". *Int. J. Rock Mech. Min. Sci.*, 41(8), 1413-1426.

Mas Ivars, D., Pierce, M.E., Darcel, C., Reyes-Montes, J., Potyondy, D.O., Young, R.P., and Cundall, P.A., (2011) "The Synthetic Rock Mass Approach for Jointed Rock Mass Modelling", *Int. J. Rock Mech. & Min. Sci.*, 48, 219–244.

Nemat-Nasser, S., and Horii, H. (1982). "Compression-induced nonplanar crack extension with application to splitting, exfoliation and rockburst". *Journal of Geophysical Research*, 87(B8) 6805-21.

Olsson, M. Ingemar Markström, Anders Pettersson, Malin Sträng (2009). "Examination of the Excavation Damaged Zone in the TASS tunnel". SKB Technical Report: *R-09-39 (October)*. Swedish Nuclear Fuel and Waste Management Co, Stockholm.

Olsson, W. A. (1974). "Grain size dependence of yield stress in marble". *Journal of Geophysical Research*, 79(32), 4859-62.

Palmstrom, A. (2005). Measurements of and correlations between block size and rock quality designation (RQD). *Tunnelling and Underground Space Technology*, 20(4), 362–377.

Park, E.S., Martin, C.D. and Christiansson, R. (2004). "Simulation of the mechanical behaviour of discontinuous rock masses using a bonded-particle model". In CD-ROM *Proc. 6th North American Rock Mechanics Symposium – NARMS04*, Houston, 1-8. NARMS 04-480.

Potyondy, D. O. (2012). The Bonded-Particle Model as a Tool for Rock Mechanics Research and Application: Current Trends and Future Directions In Proceeding 7th Asian Rock Mechanics Symposium, ARMS7, Seoul, 15-19 October 2012, pp. 1–33.

Potyondy, D. O., and Cundall, P. A. (2004). "A bonded-particle model for rock." *Int. J. Rock Mech. Min. Sci.*, 41(8), 1329-1364.

Pratt, H. R., and Black, A. D. (1972). "The effect of specimen size on the mechanical properties of unjointed diorite". *Int. J. Rock Mech. Min. Sci. & Geomech. Abstr.*, 9(4), 513-29.

Prikryl, R. (2001). "Some microstructural aspects of strength variation in rocks". *Int. J. Rock Mech. Min. Sci.*, 38(5), 671-682.

Read, R.S., Martino, J.B. Dzik, E.J., and Chandler, N.A. (1997). "Excavation stability study – analysis and interpretation of results". *Ontario Hydro, Nuclear Waste Management Division Report: 06819-REP-01200-0028-R00*,

Robert, V.P., Thomas, L.W. and Terzaghi, K. (1946). "Rock Tunneling with Steel Support". Youngstown, Ohio. [The Commercial shearing & stamping co.], p271.

Rogers, S., Elmo, D., Beddoes, R. and Dershowitz, B. (2009). "Mine scale DFN modelling and rapid upscaling in geomechanical simulations of large open pits". *International Symposium on Rock Slope Stability in Open Pit Mining and Civil Engineering*, Santiago, Chile.

Rogers, S., Moffitt, K. and Chance, A. (2006). "Using Realistic Fracture Network Models for Modelling Block Stability and Groundwater Flow in *Rock Slopes, Sea to Sky Geotechnique 2006: 59th Canadian Geotechnical Conference*: 1452-1459, Vancouver, British Columbia.

Roy, N. 1993. "Engineering behavior of rock mass through study of jointed models". Ph.d thesis. Indian Institute of Technology, Delhi.

Rutqvist, J., and Stephansson, O. (2003). "The role of hydromechanical coupling in fractured rock engineering". *Hydrogeol J.*, 11:7-40.

Sammis, C. G., and Ashby, M. F. (1986). "The failure of brittle porous solids under compressive stress states". *Acta Metallurgica*, 34(3), 511-26.

Scholtès, L., & Donzé, F.-V. (2013). A DEM model for soft and hard rocks Role of grain interlocking on strength. *Journal of the Mechanics and Physics of Solids*, 61(2), 352–369.

Shin, S.W. "Excavation disturbed zone in Lac Du Bonnet granite". PhD thesis. University of Alberta, 2010.

Sherif, H. A., and Kossa, S. S. (1991). "Relationship between normal and tangential contact stiffness of nominally flat surfaces". *Wear*, 151(1), 49-62.

Singh, B. (1973). "Continuum characterization of jointed rock masses. I. The constitutive equations". *Int. J. Rock Mech. Min. Sci. & Geomech. Abstr.*, 10(4), 311-35.

Skinner, W.J. (1959). "Experiments on the compressive strength of anhydrite". *Engineer*, 207,255-259,288-292.

Sugihara, K., Matsu, H., and Sato, T. (1999). "In situ experiments on rock stress conditions and excavation disturbance in JNC's geoscientific research program in Japan". In: *Rock mechanics of nuclear waste repositories. S.Saeb, C.Francke (eds)* Veil, Colorado, 159-183.

Tang, Chun'an. (1997). "Numerical simulation of progressive rock failure and associated seismicity". *Int. J. Rock Mech. Min. Sci. & Geomech. Abstr.*, 34(2), 249-261.

Teja, P. (2008). "An Experimental Study on Strength Behaviour of Jointed Rock Mass Through Modelling Under Uniaxial Compression". BSc Thesis, Department of Civil Engineering, National Institute of Technology, Rourkela.

Trask, P. D. (1932). "Origin and environment of source sediments of petroleum". Gulf Pub., Huston, TX, United States.

Tsang, C., Bernier, F., and Davies, C. (2005). "Geohydromechanical processes in the Excavation Damaged Zone in crystalline rock, rock salt, and indurated and plastic clays - In the context of radioactive waste disposal". *Int. J. Rock Mech. Min. Sci.*, 42(1), 109-125.

Venter, J. and Strasse, P. (1958). "Pressure and Movement in Soft Rocks". *Proceedings: International Strata Control Congress*, Leipzig. 124-136.

Wang, Y., & Tonon, F. (2010). Calibration of a discrete element model for intact rock up to its peak strength. *International Journal for Numerical and Analytical Methods in Geomechanics*, 34(5), 447–469. doi:10.1002/nag.811

Wong, T., Wong, R. H. C., Chau, K. T., and Tang, C. A. (2006). "Microcrack statistics, Weibull distribution and micromechanical modeling of compressive failure in rock". *Mech. Mater.*, 38(7), 664-681.

Yoshinaka, R., Osada, M., Park, H., Sasaki, T., and Sasaki, K. (2008). "Practical determination of mechanical design parameters of intact rock considering scale effect". *Eng. Geol.*, 96(3-4), 173-186.

Zangerl, C., Evans, K. F., Eberhardt, E., & Loew, S. (2008). Normal stiffness of fractures in granitic rock: a compilation of laboratory and in-situ experiments. *International Journal of Rock Mechanics & Mining Sciences*, 45(8), 1500–1507. doi:10.1016/j.ijrmms.2008.02.001

Zavattieri, P. D., Raghuram, P. V., and Espinosa, H. D. (2001). "A computational model of ceramic microstructures subjected to multi-axial dynamic loading". *J. Mech. Phys. Solids*, 49(1), 27-68.

Zhang, K. S., Wu, M. S., and Feng, R. (2005). "Simulation of microplasticity-induced deformation in uniaxially strained ceramics by 3-D Voronoi polycrystal modeling". *Int. J. Plast.*, 21(4), 801-834.

Zöllner, D. (2006). "Construction of Polycrystalline Microstructures". *Workshop in Bad Helmstedt*. <http://www.uni-magdeburg.de/gkmm/Folien/zoellner.ppt>.

Appendix A: Additional Results and Figures

A1. Laboratory tests and modelling on the scale effect

Table A. 1: The results of various rocks in uniaxial compression experiments.

Sample No.	lithology	velocity of longitudinal wave (m/s)	UCS R_b /MPa	tension strength σ_t /MPa	Modulus E /GPa	Poisson's ratio μ
E057	Granite	4700	125.37	7.74	44.8	0.27
E063	Granite	4148	111.63	3.77	25.5	0.26
E064	Granite	4507	81.34	4.19	27.6	0.25
E072	Marble	5780	64.83	3.71	38.1	0.43

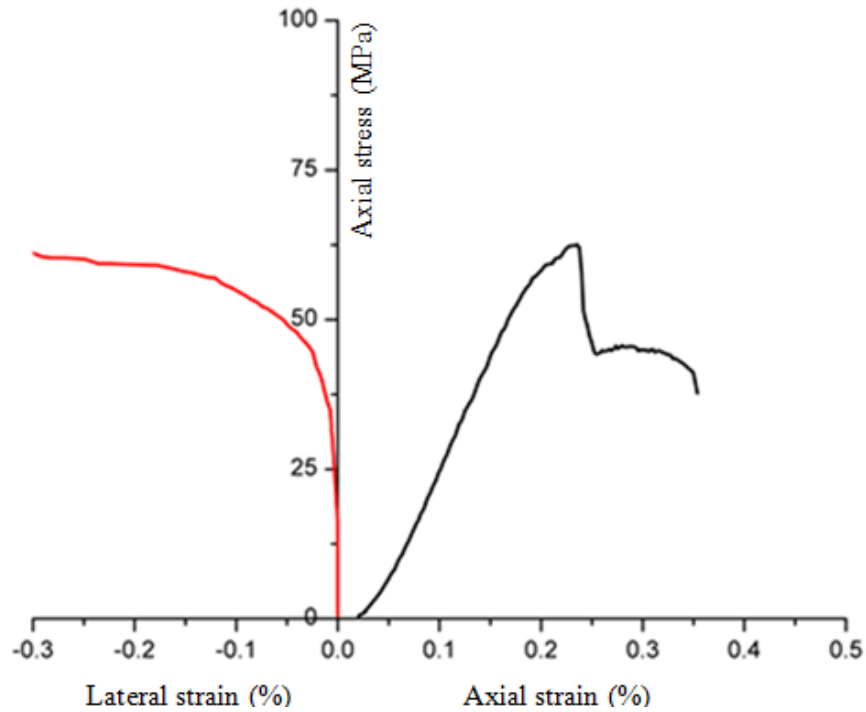
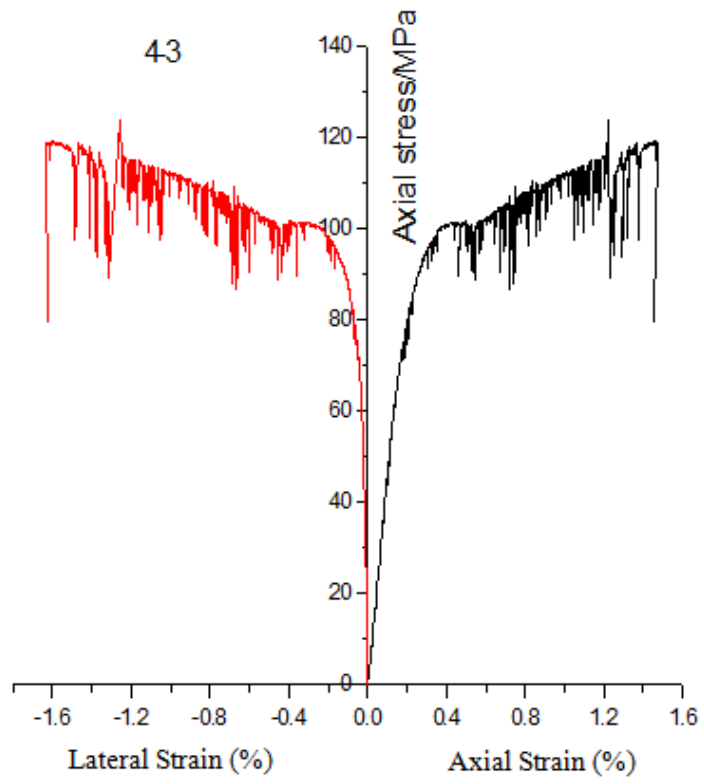


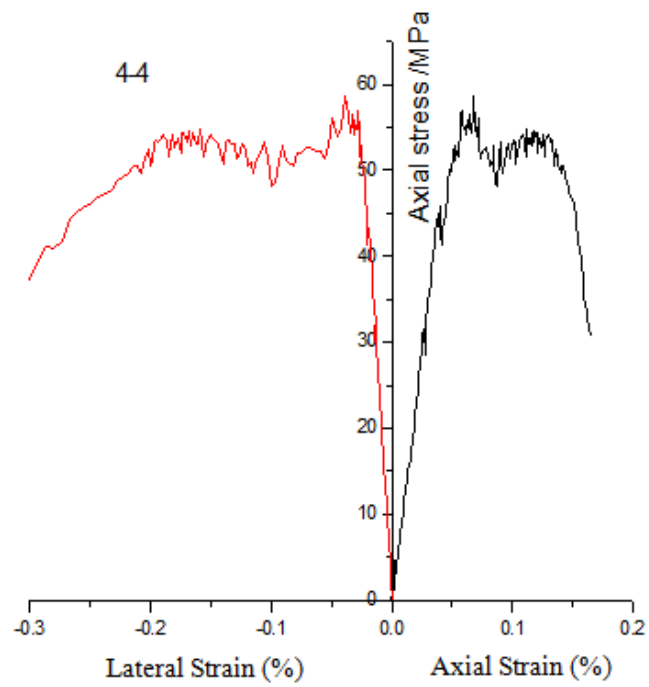
Figure A. 1: Stress-strain curve for sample E072 of UCS test.

Table A. 2: The result of the rock samples in conventional triaxial compression experiments.

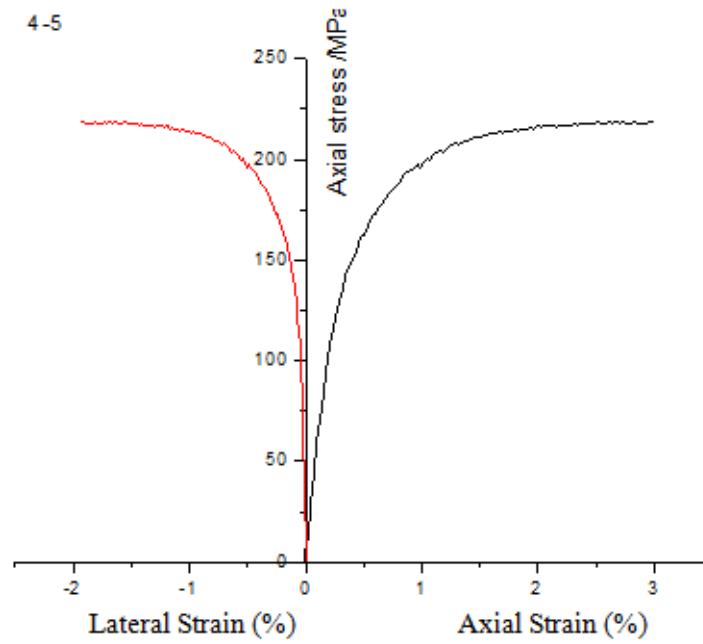
Sample No.	lithology	specimen ID	σ_1 (MPa)	σ_3 (MPa)	c (MPa)	φ
E057	Granite	1-3 [#]	324.7	20	23.2	50.2°
		1-4 [#]	438.3	40		
		1-5 [#]	457.3	60		
E063	Granite	2-3 [#]	303.5	20	20.1	48.7°
		2-4 [#]	393.8	40		
		2-5 [#]	320.9	60		
E064	Granite	3-3 [#]	238.5	20	16.5	47.7°
		3-4 [#]	344.6	40		
		3-5 [#]	200.3	60		
E072	Marble	4-3 [#]	143.8	20	18.4	34.2°
		4-4 [#]	98.7	40		
		4-5 [#]	278.6	60		
		7-4 [#]	409.6	40		
		7-5 [#]	456.5	60		



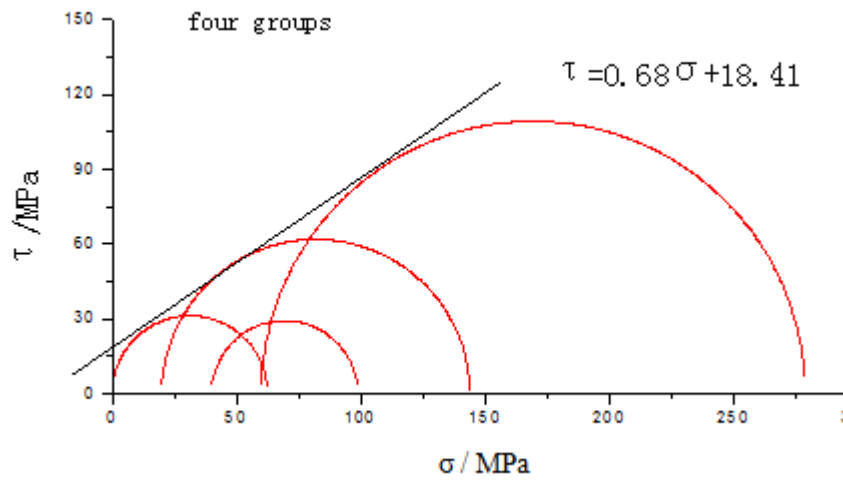
(a)



(b)



(c)



(d)

Figure A. 2: Laboratory tests results for Marbles. (a) Sample 4-3#. (b) Sample 4-4#. (c) Sample (4-5#). (d). Mohr-Coulomb failure envelop for four sets of data.

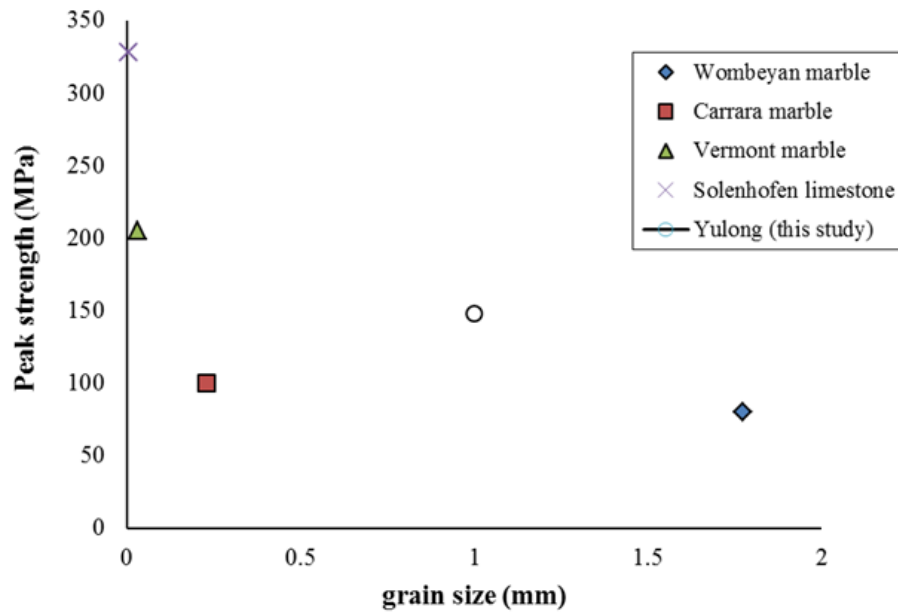


Figure A. 3: Peak strengths for various rocks with a confinement of 5MPa.

Table A. 3: Statistical analysis of tensile stress at the grain contacts for three different sized marbles.

Sample size (mm × mm)	number of tensile contacts	number of total contacts	length of tensile contacts (m)	length of total contacts (m)
30-60	52	737	3.50E-02	1.09E+00
60-120	320	2977	2.25E-01	4.42E+00
105-210	2319	9147	1.84E+00	1.33E+01

Table A. 4: Frequency of tensile stress calculated based on the tensile contacts and all contacts.

tensile stress (MPa)	Sample size					
	30-60		60-120		105-210	
	Frequency based on tensile contacts	Frequency based on all contacts	Frequency based on tensile contacts	Frequency based on all contacts	Frequency based on tensile contacts	Frequency based on all contacts
0	1.4%	19.2%	1.8%	16.6%	2.7%	10.6%
-0.5	1.1%	15.4%	1.7%	16.3%	3.1%	12.4%
-1	0.9%	13.5%	1.9%	17.5%	4.5%	17.7%
-1.5	0.7%	9.6%	1.6%	14.7%	4.1%	16.2%
-2	1.6%	23.1%	1.2%	10.9%	4.4%	17.6%
-2.5	0.8%	11.5%	1.4%	12.8%	3.3%	13.2%
-3	0.5%	7.7%	1.2%	11.3%	3.1%	12.3%

A2. Study on the geometric heterogeneity through tensile stress generation

As discussed in the previous chapters, heterogeneities play a very important role in the development of localized tensile conditions. Thus, the grain-based models are used in this thesis to resolve the issued due to complexity of various grain geometries. In this part, there is a brief discussion on the geometric heterogeneity in terms of different arrangement of grains.

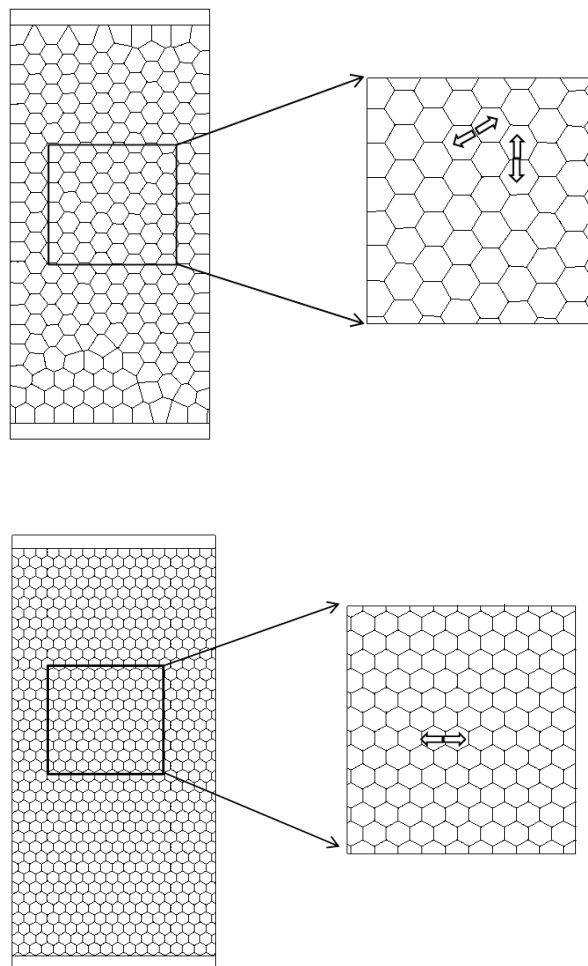


Figure A. 4: Comparison of the rock blocks between a regular voronoi model (top) and a homogeneous model (bottom).

The figure above shows an illustration of two models with different grain arrangements. The plot clearly presents the difference in the grain boundary orientation and grain system arrangement. It shows there are more degrees of freedom of allowable breakage for the regular voronoi model (honeycomb shape), compared with the homogeneous model which is more likely to rupture through the linkage of two adjacent grains in horizontal direction.

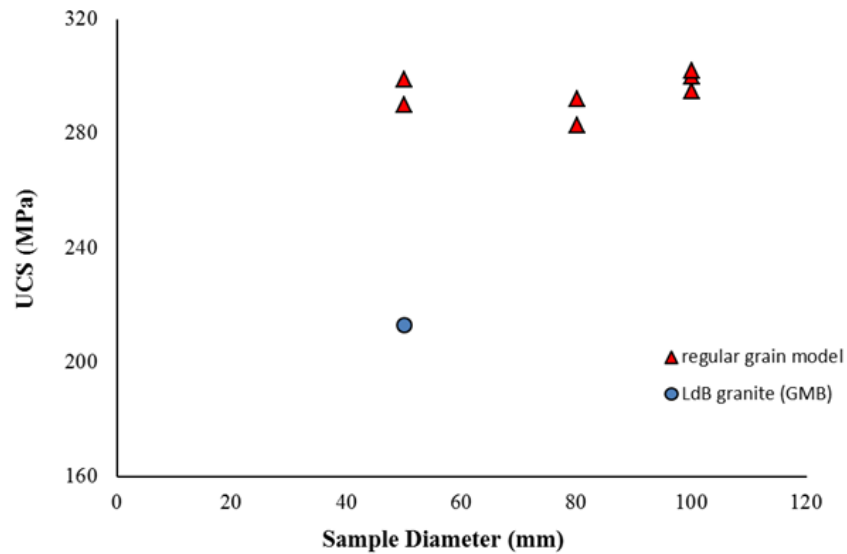
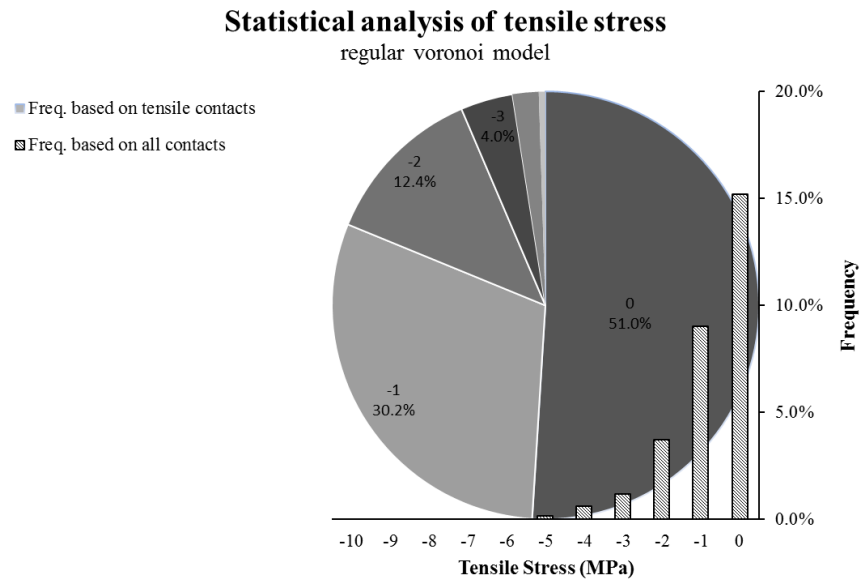
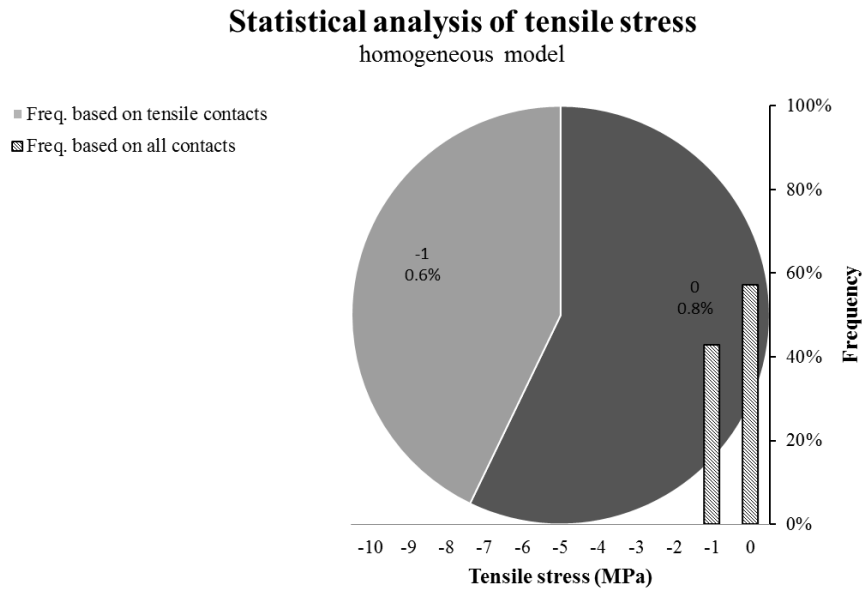


Figure A. 5: UCS results for the grain-based model and regular grain models (honeycomb shape voronoi) in three grain sizes.

From the figure above, we can find that the models of regular grain (same grain distribution) have consistent high values at over 280 MPa, compared to the LdB grain-based model. In the case, the UCS strength of homogeneous model is obtained at an unpractical high value.



(a)



(b)

Figure A. 6: Statistical analysis of tensile stress for two different models. (a) the regular voronoi model; (b) homogeneous model.

From the viewpoint of tensile stress, both regular model and the GMB have shown that the tensile stresses are generated at a range between -7MPa and 0. However, the homogeneous model presents a uniform tensile stress distribution with only -1MPa and 0, which means that the brittle failure caused by tensile stress are not predominant under the uniaxial compressive condition.

Appendix B: Primary FISH Functions used in Simulations

B1. Setting up global variable

```
; define global variable
```

```
def _arraySize
```

```
    maxNodes_ = 50000
```

```
    maxEdges_ = 50000
```

```
    maxPoint_ = 50000
```

```
    maxBlocks_ = 50000
```

```
    maxNodesPerBlock_ = 30
```

```
    maxMaterials_=30
```

```
    loop_number=1000
```

```
    reg_ = reg_
```

```
    bottom_block=-0.04*height_block
```

```
    top_block=1.04*height_block
```

```
end
```

```
=====
```

```
===
```

```
;read the size of sample (including width and height) from specimen file
```

```
def read_sampleSize
```

```
    array inn_(1)
```

```
can_ = open('specimen.dat',0,1)

can_ = read(inn_,1)

;setting up the width of the specimen

width_block = parse(inn_(1),5)

width_block = float(wid_spe)/1000

;setting up the height of the specimen

height_block = parse(inn_(1),6)

height_block = float(hei_spe)/1000

can_ = close

end
```

B2. Assigning material properties

```
;define constitutive material properties
```

```
def defineMaterial
```

```
    set matNumber=p
```

```
    loop p (1, 4)
```

```
        command ;define block material properties
```

```
        prop matNumber=p d=blockDensity_p k=block_p g=blockG_p
```

```
    endloop
```

```
end_command
```

```
end
```

```
def defineJoint ;define constitutive joint properties
```

```
    set jointNumber=q
```

```
    change jcons=5
```

```
    set jcondf=5
```

```
    loop q (1, 10) ;10 potential properties for 10 different joints
```

```
        command
```

```
            prop jointMaterial=q jkn=jKn_q jks=jKs_q jf=jFr_q jc=jCo_q
```

```
            jt=jTen_q jrf=jrFr_q jresc=jrCo_q jrt=jrTen_q
```

```
        end_command
```

```
    endloop
```

```
end
```


B3. Read flaw distribution from existing files and make plot

```
def DFNplot

    loop j (1,15)                                ;there are 15 files from Block 36-1

        can_ = open(string(j)+''.dat', 0, 1)

        inn_ = read(inn_,1)

        iMaxPoint_ = parse(inn_(1),1)

        array DFNPoint(maxPoint_)

        can_ = read(DFNPoint,iMaxPoint_)

; there are a couple of coordinates in each file from which a continuous
    line can be plotted

        loop i (1,iMaxPoint_-1)

            xvc1_ = parse(Nodes1(i),2)

            yvc1_ = parse(Nodes1(i),1)

            xvc2_ = parse(Nodes1(i+1),2)

            yvc2_ = parse(Nodes1(i+1),1)

; use x1,y1, x2, y2 to plot a line

        command

            crack xvc1_ yvc1_ xvc2_ yvc2_ id 35

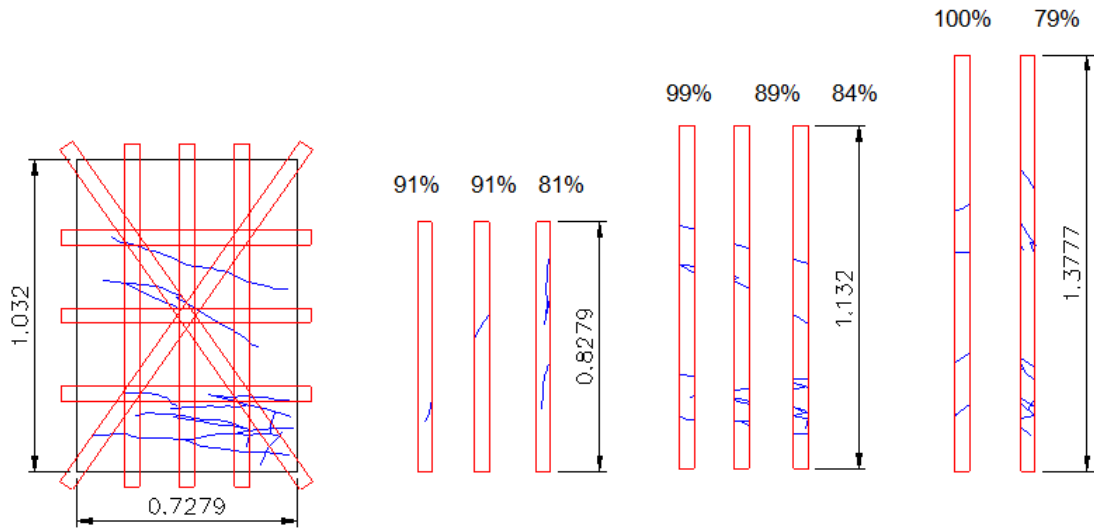
            change jmat 17 range id 35

        end_command
```

```
        end_loop
    can_=close
end_loop
end
```

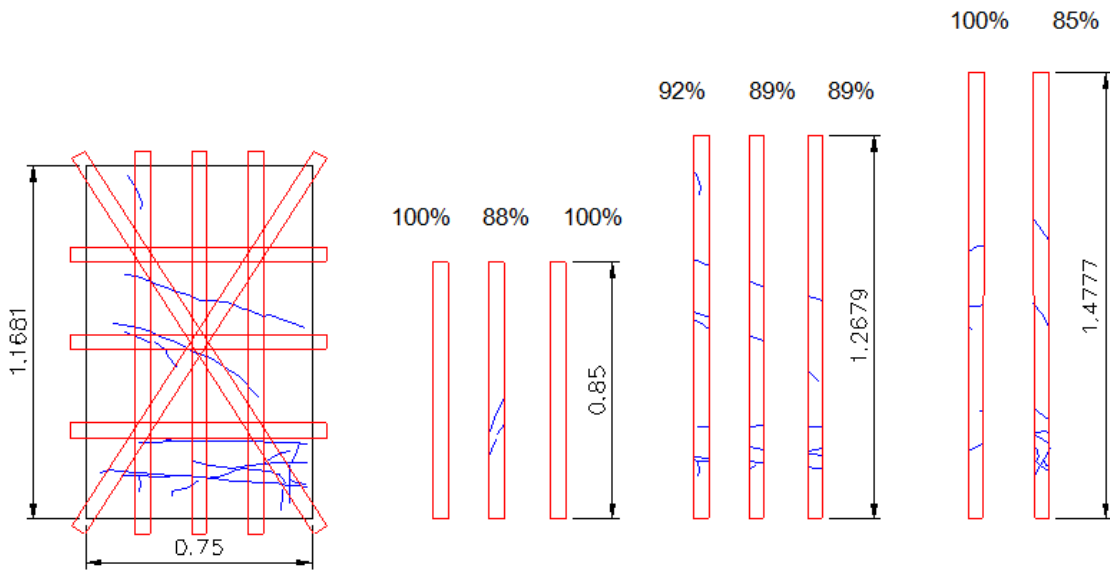
Appendix C: RQD for Block Containing Natural Fractures

BLOCK 36B-1



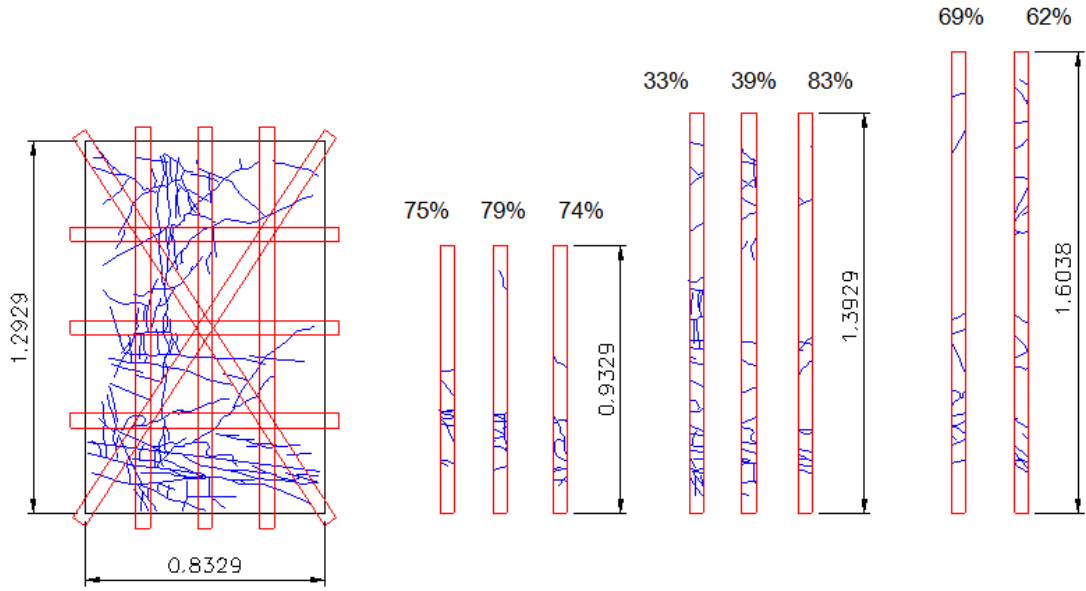
RQD=89%

BLOCK 36B-2



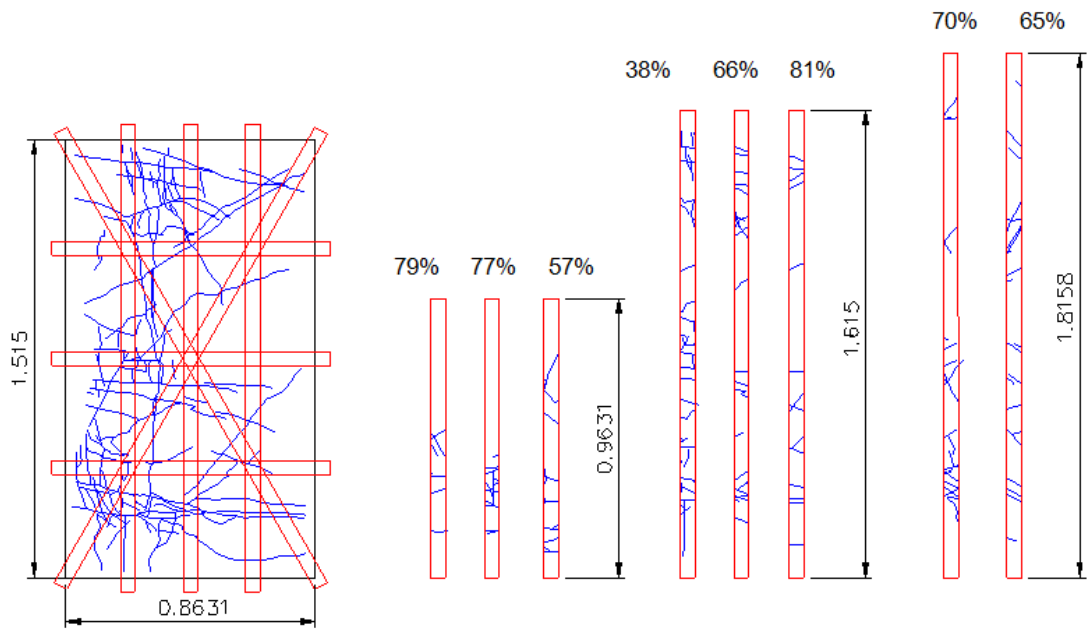
RQD=93%

BLOCK 37B-1



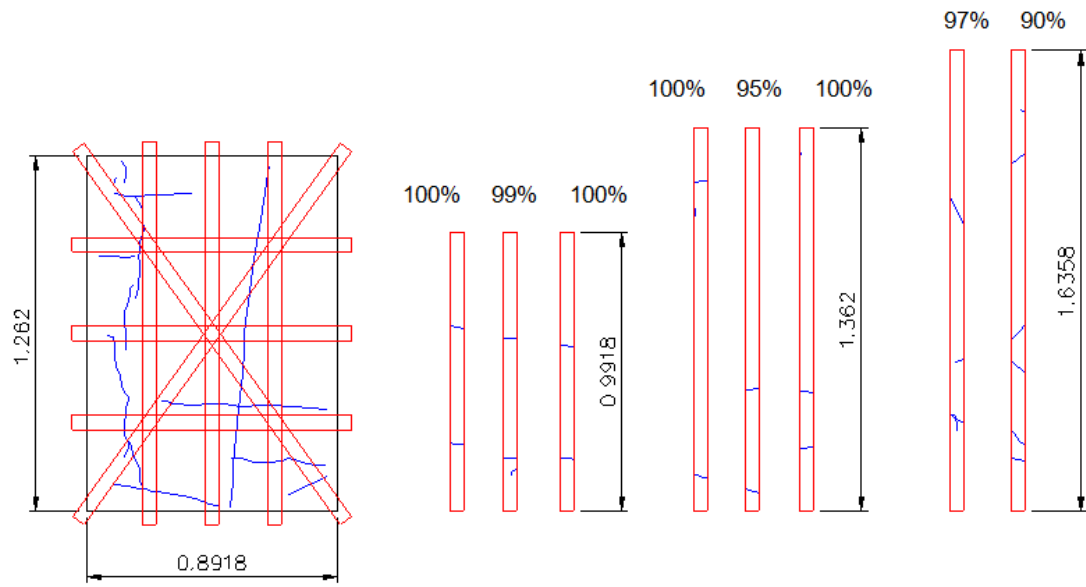
RQD=64%

BLOCK 37B-2



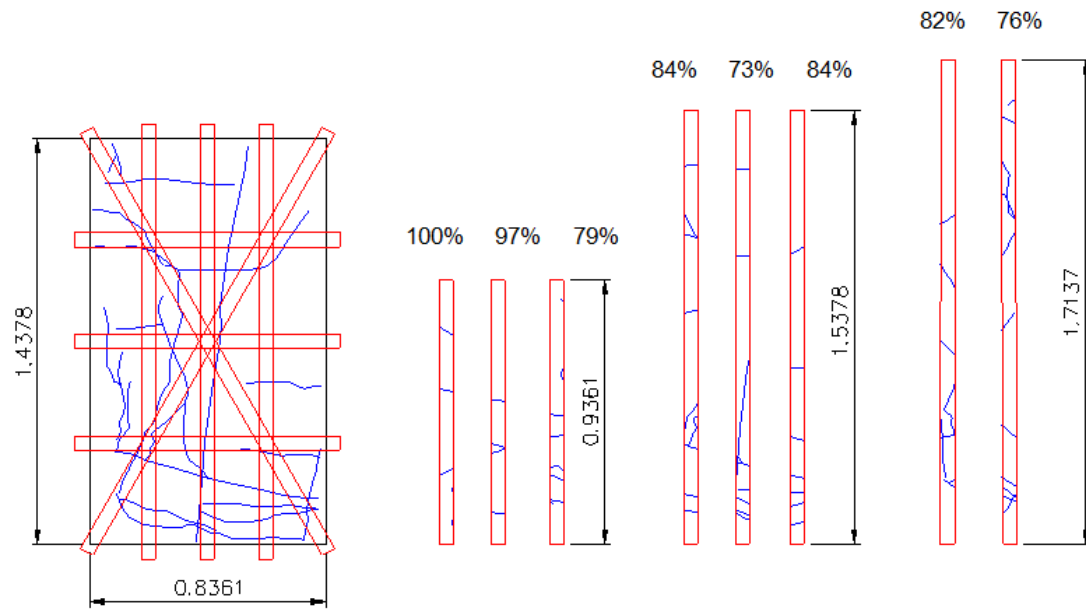
RQD=67%

BLOCK 39B-1



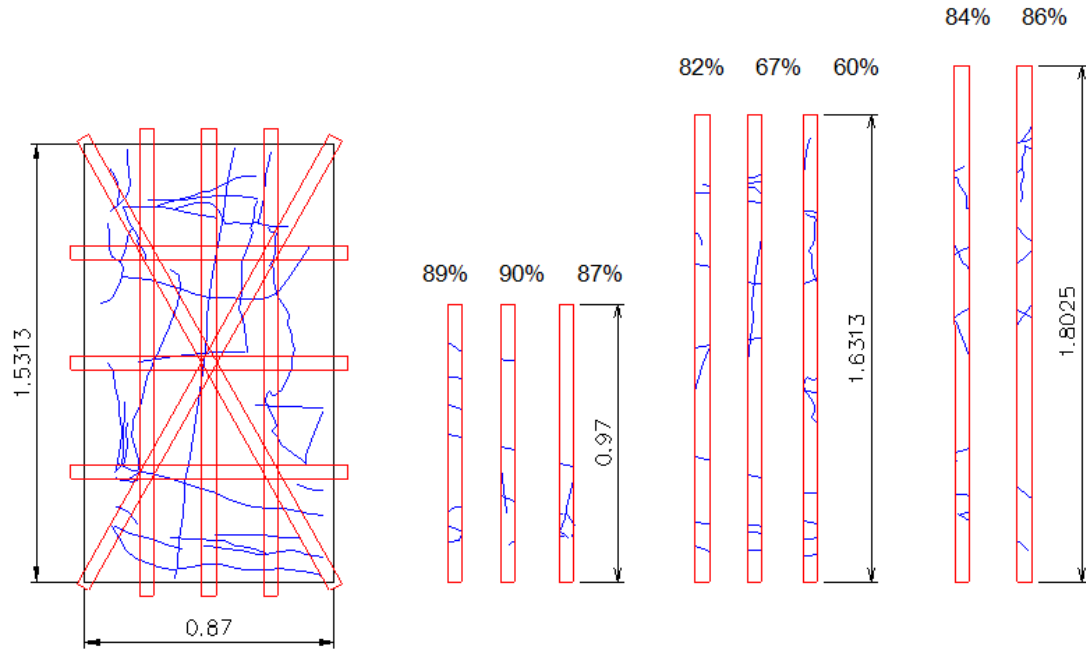
RQD=97%

BLOCK 39B-2



RQD=84%

BLOCK 39B-3

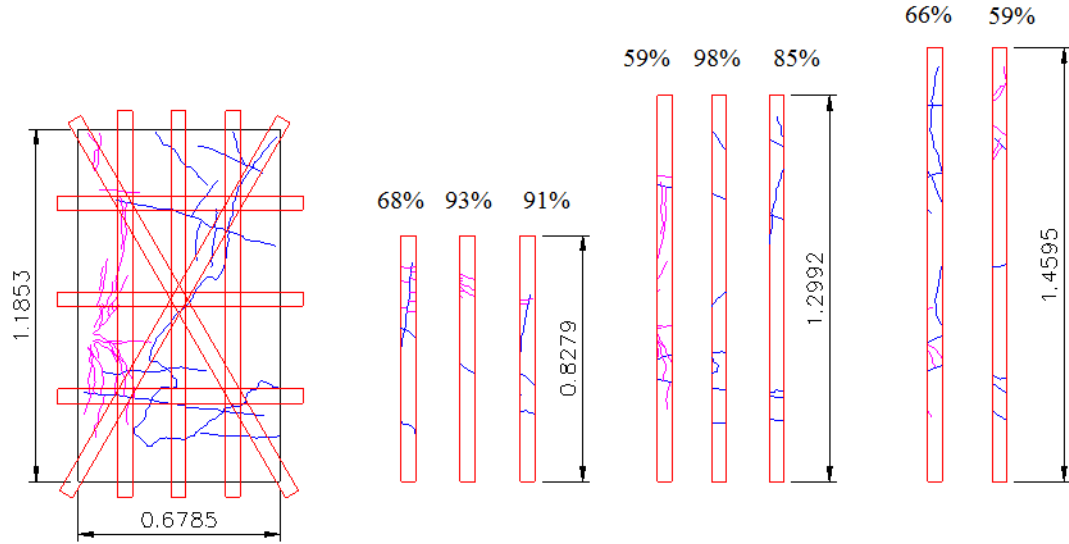


RQD=81%

Appendix D: RQD for Block Containing Blast-induced & Natural fractures

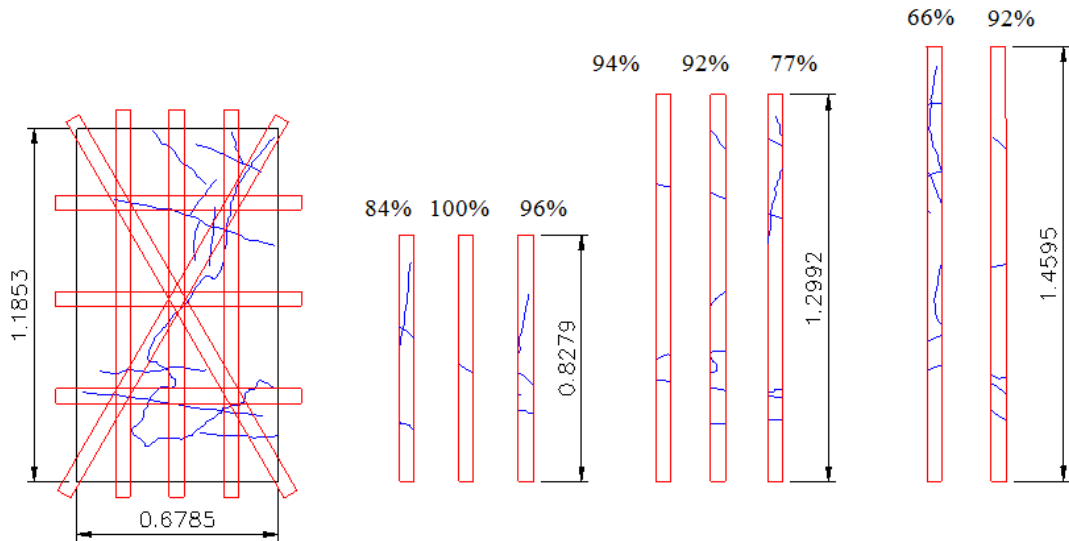
36B-06:

Combined natural and blast-induced



RQD = 76%

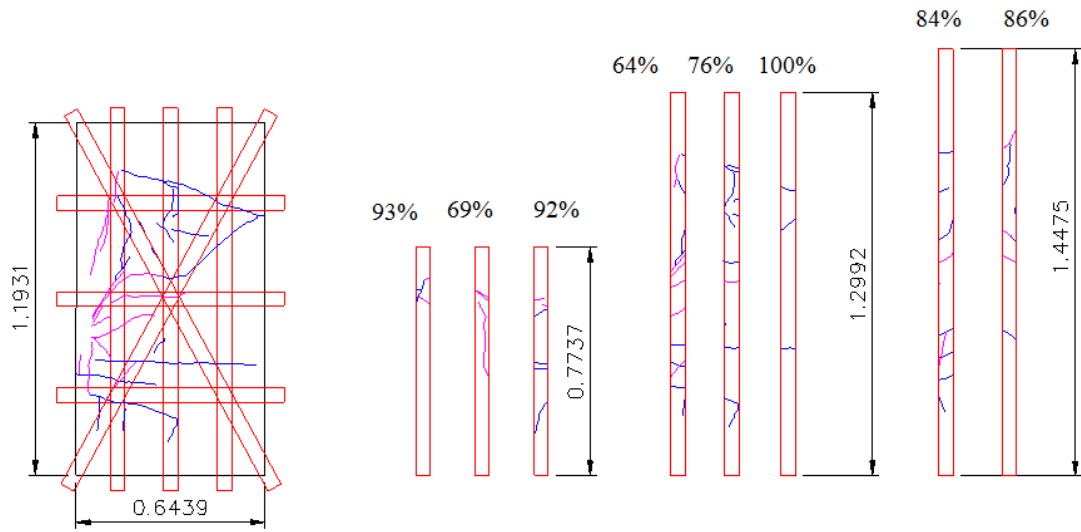
Natural



RQD = 87%

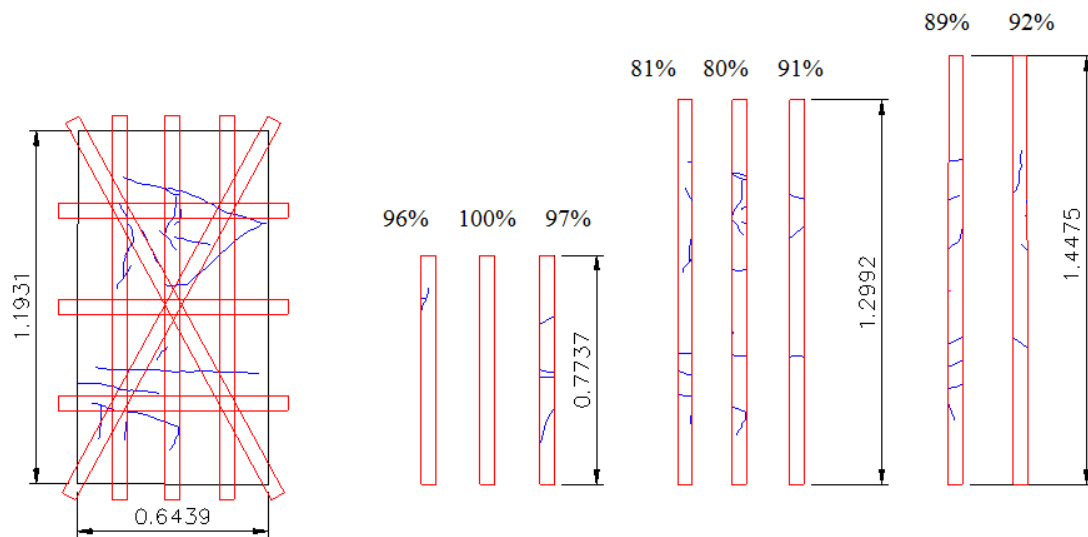
36B-08:

Combined natural and blast-induced



RQD = 83%

Natural



RQD = 91%

Appendix E: Conference Papers regarding Findings from SRM Approach

List of papers:

1. Martin, C. D., Lu, Y., and Lan, H. (2011). Scale effects in a synthetic rock mass. In Qian, Q. and Zhou, Y., editors, Proceedings 12th ISRM International Congress on Rock Mechanics, Beijing, volume CD-Rom, pages 1–6. Taylor & Francis Group, London, UK.
2. Lu, Y. C.D. Martin and H. Lan (2013) Strength of intact rock containing flaws. ARMA 13-175. In CD-ROM Proceedings of 47th US Rock Mechanics / Geomechanics Symposium held in San Francisco, CA, USA, 23-26, June 2013.
3. Martin, C. D., Yun Lu, Hengxing Lan & Rolf Christiansson (2013) Numerical Approaches for Estimating the Effect of Scale on Rock Mass Strength. In Proceedings 7th Nordic Grouting Symposium and 2nd Nordic Rock Mechanics Symposium, Gothenburg, Sweden. November 13-14, 2013.

Scale effects in a synthetic rock mass

C.D. Martin, Yun Lu & Hengxing Lan

Department of Civil & Environmental Engineering, University of Alberta, Edmonton, Canada

ABSTRACT: It is generally accepted in rock engineering that the strength of a rock mass decreases as the volume increases. There are two contributors to the rock mass strength: the strength of the intact rock, and the strength of the fractures. When creating a synthetic rock mass, the intact rock is first scaled to the volume of interest using published empirical scaling relationships. These intact-rock scaling laws are reviewed and it is shown that these scale effects are limited to 80% of the standard laboratory uniaxial compressive strength. The effect of fractures on rock mass strength is examined using model studies and numerical discrete element software. It is shown that rock mass strength decreases as the fracture intensity increases. However, the lower limit to this decrease is controlled by the orientation of a single through going fracture relative to the direction of loading, and not the fracture intensity.

Subject: Rock material and rock mass property testing (laboratory and in situ)

Keywords: lab testing, rock mass, rock properties, numerical modelling

1 INTRODUCTION

There are two contributors to rock mass strength: (1) the strength of the intact rock and (2) the strength of the fractures. The intact and fracture strengths can be measured in routine laboratory tests at small (typically centimetre) scales. Testing at larger scales is seldom practical and laboratory tests are replaced with empirical approaches such as the Geological Strength Index (Hoek, 1999). More recently, with the significant advances in computer modelling, there is a growing effort to replace the empirical approaches with a synthetic rock mass (SRM). The SRM utilizes a numerical modelling technique that combines discrete element modelling of intact rock with discrete planar fractures (Pierce et al. 2007). The discrete element modelling can utilize the bonded particle approach proposed by Potyondy and Cundall (2004) or the voronoi tessellation scheme used by Lan et al. (2010). The planar fractures are captured using a Discrete Fracture Network, a convenient method for geometrically describing the rock mass fractures (Rogers et al. 2009).

The first attempt to construct a SRM using the bonded particle model and a DFN for crystalline rock was described by Park et al. (2004). They showed that the SRM could be used to model both the intact rock and the fractured rock mass. They also showed a rock mass strength rapidly decreasing with increasing fracture density. In essence Park et al. (2004) demonstrated what is generally referred to as rock mass strength “scale effects”. However, Hoek and Brown (1980) also showed that the laboratory strength of intact rock is a function of scale. Hence when creating an SRM, what strength should be used to represent the intact rock?

In this paper the effect of scale on intact rock strength is reviewed and guidelines are proposed for selecting the intact rock strength for SRM simulations. The application of the SRM to date has been restricted to the rock types found in hard rock mines. These rocks are typically classed as low porosity rocks, i.e., porosity is less than 1% to 2% and frequently $\ll 1\%$. It is well known that as porosity increases other factors such as environmental effects can significantly

impact the intact strength. Therefore this review is limited to low porosity hard rocks.

2 SCALE EFFECTS: INTACT ROCK AND CONCRETE

The first step in creating a Synthetic Rock Mass is to calibrate the numerical intact rock properties to the laboratory properties. It is generally agreed that the volume tested does not significantly affect the deformation properties (Young’s modulus and Poisson’s ratio) of intact rock (Krmadibrata and Jones 1993). This is not surprising for low porosity rocks as long as the samples being tested are homogeneous and the sample size does not influence the test method. To minimize the effect of the sample size on the test results the ISRM “Suggested Methods for Determining the Uniaxial Compressive Strength and Deformability of Rock Materials states that the test specimen shall be right cylinders having a height to diameter ratio of 2.5–3.0 and a diameter preferably of not less than 54 mm.” The method then states that the diameter of the specimen should be greater than 10 times the largest grain in the rock (Brown, 1981).

Jackson and Lau (1990) carried out a series of uniaxial compressive tests on Lac du Bonnet granite. Their samples ranged from 33 mm to 294 mm with a height to diameter ratio 2, in order to test the 294 mm diameter samples. Sufficient testing was carried out by CANMET to establish that height to diameter ratio of 2 did not influence the results. Their tests were carried out using the procedures in the ISRM Suggested Methods. Samples were tested at each diameter to establish a mean and standard Deviation for the Young’s modulus. The tangent Young’s modulus values were taken at 50% of ultimate compressive strength as suggested by the ISRM Suggested Methods (Brown 1981). The results are shown in Figure 1, which clearly shows that the Young modulus values have a consistent mean value ranging from 60 to 62 GPa when the sample diameter is equal to or greater than 100 mm. Figure 1 also shows that sample diameters below 100 mm show an increasing Young’s Modulus with decreasing sample

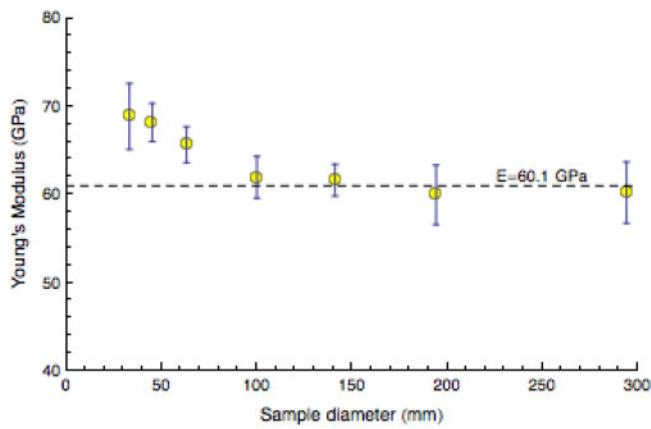


Figure 1. Effect of increasing sample diameter on Young's Modulus, data from Jackson and Lau (1990).

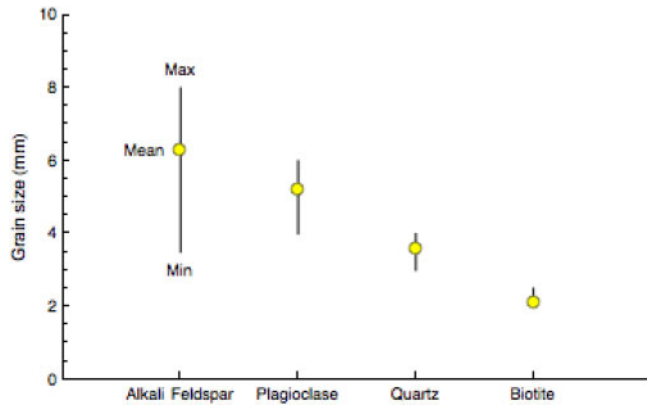


Figure 2. Grain size for the Lac du Bonnet granite samples tested by Jackson and Lau (1990).

diameter. The Lac du Bonnet granite is relatively homogeneous and hence one might conclude the results in Figure 1 show a scale effect.

The grain size of Lac du Bonnet granite was reported by Kelly et al. (1994). The results are summarized in Figure 2 and clearly show the heterogeneous nature of Lac du Bonnet granite at the grain scale. Using the grain size requirement specified by the ISRM Suggested Methods, i.e., diameter of the specimen should be greater than 10 times the largest grain, the minimum diameter of a sample that should be used to establish representative properties of Lac du Bonnet granite would be greater than 80 mm. Using this rule to analyse the results in Figure 1, one must conclude there is no scale effects for the Young's modulus. Similar conclusions have been given by Yoshinaka et al. (2008).

The reason for the rule that the diameter of the specimen should be greater than 10 times the largest grain is to create a relatively uniform stress distribution within the middle third of the sample being tested. Without this uniform stress distribution the results are not representative of the material but a combination of the material, test geometry and loading rate. While these issues do not have a significant effect on Young's modulus, the same is not true when establishing the laboratory ultimate strength.

Hudson et al. (1975) clearly showed the significant effect of specimen shape on uniaxial compressive strength, and these results led to the ISRM Suggested Method that specified the length to diameter ratio for the sample used to establish the

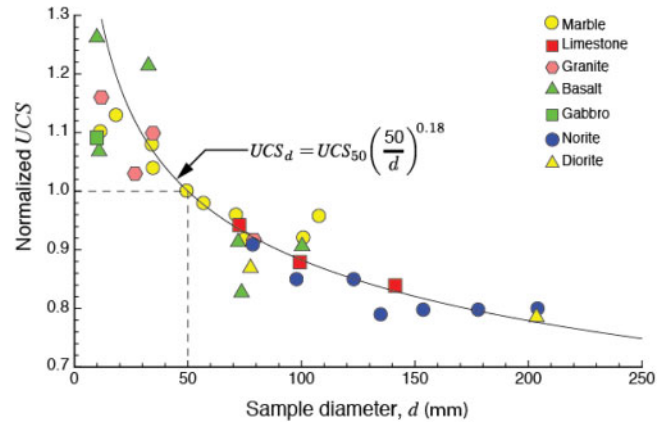


Figure 3. Effect of increasing diameter on the laboratory uniaxial compressive strength (UCS), data from Hoek and Brown (1980). The UCS has been normalized to the value obtained for 50-mm diameter.

uniaxial compressive strength (UCS) should be between 2.5 and 3. However, even if this ratio is preserved there is still a significant scale effect observed in laboratory UCS tests.

Hoek and Brown (1980) compiled the laboratory test results from high quality tests ranging in diameter from 10 mm to 200 mm diameter. Their results are summarized by rock type in Figure 3. Hoek and Brown (1980) presented their results normalized to the UCS for 50-mm-diameter core as that is a common core size and for many rocks would satisfy both testing criteria given by the ISRM. Hoek and Brown (1980) suggested that the observed scale effect in Figure 3 could be approximated by:

$$UCS_d = UCS_{50} \left(\frac{50}{d} \right)^{0.18} \quad (1)$$

Equation 1 is often used to establish the representative UCS strength when modelling intact rock using the Synthetic Rock Mass approach (Pierce et al. 2009). The volume involved in the synthetic rock mass calibration typically varies from 1 to 5 m³ depending on the size of the micro and macro fracture patterns that are being represented. Consequently, if Equation 1 is used to estimate the intact strength, the intact strength for the Synthetic Rock Mass starts at UCS values that are significantly less than the measured laboratory strengths.

Jackson and Lau (1990) investigated the effect of scale on the UCS values for samples of Lac du Bonnet granite ranging from 33 mm to 294 mm diameter. Unlike the Young's Modulus data, if the samples that are less than 50 mm diameters are removed the data still shows a noticeable scale effect (Figure 4). Jackson and Lau (1990) suggested that Equation 1 could also be used to model this observed UCS scale effect.

To the authors knowledge there are no tests results for intact hard rocks that have diameters greater than those used by Jackson and Lau (1990). Hence to explore the effect of larger diameters on the UCS, the data from concrete was also examined. Concrete has many of the same characteristics as hard rocks with the added advantage that the aggregate size and the sample size can be controlled.

The most extensive concrete testing program carried out to examine the effect of scale on uniaxial compressive was reported by Blanks and McNamara (1935). The tests were carried out by the Bureau of Reclamation as part of their mass concrete research for the Boulder dam (later named the Hoover

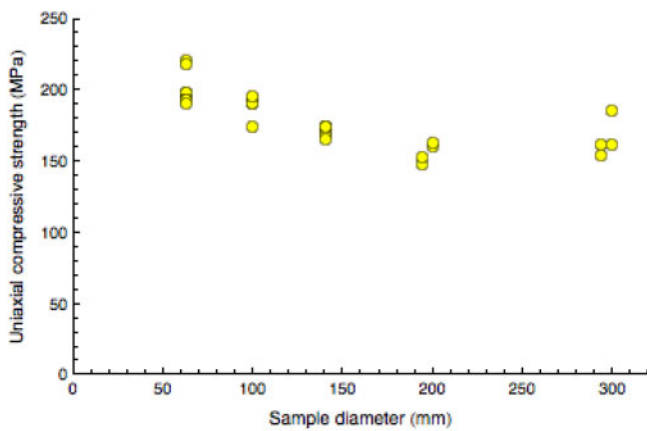


Figure 4. Uniaxial compressive strength for samples of Lac du bonnet granite, data from Jackson and Lau (1990).

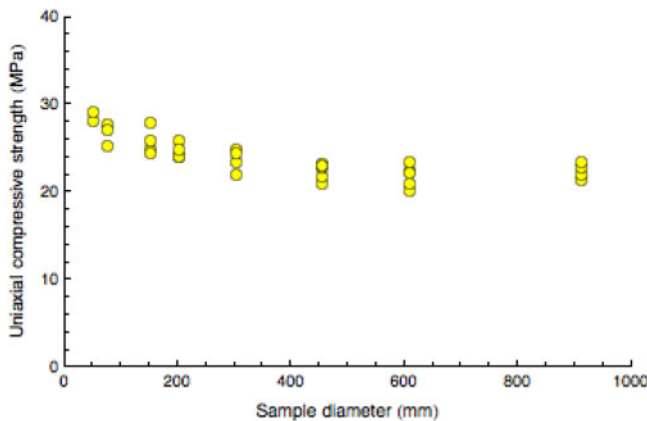


Figure 5. Effect of sample diameter on the uniaxial compressive strength of concrete, data from Blanks and McNamara (1935).

Dam). The tests varied in diameter from 50 mm to 914 mm with a length to diameter ratio of 2. The maximum aggregate size used for concrete mixes varied from 9.5 mm to 228.6 mm. The tests were used to determine the effect of various factors on compressive strength and Young's Modulus.

Blanks and McNamara (1935) concluded from their extensive testing program that:

- “The strength of the concrete decreases as the size of specimen is increased. The average relative strengths were found to be 100 per cent for 152 mm., 108 per cent for 51 mm and 84 per cent for 914 mm diameter cylinders.
- The elastic properties of concretes are not affected by the size of test cylinder.
- For consistent results, the diameter of the test cylinder should be equal to or greater than four times the maximum size of aggregate included in the concrete to be tested.”

The results from Jackson and Lau (1990) and those from Blanks and McNamara (1935) reinforce the recommendation by the ISRM that for consistent results the grain size of the intact material must be considered in determining the minimum test diameter for establishing consistent compressive strengths. The data from all the tests results discussed thus far are summarized in Figure 6. The uniaxial compressive strength and the diameters in Figure 6 have been normalized to the UCS and diameter that are considered representative of the material tested in order to compile the data on a single plot. The data

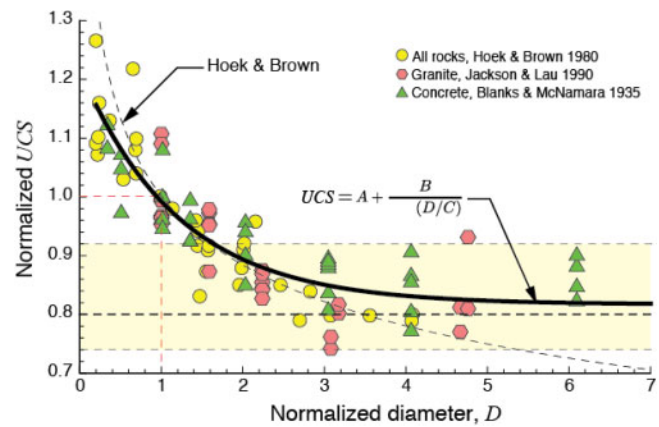


Figure 6. Summary of UCS data, normalized to the minimum representative diameter, (Hoek & Brown = 50 mm, Jackson & Lau = 63 mm and Blanks & McNamara = 152 mm).

in Figure 6 shows a marked scale effect for normalized diameter less than approximately 3 but that there is no scale effect when the sample diameter is at least 3 times the representative diameter. The Hoek-Brown Equation 1 was also normalized and, as shown in Figure 6, provides a reasonable fit to the data showing the scale effect. However the Hoek-Brown equation significantly under-predicts the strength for normalized diameter greater than 3, where the data shows no scale effect. A better fit to the normalized data can be obtained using:

$$UCS = A + \left(\frac{B}{\text{Exp} \left(\frac{D}{C} \right)} \right) \quad (2)$$

where $A = 0.81$, $B = 0.4$, $C = 1.21$ and D is the normalized diameter. Equation 2 illustrates that the reduction in UCS due to scale effects is limited to 0.8 of the representative laboratory UCS determined for the intact material. This value of 0.8 is also consistent with the original data from Hoek and Brown (1980); see Figure 3. Laubscher and Jakubec (2001) also suggested that the strength of a homogenous rock block should be reduced to 80% of the of laboratory tests to account for the small to large specimen effect.

The notion that all three data sets indicate that the uniaxial compressive strength should be reduced to 80% of the representative laboratory strength to obtain a large-scale or operational strength may appear fortuitous. Determining the operational strength of bonded geomaterials is a major challenge in geotechnical engineering. Peak and residual strength are customarily obtained from traditional laboratory tests for such purpose. However, bonded geomaterials also display marked changes in their behaviour before reaching the laboratory peak strength. Careful inspection of laboratory stress-strain curves, based on local strain measurements, acoustic emissions, and imaging techniques show that for a wide spectrum of geomaterials, the onset of strain localization begins well before peak strength is achieved. The onset of stain localization can be readily determined using the volumetric strain data from standard laboratory tests (Figure 7).

Abdelaziz et al. (2005) examined the laboratory stress-strain curves based on local and global strain measurements for a wide spectrum of geomaterials. In all cases the onset of strain localization determined by volumetric strain reversal from the stress-strain data was confirmed by additional

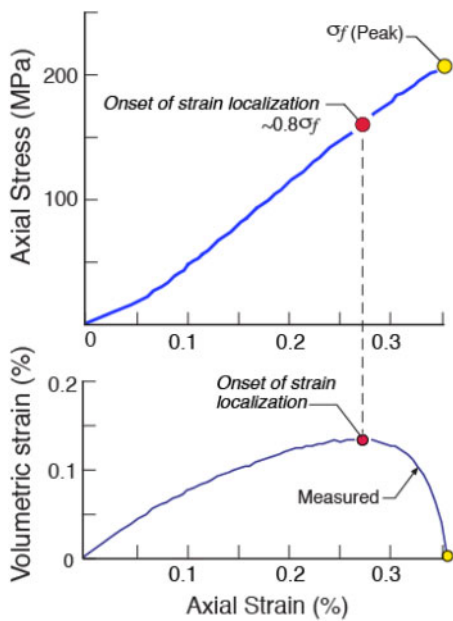


Figure 7. Typical stress-strain response for granite measured in laboratory tests and the onset of strain localization based on the change in the volumetric strain.

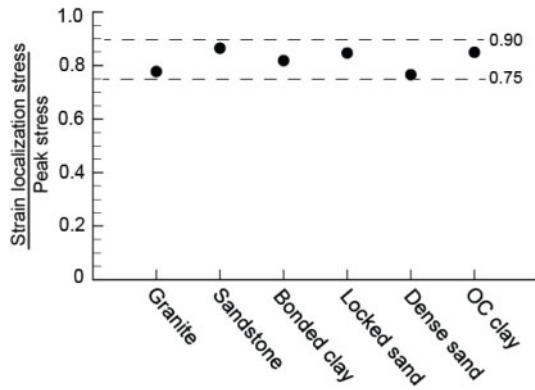


Figure 8. Stress associated with the onset of strain localization in various soils and rocks, normalized to peak stress. The onset of strain localization was determined using the volumetric strain, data from Abdelaziz et al. 2005.

techniques such as acoustic emission monitoring and imaging analyses. In most cases the onset of strain localization was found to be an excellent indicator of the initiation of shear band formation. The acoustic emission monitoring and the image analyses also showed the progressive development of the shear bands from the onset of strain localization through peak and into the post peak region. Abdelaziz et al. (2005) examined a range of soils and rocks and concluded that the onset of strain localization ranged between 0.76 and 0.86 when normalized to the peak strength (Figure 8). They suggested that the operational strength for such soils and rocks was not the laboratory peak strength as is typically assumed but the onset of strain localization that can be easily defined by examining the volumetric strain, see Figure 7. Desayi and Viswanatha (1967) assessed various methods to establish “true ultimate strength” of concrete and concluded that volumetric strain provided a reliable estimate, and the “true ultimate strength” was 77 to 85% of the measured compressive strength.

Recent studies have shown that the scale effects observed in concrete testing can be explained by considering the effect

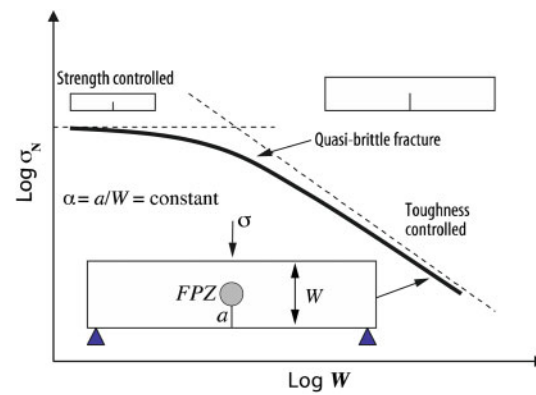


Figure 9. Scale Effect for geometrically similar specimens ($\alpha = a/W = \text{constant}$) in concrete testing, modified from Hu and Duan (2008).

of the size of the strain localization, i.e., fracture process zone (FPZ) relative to the sample boundary (Figure 9). Hu and Duan (2008) showed that the “scale-dependent” quasi-brittle fracture transition shown in Figure 9 is actually due to the interaction of FPZ with the nearest boundary and therefore the scale effects reflect the FPZ/boundary interaction. Hu and Duan (2008) concluded that in order to remove the scale effects ($W - a \geq 10a_{FPZ}$). Hence if this approach was applied to the compressive testing of rock, the minimum sample diameter that would remove the observed scale effects in Figure 6 would be based on the size of the strain localization zone and not the grain size of the material, discussed previously. The size of the strain localization zone in rocks has not been measured but it would certainly involve more than a single grain. Inspection of Figure 6 would suggest that a sample size that is 3 times what it considered “normal testing size” would be required to remove the interaction of the strain localization zone with the sample boundary.

The test results presented in this section clearly demonstrate that the scale effects in intact rock are relatively minor and caused by the sample test size, and not a material property. A reasonable lower bound estimate for the intact strength using laboratory test results based on traditional sample diameters of 50 to 63 mm, is 80% of the UCS. This assumes that the intact rock is homogeneous. If the sample contains micro-defects, such as filled veins, the rock strength may decrease to less than 80% of the UCS. This aspect or rock mass strength is explored in the next section.

3 EFFECT OF STRUCTURE ON ROCK STRENGTH

The structure in a rock mass can occur at several scales: (1) centimetre scale where the micro-defects are healed with infilling that is usually weaker than the intact rock (Figure 10) and (2) metre-scale where the fractures generally lack infilling and are classed as open. In the synthetic rock mass, the rock fractures are described using the geometrical descriptions associated with the Discrete Fracture Network (DFN). Rogers et al. (2007) provided an overview of the essential elements used in developing a DFN for a rock mass. The fracture intensity description in a DFN is given by:

1. P_{10} = No of fractures per unit length, #/m
2. P_{21} = Trace length of fractures per unit area, m/m²
3. P_{32} = Area of fractures per unit volume, m²/m³



Figure 10. Example of micro-defects in 51 mm core diameter.

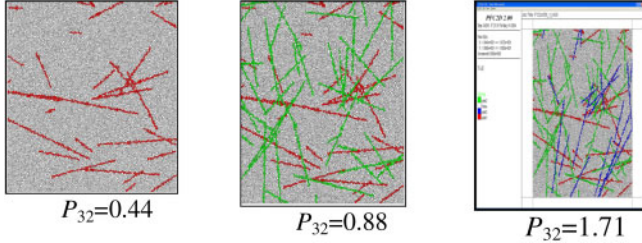


Figure 11. The rock mass model with fracture traces in PFC2D, data from Park et al. (2004).

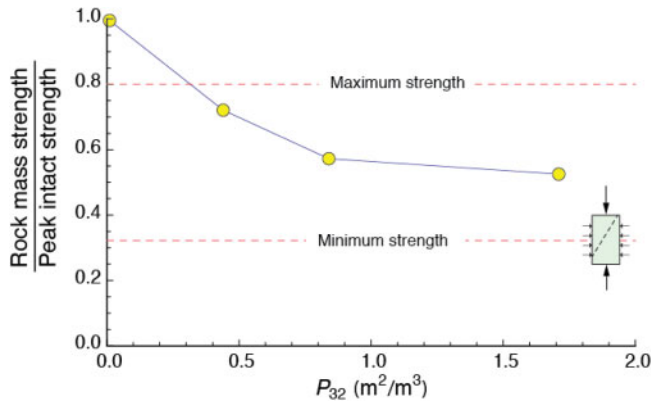


Figure 12. Effect of fracture intensity on rock mass strength.

The rock mass at the Äspö Hard Rock Laboratory (HRL), Sweden, is typical of the granitic rock masses found in the Scandinavian Shield. It contains several joint sets that vary in both trace length and fracture frequency. A discrete fracture network (DFN) model was developed for the Äspö HRL and the three fracture sets with their fracture intensity values (expressed as P_{32}) are provided in Figure 11.

Park et al. (2004) modelled the fractures in Figure 11 using the Particle Flow Code software to examine their effect on rock mass strength. In their modelling the fracture sets were incrementally added to assess the effect of each fracture set on rock mass strength. The results from their modelling are provided in Figure 12 as a function of fracture intensity, and show that as the fracture intensity increases the rock mass strength decreases. If the rock mass was intact the expected maximum strength reduction using the results from Figure 6 would be 80% of the peak strength. According to Jaeger et al. (2007) the minimum strength of a single through-going fracture in compression can be estimated from:

$$\sigma_1 = \sigma_3 + \frac{\lambda(c + \sigma_3 \tan \phi)}{(1 - \tan \phi \cot(90 - \beta)) \sin 2(90 - \beta)} \quad (3)$$

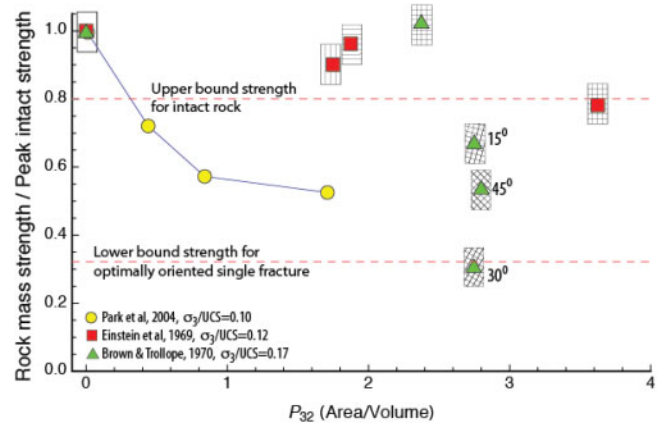


Figure 13. Effect of fracture intensity and fracture orientation on confined rock mass strength.

where β is the angle between σ_1 and the fracture plane. This strength provided by Equation 3, which is considered a lower bound strength, is also shown Figure 12.

Brown and Trollope (1970) and Einstein et al. (1969) conducted a number of physical model tests to establish the effect of fractures on rock mass strength. Their tests were carried out using a plaster model with continuous fracture planes. The results from their model studies are shown in Figure 13 along with the results from Figure 12. The fracture intensity in Figure 13 is expressed as fracture area per unit volume. For the model tests the volume of each test is considered the unit volume. The results in Figure 13 show that regardless of the fracture intensity, the persistence of a single fracture can reduce the strength of the rock mass to its lower bound strength.

4 CONCLUSIONS

Laboratory results were used in conjunction with physical and numerical model results to examine (1) the strength of the intact rock and (2) the strength of a fractured rock mass. The findings suggest that scale effects in intact rock are limited to 80% of the standard laboratory uniaxial compressive strength. The physical and numerical modelling results suggest that the rock mass strength decreases as the fracture intensity, expressed as fracture area per unit volume, increases. However, the lower limit to this decrease is controlled by the fracture orientation and persistence, regardless of the fracture intensity. Hence fracture intensity alone may not be an adequate parameter when estimating rock mass strength using discrete fracture networks.

ACKNOWLEDGEMENTS

The authors wish to acknowledge the contributions from the Swedish Nuclear Fuel and Waste Management Co. (SKB, Stockholm) and the Decovalex Project (Decovalex 2011). The support of the Natural Sciences and Engineering Council of Canada, One Hundred Talents Program of Chinese Academy of Sciences, and National Key Technology R&D Program of China (2008BAK50B05) are also acknowledged.

REFERENCES

- Abdelaziz, T., Martin, C. D. and Chalaturnyk, R. 2005. The onset of dilation in soils and rocks. In *Proc. 58th Canadian Geotechnical Conference & 6th Joint CGS & IAH-CNC Groundwater Specialty Conference*, Saskatoon, September 18–21, volume 1, pages 319–325.
- Blanks, R. and McNamara, C. 1935. Mass concrete tests in large cylinders. *ACI Journal Proceedings*, 31(1):280–303.
- Brown, E. T., editor (1981). *Rock Characterization, Testing and Monitoring, ISRM Suggested Methods*. Pergamon Press, Oxford.
- Brown, E. T. and Trollope, D. H. 1970. Strength of a model of jointed rock. *ASCE Journal of the Soil Mechanics and Foundations Division*, 96(2):685–704.
- Desayi, P. and Viswanatha, C. S. 1967. True ultimate strength of plain concrete. *Bulletin RILEM* 36:163–173
- Einstein, H. H., Nelson, R. A., Bruhn, R. W. and Hirschfeld, R. C. 1969. Model studies of jointed-rock behaviour. In *Proceedings 11th U.S. Symposium on Rock Mechanics*, Berkeley, pages 83–103.
- Hoek, E. 1999. The Second Glossop Lecture: Putting numbers to geology – an engineer’s viewpoint. *Quarterly Journal of Engineering Geology*, 32:1–19.
- Hoek, E. and Brown, E. T. 1980. *Underground Excavations in Rock*. The Institution of Mining and Metallurgy, London.
- Hu, X. and Duan, K. 2008. Size effect and quasi-brittle fracture: the role of FPZ. *International Journal of Fracture*. 154(1):3–14
- Hudson, J. A., Brown, E. T., and Fairhurst, C. (1972). Shape of the complete stress-strain curve for rock. In Cording, E., editor, *Proc. 13th U.S. Symp. on Rock Mechanics*, Urbana, pages 773–795, New York. American Society of Civil Engineers.
- Jackson, R. and Lau, J. S. O. (1990). The effect of specimen size on the mechanical properties of Lac du Bonnet grey granite. In da Cunha, A. P., editor, *Proc. 1st. Int. Workshop on Scale Effects in Rock Masses*, Loen, Norway, pages 165–174. A.A. Balkema, Rotterdam.
- Jaeger, J. C., Cook, N. G. W., and Zimmerman, R. 2007. *Fundamentals of Rock Mechanics*. Blackwell Publishing Limited, London, fourth edition.
- Krmdibrata, S. and Jones, I. O. 1993. Size effect on strength and deformability of brittle intact rock. In Cunha, P., editor, *Proceedings Scale Effect in Rock Masses*, pages 277–284. A.A. Balkema, Rotterdam.
- Kelly, D. D., Peck, D. C., and James, R. S. 1994. Petrography of granite rock samples from the 420 Level of the Underground Research Laboratory, Pinawa, Manitoba. Contract report for AECL, Laurentian University, Sudbury, Canada.
- Lan, H., Martin, C. D., and Hu, B. 2010. Effect of heterogeneity of brittle rock on micromechanical extensile behavior during compression loading. *Journal Geophysical Research*, 115:B01202, 1–14.
- Laubscher, D. H. & Jakubec, J. 2001. The MRMR Rock Mass Classification for Jointed Rock Masses. In *Underground Mining Methods: Engineering Fundamentals and International Case Studies*, pp 475–481, Society of Mining Metallurgy and Exploration, SMME.
- Park, E-S., Martin, C. D., and Christiansson, R. 2004. Simulation of the mechanical behavior of discontinuous rock masses using a bonded-particle model. In Yale, D. P., Willson, S. M., and Abou-Sayed, A. S., editors, *CD-ROM Proc. 6th North American Rock Mechanics Symposium – NARMS04*, Houston, pages 1–8. NARMS 04–480.
- Pierce, M. E., Gaida, M., and DeGagne, D. 2009. Estimation of rock block strength. In Diederichs, M. and Grasselli, G., editors, *CD-ROM Proceedings 3rd CANUS Rock Mechanics Symposium*, Toronto, page Paper 4360.
- Pierce, M., Mas Ivars, D., Cundall, P. A., and Potyondy, D. O. 2007. A synthetic rock mass model for jointed rock. In Eberhardt, E., Stead, D., and Morrison, T., editors, *Proceedings 1st Canada-US Rock Mechanics Symposium*, Vancouver, volume 1, pages 341–349. Taylor & Francis Group, London.
- Potyondy, D. O. and Cundall, P. A. 2004. A bonded-particle model for rock. *International Journal Rock Mechanics and Mining Science*, 41(8):1329–1364.
- Rogers, S., Elmo, D., Beddoes, R., and Dershowitz, W. 2009. Mine scale DFN modelling and rapid upscaling in geomechanical simulations of large open pits. In *In CD-ROM Proceedings of International Conference on Slope Stability*, Santiago Chile, pages 1–9.
- Yoshinaka, R., Osada, M., Park, H., Sasaki, T., and Sasaki, K. 2008. Practical determination of mechanical design parameters of intact rock considering scale effect. *Engineering Geology*, 96(3–4): 173–186.

Strength of intact rock containing flaws

Yun Lu, C. Derek Martin, Hengxing Lan

Dept. of Civil and Environmental Engineering, University of Alberta, Edmonton, AB, Canada

Copyright 2013 ARMA, American Rock Mechanics Association

This paper was prepared for presentation at the 47th US Rock Mechanics / Geomechanics Symposium held in San Francisco, CA, USA, 23-26 June 2013.

This paper was selected for presentation at the symposium by an ARMA Technical Program Committee based on a technical and critical review of the paper by a minimum of two technical reviewers. The material, as presented, does not necessarily reflect any position of ARMA, its officers, or members. Electronic reproduction, distribution, or storage of any part of this paper for commercial purposes without the written consent of ARMA is prohibited. Permission to reproduce in print is restricted to an abstract of not more than 200 words; illustrations may not be copied. The abstract must contain conspicuous acknowledgement of where and by whom the paper was presented.

- **ABSTRACT:** There are two contributors to rock mass strength: (1) the strength of the intact rock and (2) the strength of the fractures or flaws. The flaws in a rock can occur at several scales: (1) centimetre scale where the micro-defects are healed with infilling that is usually weaker than the intact rock and (2) metre-scale where the fractures generally lack infilling and are classed as open. A number of numerical simulations were used in this study to establish the effect of flaws on uniaxial rock strength. The flaw arrangements varied from (1) a single flaw at various orientations relative to the applied load; (2) uniformly distributed discontinuous flaws, and (3) randomly distributed discontinuous flaws. For uniformly distributed discontinuous flaws the distance of the flaw to the free boundary plays a significant role in the uniaxial strength. And, for randomly distributed discontinuous flaws, the uniaxial strength decreases as the fracture intensity, expressed as P_{21} , increases. There appears to be a threshold fracture intensity where the strength rapidly decreases but this threshold value is non-unique but related to flaw length.

1. INTRODUCTION

A rock mass is typically described using the geometry and properties of the planes of weakness and the properties of the intact rock units. Jaeger [1] clearly showed that an optimally oriented through going single plane of weakness in otherwise intact rock controlled the strength of the rock mass. Jaeger, also illustrated that the intact strength was recovered once the orientation of the plane was at a large angle to the applied load. Those early studies by Jaeger and others highlighted that the strength variation in a rock mass was directly related to the distribution of flaws in the intact rocks, their orientation and shear strength. The upper and lower bounds for the rock mass strength are readily determined when dealing with simple geometries such as a discrete plane. However this simplicity of rock mass strength is lost when the flaws take on more complex distributions and lack the through-going nature of Jaeger's model.

We use a numerical approach for estimating the strength of intact rock based on the discrete element formulation. Flaws with varying intensities are introduced into the discrete element formulation to examine the effect of these flaws on the intact strengths. Various flaw arrangements are used varying from a single flaw at different orientations, regularly distributed flaws and randomly distributed flaws. In this paper, we summarize the results from these numerical models and examine the fundamental parameters that influence the strength of intact rock containing discontinuous flaws.

2. GRAIN BASED MODEL

At the grain-scale most intact rocks consist of a variety of mineral grains at different sizes. Mineral grains and associated contacts are two microstructural elements. These features give rise to several types of microscopic heterogeneity: geometric heterogeneity resulting from angular shape and grain size, elastic heterogeneity due to the stiffness contrast of different grains, and contact heterogeneity resulting from the anisotropy of contact distributions (length and orientation) and stiffness anisotropy. Potyondy and Cundall [2] introduced a numerical approach for modeling intact rock that captured many of these heterogeneities. Their Bonded Particle Model (BPM) used disk-shape particles bonded together at their contacts. A significant shortcoming of this approach was identified by Cho et al. [3, 4]. They proposed that these shortcomings could be overcome by introducing a clumping technique that captured the particle grain geometry. By simply capturing the geometry of the mineral grains, the clumped-BPM approach captured all aspects of intact rock failure observed in laboratory tests, i.e., correct tensile to compressive strength ratio, a nonlinear failure envelope and appropriate stress-strain response. More recently Lan et al. [5] introduced the grain-based model based on the discrete element formulation used in the Universal Distinct Element Code (UDEC). A limitation of this grain-based approach is that the grains are unbreakable and hence damage is along grain boundaries. The grains can be made to yield using an appropriate constitutive

model and failure criterion. However in most case assessing the peak strength is adequate and the non-breakable grains has little influence on peak strength.

The grain-based model (GBM) has a capability of dealing with a composition of multiple minerals to simulate the heterogeneous grain structure. The mineral grains are created using polygonal blocks based on a voronoi tessellation scheme. This tessellation scheme is created outside the UDEC program to generate a grain size distribution that matches the grain size distribution

of the intact rocks (Lan et al. [5]). As with all discrete element formulations used to simulate intact rock, a calibration process is required to find the model parameters that match the laboratory properties. The properties of the grain contacts play a more important role in controlling macroscopic mechanical behaviors of the intact rock. A detailed procedure regarding modeling and generation of a model in grain scale is shown in the flow chart in Figure 1 (left). Figure 1 (right) illustrates the geometric model and the distribution of the voronoi tessellation that mimics the mineral grains.

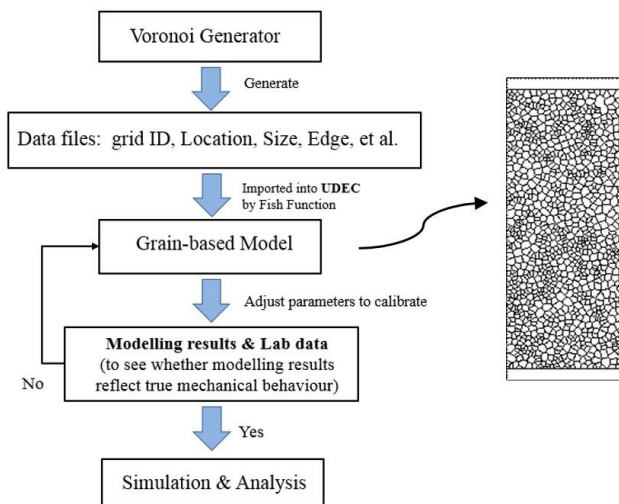


Fig. 1. Illustration of generation of grain-based model combined with voronoi tessellation and a flow chart presenting the procedure of numerical modeling including data import and parameter calibration.

The laboratory properties of Lac du Bonnet (LdB) granite have been extensively characterized and reported (Martin & Chandler [6], Eberhardt et al. [7]; Lau and Chandler [8]). In addition to the traditional laboratory testing, extensive work was also carried out by Jackson and Lau [9] to establish the effect of scale on these laboratory properties. The grains of LdB granite is composed of four major mineral: plagioclase, K-feldspar, quartz and biotite. They account for over 90% of mineral composition of LdB granite. The material properties and mineral compositions are shown in the percentage of total grains representing the grain size distribution in Table 1.

Table 1. Mineral composition of LdB granite and properties of four major grains (from Lan et al. [5])

Grain Type (%)	Unit weight (N/m ³)	Young's Modulus (GPa)	Bulk/Shear Modulus K,G (GPa)	Poisson's ratio
K-feldspar (47.6%)	2580	69.7	53.7, 27.2	0.31
Plagioclase (10.8%)	2680	80.4	50.8, 29.3	0.30
Quartz (33.1%)	2620	95.6	37, 44	0.08
Biotite (7.8%)	3090	88.1	41.1, 12.4	0.25

It is well know that grain size distribution and the size of mineral grains can influence rock strength (Fredrich et al. [10]; Berbenni et al. [11]). In order to reflect the micro-geometric heterogeneity due to various mineral sizes and their distribution, the grain-based model is created using the mean grain size of the four minerals in Table 1 (see Fig. 2). In addition to the mean grain sizes the distribution of the grain sizes is expressed using the sorting coefficient (S_0) developed by Trask [12] which describes the distribution of grain sizes and the degree of sorting. S_0 is defined as:

$$S_0 = \sqrt{Q_1/Q_2} \quad (1)$$

where Q_1 is the diameter that has 75% of the cumulative size-frequency (by weight) distribution smaller than itself and 25% larger than itself, and Q_2 is that diameter having 25% of the distribution smaller and 75% larger than itself. As the sorting coefficient approaches 1, the grain size distribution becomes more uniform. The mean grain size of the four main mineral grains of LdB granite and their cumulative frequency are illustrated in Figure 2.

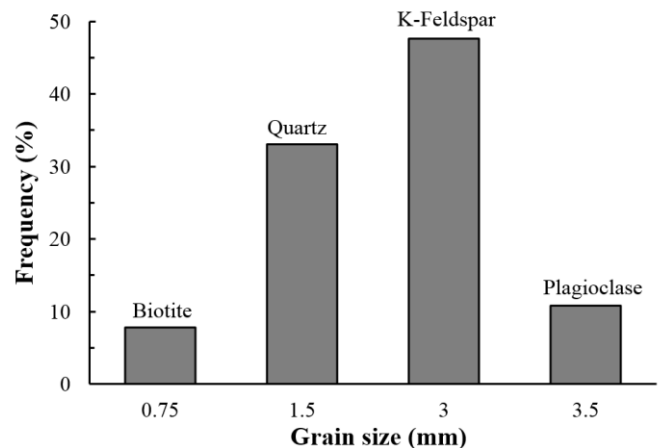


Fig. 2. Mean grain size of four representative minerals for LdB granite (From Kelly et al. [13]).

The minimum and maximum grain size distribution for LdB granite was established by Kelly et al. [13] and illustrated in Figure 3. A grain-based model with a S_0 equal to 1.25 was created using the mean grain size for each mineral and the voronoi generator. This grain size distribution formed the bases of all the grain-based modeling discussed in the following sections.

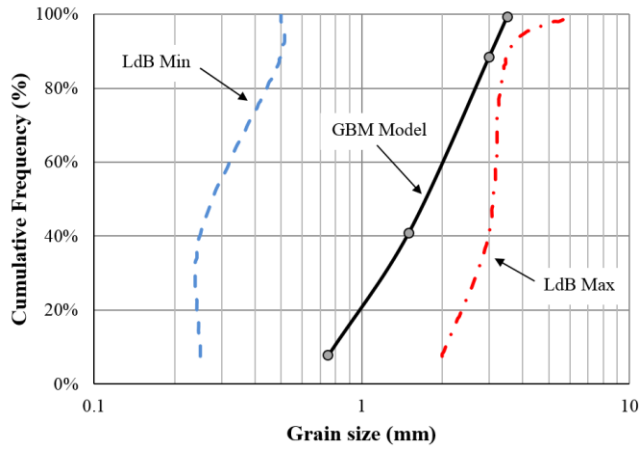


Fig. 3. Grain size distributions of LdB granite. (modified from Lan et al. [5] using data from Kelly et al. [13])

3. SINGLE FLAW

The effect of through-going weak planes has been examined by many researchers since the pioneering work of Donath [14]. The strength of the intact rock and the shear strength of the single discrete flaws can be measured in the laboratory using well-established testing procedures. In this section, the relationship between the rock strength and a single through-going flaw is examined using the grain based model and compared to laboratory test results

The strength of a through going plane was examined by Jaeger [1]. According to Brady and Brown [15], the principal stress σ_1 required to produce slip can be expressed as:

$$\sigma_1 \geq \sigma_3 + \frac{2(c + \sigma_3 \tan \phi)}{(1 - \tan \phi \cot \beta) \sin 2\beta} \quad (2)$$

where c, ϕ are the Mohr-Coulomb shear strength parameters cohesion and friction angle, respectively. The other parameters in Equation 2 are defined in Figure 4.

For those combinations of c, ϕ, σ_1 and β for which the inequality of equation above is not satisfied, slip on the plane cannot occur and the only alternative is fracture of the intact rock independent of the presence of the discontinuity. Figure 4 shows the occurrence of slip as a function of β .

Laboratory tests were carried out by Roy [16] and Teja [17] to examine the effect of a through-going flaw on the uniaxial compressive rock strength of 38 mm-diameter samples. Their tests used plaster of Paris to create a

single through-going flaw illustrated in Figure 4. The orientations of the flaws ranged from $0^\circ - 90^\circ$. The results from their experiments are given in Figure 5 and are in general agreement with the theoretical strength illustrated in Figure 4.

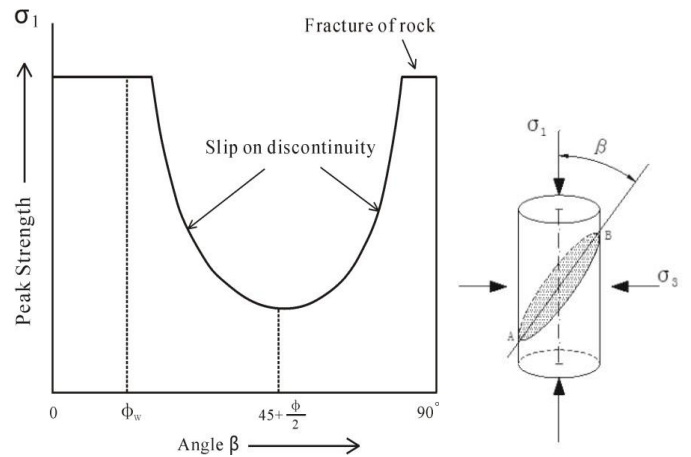


Fig. 4. Variation of the peak strength of rock with a weak plane inclined at different angle of β (From Hoek and Brown [18]).

The grain-based UDEC model was used to simulate the laboratory experiments carried out by Roy [16] and Teja [17]. The models were 50 mm wide and 125 mm high and are described in Table 2. However in this case, the grain-based model utilized the properties for Lac du Bonnet granite instead of the plaster of Paris used by Roy [16] and Teja [17]. The results from the grain-based UDEC model are also presented in Figure 5. All the uniaxial compressive strengths in Figure 5 are normalized to the intact uniaxial compressive strength. The results from the GBM are in reasonable agreement with the laboratory test results.

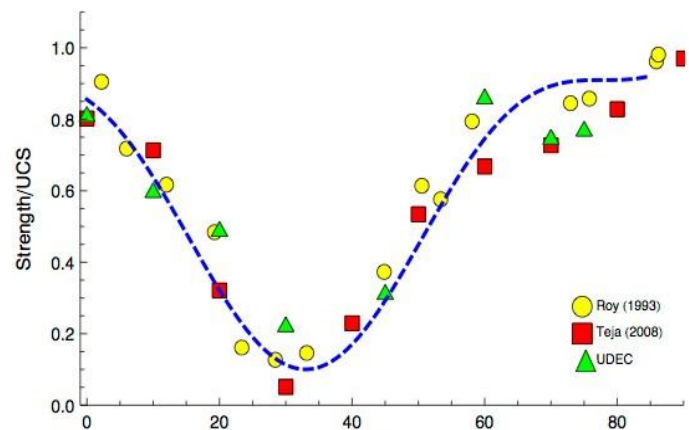
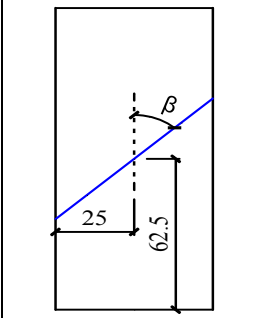


Fig. 5. Laboratory test results compared to the grain-based model results for samples containing a single through-going flaw inclined at various angles (β) relative to the uniaxial applied load. The dashed line is given by Equation 3.

Table 2. The configuration of sample and UCS test results of grain-based UDEC models with a through-going single flow.

Test Description	Dimensions (mm)	UCS (MPa)
one through-going flow dipping at various angles: (a. 0°; b. 10°; c. 20°; d. 30°; e. 45°; f. 60°; g. 70°; h. 75°). The flaw is centered in the middle of the sample.		a=187 b=152 c=84 d=29 e=69 f=164 g=179 h=186

The relationship between the strength and angle β in Figure 5 can be expressed as a continuous function given by:

$$S_i = A + B[\cos 2(\beta - \beta_{\min})]^n \quad (3)$$

where A , B and n are constants; β_{\min} is the value of β corresponding to minima in S_i . The dashed line in Figure 5 has $A=0.91$, $B=0.81$, $\beta_{\min}=33$ and $n=3$.

4. UNIFORMLY DISTRIBUTED FLAWS

The previous section established that the grain-based modeling approach was suitable for investigating the effect of a single flaw on rock strength. The most challenging situation encountered in rock engineering is establishing the rock mass strength when the flaws are discontinuous. Two general situations are investigated in this section: (1) discontinuous parallel flaws inclined at 45° in the center domain of the sample, and (2) discontinuous regularly distributed and uniformly spaced vertical flaws.

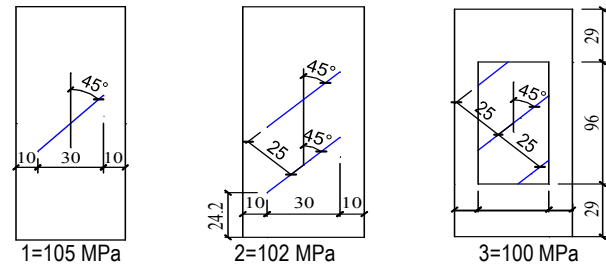
In the grain-based model when the grain-boundary contacts representing intact rock reach their peak strength, a residual strength models is used to capture the brittle nature of grain boundary fracture. Once the tensile or shear strength reaches the internal flag set for each grain contact strength, residual strength value is assigned to the ruptured contact, which creates an associated stress redistribution. While this creates long run times, the process is considered representative of compressive loading of intact rocks. (Lan et al. [5])

4.1. Discontinuous parallel inclined flaws

Multiple flaws fully penetrating the sample would result in a dramatic decrease of strength. To avoid this condition the flaws are contained within a region 30mm wide and 96mm height. This means that the flaws are 10mm away from the free boundary and failure must occur through intact rock (Table 3). The uniaxial strength from the three models tested is also summarized in Table 3. From Table 3, we can see that all three

models have very similar strength values although the numbers of flaws in the rock increase from one to three.

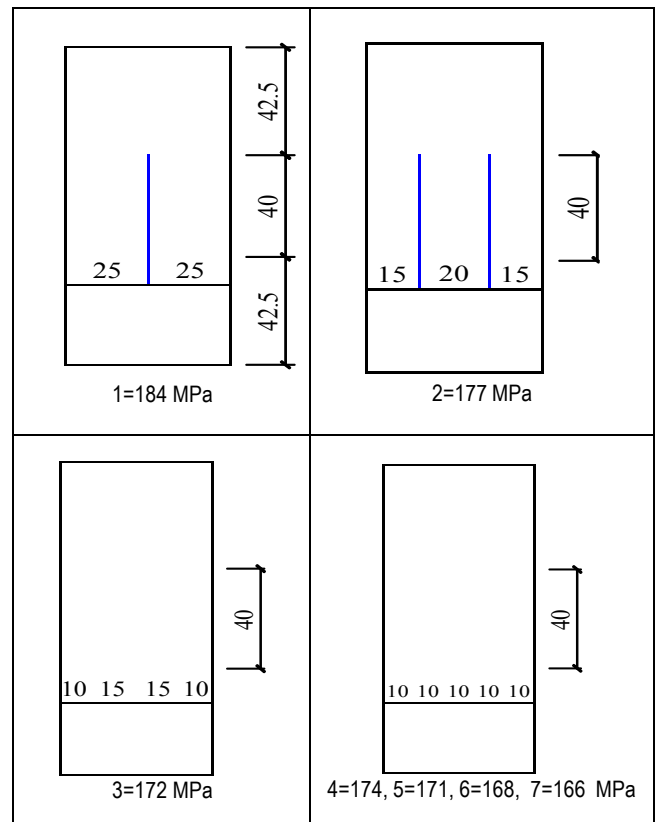
Table 3. Test configuration and results for samples with inclined discontinuous flaws.



4.2. Discontinuous parallel vertical flaws

As discussed previously the inclined flaws create an obvious anisotropic influence on the rock strength. In this section, all the flaws are vertical in order to evaluate the effect of the number of flaws and flaw spacing on uniaxial strength. The samples were created with the number of vertical flaws ranging from 1 to 7 (Table 4). This means that the spacing between the flaws varies from 10 mm to 20 mm. The length of each flaw was limited to 40 mm and located in the middle 1/3 of the sample. Table 4 shows a general configuration of the model with the discontinuous vertical flaws.

Table 4. Test configuration and uniaxial strength for samples with discontinuous vertical flaws.



The uniaxial strength for the sample conditions in Table 4 normalized to the intact strength is plotted in Figure 6a as a function of the number of flaws. Figure 6a, clearly shows the reduction in uniaxial strength from 0.83 to 0.75 as the number of flaws increases from one to four, respectively. When there are more than four flaws in the model, the strength reduction becomes more scattered with the highest variability occurring when the number of flaws reaches 6 or 7. Especially when the spacing of flaws is separated evenly in the middle of the model, the strength will drop dramatically (Point c, d in Figure 6a).

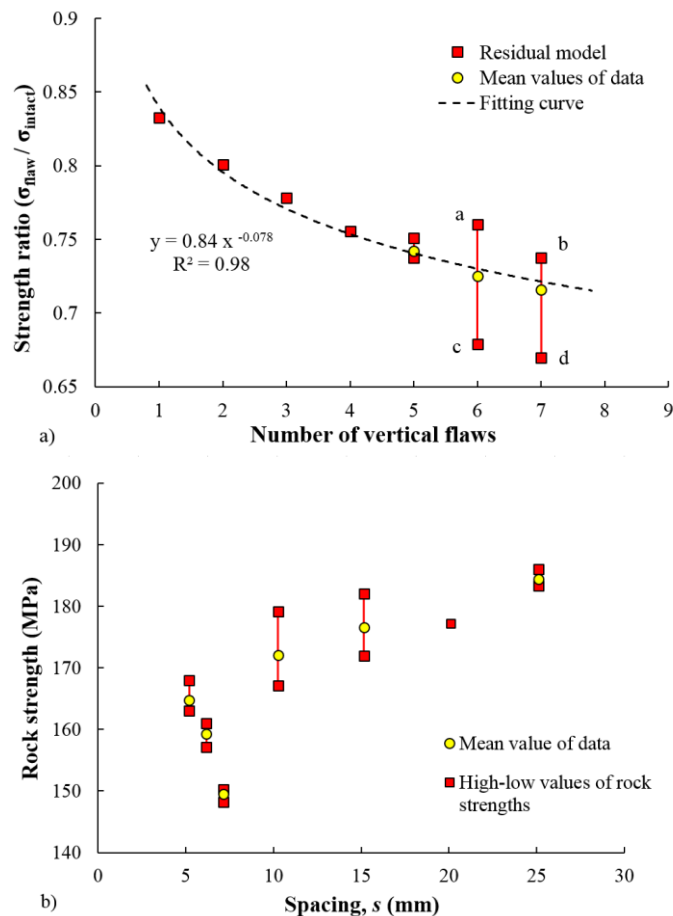


Fig. 6. The illustrations of two influence factors regarding rock strength. a) The effect of number of flaws on the rock strength. b) Spacing effect (the range of strength is plotted in terms of same spacing value but different number of flaws)

Figure 6b, shows the results for the uniaxial strength for the samples in Table 4 as a function of spacing between the flaws. There is a clear increase in strength with flaw spacing when the spacing exceeds 10 mm. However, when the spacing is less than 10 mm, the uniaxial strength does not appear to be a function of the spacing between the flaws.

It is well known that strain localization in compression loading of laboratory sample initiates on the boundary of the sample. Figure 7 shows the uniaxial strength as a function of the distance of the nearest flaw from the sample boundary. In general, the uniaxial strength

increases as the distance from the flaw to a free surface increases. This trend appears more pronounced in the samples with more than three flaws. By increasing the distance from the free boundary from 5mm to 10 mm the uniaxial strength increases approximately 150 MPa to about 165-170 MPa.

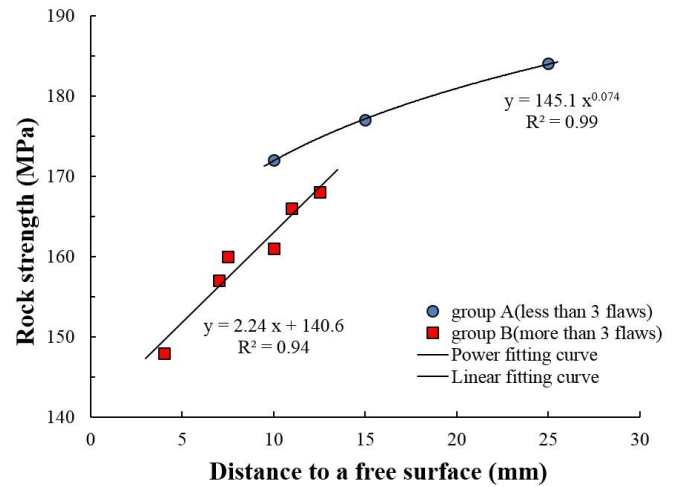


Fig. 7. Variation of rock strength as a function of distance between the flaw and the free boundary surface.

5. STRENGTH AND RANDOMLY DISTRIBUTED DISCONTINUOUS FLAWS

It is generally accepted that at the scale of engineering problems, i.e., tunnels and slopes, even massive rocks will likely contains some flaws. These flaws can occur at various scales, i.e. centimetre-scale where the flaws may be healed with infillings weaker than the intact rock or at the metre-scale where the flaws generally referred to as fractures, may be open.

5.1. Fracture intensity

Dershowitz and Einstein [19] suggested the following four parameters are required to describe the fracturing found in rock masses: (1) Orientation of the fractures, (2) Fracture size, (3) Fracture intensity, and (4) Spatial variation of the fractures. These four fundamental parameters describe the complexity and variability of the fractures. Today these parameters are quantified using the Discrete Fracture Network (DFN). Rogers et al. [20] provided an overview of the essential elements used in developing a DFN for a rock mass.

Among the parameters described by Dershowitz and Einstein [19], fracture intensity is used to describe the heterogeneous statistical nature of fracture systems. The fracture intensity is expressed using a P_{ij} system (P_{10} , P_{21} and P_{32}), describing the fractures in 1, 2 or 3 dimensions (Rogers et al., [20], [21]). The simplest fracture intensity measurement, P_{10} , describes the numbers of fractures per unit length of scan line [$\#/L^{-1}$]. P_{21} is defined as the length of fractures per unit area. As P_{21} directly incorporates fracture size and it is not scale-dependent.

Consequently P_{32} is defined as the area of fractures per unit volume in the three dimensions of the measurement. P_{21} , and P_{32} provides more information than fracture spacing alone.

5.2. Randomly distributed flaws

A number of grain-based models were used to assess the effect of randomly distributed discontinuous flaws on uniaxial strength. All flaws have the same properties and length with only their orientation randomly distributed.

Figure 8 shows the typical distribution of flaws in a sample. In all of these samples the fracture intensities, as defined by P_{21} , are the same. Because of the two-dimensional nature of the grain based model, P_{21} is equal to P_{32} .

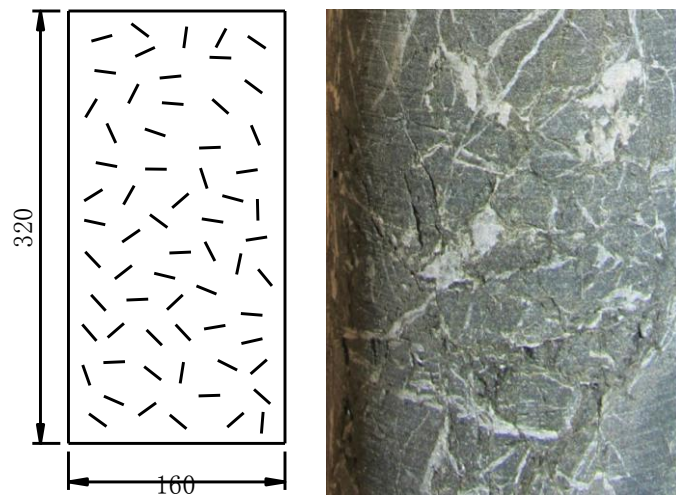


Fig. 8. Grain-based model with randomly distributed flaws compared to the flaws in a drill core. The length of each flaw is constant in the model.

In the sample in Figure 8, a single flaw length (c_i) was set equal to 14mm, which is approximately 3~5 times the mean grain size. The number of flaws in the each sample can be determined by fixing P_{21} equal to a constant. For example using $P_{21}=0.02$, a 50mm×100mm sample, the total length $\sum c = P_{21} \times 50 \times 100 = 100$. Hence,

the number of flaws: $n = (\sum c) / c_i = 100/14 \cong 7$. With an increase in sample size, the number of flaws will also increase accordingly in order to meet the requirement of constant fracture intensity. Alternatively, if the number of flaws are increased but the sample volume remains constant the fracture intensity increases.

The UCS results for grain-based samples with randomly distributed flaws and increasing fracture intensity are listed in Table 5. The first group of models were carried out with a flaw length of 14 mm. As shown in Table 5, as the fracture intensity increases from 0.02 to 0.10, i.e., number of flaws increases from 7 to 36, the UCS decreases from 206 MPa to 114 MPa. The same grain-based models were re-run with the flaw length increased from 14 mm to 16 mm. In order to keep the same

fracture intensity, the number of flaws was reduced. Table 5 also provides the UCS results for the $l = 16$ mm models.

Table 5. Modelling results of UCS tests for the samples (50mm×100mm) with two different configurations of flaw length. Parameter 'n' represents the number of pre-existing flaws in the sample.

P_{21}	$l = 14\text{mm}$		$l = 16\text{mm}$	
	n	UCS (MPa)	n	UCS (MPa)
0.02	7	206	6	196
0.03	11	202	10	189
0.04	14	194	13	183
0.05	18	188	16	177
0.06	21	178	20	138
0.08	28	169	25	94.8
0.10	36	114	32	71.4

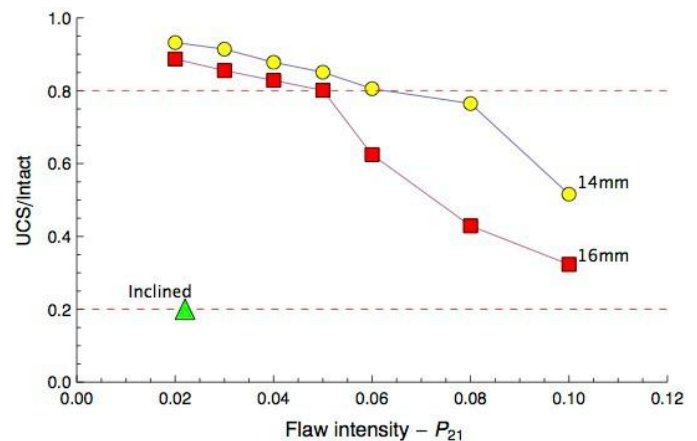


Fig. 9. The relationship between fracture intensity and strength for the grain-based models in Table 5.

The strength results for the grain-based models in Table 5 are normalized to the intact strength (221 MPa) with no flaws and are summarized in Figure 9. As expected the strength decreases as the fracture intensity increases. However, as shown in Figure 9 the strength reduction is not linear but appears to decrease significantly when the fracture intensity reaches a threshold value. This threshold value appears not to be a unique value but a function of the length of the flaw. For reference, also plotted in Figure 9 is the strength of the single through-going inclined flaw discussed in Section 3. The fracture intensity for the through-going flaw was taken with the strength a minimum in Equation 3. It is clear from Figure 9, the relationship between fracture intensity and strength is not unique. Nonetheless, such approaches may be useful for bounding rock mass strength.

6. CONCLUSIONS

A numerical grain-based model was successfully created that can capture the micro-structure and heterogeneity of rocks. The model allows for the modeling of intact rock and the inclusion of flaws within the intact rock matrix. The grain-based model was calibrated using laboratory results for an inclined through-going fracture. The model was then used to investigate the effect of various flaw distributions of the uniaxial compressive strength.

The findings from this work are:

- The uniaxial strength is directly related to the flaw inclination when there is only one through-going flaw. The peak strength approaches that of the intact rock when flaw is approximately vertical or horizontal. The strength reaches its minimum value when the flaw inclination ranges between 20-30°
- For uniform discontinuous flaw, both the inclination angle and number of flaws determine the uniaxial strength. For uniform flaws inclined at 45°, the strength is not significantly influenced by the number of flaws. However, the number of flaws and flaw spacing influences the strength of samples containing vertical flaws. Moreover, the strength decreases significantly as distance of the flaw to the free boundary decreases.
- For randomly distributed discontinuous flaws, the uniaxial strength decreases as the fracture intensity, expressed as P_{21} increases. There appears to be a threshold fracture intensity where the strength rapidly decreases but this threshold value is non-unique.

ACKNOWLEDGEMENTS

Swedish Nuclear Fuel and Waste Management Co. (SKB) Sweden, the Canadian Nuclear Waste Management Organization (NWMO) and the Natural Sciences and Engineering Research Council of Canada provided funding for this work.

REFERENCES

1. Jaeger, J.C. 1960. Shear failure of anisotropic rocks. *Geol. Magazine*.97: 65-72.
2. Potyondy, D.O., P.A. Cundall. 2004. A bonded-particle model for rock. *Int. J. Rock Mech. Min. Sci.* 41: 1329-1364.
3. Cho, N., C.D. Martin, and D.S. Segol. 2007. A clumped particle model for rock. *Int. J. Rock Mech. Min. Sci.* 44: 997-1010, doi: 10.1016/j.ijrmms.2007.02.002.
4. Cho, N. 2008. Discrete Element Modelling of rock: pre-peak fracturing and dilation. *PhD thesis, University of Alberta.*
5. Lan, H.X., C.D. Martin, B. HU. 2010. Effect of heterogeneity of brittle rock on micromechanical extensile behavior during compression loading. *J. of Geophys. Research, Vol. 115, B01202.*
6. Martin, C.D., and N. A. Chandler. 1993. Stress heterogeneity and geological structures. *Int. J. Rock Mech. Min. Sci. and Geomech. Abstract*, 30(7): 993-999.
7. Eberhardt, E, B. Stimpson, and D. Stead. 1999. "Effects of Grain Size on the Initiation and Propagation Thresholds of Stress-Induced Brittle Fractures." *Rock Mechanics and Rock Engineering* 32 (2) (May 19): 81–99.
8. Lau, J. S. O., and N A Chandler. 2004. "Innovative Laboratory Testing." *International Journal of Rock Mechanics & Mining Sciences*, 41(8) (December): 1427–1445.
9. Jackson, R., and J. S. O. Lau. 1990. "The Effect of Specimen Size on the Laboratory Mechanical Properties of Lac Du Bonnet Grey Granite." In, ed. A Pinto da Cunha, Proceedings of the First International Workshop On Scale Effects in Rock Masses, LEON, Norway, June 7-8, 165–174.
10. Fredrich, Joanne T., Brian Evans, and Teng-Fong Wong. 1990. "Effect of Grain Size on Brittle and Semibrittle Strength: Implications for Micromechanical Modelling of Failure in Compression." *Journal of Geophysical Research* 95 (B7): 10907–10920.
11. Berbenni, S, V Favier, and M Berveiller. 2007. "Impact of the Grain Size Distribution on the Yield Stress of Heterogeneous Materials." *International Journal of Plasticity* 23 (1) (January): 114–142.
12. Trask, P.D. 1932. *Origin and environment of source sediments of petroleum.* Gulf Pub., Huston.
13. Kelly, D.C., D.C. Peck, and R.S. James. 1994. Petrography of granitic samples from the 420 m level of the Underground Research Laboratory, Pinawa, Manitoba, report, Laurentian University, Sudbury, Ontario, Canada.
14. Donath, F.A. (1961). "Experimental study of shear failure in anisotropic rocks." *Geophysical Society of America Bulletin. Vol. 72*, June, pp. 985-990.
15. Brady, B.H.G, and E.T. Brown. 1993. *Rock Mechanics for Underground Mining.* Chapman & Hall.
16. Roy N. 1993. Engineering behavior of rock mass through study of jointed models. *Ph.d thesis. Indian Institute of Technology, Delhi.*
17. Teja, P. 2008. "An Experimental Study on Strength Behaviour of Jointed Rock Mass Through Modelling Under Uniaxial Compression." *BSc Thesis, Department of Civil Engineering, National Institute of Technology, Rourkela.*
18. Hoek, E., E.T. Brown. 1980. *Underground excavations in rock.* London: The Institution of Mining and Metallurgy.

19. Dershowitz, W.S., H.H. Einstein. 1988. Characterizing Rock Joint Geometry with Joint System Models. *Rock Mech. and Rock Eng. Vol 21*: 21-51.
20. Rogers, S., K.M. Moffitt and K.M. Kennard. 2006. Probabilistic slope and tunnel block stability analysis using realistic fracture network models. In *Proceeding of 41st U.S. Symposium on Rock Mechanics, Golden, CO*. ARMA/USRMS, 06-1052.
21. Rogers, S., D. Elmo and R. Beddoes & W. Dershowitz. 2009. Mine scale DFN Modelling and rapid upscaling in geomechanical simulations of large open pits. In *Proceeding of Slope Stability Conference on Large Open Pit Mine, Santiago, Chile, 09-11 November, 2009*.

NUMERICAL APPROACHES FOR ESTIMATING THE EFFECT OF SCALE ON ROCK MASS STRENGTH

C. Derek Martin, Yun Lu & Hengxing Lan

Dept. of Civil and Environmental Engineering, University of Alberta, Canada

Rolf Christiansson

SKB, Sweden

Summary

Scale effect is a general term that is often used to justify the decrease in rock strength as the sample size is increased. A review of laboratory results from 50 mm to 914 mm suggests that scale effects for intact rock are limited to approximately 80% of the standard laboratory strength obtained from 50-mm diameter cylindrical samples.

A discrete element formulation for simulating intact rock and discrete fractures was used in this study to examine the effect of fractures on rock strength. The results from the numerical model with uniform through-going fractures at various orientations relative to the applied load showed that the orientation of the fractures relative to the applied load controlled the rock strength and not the presence of multiple fractures.

The strength of a naturally fractured rock mass was also assessed numerically. Detailed mapping was used to quantify the spatial location of fractures in blocks extracted from the sidewall of a tunnel. Numerical simulations were used to establish the effect of confining pressures on the rock mass strength containing these fractures. The presence of these fractures reduced the unconfined strength to approximately 65 MPa while the intact strength was 211 MPa. A Geological Strength Index of 75 to 85 provides a reasonable fit to rock mass strength for confining stresses less than 5 MPa. RQD appears to be a better estimator for quantifying Geological Strength Index compared to block size.

1 Introduction

There are two contributors to rock mass strength: (1) the strength of the intact rock and (2) the strength of the fractures. The strength of intact rock and fractures can be measured in routine laboratory tests at small (typically centimetre) scales. Testing at larger scales is seldom practical and laboratory tests are replaced with empirical approaches such as the

Geological Strength Index. More recently, with the significant advances in computing power, there is a growing effort to replace the empirical approaches with numerical modelling that simulates the strength of the intact rock and that of the fractures. This approach utilizes a numerical technique that combines discrete element modelling of intact rock with discrete planar fractures.

A number of numerical simulations were used in this study to establish the effect of fractures on rock strength. The results from the numerical model with uniform through-going fractures at various orientations relative to the applied load are compared to findings from physical model studies. We then examine the strength of a naturally fractured rock mass where detailed mapping was used to quantify the spatial distribution of the fractures mapped on large blocks extracted from a tunnel wall. In both cases the results are compared to the strength derived from the Geological Strength Index and the Hoek-Brown failure criterion.

2 Scale effects in intact rock

The unconfined compressive strength of intact rock forms the cornerstone of rock mass classification systems when being used to estimate the rock mass strength. Hoek and Brown (1980) compiled the laboratory test results from high quality tests ranging in diameter from 10 mm to 200 mm diameter and normalized the data to a diameter (d) of 50 mm (UCS_{50}). Hoek and Brown (1980) suggested that the observed scale effect in Figure 1 could be approximated by:

$$UCS_d = UCS_{50} \left(\frac{50}{d}\right)^{0.18} \tag{1}$$

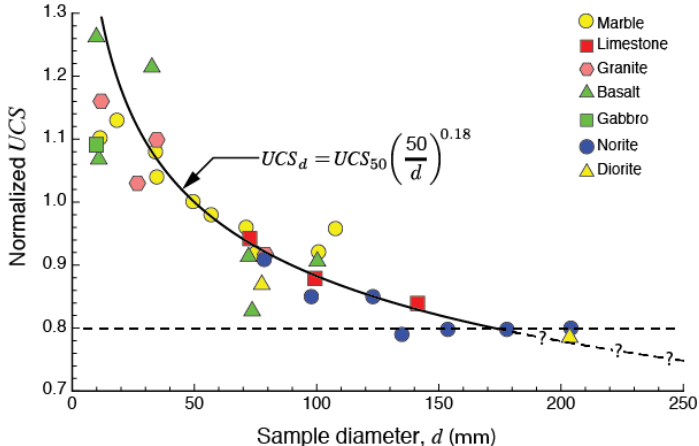


Figure 1. Effect of increasing diameter on the laboratory uniaxial compressive strength (UCS), data from Hoek and Brown (1980). The UCS has been normalized to the value obtained for 50-mm diameter.

The UCS predicted by Equation 1 offers no limits, hence if a laboratory UCS value of 200 MPa is measured, the UCS value at the scale of a typical tunnel, e.g., 5 m diameter, should be scaled to 87 MPa, approximately 0.4 UCS. Inspection of Figure 1 reveals that there is no data to support the reduction in the UCS value below approximately 0.8 UCS. One of the issues with the curve fit from Figure 1 is that the data is compiled from a variety of rock types, and no tests were carried out on samples greater than 200 mm diameter.

Jackson and Lau (1990) investigated the effect of scale on the UCS values for samples of Lac du Bonnet granite ranging from 33 mm to 294 mm diameter. They also observed a scale effect and suggested that Equation 1 could also be used to model the observed UCS scale effect up to about 150 mm diameter. Beyond 150-mm-diameter their data also showed there was no evidence of a scale effect on the intact strength.

Concrete has many of the same characteristics as hard rocks with the added advantage that the aggregate size and the sample size can be controlled. The most extensive concrete testing program carried out to examine the effect of scale on uniaxial compressive was reported by Blanks and McNamara (1935). The tests were carried out by the Bureau of Reclamation as part of their mass concrete research for the Boulder dam (later named the Hoover Dam). The tests varied in diameter from 50 mm to 914 mm with a length to diameter ratio of 2. The maximum aggregate size used for concrete mixes varied from 9.5 mm to 228.6 mm. The tests were used to determine the effect of various factors on compressive strength and Young's Modulus.

Blanks and McNamara (1935) concluded from their extensive testing program that the strength of the concrete decreases as the size of specimen is increased and for 914 mm diameter cylinders the strength reduced to 84 per cent of the small diameter samples (Figure 2).

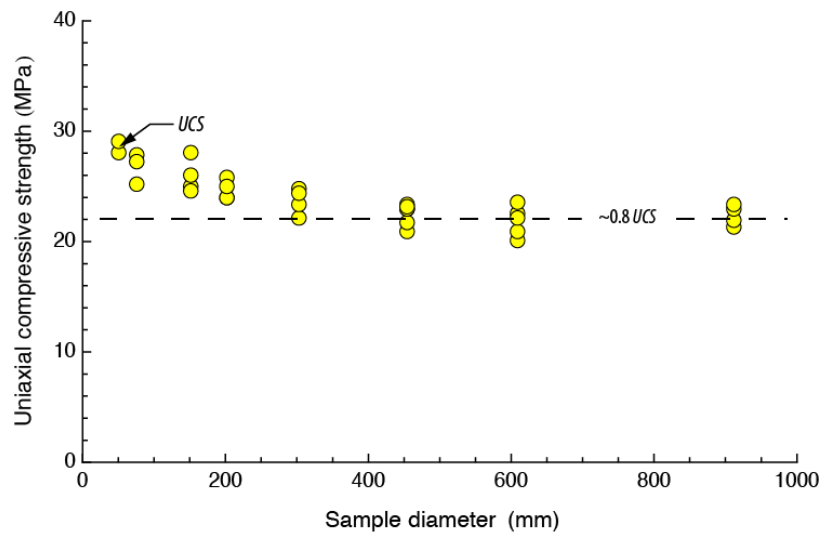


Figure 2: Effect of sample diameter on the uniaxial compressive strength of concrete, data from Blanks and McNamara (1935).

The results from Jackson and Lau (1990) and those from Blanks and McNamara (1935) on uniform intact material support the notion, that there is no evidence for scaling the intact laboratory UCS value (nominal diameter of 50 mm) to values lower than 0.8 UCS, regardless of large scale. This value of 0.8 is also consistent with the original data from Figure 1 and with the recommendation of Laubscher and Jakubec (2001) that the strength of a homogenous rock block should be reduced to 80% of the of laboratory tests to account for the small to large scale specimen effect.

3 Estimating Rock mass Strength

At the grain-scale most intact rocks consist of a variety of mineral grains at different sizes. These features give rise to several types of microscopic heterogeneity: geometric heterogeneity resulting from angular shape and grain size, elastic heterogeneity due to the stiffness contrast of different grains, and contact heterogeneity resulting from the anisotropy of contact distributions (length and orientation) and stiffness anisotropy. Lan et al. (2010) introduced the grain-based model based on the discrete element formulation used in the Universal Distinct Element Code (UDEC). A limitation of this grain-based approach is that the grains are unbreakable and hence damage is along grain boundaries. The grains can be made to yield using an appropriate constitutive model and failure criterion. However in most case assessing the peak strength is adequate and the non-breakable grains has little influence on peak strength.

The grain-based model (GBM) has a capability of dealing with a composition of multiple minerals to simulate the heterogeneous grain structure. The mineral grains are created using polygonal blocks based on a voronoi tessellation scheme. This tessellation scheme is created outside the UDEC program to generate a grain size distribution that matches the grain size distribution of the intact rock (Lan et al. 2010). As with all discrete element formulations used to simulate intact rock, a calibration process is required to find the model parameters that match the laboratory properties. The properties of the grain and their contacts play an important role in controlling macroscopic mechanical behaviors of the intact rock. A detailed procedure regarding modeling and generation of a model in grain scale is shown in Figure 3.

Lan et al (2010) demonstrated the importance of capturing the heterogeneity introduced by the block size, i.e., the grain size in intact rock. This block size is often used to capture the scale effects in rock masses. For example Cai et al (2004) attempted to quantify the well-known Geological Strength Index (GSI) by using Block Volume (Figure 4). The challenge of using a block volume is that while the strength index can be made scale dependent inserting the effect of project scale dependency is problematic. For example a GSI value of 30 in Figure 4, for a power house cavern would lead to very different strength issue if the cavern was replaced with a small diameter tunnel. Hence block volume, while compelling lacks the influence of project scale. More recently Hoek et al (2013) showed that two simple linear scales, Rock Quality Designation (RQD) and Bieniawski's Joint Condition (JCond₈₉), can be used to capture the blockiness and quality of the rock mass when combined with discontinuity surface conditions (Figure 5). This approach avoids the scale-issue introduced by rock volume.

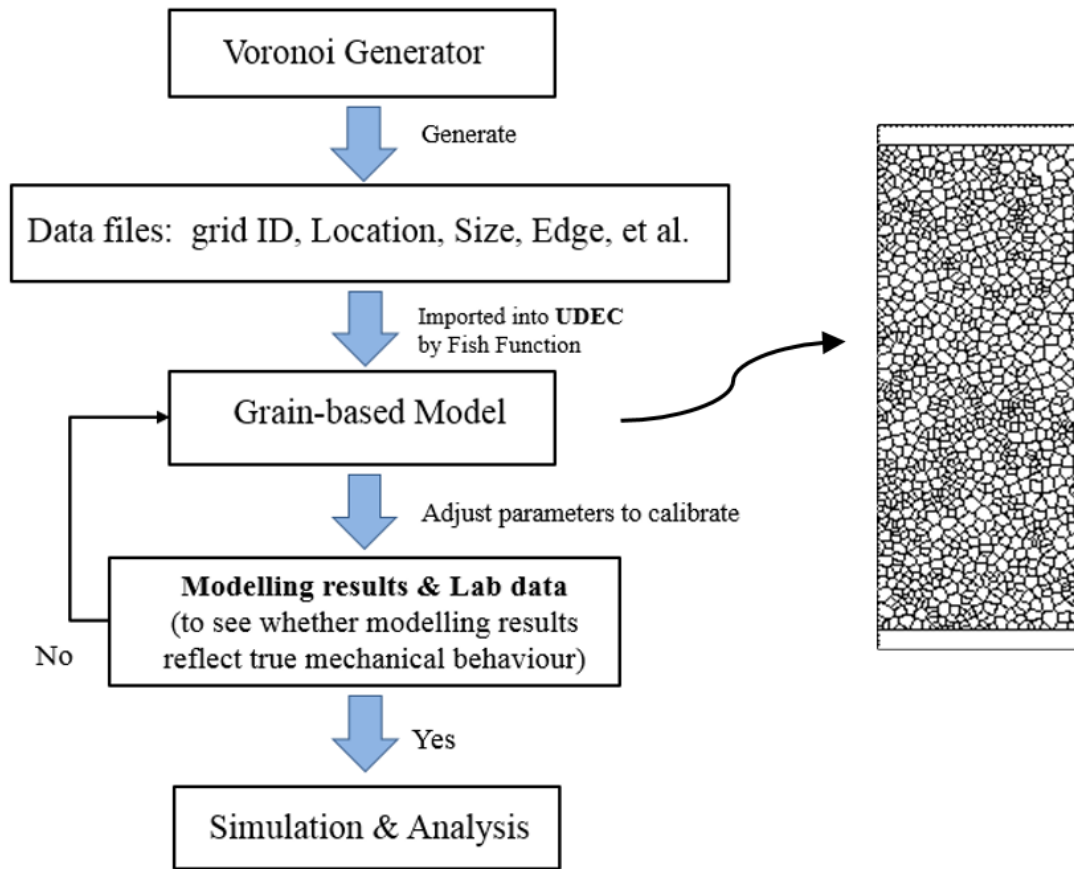
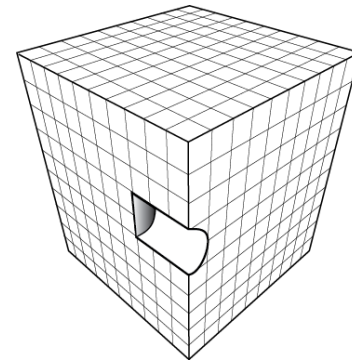
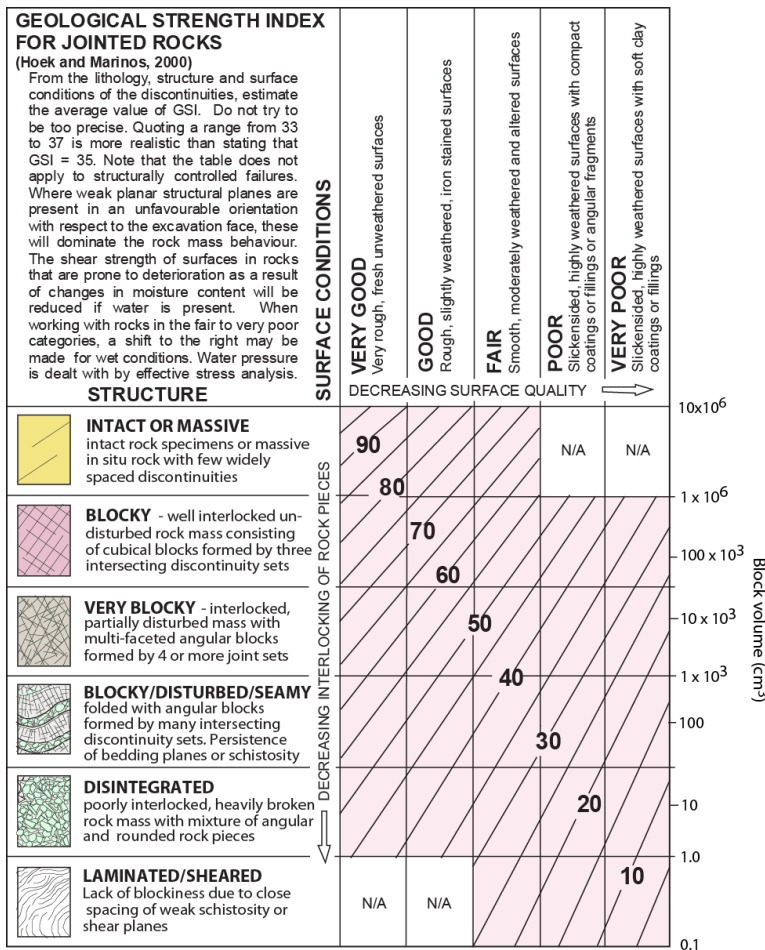


Figure 3: Illustration of generation of grain-based model combined with voronoi tessellation and a flow chart presenting the procedure of numerical modeling including data import and parameter calibration.



b) Illustration of block size and project scale.

a) GSI and Block volume

Figure 4: Illustration of the importance of block size on rock mass strength, (modified from Cai et al (2004).

The Geological Strength Index was introduced to obtain rock mass properties for input into numerical models. However, unless GSI is calibrated with in situ measurements, there is essentially no way of knowing if the predicted rock mass strength is valid. Diederichs et al (2010) showed that the input parameters determined using GSI did not provide an adequate estimate of the rock mass spalling strength. Hence in order to have confidence in the empirical approach provided by the Geological Strength Index, there is a need to find alternative means to calibrate the results. In the following section the Grained Based Model is used to estimate rock mass strength.

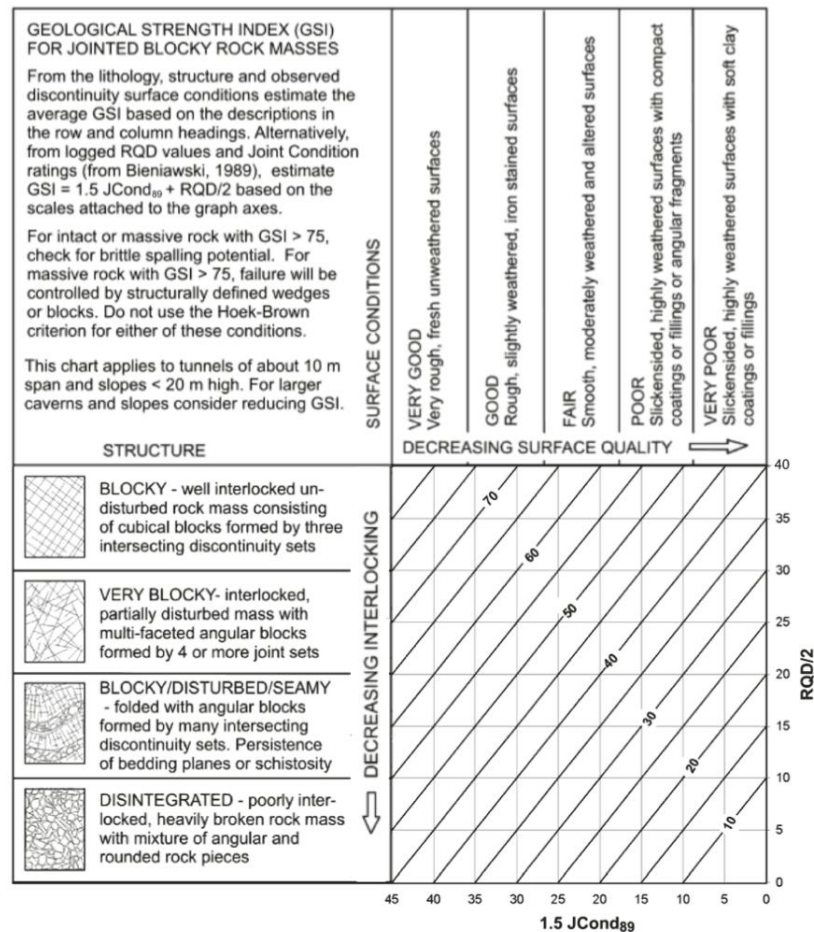


Figure 5: Quantification of GSI by Joint Condition and RQD, from Hoek et al., 2013.

4 Uniform fracture geometry and strength

Lan et al (2010) demonstrated that the grain-based modeling approach was suitable for investigating the behaviour of intact rock and Lu et al (2013) showed that the same approach could be used for estimating rock strength containing continuous and discontinuous flaws. In this section the grain-based model is used to estimate the strength of a synthetic rock with regular through going fractures.

Brown and Trollope (1970) and Einstein et al. (1969) conducted a number of physical model tests to establish the effect of fractures on rock mass strength. Their tests were carried out using a plaster model with continuous fracture planes. Figure 6 shows the nominal 100mm x 100mm x 200mm physical models used by Brown and Trollope (1970). The uniaxial compressive strength of the solid material was 20.75 MPa with a porosity of

30% and the confinement used for the tests ranged from 0 to 6.9 MPa. While the porosity of the plaster is far greater than that observed in most rocks, plaster reproduces many of the brittle characteristics of rock provided the confining stress is relatively low. The results from the model studies carried out by Brown and Trollope (1970) are shown in Figure 7. The results in Figure 7 have been normalized to the unconfined compressive strength of the intact sample (20.75 MPa). The results in Figure 7 clearly demonstrate the effect of confinement and the inclination of the through-going fractures on the model strength. It is also clear from Figure 7 that at the high confining stress stresses, the brittle nature of the plaster was replaced with more ductile/plastic behaviour.

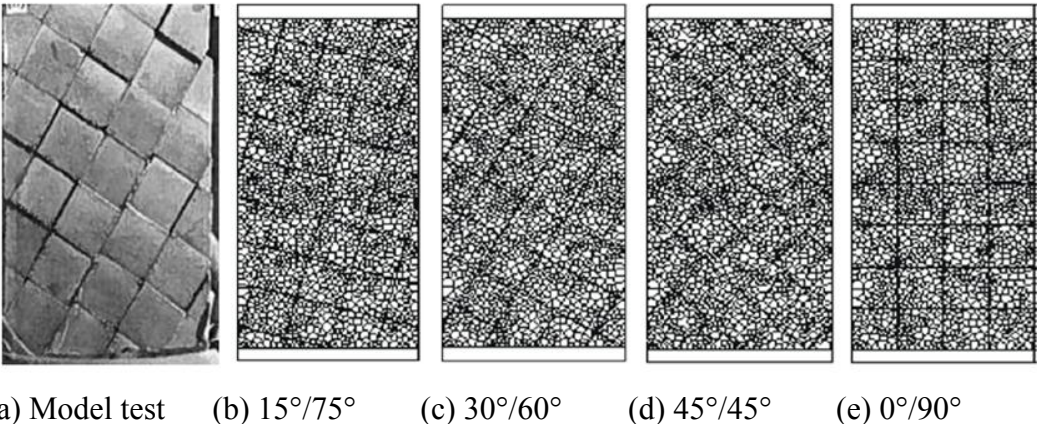


Figure 6: Physical model samples and the inclination of the through going flaws used by Brown and Trollope (1970).

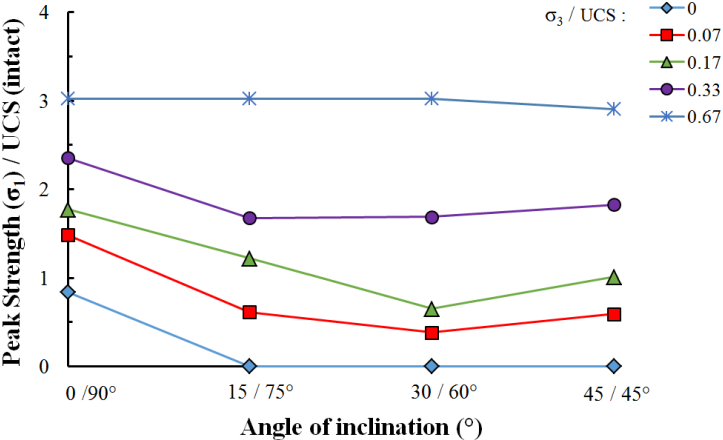


Figure 7: Test results from Brown & Trollope (1970) for gypsum plaster. The results have been normalized to unconfined compressive strength of the intact sample (20.75 MPa).

The physical models used by Brown and Trollope (1970) were created and analyzed using the grained based model to establish the robustness of the modelling approach. Instead of using the plaster samples, four samples of Lac du Bonnet (LdB) granite were created. The intact properties of LdB were established by Lan et al (2010) and the through-going fractures were assigned the same inclination and geometry as that given in Figure 6. The LdB block had a width of 50mm with a height of 100mm and each of the small blocks measured 12.5mm × 12.5mm. The strength of the through-going fractures was set to 30 degrees with zero cohesion. The confining stress used in the simulations was 0, 15, 35, 55 and 70 MPa. The results for Lac du Bonnet granite are shown in Figure 8 and like the results from Brown and Trollope (1970) illustrate that the orientation of the fractures when the fracture is inclined to the direction of loading controls the strength. The blocky nature of the material had no effect on the ultimate strength when fractures were inclined parallel and perpendicular (0/90°) to the direction of loading. In fact the blocks at this orientation had essentially the same strength as the uniaxial compressive strength of the intact material suggesting no scale effects for this inclination. These results also highlight the difficulty of determining the strength based only on block size.

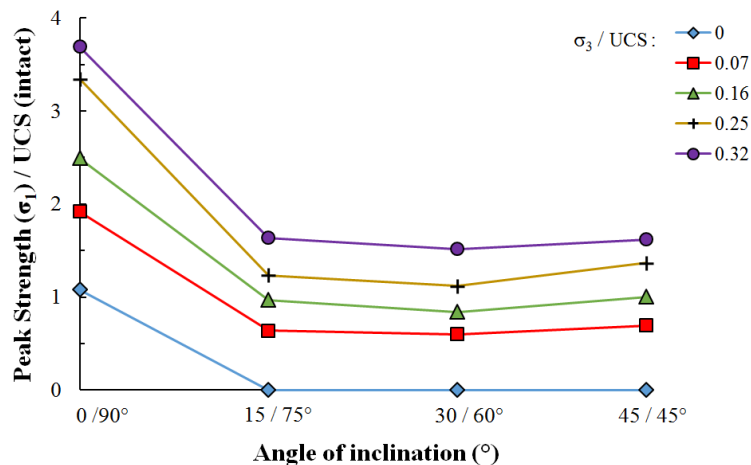


Figure 8: The effect of fracture inclination on the strength of Lac du Bonnet granite. The model geometry is given in Figure 6.

5 Heterogeneous fracture geometry and strength

The previous section demonstrated the importance of through-going fractures and their orientations relative to loading direction on rock strength. In tunnel excavations, the potential instabilities are generally associated with the tunnel perimeter where fractures are loaded by the tangential boundary stresses. The rock mass at the Äspö Hard Rock Laboratory (HRL), Sweden, is typical of the granitic rock masses found in the Scandinavian Shield. It contains several fracture sets that vary in both trace length and

fracture frequency. A number of blocks 1m wide along the tunnel axis and 0.6 to 1m deep by 1.5m high were extracted from the wall of tunnel located at the 450 Level of the Äspö (Figure 9). These blocks cut into 100mm thick slabs and were mapped in detail to extract the geometry for the fracture network encountered in the tunnel wall (Christiansson et al, 2009). The mapped fractures were either blast-induced, sealed natural fractures or open natural fractures. Figure 10 shows an example block/slab and the mapped open natural fractures. These natural fractures were mapped to within 1 mm accuracy and red dye was used to help locate the termination of the fractures. The x-y coordinates of these mapped open fractures were then used to create a numerical fractured rock mass by adding them to the grain-based model.

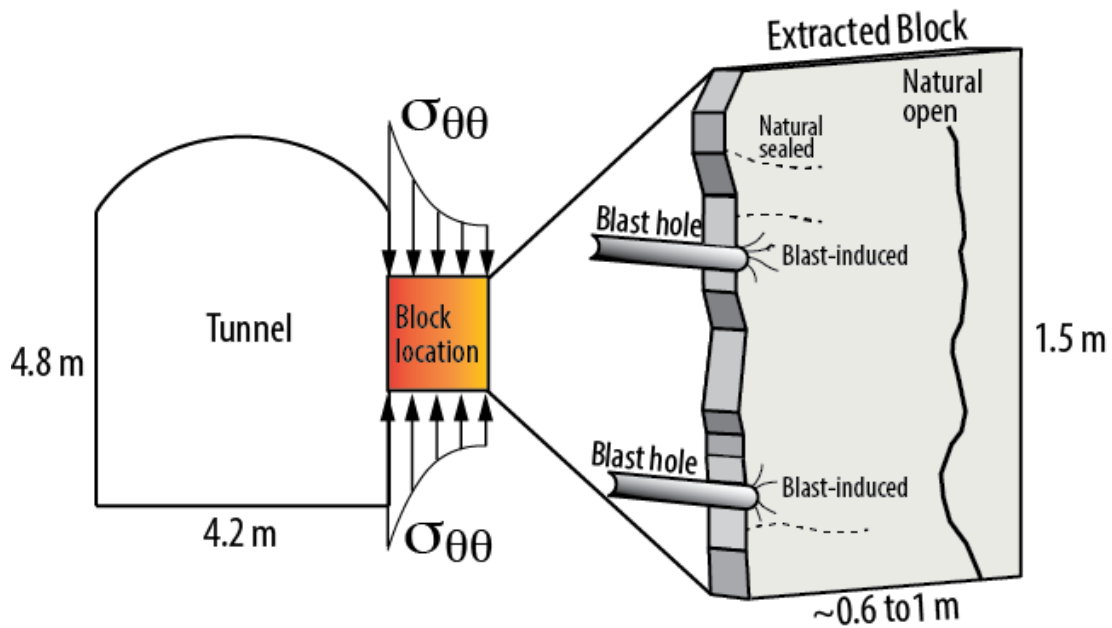


Figure 9: Illustration of the location of the blocks for detailed fracture mapping and boundary loading conditions.



(a) Identified fractures



(b) Fracture trace map

Figure 10: Example of the detailed fracture mapping for block VS0039B03 and the fracture traces used in the numerical model. The colouring of the block resulted from the red dye used to help locate the fractures. See Olsson et al 2009 for details on the block mapping procedure.

Once the numerical rock mass was created a series of bi-axial tests were carried out to establish the rock mass strength as a function of confining stress. When building the numerical rock mass, the fractures were not allowed to penetrate the block boundary. This was purposely chosen to remove the effect of the strength being dominated by a single through-going fracture. For comparison purposes a series of bi-axial numerical tests were also carried out on a block of intact rock. The results from both the intact and fractured rock blocks are summarized in Figure 11a. It is clear from Figure 11a, the strength of the fractured rock is considerably less than that of the intact rock, despite the lack of through-going fractures in the numerical samples.

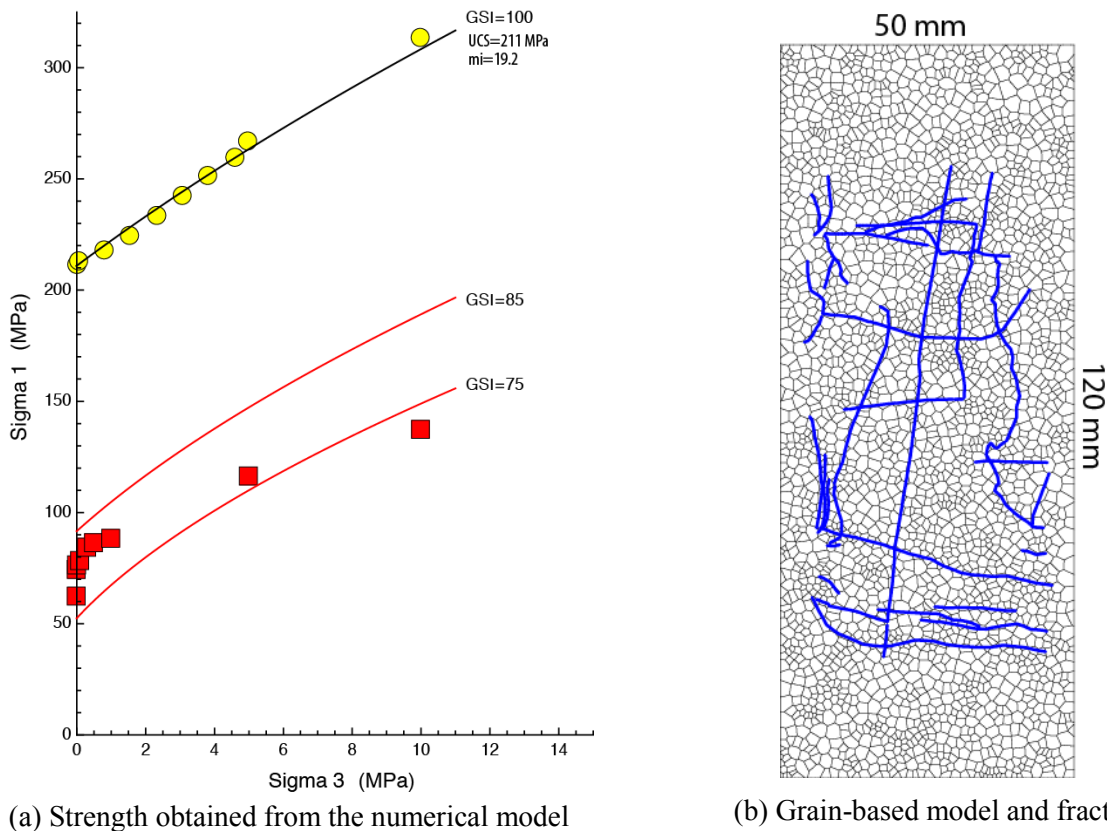


Figure 11: Comparison of the numerical strength of the block in Figure 9 with that predicted by Hoek-Brown and GSI.

The results from the intact and fractured numerical models were compared to the Hoek-Brown failure criterion. The equations used in the Hoek-Brown failure criterion are given in Hoek et al (2002) and are not repeated here. An excellent fit to the intact strength is obtained using a uniaxial compressive strength of 211 MPa, and a m_i value of 19.2, with $a=0.5$. For the fractured rock mass, the GSI values between 75 and 85, and the associated Hoek-Brown parameters provide a reasonable fit to the data for confining stresses less than 5 MPa but tend to over predict the strength at confining stresses above 5 MPa. As noted by Marinos and Hoek (2000) GSI values should not be reported as precise values but instead given as a range. The finding from this limited data set support that notion.

At present there is no way to link the GSI value to the fractures mapped in the rock block. Inspection of Figure 4, would suggest that for a GSI value between 75 and 85, a block size of $1 \times 10^6 \text{ cm}^3$ should be expected. However, the fractures locations in Figure 10 illustrates that this block size is not adequate for describing the fractures encountered in the tunnel wall.

Figure 5 shows the correlations between GSI and RQD recently proposed by Hoek et al (2013). Eight scan lines, 3 horizontal, 3 vertical and 2 diagonal, were used to calculate the RQD value for the block geometry in Figure 10. The RQD values ranged from 63 to 93 with a mean RQD value of 82. This value of 82 when combined with the fracture condition number would give a GSI value in the 75 to 85 range and is in agreement with the back-calculated GSI value.

An alternative to the RQD and block volume is the fracture intensity. Defining fracture intensity offers a wide range of possible measures. A unified system of fracture intensity, expressed as P_{ij} , was described in Dershowitz and Herda (1992) and summarized by Rogers et al (2009). An alternative to the P_{10} fracture intensity expressed as the number of fractures per unit length of borehole, is P_{21} expressed as fracture trace length per unit area. The fracture trace length per unit area for the block in Figure 10 is 0.307 m/m^2 . Currently there is no simple means of relating fracture trace length per unit area with GSI values, and additional data is needed to see if such a correlation can be developed.

6 Conclusion

Scale effect is a general term that is often used to justify the decrease in rock strength as the sample size is increased. A review of laboratory results from 50 mm to 914 mm suggests that scale effects for intact rock are limited to approximately 80% of the standard laboratory strength obtained from 50-mm diameter cylindrical samples.

A grain-based model that relies on discrete element formulation for simulating intact rock and discrete fractures was used in this study to examine the effect of fractures on rock strength. The results from the numerical model with uniform through-going fractures at various orientations relative to the applied load showed that the orientation of the fractures relative to the applied load controlled the rock strength and not the presence of multiple fractures. When the fractures were oriented perpendicular and parallel to the direction of loading the rock strength was essentially the same as the intact rock strength without the fractures.

The strength of a naturally fractured rock mass was also assessed using the same grain-based model. Detailed mapping was used to quantify the spatial location of the blast induced and natural fractures in blocks extracted from the sidewall of a tunnel. A number of numerical simulations were used to establish the effect of confining pressures on the rock mass strength containing these fractures. The presence of these fractures reduced the unconfined strength to approximately 65 MPa while the intact strength was 211 MPa. A Geological Strength Index of 75 to 85 provides a reasonable fit to rock mass strength for

confining stresses less than 5 MPa. Above confining stresses above 5 MPa, the GSI approach overestimates the rock mass strength.

Despite the advances in the numerical approach there does not appear to be a straightforward method for correlating empirical GSI derived strengths to the numerically derived strengths. From these limited results the simple Rock Quality Index (RQD) appears to be a better descriptor for quantifying GSI.

Acknowledgements

Swedish Nuclear Fuel and Waste Management Co. (SKB) Sweden, the Canadian Nuclear Waste Management Organization (NWMO) and the Natural Sciences and Engineering Research Council of Canada (NSERC) provided funding for this work.

References

- Brown, E. T. and Trollope, D. H. 1970. Strength of a model of jointed rock. *ASCE Journal of the Soil Mechanics and Foundations Division*, 96(2):685–704.
- Cai, M., P. Kaiser, H. Uno, Y. Tasaka, and M. Minami. 2004. Estimation of rock mass deformation modulus and strength of jointed hard rock masses using the GSI system. *International Journal of Rock Mechanics & Mining Sciences*, Vol. 41, No. 1, pp. 3–19.
- Christiansson, R., L. O. Ericsson, and G. Gustafson. 2009. Hydraulic Characterisation And Conceptual Modelling Of The Excavation Disturbed Zone (EDZ). In *Proc. ISRM-Sponsored International Symposium on Rock Mechanics: Rock Characterisation, Modelling and Engineering Design Methods*, SINOROCK 2009. Paper No 126.
- Dershowitz, W. S., and H. H. Herda. 1992. Interpretation of fracture spacing and intensity. In *Proceedings of the 33rd US Symposium on Rock Mechanics*, Santa Fe. Edited by: J R Tillerson and W R Wawersik, pp. 757-766.
- Diederichs, M. S., T. Carter, and C. D. Martin. 2010. Practical Rock Spall Prediction in Tunnels. In *Proceedings ITA World Tunnel Congress, Vancouver*, No. CD-ROM, E. Eberhardt, ed., pp. 1–8.
- Einstein, H. H., Nelson, R. A., Bruhn, R. W., and Hirschfeld, R. C. 1969. Model studies of jointed-rock behaviour. In *Proceedings 11th U.S. Symposium on Rock Mechanics*, Berkeley, pages 83–103.
- Hoek, E., Carranza-Torres, C., and Corkum, B. (2002). Hoek-Brown failure criterion - 2002 edition. In Hammah, R., Bawden, W., Curran, J., and Telesnicki, M., editors, *Proc. 5th North American Rock Mechanics Symposium and 17th Tunnelling Association of Canada Conference: NARMS- TAC*, Toronto, vol. 1, pp. 267–273. University of Toronto Press.

- Hoek, E., T. G. Carter, and M. S. Diederichs. 2013. Quantification of the Geological Strength Index chart. In CD-ROM Proceedings 47th US Rock Mechanics/Geomechanics Symposium, San Francisco.
- Lan, H., C. D. Martin, and B. Hu. Jan. 2010. Effect of heterogeneity of brittle rock on micromechanical extensile behavior during compression loading. *Journal of Geophysical Research*, Vol. 115, No. B1, p. B01202.
- Laubscher, D. H. & Jakubec, J. 2001. The MRMR Rock Mass Classification for Jointed Rock Masses. In *Underground Mining Methods: Engineering Fundamentals and International Case Studies*, pp 475–481, Society of Mining Metallurgy and Exploration, SMME.
- Lu, Y, C.D. Martin, and H. Lan. 2013. Strength of intact rock containing flaws. In CD-ROM Proceedings 47th US Rock Mechanics/Geomechanics Symposium, San Francisco.
- Marinos, P. and Hoek, E. (2000). GSI: A geological friendly tool for rock mass strength estimation. In Proc. GeoEng2000, An International Conference on Geotechnical & Geological Engineering Melbourne, volume 1: Invited Papers, pages 1422–1440, Lancaster. Technomic Publishing Co., Inc.
- Olsson, Mats; Ingemar Markström, Anders Pettersson, and Malin Sträng (2009) Examination of the Excavation Damaged Zone in the TASS tunnel, Äspö HRL. SKB Report R-09-39, Swedish Nuclear Fuel and Waste Management Co, Stockholm. www.skb.se
- Rogers, S., D. Elmo, and R. Beddoes. 2009. Mine scale DFN modelling and rapid upscaling in geomechanical simulations of large open pits. In CD-ROM Proceedings of International Conference on Slope Stability, Santiago Chile.